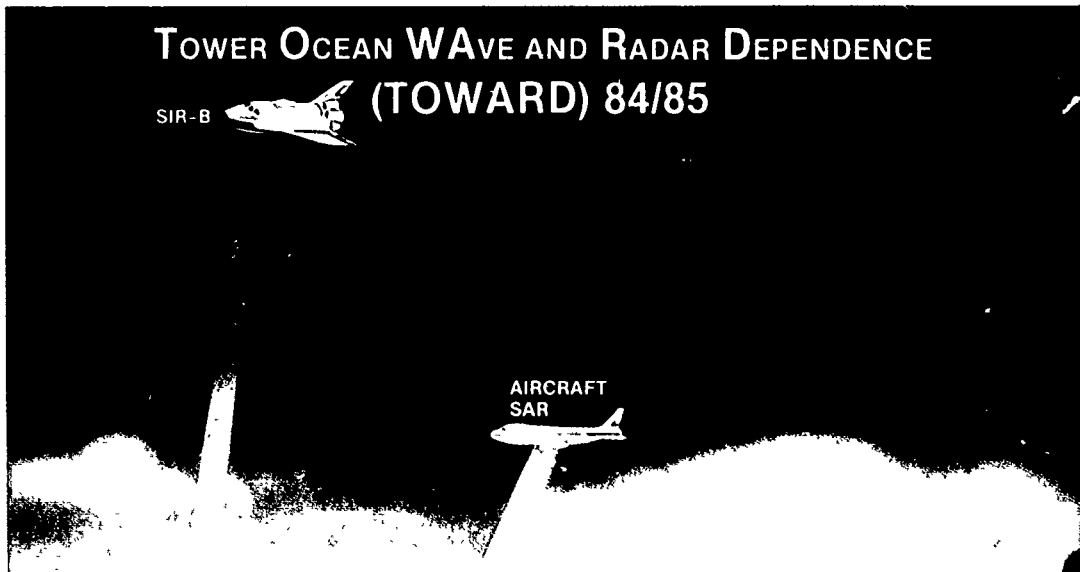
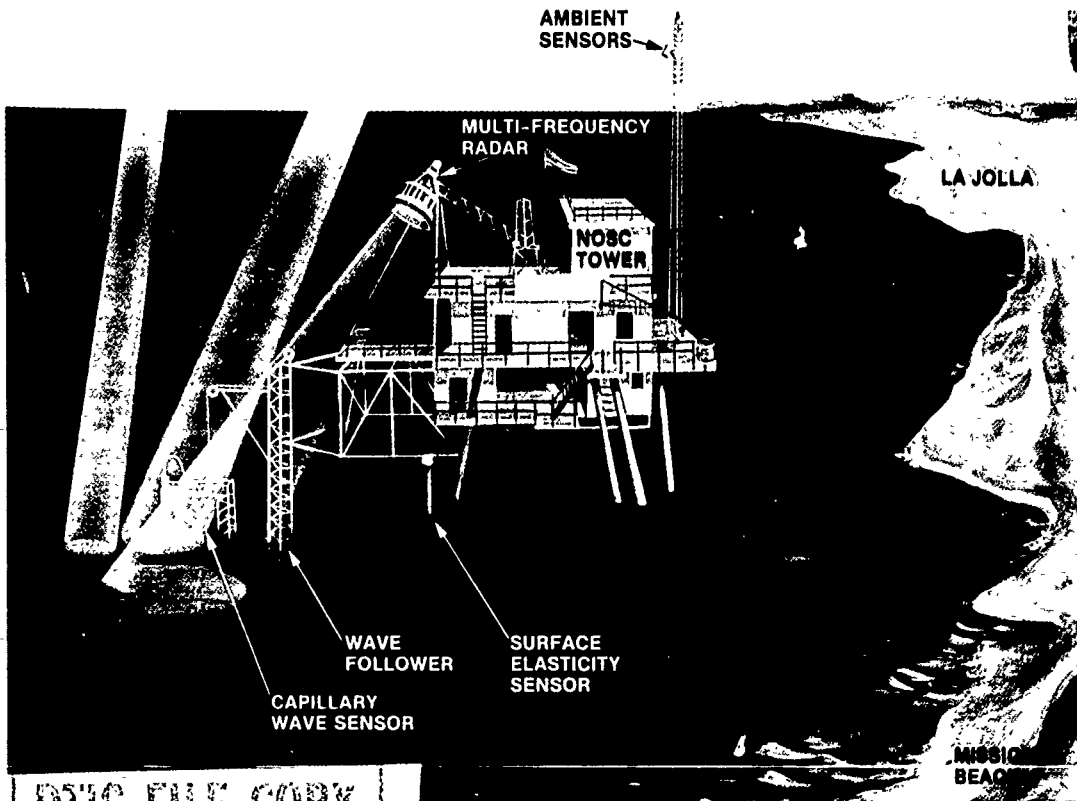


1



DTIC  
ELECTE  
APR 15 1991



DTIC FILE COPY

# Tower Ocean Wave and Radar Dependence

Reprinted from the Journal of Geophysical Resea

DISTRIBUTION STATEMENT A  
Approved for public release  
Distribution Unlimited

91 1 31 01W

# Tower Ocean Wave and Radar Dependence

*From the Journal of Geophysical Research*

Volume 93, Number C11, November 15, 1988

Volume 95, Number C9, September 15, 1990

Per phonecon 4/9/91. Available for  
\$10.00 from American Geophysical Union  
2000 Florida Ave; DC 20009  
JK 4/9/91

Accession For	
NTIS CR/CI	<input checked="" type="checkbox"/>
DTIC TAB	<input type="checkbox"/>
Unannounced	<input type="checkbox"/>
J. Allocation	
By <u>10.00</u>	
Distribution /	
Availability Codes	
Dist	Avail and/or Special
<u>A-1</u>	<u>21</u>



PUBLISHED BY AMERICAN GEOPHYSICAL UNION

This artistic sketch depicts the experiment entitled Tower Ocean Wave and Radar Dependence (TOWARD). The experiment was conducted from the Naval Ocean Systems Center (NOSC) tower, offshore of Mission Beach, immediately south of La Jolla, California, during October 1984 to January 1986. The measurements included in situ oceanographic and surface hydrodynamic measurements, near-surface radar backscatter measurements, and airborne and spaceborne radar measurements. The spaceborne element did not materialize. The remaining set constitutes the basis for the scientific contributions included in this publication. This work was supported by the Office of the Chief of Naval Research (OCNR), and Synthetic Aperture Radar Program with H. Dolezalek as scientific officer.

*O. H. Shemdin*  
*Ocean Research and Engineering*  
*Pasadena, California*

Copyright 1990 American Geophysical Union, 2000 Florida Avenue, N.W., Washington, D. C. 20009. Figures, tables, and short excerpts may be reprinted in scientific books and journals if the source is properly cited; all other rights reserved.

ISBN: 87590-765-2

TOWER OCEAN WAVE AND RADAR DEPENDENCE (TOWARD)

- Tower Ocean Wave and Radar Dependence Experiment: An Overview (Paper 88JC03199)  
*O. H. Shemdin* 13,829
- Theory for Synthetic Aperture Radar Imaging of the Ocean Surface: With Application to the Tower Ocean Wave and Radar Dependence Experiment on Focus, Resolution, and Wave Height Spectra (Paper 8C0364)  
*Dayalan P. Kasilingam and Omar H. Shemdin* 13,837
- Multifocus Processing of *L* Band Synthetic Aperture Radar Images of Ocean Waves Obtained During the Tower Ocean Wave and Radar Dependence Experiment (Paper 88JC03067)  
*E. K. Tajirian* 13,849
- An Analytic Representation of the Synthetic Aperture Radar Image Spectrum for Ocean Waves (Paper 8C0249)  
*David R. Lyzenga* 13,859
- Comparisons of Simulated and Actual Synthetic Aperture Radar Gravity Wave Images (Paper 8C0187)  
*Robert O. Harger and Can E. Korman* 13,867
- Comparison of Measured and Predicted Sea Surface Spectra of Short Waves (Paper 88JC03151)  
*O. H. Shemdin and P. A. Hwang* 13,883
- Directional Measurement of Short Ocean Waves With Stereophotography (Paper 88JC03064)  
*Omar H. Shemdin, H. Minh Tran, and S. C. Wu* 13,891
- The Dependence of Sea Surface Slope on Atmospheric Stability and Swell Conditions (Paper 8C0363)  
*Paul A. Hwang and Omar H. Shemdin* 13,903
- Wind Stress Measurements During the Tower Ocean Wave and Radar Dependence Experiment (Paper 8C0233)  
*G. L. Geernaert, K. L. Davidson, S. E. Larsen, and T. Mikkelsen* 13,913
- Tower Ocean Wave and Radar Dependence Experiment: A Synthesis (Paper 90JC00764)  
*O. H. Shemdin* 16,241
- Focusing Simulations of Synthetic Aperture Radar Ocean Images (Paper 90JC00765)  
*D. W. Hayt, W. Alpers, C. Brüning, R. DeWitt, F. Henyey, D. P. Kasilingam, W. C. Keller, D. R. Lyzenga, W. J. Plant, R. L. Schult, O. H. Shemdin, and J. A. Wright* 16,245
- Models for Synthetic Aperture Radar Imaging of the Ocean: A Comparison (Paper 90JC00766)  
*Dayalan P. Kasilingam and Omar H. Shemdin* 16,263
- Cross Sections and Modulation Transfer Functions at *L* and *K<sub>u</sub>* Bands Measured During the Tower Ocean Wave and Radar Dependence Experiment (Paper 90JC00345)  
*William C. Keller and William J. Plant* 16,277
- The Modulation of a Radar Signal From the Ocean Surface Due to Slope and Hydrodynamic Effects (Paper 88JC04252)  
*James C. West, Paul A. Hwang, Richard K. Moore, Julian C. Holtzman, and Omar H. Shemdin* 16,291
- Evidence of Bragg Scattering in Microwave Doppler Spectra of Sea Return (Paper 89JC00787)  
*William J. Plant and William C. Keller* 16,299
- Modulation of Short Waves by Surface Currents: A Numerical Solution (Paper 89JC01589)  
*Paul A. Hwang and Omar H. Shemdin* 16,311
- Synthetic Aperture Radar Imaging of Ship Wakes in the Gulf of Alaska (Paper 90JC00486)  
*Omar H. Shemdin* 16,319

# Tower Ocean Wave and Radar Dependence Experiment: An Overview

O. H. SHEMDIN<sup>1</sup>

*Jet Propulsion Laboratory, California Institute of Technology, Pasadena*

The Tower Ocean Wave and Radar Dependence Experiment (TOWARD) is a coordinated effort, involving both field experimentation and theoretical investigations, to address the divergent hypotheses on the mechanisms involved in synthetic aperture radar (SAR) imaging of the ocean surface. In the formulation of the experiment it was recognized that three distinct disciplines were to be addressed: (1) hydrodynamics, (2) radar backscatter, and (3) SAR image processing. The field operations were executed in three 6-week segments during the period October 1984 to January 1986. The Naval Ocean Systems Center tower, located offshore of Mission Beach, San Diego, California, was used as the focal point for the field operations. The primary measurements included in situ capillary and short gravity waves, long surface waves and internal waves, ambient current and detailed meteorological measurements, stereophotography, tower-based multifrequency radars and an L band SAR deployed on board the NASA CV-990. The single most significant result is the determination that none of the available hypotheses on SAR imaging of long surface waves could be demonstrated to explain all the SAR observations obtained in TOWARD. Specific results are reported.

## 1. INTRODUCTION

The dynamics of short waves are intimately related to our ability to understand microwave remote sensing techniques, especially the synthetic aperture radar (SAR). As a result of recent field experiments, major insights were gained on the dynamics of 30-cm long waves (L band). The shorter 3.0-cm waves (X band) are more sensitive to near-surface currents; hence their dynamics are less understood [Hsiao and Shemdin, 1983]. There is need for a systematic investigation of the dynamics of short waves with wavelengths of 1-100 cm in order to amend critical gaps in our present knowledge.

Radar backscatter from the sea surface is known to be dominated by specular backscatter for incidence angles of less than 20° (nadir is 0) and by Bragg backscatter for incidence angles in the range 20°-70° [Valenzuela, 1978]. At incidence angles greater than 70°, wave sheltering plays an important role. Such a relatively simplified description of backscatter has been questioned recently by Kwoh and Lake [1983], who suggest, on the basis of laboratory studies, that specular and wedge type backscattering may be significant at incidence angles greater than 20°.

Backscatter from the ocean is clearly dependent on such environmental parameters as wind speed, atmospheric stability, local currents induced by orbital velocities of long surface waves or internal waves, and surface compressibility. A detailed understanding of the nature of backscattering mechanisms can be achieved only if (1) an in situ description of the sea surface is obtained simultaneously in wave number scales that contribute to radar backscatter and (2) the ambient environment is specified in its vicinity during the same period.

While significant progress has been achieved to date on SAR imaging of ocean surface features, gaps remain that require immediate investigation. These gaps fall into three categories: (1) The hydrodynamic description of the ocean surface, in wave number scales that contribute to back

scattering, under various environmental conditions. (2) Radar backscatter mechanisms from the ocean surface these include Bragg, specular, wedge, and tilt mechanisms; First- and higher-order Bragg scattering also require additional investigation. (3) The quantitative determination of the relative importance of various modulation mechanisms on SAR imaging of the ocean surface, under various geometries and environmental conditions. These include, but are not limited to, the relationship between the ocean surface wave height spectrum and the SAR image spectrum, the effects of focus adjustment, wave height, and wavelength on detectability, and the detection of ocean surface features induced by slicks or by the convergence or divergence of surface currents. These above processes are depicted schematically in Figure 1.

The specific scientific objectives of the TOWARD experiment are (1) to investigate experimentally the linear and nonlinear hydrodynamics of short surface waves modulated by long waves, (2) to verify assumptions stipulated in radar backscatter theory that are used in SAR imaging of the ocean surface, and (3) to develop a verifiable theory for SAR imaging of the ocean surface.

Because it was recognized from the outset that a multidisciplinary data set is required to resolve the outstanding issues, the following guidelines were adopted for the TOWARD experiment: (1) Use a stable platform so that measurements of short waves and radar backscatter can be free of platform motion. (2) Provide simultaneous measurements of short waves, long waves, and relevant environmental parameters. (3) Obtain SAR images of the ocean surface at various azimuthal angles, height-to-velocity ratios, and environmental conditions. (4) Provide SAR digital recording and processing to facilitate precise variations in SAR processing parameters. (5) Incorporate specialized sensors for measuring surface tension, decay rate of short waves, and near-surface wind speed.

## 2. THE FIELD SITE AND MEASUREMENT CAPABILITIES

The Naval Ocean Systems Center (NOSC) tower was used as the stable platform for the TOWARD experiment. The

<sup>1</sup>Now at Ocean Research and Engineering, Pasadena, California.

Copyright 1988 by the American Geophysical Union.

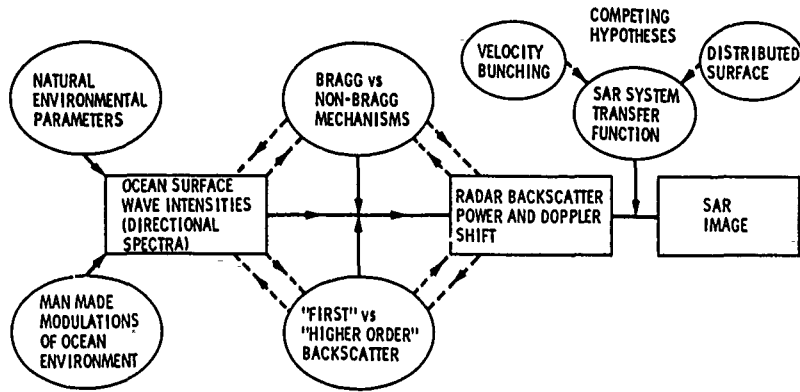


Fig. 1. Schematic of processes involved in SAR imaging of the ocean surface.

tower is located at 32°47'N and 117°17'W, 1.4 km offshore of Mission Beach, San Diego, California, in 18-m water depth.

The NOSC tower is situated in the Southern California Bight, the western end of which is delineated by the Channel Islands of southern California (see Figure 2). The North Pacific storms generate waves which propagate as swell to southern California and enter the Southern California Bight through the windows between the Channel Islands. A typical storm is shown in Figure 3. Southern swell is also encountered at the tower from distinct South Pacific storms. The latter is generally smaller in amplitude and longer in period than the North Pacific swell.

The bathymetry surrounding the NOSC tower is given by Tajirian [this issue]. The water depth 10 km offshore of the

tower exceeds 100 m (50 fathoms). The water depth decreases gradually to 18 m at the tower site. The window to the North Pacific Ocean is oriented at 290°T from the tower site. This orientation was used to align the flight pattern over the tower, as is discussed by Tajirian [this issue].

The TOWARD data sets were obtained during three phases of intensive measurements. Phase I was executed during October 2 to November 7, 1984, and phase II was executed during March 4 to April 1, 1985. The wind speed and significant wave height occurrences in both phases I and II are shown in Figure 4. Phase I corresponded to less active environmental conditions and a well-defined mixed layer. Phase II corresponded to more intense wind and waves and no mixed layer. A third phase of measurements, denoted by

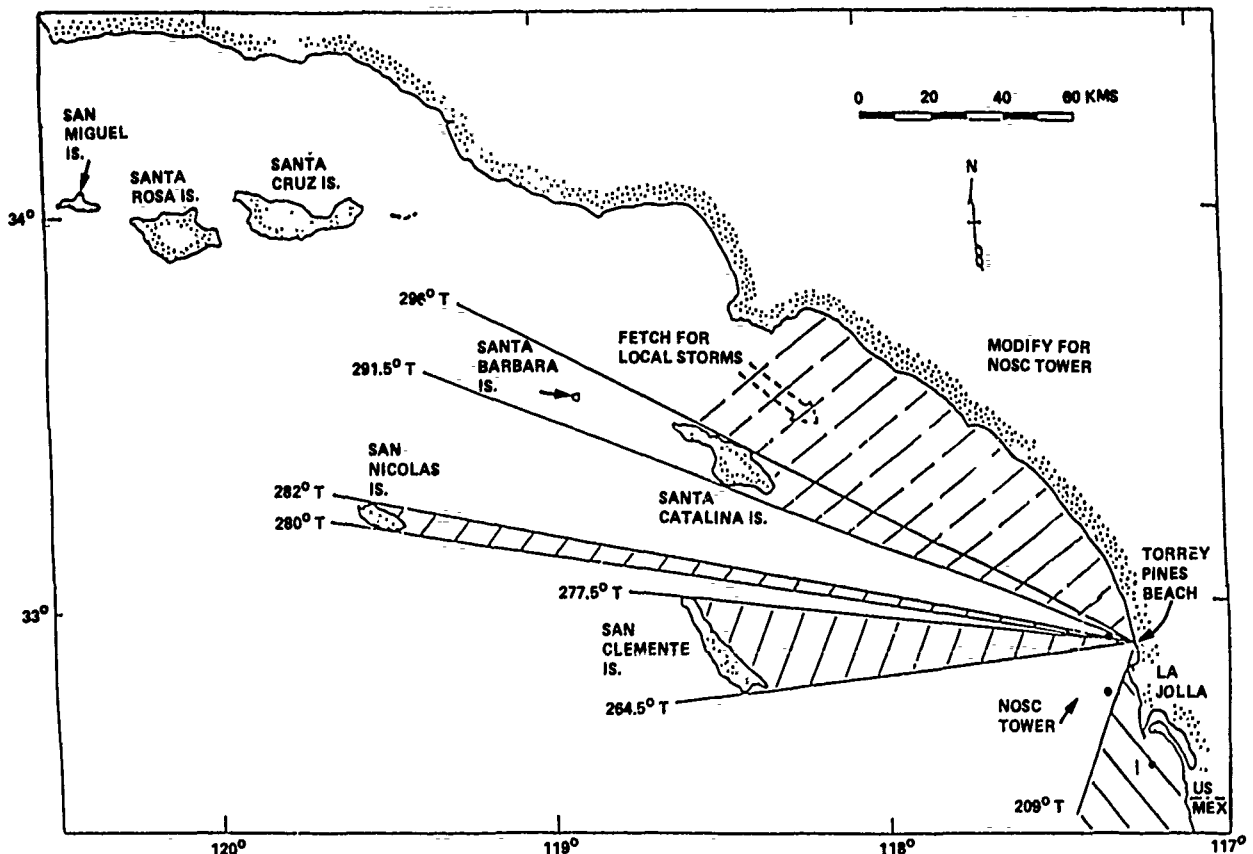


Fig. 2. Southern California Bight, showing the location of the NOSC tower and windows of wave approach from the North Pacific to Torrey Pines Beach and the NOSC tower [after Guza, 1986].

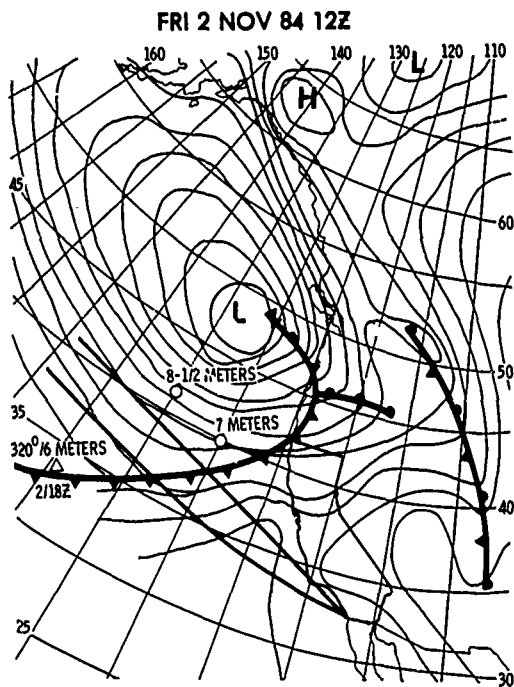


Fig. 3. Typical winter storm in the North Pacific from which swell propagates to and penetrates the Southern California Bight. This event was depicted at 1200 UT on November 2, 1984.

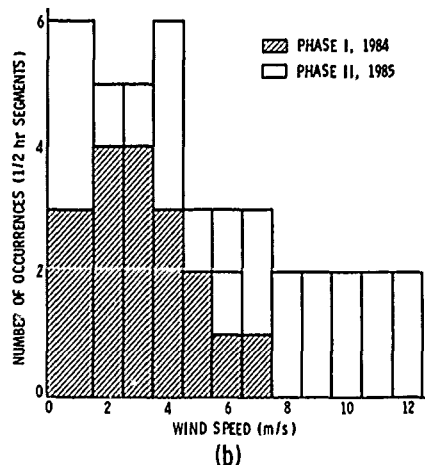
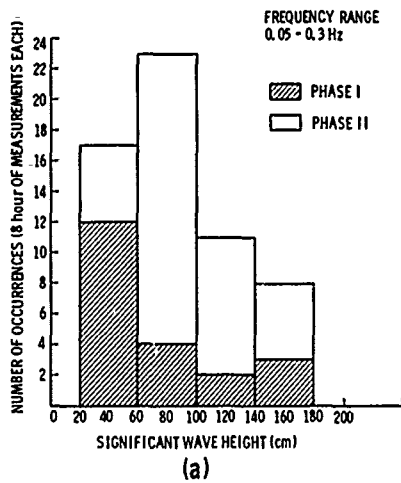


Fig. 4. Environmental conditions encountered in phases I and II of TOWARD 1984-1985. (a) Significant wave height. (b) Wind speed.

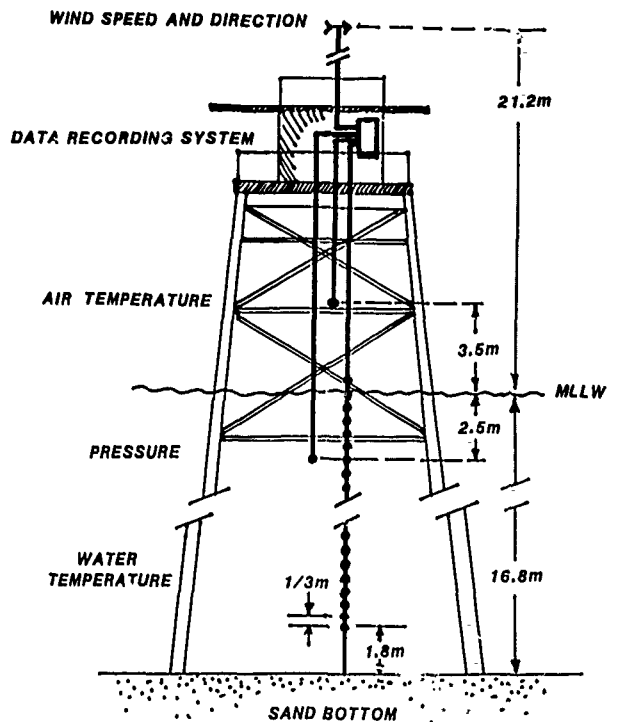


Fig. 5. Subsurface and atmospheric measurements recorded at NOSC in support of TOWARD.

“Mini-TOWARD,” was executed during December 15-20, December 1985, and January 21-24, 1986. The latter phase was added to obtain a complementary data set on wind measurements very close to the water surface, using the wave follower as a platform.

The experimental resources utilized are briefly reviewed below.

2.1. In Situ Measurements

The in situ measurements included the following:

*Directional short waves.* The wave follower, discussed by Shemdin and Hwang [this issue], was used to measure two components of wave slope and the wave height of short waves. Optical sensors that were mounted on the wave follower were used. A laser and optical receiver system was mounted on a C frame, forming an optical bench that followed the water surface displacement of long waves while measuring slopes and heights of the short waves.

*Directional long waves.* A submerged pressure gauge array, composed of four pressure sensors, was used at the NOSC tower for this purpose. In addition, an electromagnetic current meter and a pressure gauge were placed on the fixed frame of the wave follower to provide directional properties of long waves at the wave follower position. Both systems provided directional properties of long waves to within a directional resolution of  $\pm 25^\circ$ .

A third system, composed of an electromagnetic current meter mounted on the C frame, provided two horizontal components of current in the wave following frame. The latter system was used primarily to provide near-surface current measurements needed to remove the Doppler contribution to frequency in the wave slope and height measurements.

A C frame vertical displacement sensor was included to provide, in combination with the C frame error gauge, the



Fig. 6. Surface waves, 30 cm long, generated by the circular wave generator.

local vertical water surface displacement. This measurement is comparable to that provided by the pressure sensor that is mounted on the fixed frame. The pressure gauge provided more accurate measurements at frequencies below the cutoff

TABLE 1. System Characteristics of JPL L Band Synthetic Aperture Radar on the CV-990 Aircraft

Parameter	Value
Center frequency, GHz	1.225
Wavelength, cm	24.5
Pulse length, $\mu$ s	4.9
Bandwidth, MHz	19.3
Peak power, kW	4
Antenna azimuth beam width, deg	18
Antenna range beam width, deg	75
Antenna beam center gain, dB	12
Nominal altitude, km	6-12
Nominal ground speed, m/s	225
Sweep time (optical), $\mu$ s	55
Sweep length (optical), mm	25
Nominal pulse repetition frequency	700 pps
Swath width (quadrature polarization mode)	7
Resolution (4 looks)	
Slant range $\times$ azimuth (Digital), m	8 $\times$ 13
Slant range $\times$ azimuth (Optical), m	12 $\times$ 15
Incidence angle, deg	Nadir to 57
Polarization	HH, VV, HV, VH
Linear dynamic range—Power, dB	
Digital	22
Optical	12
Azimuth pixel spacing, m	11.0
Slant range pixel spacing, m	7.5
Ground range pixel spacings, m	
At 30°	15
At 50°	9.8
Number of pixels (range $\times$ azimuth)	927 $\times$ 1024

frequency (0.3 Hz) which is imposed by the depth position of the sensor. For frequencies higher than 0.3 Hz the C frame displacement sensor provided superior measurements.

**Surface energy tension.** A system that utilizes the concept of surface adhesion between a plate and ocean water was used to measure surface tension.

**Meteorological measurements.** A complete set of meteorological measurements, including wind stress, were obtained, as reported by *Geernaert et al.* [this issue]. A second set of measurements which included only wind speed and direction, air temperature, and water temperature were acquired by NOSC (see Figure 5).

**Ambient oceanographic measurements.** A thermistor chain, shown in Figure 5, was used to measure instantaneous temperatures at several elevations distributed over the entire water column. An electromagnetic current meter was deployed 5.0 m below the water surface to provide the two horizontal components of the ambient current. The ther-

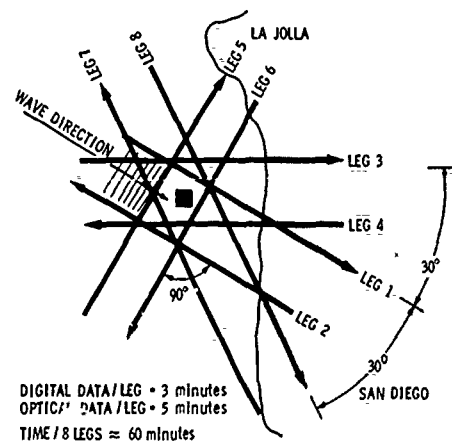


Fig. 7. CV-990 SAR flight pattern over the NOSC tower.

TABLE 2. SAR Data Processing Characteristics

Parameter	Value
Four optical channels	HH, VV, HV, VH
Four digital subframes	HH, VV, HV, VH
Angle of incidence at center of image, deg	35
Optical/digital slant range coverage, km	
Quadrature polarization mode	7
Dual polarization mode	12
Along track coverage, km	
Optical	60
Digital (raw)	30
Digital (image)	11
Digital image size	927 pixels range × 1024 pixels azimuth
Optical image size,	
Cross track	50 mm
Along track	1:250,000
Pulse repetition frequency	3 × (CV-990 ground speed, m/s)
At 200 m/s	600
At 250 m/s	750
Digital image pixel spacings, m	7.5 m slant range × 11.0 azimuth

mistor chain and current meter were operated continuously throughout phases I and II but were removed in phase III.

*Bragg wave generator ("bobbing buoy")*. This device is basically a free-floating buoy that has within it a moving mass which is capable of oscillating the buoy vertically at a prescribed frequency set by the frequency of the interior mass motion. The buoy was designed to generate waves in the frequency range 2.5–3.5 Hz, which correspond to circular waves with lengths in the *L* band range. A typical wave system generated by this buoy is shown in Figure 6. An extensive set of measurements were obtained in mini-TOWARD; the bobbing buoy was operated in the proximity of the wave follower and in the view of the stereo cameras.

### 2.2. Tower-Based Radar Measurements

The tower-based remote measurement capabilities deployed at the site are briefly reviewed below.

*Multifrequency radars*. Two multifrequency radar systems were operated at the tower, in both phases I and II of TOWARD. One was operated by the Jet Propulsion Laboratory (JPL), and the other was operated by the University of Kansas. Both systems covered the frequency range 1–15 GHz. In addition, the Naval Research Laboratory (NRL) operated an *L* band radar in phase I and *L* and *K<sub>u</sub>* band radars in phase II.

*Stereophotography*. An extensive set of wave height measurements using stereophotography was obtained during all three phases of TOWARD. All the photographs were taken from the tower. The cameras were placed apart at an elevation above the mean water level such that a minimum base-to-height ratio of 0.4 could be achieved. A horizontal T bar was placed approximately 3.0 m above the mean water level to provide target calibration for the cameras. The lenses were set at different incidence angles to capture various scales of the sea surface.

### 2.3. Airborne Measurements

The primary aircraft in the TOWARD experiment was the NASA CV-990 on which the JPL *L* band SAR was deployed. This SAR system was equipped with both optical and digital recording and processing capabilities. The system characteristics are given in Table 1. The flights followed a prescribed pattern that is shown in Figure 7. The nominal altitudes were 11,585, 6098, and 2134 m; they were flown to vary the aircraft range-to-velocity ratio. Variation of the latter was achieved in the range 15–50 s. The data processing characteristics of this system, in both optical and digital modes, are given in Table 2.

## 3. PARTICIPATION

The organizations, investigators, and associated activities in the field operations of the experiment are shown in Table 3.

The data analysis was supervised by three discipline review committees. The hydrodynamics committee consisted of S. R. Borchardt (chair), W. D. Garrett, G. Geernaert, R. Guza, B. A. Hughes, P. Hwang, M. S. Longuet-

TABLE 3. Participation in TOWARD Experiment

Organization	Investigator(s)	Activity
Jet Propulsion Laboratory	T. W. Thompson	aircraft SAR measurements
	D. Hoff	wave follower construction and operation
	S. V. Hsiao	in situ short waves and wind data processing
	D. Held W. Brown	SAR digital image processing multifrequency tower radar measurements, stereophotography
Naval Postgraduate School	K. Davidson, S. Larsen, G. Geernaert	wind stress measurements with sonic and hot film sensors
Naval Ocean Systems Center	P. Hanson, J. Olsen	tower support; environmental measurements
Naval Research Laboratory	W. Plant, W. Keller W. Garrett	<i>L</i> band tower radar measurements; SAR simulation of "velocity bunching" model measurement, analysis, and modification of surface slicks and surface compressibility
Scripps Institution of Oceanography	R. Guza	Directional longwave measurements, ambient tower measurements
University of Kansas	R. Moore	Multifrequency tower radar
University of Maryland	R. Harger	SAR simulation of "distributed surface model"

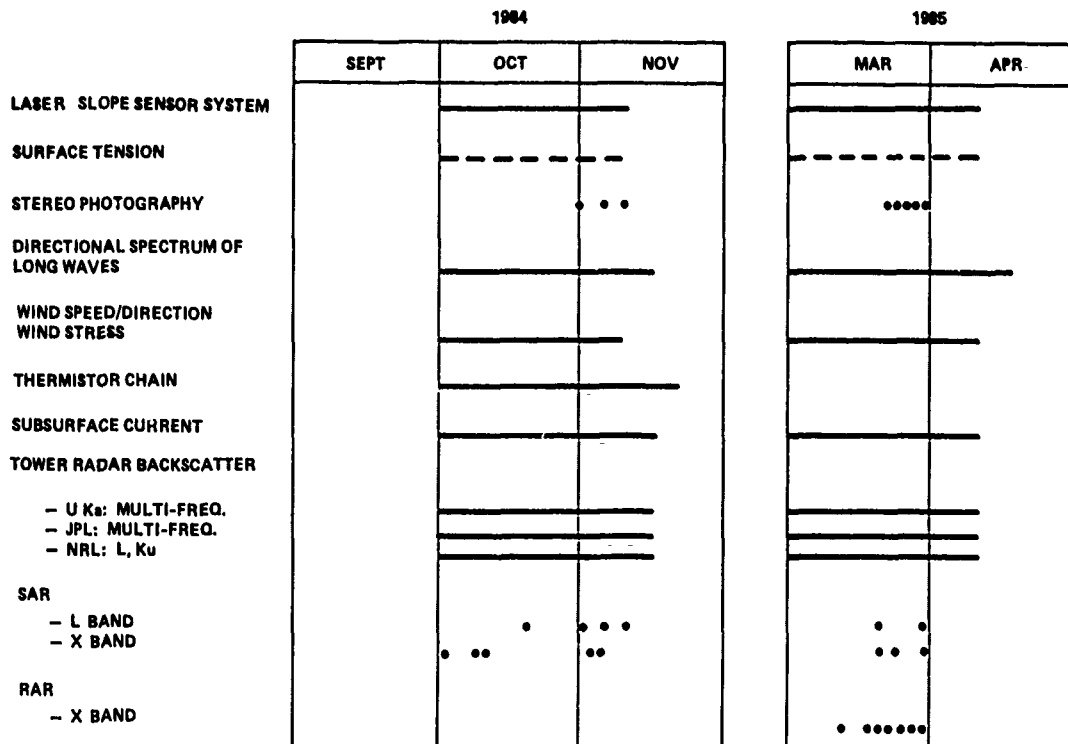


Fig. 8. TOWARD data summary in phases I and II.

Higgins, O. M. Phillips, and J. Wu. The radar backscatter committee comprised R. K. Moore (chair), W. E. Brown, Jr., K. Davidson, G. P. deLoor, A. K. Fung, S. P. Gogineni, B. Green, W. Keller, D. Kwok, W. J. Pierson, and M. G. Wurtele. The SAR imaging committee comprised W. J. Plant (chair), W. Alpers, W. E. Brown, Jr., R. O. Harger, K. Hasselmann, D. Held, and D. R. Lyzenga.

These committees reviewed the acquired data sets and established analysis priorities in relation to the stated-TOWARD objectives. They also reviewed the data report and results presented by the investigators in periodic review meetings held for this purpose.

4. DATA ANALYSIS APPROACH AND OVERVIEW OF RESULTS

The acquired TOWARD data sets and corresponding periods of measurements are shown in Figure 8. Table 4 shows the data sets in relation to the objectives stated for the TOWARD experiment.

Initial priority in data analysis was assigned to those data sets needed to validate the SAR imaging models. For this purpose, priority was assigned to those days where high-quality SAR images were obtained in desirable oceanographic environments. These are shown in Tables 5 and 6 for phases I and II, simultaneously. For example, high priority was assigned to the data sets recorded on October 31, 1984. On this day a dominant swell propagated through the tower site, the SAR images of ocean waves were of good quality, and the in situ and tower-based radar measurements had been recorded successfully during the flight period.

During the SAR overflights the near-surface and in situ measurements at the tower site were coordinated (1) to yield data sets that complemented the SAR data (for example, tower-based radars were set at the same incidence angles,

35°, as the tower location in the SAR image) and (2) to provide ocean surface measurements that could be used as input for simulating the SAR image. Here, the emphasis was on providing data sets that could be utilized for validating the SAR imaging models.

The L band SAR images from all flights were carefully scrutinized to determine the influence of environmental parameters on SAR imaging. Optical images were used to scan a large area of the ocean in the vicinity of the NOSC tower. Digitally processed images were compared with optically processed ones to establish the gain achieved with digital processing. From these standard products, 10 digital frames were selected from the phase I flights for detailed focusing studies as described by Tajirian [this issue].

TABLE 4. Matrix of TOWARD Science Objectives Versus Acquired Data Sets

Data Set	Test SAR Imaging Theories	Test Radar Backscatter Models	Understand Hydrodynamic Modulation of Short Waves
Laser slope sensor system	X	X	X
Stereophotography	X	X	X
Surface tension	X	X	X
Directional spectrum of long waves	X	X	X
Meteorological data	X	X	X
Thermistor chain			X
Subsurface current			X
Multifrequency tower radars			X
L band SAR	X	X	
X band SAR	X		
X band RAR	X	X	

RAR, real aperture radar.

TABLE 5. Environmental Conditions During Flights in October–November 1984: Phase I [after Guza, 1986].

	Oct. 17, 1984	Oct. 31, 1984	Nov. 4, 1984	Nov. 7, 1984
Time analyzed*	1250–1413	1300–1600	1512–1625	1412–1625
Wind speed, knots†	15	6–8	5–7	10
Wind direction, deg	~275	~280	~300	~250
Mean current 5 m below surface, cm/s	<5	<5	<5	~10
Significant wave height, cm	126	124	158	110
Air temperature, °C	17.2	17.5	18.5	17.5

\*Times are in Pacific daylight time before and Pacific standard time after 0200 October 28, 1984.

†One knot equals 0.51 m/s.

In the intervals without SAR overflights, the tower measurements were coordinated to provide fundamental understanding of the hydrodynamics of short wave modulation by long waves and to understand the mechanisms of radar backscatter from the ocean surface. Here, simultaneous measurements with the different tower radars, the stereo-cameras, and the wave follower with laser-optical slope sensor were recorded. For example, at small incidence angles, the stereo cameras and the laser-optical slope sensor were operated simultaneously over ocean patches in close proximity of each other. For other (higher) incidence angles, radar backscatter measurements and stereophotographs were obtained in overlapping footprints. Simultaneous with the above measurements, recordings of the ambient environment (e.g., wind stress, wind speed and direction, current both near the water surface and 5.0 m below the mean water level, air and water temperatures, and surface energy) were obtained at the same location.

The first scientific output from TOWARD is a collection of eight papers presented in this issue. The results to date are outlined below:

1. The probability density functions of wave slope suggest Gaussian distribution for wave frequencies of less than 2.5 Hz and non-Gaussian distribution for wave frequencies greater than 7.5 Hz. It is inferred that the longer ocean waves are weakly coupled, as expected, but that the very short waves are strongly coupled, i.e., that they experience possibly strong nonlinear interaction. The transition from weakly to strongly coupled short waves is expected to be dependent on wind speed and sea state [Hwang and Shemdin, 1988].

2. The measured wave slope spectra in TOWARD have

significantly different intensity levels compared to predictions by Pierson and Stacy [1973] for equivalent wind speeds [Shemdin and Hwang, this issue].

3. Radar backscatter results from the University of Kansas multifrequency radar suggest that sea spikes do not contribute significantly to the average backscattered power at L band for the geometries implemented in TOWARD. Sea spike occurrence increases with radar frequency and with wind speed [Shemdin et al., 1986].

4. Radar backscatter results suggest that cross-wind or cross-wave modulation does occur and that it constitutes an important mechanism for SAR imaging of azimuthally traveling waves. There is also data indicating that the radar backscatter spectrum has a small peak near the dominant frequency of long waves [Shemdin et al., 1986].

5. SAR focusing results for azimuth-traveling waves indicate that waves are most detectable at a focus setting that is of the order of the wave-phase velocity [Tajirian, this issue].

6. Based on data analysis results to date, neither the "velocity bunching" model nor the "distributed surface" model can explain all the TOWARD observations. A comprehensive theory is advanced that incorporates both velocity bunching and distributed surface concepts [Harger and Korman, this issue; Kasilingam and Shemdin, this issue; Lyzenga, this issue].

7. Stereophotography provides a reasonable estimate of the directional wave number spectrum in the wavelength range 6–60 cm. The omnidirectional spectrum in this range does not validate the Donelan and Pierson [1987] model [Shemdin et al., this issue].

TABLE 6. Environmental Conditions During Flights in March 1985: Phase II [after Guza, 1986]

	Day in March 1985							
	13	18	19	20	24	25	26	27
Time analyzed, PST	1320–1630	1230–1420	1300–1530	1300–1600	1310–1500	1300–1450	1240–1520	1320–1600
Wind speed, knots*	7–4 (D)	5–10 (I)	8	8	4–6	8	7	8
Wind direction	180°–290°	300°–310°	265°–280° (V)	300°–310°	280°–300° (V)	240°	240°–260° (V)	230°–260° (V)
Mean current 5 m below surface, cm/s	<3	4–8	<3	<5	<3	<3	1–7	3–6
Significant wave height, cm	88	79	143	129	85	127	144	104
Air temperature, °C	11–14 (I)	11.5–13 (I)	13.7	13.6	13.5	13.4	13.7	13.3

Notation is as follows. I, increasing; D, decreasing; V, veering.

\*One knot equals 0.51 m/s.

*Acknowledgments.* The success of the TOWARD experiment would not have been possible without the operational support provided by a number of organizations, which is gratefully acknowledged here. The tower facility and support for operation were provided by Naval Ocean Systems Center (NOSC) through Jurgin H. Richter. Daily weather forecasts were provided by Collin Campbell of the Navy Oceanographic Command Facility, San Diego. Robert Lawson of the Office of Naval Research, Pasadena, coordinated and controlled the TOWARD flights over the NOSC tower with the Radar Air Traffic Control Center, located at Naval Air Station, Miramar. The NASA CV-990 aircraft was operated by Ames Research Center. The aircraft participation was arranged through John Keller; George Grant acted as mission director. The U.S. Marine Corps (VMFP-3) at El Toro, California, provided RF-4B aircraft with X band synthetic aperture radars. The U.S. Army (III Corps) at Fort Hood, Texas, provided OV-1(D) aircraft with X band real aperture radars. Water transportation between Mission Beach and the tower was provided by NOSC. The responsive support of EN-2 William Edward Ball and his crew aboard "Florida 33" contributed frequently to successful data sessions, especially in changing weather conditions. Logistical support and coordination were provided by Bobbie Videon, test director. Instrumentation support (two electromagnetic current meters) during "Mini-TOWARD" was provided by Ed Thornton of the Naval Postgraduate School, Monterey. The foresight and support of Robert Winokur in the planning and early execution stages are credited for the technical successes that followed. The Office of the Chief of Naval Operations provided support for the principal investigator in the planning and early execution stages of the experiment. Most importantly, the unwavering endorsement and support of the synthetic aperture radar Program of the Office of Naval Research, with Cdr. Thomas S. Nelson as program manager and Hans Doležalek as scientific officer, is responsible for the successful conclusion of this effort.

#### REFERENCES

- Donelan, M. A., and W. J. Pierson, Jr., Radar scattering and equilibrium ranges in wind-generated waves with application to scatterometry, *J. Geophys. Res.*, 92, 4971-5029, 1987.
- Geernaert, G. L., K. L. Davidson, S. E. Larsen, and T. Mikkelsen, Wind stress measurements during the Tower Ocean Wave and Radar Dependence Experiment, *J. Geophys. Res.*, this issue.
- Guza, R. T., Surface gravity wave measurements, in *Investigation of Physics of Synthetic Aperture Radar in Ocean Remote Sensing, TOWARD Interim Report*, vol. II, Jet Propulsion Laboratory, Pasadena, Calif., 1986.
- Harger, R. O. and C. E. Korman, Comparisons of simulated and actual synthetic aperture radar gravity wave images, *J. Geophys. Res.*, this issue.
- Hsiao, S. V., and O. H. Shemdin, Measurement of wind velocity and pressure with a wave-follower, *J. Geophys. Res.*, 88, 9841-9849, 1983.
- Hwang, P. A., and O. H. Shemdin, The dependence of sea surface slope on atmospheric stability and swell conditions, *J. Geophys. Res.*, this issue.
- Kasilingam, D. P., and O. H. Shemdin, Theory for synthetic aperture radar imaging of the ocean surface: With application to the Tower Ocean Wave and Radar Dependence Experiment on focus, resolution, and wave height spectra, *J. Geophys. Res.*, this issue.
- Lawoh, D., and B. Lake, Microwave backscattering from short gravity waves: A deterministic, coherent, and dual-polarized laboratory study, *Rep. 37564-6001-UT-00*, TRW, Redondo Beach, Calif., 1983.
- Lyzenga, D. R., An analytic representation of the synthetic aperture radar image spectrum for ocean waves, *J. Geophys. Res.*, this issue.
- Pierson, W. F., Jr., and R. A. Stacy, The elevation, slope, and curvature spectra of a wind roughened sea surface, NASA Contract Rep., CR-2247, 126 pp., 1973.
- Shemdin, O. H., TOWARD 84/85 science plan, technical report, 54 pp., Jet Propul. Lab., Calif. Inst. of Technol., Pasadena, 1984.
- Shemdin, O. H., and P. A. Hwang, Comparison of measured and predicted sea surface spectra of short waves, *J. Geophys. Res.*, this issue.
- Shemdin, O. H., et al., *Investigation of Physics of Synthetic Aperture Radar in Ocean Remote Sensing, TOWARD Interim Report*, 2 vols., Jet Propulsion Laboratory, Pasadena, Calif., 1986.
- Shemdin, O. H., H. M. Tran, and S. C. Wu, Directional measurement of short waves with stereophotography, *J. Geophys. Res.*, this issue.
- Tajirian, E. K., Multifocus processing of L band synthetic aperture radar images of ocean waves obtained during the Tower Ocean Wave and Radar Dependence Experiment, *J. Geophys. Res.*, this issue.
- Valenzuela, G. R., Theories for the interaction of electromagnetic and ocean waves: A review, *Boundary Layer Meteorol.*, 13, 63-85, 1978.

O. H. Shemdin, Ocean Research and Engineering, 255 South Marengo Avenue, Pasadena, CA 91101.

(Received September 7, 1987;  
accepted June 23, 1988.)

# Theory for Synthetic Aperture Radar Imaging of the Ocean Surface: With Application to the Tower Ocean Wave and Radar Dependence Experiment on Focus, Resolution, and Wave Height Spectra

DAYALAN P. KASILINGAM

*Ocean Research and Engineering, Pasadena, California*

OMAR H. SHEMDIN<sup>1</sup>

*Jet Propulsion Laboratory, Pasadena, California*

A one-dimensional model is developed to simulate azimuthal synthetic aperture radar (SAR) imaging of the ocean surface. The model developed here is general and can admit both the "distributed surface" and the "velocity bunching" approaches. Computer simulations are performed to test the validity of this model. The simulations show that the time-dependent modulation patterns due to the radar cross section variation and the velocity bunching effects give optimum focusing around half the phase velocity of the long wave. It is shown that the focus dependence is due to an incoherent integration process and not due to motion induced phase errors. It is argued that the radar reflectivity is correlated over distances small in comparison with the SAR resolution. In the simulations the radar reflectivity is assumed to be spatially decorrelated. Also given are the relative importance of the various effects that degrade the azimuthal resolution. It is shown that the limited radar temporal coherence due to the velocity spread of short-waves degrades the azimuthal resolution of the SAR. This coherence time depends on sea state and radar wavelength. It is shown that the orbital acceleration effects are small in comparison with the smearing due to the velocity spread. It is found that the degraded azimuthal resolution of the radar minimizes the nonlinear effects of velocity bunching. The simulations show that in the Tower Ocean Wave and Radar Dependence Experiment (TOWARD), SAR imaging at *L* band is reasonably linear.

## I. INTRODUCTION

The imaging of stationary scenes using synthetic aperture radar (SAR) is well understood [Brown, 1967; Harger, 1970]. The imaging of moving scenes has also been studied successfully to the extent that one is able to interpret images of rigid targets moving with regular velocities and accelerations [Raney, 1971]. But the same cannot be said about imaging moving, nonrigid, distributed targets like the ocean surface. Considerable work is reported on SAR imaging of the ocean surface. Various imaging models have been proposed, of which two have been recognized to represent the primary viewpoints. One viewpoint is the so called "distributed surface" or "phase velocity hypothesis" model [Jain, 1978, 1981; Harger, 1986], and the other is the so called "velocity bunching" or "orbital velocity hypothesis" model [Elachi and Brown, 1977; Swift and Wilson, 1979; Alpers and Rufenach, 1979; Plant and Keller, 1983]. Unfortunately, neither model has been able to successfully predict all the observations in the Tower Ocean Wave and Radar Dependence Experiment (TOWARD). In this paper a model is developed from fundamental radar backscatter and SAR imaging theories to explain the peculiarities of imaging the ocean surface. The theory has been formulated in such a manner that it elucidates not only the imaging mechanisms but also the focus dependence, image resolution and scattering processes. An attempt is also made to merge the finer points of the existing theories into one comprehensive model. It is suggested that the proposed model has a general

application, the limits of which will be determined from TOWARD and other experiments.

The velocity bunching theory is based on the premise that in SAR imaging, targets with slant range directed velocities are shifted in the azimuthal direction of the image plane [Raney, 1971]. For azimuth-traveling ocean waves, the variable orbital velocities result in scattering elements on the ocean surface being shifted by different amounts in the azimuthal direction. This in turn results in these scatterers bunching and dilating in the image plane. Larson *et al.* [1976] were the first to suggest this modulating mechanism. Swift and Wilson [1979] and Alpers and Rufenach [1979] developed most of the theory associated with the velocity bunching effect. The basic assumption behind this theory is that the surface may be divided into scattering elements whose dimensions are smaller than the intrinsic resolution of the synthetic aperture radar and that the radar return from each element is completely decorrelated from the others. The latter assumption appears to be valid, as no evidence to the contrary exists. Associated with each scattering element is the local orbital velocity and orbital acceleration of the moving ocean surface. For azimuth-traveling waves, the orbital velocity modulates the image through the velocity bunching mechanism. The orbital acceleration smears the image in the azimuthal direction. The spatial variability of this smear also results in a weak image modulation. Hasselmann *et al.* [1985] give a good review of the principles on which the velocity bunching phenomenon is based. Unfortunately, velocity bunching has not explained the focus dependence of the imaging process and especially its connection to the phase velocity of the dominant wave. Alpers *et al.* [1981] state explicitly that the optimum focus setting has no relation to the phase velocity of the dominant wave. They also maintain that focusing is determined by

<sup>1</sup>Now at Ocean Research and Engineering, Pasadena, California.

the orbital acceleration only, instead of the general space-time variability of the ocean surface. This has led the velocity bunching theory to give unrealistic estimates of the degradation of azimuthal resolution. More recently, the concept of coherence time of the radar reflectivity has been incorporated in the velocity bunching model [Alpers and Bruening, 1986].

The distributed surface model was first suggested by Jain [1978]. This theory predicts that the SAR image is a combination of an amplitude modulation due to straining of short waves by long waves and a phase modulation due to tilting by long waves. It implicitly assumes that the ocean surface is correlated over distances greater than the SAR intrinsic resolution. Owing to the lack of reliable experimental evidence this question still remains a contentious issue. Jain [1981] shows that a variable azimuthal shift due to slant range directed velocities may be obtained. But he views this as only a smearing process and not a "fundamental imaging mechanism." Harger [1986], also using a distributed surface theory, shows that the SAR image is obtained by superposing individual images from separate shortwave components riding on a single long wave. The hydrodynamic description incorporated by Harger is based on Phillips' [1981] model, which is a two-scale sinusoidal interaction between short waves and long waves. The latter model specifies shortwave characteristics at all phase locations of the long waves. In the ocean the shortwave spectral components are correlated over distances of the order of a few wavelengths [de Loor, 1983]. For SAR in the region where Bragg scattering holds, this implies that the radar reflectivity is correlated over distances of the order of a few Bragg wavelengths. Harger's treatment of SAR imaging aspects, however, appears to be realistic. Jain and Harger predict focusing around the phase velocity.

In this paper a theory is developed based on well-accepted SAR-concepts. The ideas are expanded in such a manner that one is able to bring together the different imaging mechanisms as predicted by the distributed surface and the velocity bunching viewpoints. An attempt is made to study the relative importance of the different modulating mechanisms. The theory has been developed so that the velocity bunching effect and the radar cross section modulation due to tilting and straining are clearly discernible. More importantly, the focusing effect of the azimuthal processor [Tajirian, 1986; Jain and Shemdin, 1983] on the different modulating mechanisms is examined. It is shown that the velocity bunching process gives optimum focus around half the phase velocity of the dominant wave. The radar cross section modulation also focuses around half the phase velocity. The degradation in the azimuthal resolution of SAR is found to be due to the limited temporal coherence of the radar reflectivity. In this paper an attempt is made to delineate this effect. It is shown that the primary factor is the time variability of the short and intermediate waves and that this effect is defined by a radar coherence time.

The model proposed here requires estimates of the correlation distance and the coherence time of the radar reflectivity of the ocean surface. Basically, these two quantities may be obtained experimentally from field data. The TOWARD data sets allow experimental determination of the coherence time but not the correlation distance. The radar coherence time limits the useful integration time of the SAR and therefore restricts the SAR resolution. Attempts have been made to determine this quantity theoretically [Tucker, 1985b; Alpers and Bruening, 1986], but there is uncertainty about the validity of these theoretical values. It appears more certain to use field data to determine the coherence time. Such work is presently

in progress using TOWARD measurements. Some preliminary results are included in the appendix.

As was stated previously, the correlation distance of the radar reflectivity is also important. If the radar correlation distance is greater than the intrinsic azimuthal resolution of the SAR, the radar returns from adjacent image cells will be correlated. In this case the radar return will have a strong dependence on the local longwave slope which moves at the phase velocity of the long wave. The experimental evidence, which is minimal, suggests that the radar correlation distance is smaller than the intrinsic resolution of the radar. It is recommended that tests be incorporated in future experimentation to clarify this point. A description of the correlation distance is given in the appendix. The present model also requires adequate knowledge of the radar cross section modulation (tilt and hydrodynamic) which is used as an input. Considerable work has been reported on measuring this quantity [Plant et al., 1983; Moore et al., 1986; Wright et al., 1980]. Nevertheless, there remain questions about magnitude of the modulation transfer function of azimuthally traveling waves and especially concerning the assumption of its linear dependence on the wave slope. In this paper the best estimates of these quantities are used, based on the TOWARD measurements.

The present analysis concentrates on azimuth-traveling waves and azimuthal imaging, because it is this aspect of the imaging process that is least understood. The theory developed here is described in section 2 and is first applied to monochromatic, azimuthally traveling ocean waves in section 2.1. Such idealized analysis provides useful insight into the physics of SAR imaging of ocean waves. Next, the analysis is extended to random ocean waves specified by a given ocean wave spectrum in section 2.2. Monte Carlo simulations are carried out to study the imaging of the ocean surface. The latter analysis helps to understand the process of wave number filtering and the effects of nonlinear imaging. Numerical computations based on the above theory are presented in section 3. The results are discussed in section 4.

## 2. SAR IMAGING OF THE OCEAN SURFACE

The two-scale model [Wright, 1968; Valenzuela, 1978] has been used extensively to model radar backscatter from the ocean surface. Tucker [1985a] introduced a variation of this model, the so-called SAR two-scale model, which is more applicable to SAR simulations. This model divides the ocean surface into two scales: the long scale, nominally given by wave numbers of less than the SAR azimuthal cutoff wave number, and the short scale, given by wave numbers greater than this wave number. In the analysis introduced here the SAR two-scale model is assumed implicitly.

The SAR imaging process is shown schematically in Figure 1. The antenna is mounted on an aircraft moving in the  $x$  direction (azimuth) with velocity  $V$  (in meters per second) at a slant range of  $R_0$ . The radar return signal at time  $t$  is given by [Jasik, 1961]

$$g(t) = \int_{-x}^{+x} \int_{-x}^{+x} \rho(x, y, t) F(t - 2R_0/c) \cdot A(x - Vt, y) dx dy \quad (1)$$

where  $\rho(x, y, t)$  is the time-variant reflectivity of the ocean surface,  $F(t - 2R_0/c)$  is the radar pulse function, and  $A(x - Vt, y)$  is the antenna pattern. The reflectivity includes both Bragg and specular scattering components.

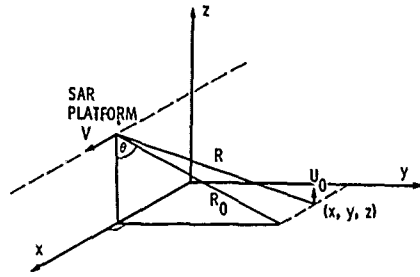


Fig. 1. Geometry of SAR imaging of ocean waves.

For clarity and simplicity it is assumed that the azimuth-directed antenna pattern is a Gaussian as follows:

$$A(x, y) = \exp(-2x^2/V^2 T_0^2) A_y(y) \tag{2}$$

where  $T_0$  is the SAR integration time. This assumption allows simplification of the algebra considerably without sacrificing fundamental aspects of mechanisms involved in the imaging process. The radar pulse function is of the form

$$F(t) = \exp[-i(2\pi f_r t + \alpha t^2)] \text{rect}(t/\tau_0) \tag{3}$$

where  $f_r$  is the radar frequency,  $\alpha$  is the chirp rate (for ranging), and  $\tau_0$  is the duration of the pulse. The range dependence of  $F(t - 2R_0/c)$  introduces a quadratic phase dependence on  $x$ .

The antenna output is passed through a matched filter to integrate and focus the SAR image. The matched filter impulse response is taken to be

$$h(t) = \exp[i(k_0 U t^2/R_0 + \alpha t^2)] \tag{4}$$

where  $k_0$  is the radar wave number and  $U$  is the matched filter velocity parameter given by

$$U = V(1 - \chi) \tag{5}$$

where  $\chi$  is the focusing parameter. For stationary scenes, focusing is achieved when  $\chi = 0$ . The filter output is the convolution of  $g(t)$  with the filter impulse response and is given by

$$f(t) = \int_{-\infty}^{+\infty} g(\tau)h(t - \tau) d\tau \tag{6}$$

The ranging is done at half the velocity of light. Therefore the time variance of the scene can be neglected in range. In this analysis the range integration ( $y$  direction in (1)) is not considered so as to focus on azimuthal imaging. The SAR response function in the slant range direction is given by Jain [1981] and Wakasugi et al. [1986]. Furthermore, if the pulse rate is sufficiently high to satisfy the sampling criteria in azimuth, then one may replace the pulsed return with a continuous return. Therefore for simplicity the pulse function,  $F(t - 2R_0/c)$ , is dropped except for the quadratic phase term,  $\exp(-ik_0 x^2/R_0)$ . The image intensity is given by the square of the amplitude of the output,  $f(t)$ . These modifications in equations (1), (4), and (6) give the mean image intensity as

$$\begin{aligned} \langle I(t) \rangle = & \int_{-\infty}^{+\infty} \int_{-\infty}^{+\infty} \int_{-\infty}^{+\infty} \int_{-\infty}^{+\infty} \langle \rho(x_1, \tau_1) \rho^*(x_2, \tau_2) \\ & \cdot \exp[2ik_0 h'(x_1, \tau_1)] \exp[-2ik_0 h'(x_2, \tau_2)] \rangle \\ & \cdot \exp[-ik_0(x_1 - V\tau_1)^2/R_0] \\ & \cdot \exp[-2(x_1 - V\tau_1)^2/V^2 T_0^2] \end{aligned}$$

$$\begin{aligned} & \cdot \exp[ik_0 U^2(t - \tau_1)^2/R_0] \exp[ik_0(x_2 - V\tau_2)^2/R_0] \\ & \cdot \exp[-2(x_2 - V\tau_2)^2/V^2 T_0^2] \\ & \cdot \exp[-ik_0 U^2(t - \tau_2)^2/R_0] dx_1 dx_2 d\tau_1 d\tau_2 \end{aligned} \tag{7}$$

where  $h'(x, \tau)$  is equal to the projection of the longwave height onto the slant range direction. This dependence of (7) on the longwave height is due to the advection of the short waves by the long waves.

The following new variables are defined:

$$x = x_1 - x_2 \tag{8a}$$

$$X = \frac{(x_1 + x_2)}{2} \tag{8b}$$

$$\tau = \tau_1 - \tau_2 \tag{8c}$$

$$T = \frac{(\tau_1 + \tau_2)}{2} \tag{8d}$$

$$\begin{aligned} \langle \rho \rho^* \rangle(x, X, \tau, T) = & \langle \rho(x_1, \tau_1) \rho^*(x_2, \tau_2) \\ & \cdot \exp[2ik_0 h'(x_1, \tau_1)] \exp[-2ik_0 h'(x_2, \tau_2)] \rangle \end{aligned} \tag{8e}$$

Substituting (8) into (7) yields

$$\begin{aligned} \langle I(t) \rangle = & \int_{-\infty}^{+\infty} \int_{-\infty}^{+\infty} \int_{-\infty}^{+\infty} \int_{-\infty}^{+\infty} \langle \rho \rho^* \rangle(x, X, \tau, T) \\ & \cdot \exp[-(x - VT)^2/V^2 T_0^2] \\ & \cdot \exp[-4(X - VT)^2/V^2 T_0^2] \\ & \cdot \exp[-2ik_0 x(X - VT)/R_0] \\ & \cdot \exp[2ik_0 V(X - U^2 t/V)\tau/R_0] \\ & \cdot \exp[-2ik_0(V^2 - U^2)T\tau/R_0] dx dX d\tau dT \end{aligned} \tag{9}$$

Equation (9) shows that the mean image is a map of the time-dependent covariance of the complex radar reflectivity given by (8e). The variables  $x$  and  $\tau$  reflect the SAR image's dependence on the spatial correlation and on the time coherence of the radar reflectivity, respectively. Most field data imply that the radar return is only coherent over a finite time period [Plant and Keller, 1983]. At the same time the evidence suggests that the radar correlation distance is generally smaller than the intrinsic resolution of the SAR (11 x 11 m for the system used in TOWARD). In the following derivation the radar reflectivity is assumed to be spatially decorrelated while having partial temporal coherence. The covariance of the reflectivity may be assumed to be (see the appendix)

$$\begin{aligned} \langle \rho \rho^* \rangle(x, X, \tau, T) = & \sigma(X, T) \exp[2ik_0 \tau U_0(X, T) \\ & \cdot \cos \theta] \exp(-\tau^2/\tau_c^2) \delta(x) \end{aligned} \tag{10}$$

where  $\tau_c$  is the coherence time of the ocean surface radar reflectivity,  $\sigma(X, T)$  is the time-dependent radar cross section,  $\theta$  is the angle of incidence and  $U_0(X, T)$  is the vertical component of the orbital velocity. Substituting (10) into (9) yields

$$\begin{aligned} \langle I(t) \rangle = & \int_{-\infty}^{+\infty} \int_{-\infty}^{+\infty} \int_{-\infty}^{+\infty} \sigma(X, T) \exp(-\tau^2/\tau_c^2) \\ & \cdot \exp[2ik_0 \tau U_0(X, T) \cos \theta] \exp(-\tau^2/T_0^2) \\ & \cdot \exp[-4(X - VT)^2/V^2 T_0^2] \\ & \cdot \exp[2ik_0 V(X - U^2 t/V)\tau/R_0] \\ & \cdot \exp[-2ik_0(V^2 - U^2)T\tau/R_0] dX d\tau dT \end{aligned} \tag{11}$$

Note that the time dependence of the orbital velocity is preserved.  $U_0(X, T)$  includes the acceleration effect. But unlike the velocity bunching approach, in this method the general space time variability of the orbital velocity is utilized. This approach results in a proper understanding of the azimuthal focusing effect. In (11), integrating in  $\tau$  gives

$$\begin{aligned} \langle I(t) \rangle &= \pi^{1/2} T_0' \int_{-\infty}^{+\infty} \int_{-\infty}^{+\infty} \sigma(X, T) \\ &\cdot \exp [-4(X - VT)^2 / V^2 T_0'^2] \\ &\cdot \exp \{-\pi^2 [X - U't - V'T \\ &+ (R_0/V) U_0'(X, T)]^2 / \epsilon_0^2\} dT dX \end{aligned} \quad (12a)$$

where the azimuthal resolution is

$$\epsilon_0 = \frac{\lambda_0 R_0}{2VT_0'} \quad (12b)$$

and the effective integration time  $T_0'$  is given by

$$\frac{1}{T_0'^2} = \frac{1}{T_0^2} + \frac{1}{\tau_c^2} \quad (12c)$$

The velocities  $U'$ ,  $V'$ , and  $U_0'$  are given by

$$U' = \frac{U^2}{V} \quad (12d)$$

$$V' = \frac{(V^2 - U^2)}{V} \quad (12e)$$

$$U_0'(X, T) = U_0(X, T) \cos \theta \quad (12f)$$

The Gaussian dependence of the antenna pattern results in a response function that is also Gaussian. This is because the SAR response function is the Fourier transform of the azimuthal antenna pattern. One may substitute any other antenna pattern by simply replacing the Gaussian in (12a) by the Fourier transform of the real antenna pattern.

Equation (12) is the basic SAR equation for azimuthal imaging of ocean waves. It shows that the imaging process effectively maps a two-dimensional input function onto a one-dimensional output function. This equation may be solved for different forms of  $\sigma(X, T)$  and  $U_0(X, T)$ . The former is an amplitude modulation effect and is due to the tilting and straining of short waves by the long waves. The second modulating term is a frequency modulation due to the motion effects and results in the velocity bunching phenomenon.

### 2.1. SAR Imaging of Monochromatic Ocean Waves

In the TOWARD experiment the ocean surface was imaged during a period of dominant swell. The swell system was reasonably narrow band and may be idealized by monochromatic ocean waves. In this section, (12) is solved for a monochromatic wave to gain the simplified insight into the SAR imaging mechanisms of ocean waves. For such a monochromatic wave it may be assumed that both radar cross section and orbital velocity modulations are sinusoidal. That is,  $\sigma(X, T)$  and  $U_0(X, T)$  have the forms

$$\sigma(X, T) = \sigma_0 [1 + R_1(U_0/C) \cos(k_i X - \omega_i T + \phi_i)] \quad (13a)$$

$$U_0'(X, T) = U_0' \sin(k_i X - \omega_i T) \quad (13b)$$

where  $\sigma_0$  is the mean radar cross section and  $R_1$  and  $\phi_i$  are the

magnitude and phase of the modulation transfer function [Wright et al., 1980; Plant et al., 1983], respectively.  $U_0$ ,  $C$ ,  $k_i$  and  $\omega_i$  are the vertical component of the longwave orbital velocity, phase velocity, wave number, and frequency, respectively. It has been implicitly assumed that the radar cross section is linearly related to the longwave height. Linear wave theory relates the orbital velocity of the long waves to their wave height. Substituting (13) in (12) yields

$$\begin{aligned} \langle I(t) \rangle &= \pi^{1/2} T_0' \int_{-\infty}^{+\infty} \sigma_0 [1 + R_1(U_0/C) \cos(k_i X - \omega_i T + \phi_i)] \\ &\cdot \exp [-4(X - VT)^2 / V^2 T_0'^2] \\ &\cdot \exp \{-\pi^2 [X - U't - V'T \\ &+ (R_0/V) U_0' \sin(k_i X - \omega_i T)]^2 / \epsilon_0^2\} dT dX \end{aligned} \quad (14)$$

Noting that both radar cross section modulation and Doppler velocity modulation have similar functional dependences on  $X$  and  $T$ , making the substitution

$$X' = X - CT \quad (15a)$$

$$VT' = VT - X \quad (15b)$$

and integrating in  $T'$ , one gets

$$\begin{aligned} \langle I(t) \rangle &= \frac{\pi T_0' T_0}{2} \left( \frac{V}{V - C} \right) \\ &\cdot \int_{-\infty}^{+\infty} \sigma_0 [1 + R_1(U_0/C) \cos(k_i X' + \phi_i)] \\ &\cdot \exp \{-\pi^2 [X' - U''t + (R_0/V) U_0'' \\ &\cdot \sin(k_i X')]^2 / \epsilon^2\} / (\epsilon/\epsilon_0) dX' \end{aligned} \quad (16a)$$

where

$$U'' = V - C \quad (16b)$$

$$U_0'' = \frac{V - C}{V - V'} U_0' \quad (16c)$$

$$\epsilon = \epsilon_0 \left( \frac{V - C}{V - V'} \right) \left\{ 1 + \left[ \frac{\pi V T_0' T_0 (V^2 - U^2 - VC)}{R_0 \lambda_0 (V - C)} \right]^2 \right\}^{1/2} \quad (16d)$$

Equation (16) is the imaging equation for monochromatic ocean waves. Note how the resolution depends on the focusing parameter  $U$  and how the velocity bunching effect is dependent on the focus-dependent parameter  $U_0''$ . This equation is utilized to determine the focus dependence, the resolution, and the image quality for a sinusoidal long wave.

A close examination of (16) shows the stretching (or shrinking) effects of the longwave phase velocity. Unless properly corrected, the dominant wavelength of the image will be  $V/(V - C)$  the wavelength of the ocean surface wave. If the wave is traveling in the same direction as the SAR platform it will result in a decrease in the azimuthal wave number, and if it is traveling in the opposite direction it will result in an increase in the azimuthal wave number. For waves traveling at an angle to the SAR platform velocity this effect would result in a rotation of the waves.

### 2.2. Imaging of Random Ocean Surfaces

A more general model of the ocean surface is to assume the ocean surface to be random with a specific spectral shape.

Many theoretical and experimental forms such as the JONSWAP spectrum [Hasselmann *et al.*, 1973], the Pierson-Moskowitz spectrum [Pierson and Moskowitz, 1964] and the Phillips spectrum [Phillips, 1977] have been proposed. In this section the spectrum is assumed to be simply  $P(k)$ . Using the Karhunen-Loève expansion [Papoulis, 1965], the ocean surface wave height may be represented by a linear superposition of different harmonics. The wave height is specified to be

$$h(X, T) = (2\Delta k)^{1/2} \sum_{i=1}^N P^{1/2}(k_i) \cos(k_i X - \omega_i T + \phi_i) \quad (17)$$

where the phase  $\phi_i$  has a uniform distribution with a second moment given by

$$\langle \phi_i \phi_j^* \rangle = \frac{\pi^2}{3} \delta_{ij} \quad (18)$$

$\Delta k$  is the step size in the spectral domain and is given by  $\Delta k = k_{i+1} - k_i$ .

Assuming linear wave theory, the orbital velocity is given by a similar superposition

$$U_o(X, T) = (2\Delta k)^{1/2} \sum_{i=1}^N \omega_i P^{1/2}(k_i) \sin(k_i X \omega_i T \phi_i) \quad (19)$$

Similarly, the radar cross section is assumed to be

$$\sigma(X, T) = \sigma_0 \left[ 1 + (2\Delta k)^{1/2} \sum_{i=1}^N R_i k_i P^{1/2}(k_i) \cdot \cos(k_i X - \omega_i T + \phi_i + \psi_i) \right] \quad (20)$$

where  $R_i$  and  $\psi_i$  are the magnitude and the phase of the modulation transfer function at the different harmonics, respectively. The cross section modulation is assumed to be linear. This assumption is based on the two-scale model of Wright [1968]. The validity of this linearity assumption remains unresolved.

The crucial difference between the model presented here and that of Alpers and Bruening [1986] is that this model preserves the time dependence of the radar cross section and the orbital velocity. In the present theory, (12a) is an integration in space and time. The theory of Alpers and Bruening assumes a "frozen" ocean surface and integrates in space only. The time variability of the orbital velocity in their theory is included incorrectly by an acceleration term. It is the space-time dependence in the radar cross section and in the orbital velocity that generate the focus dependence on the phase velocity of the long wave. The difference explains why Alpers and Bruening have not produced estimates of the focus shift that are consistent with observations.

Substituting (19) and (20) into (12), the SAR image corresponding to a random ocean surface is obtained, subject to the assumptions stipulated above. One may extend the analysis to do Monte Carlo or other forms of statistical simulations of the ocean wave height spectra. The numerical results obtained in this paper are given in the next section.

### 3. NUMERICAL ANALYSIS

The TOWARD ocean conditions are assumed to be  $R_0 = 14.0$  km (aircraft altitude of 11.5 km),  $V = 225$  m/s,  $T_0 = 1.75$  s, and  $\theta = 35^\circ$ . The radar is assumed to be  $L$  band with a nominal wavelength of 25 cm. Analytical expressions for the coherence time of the radar reflectivity of the ocean surface

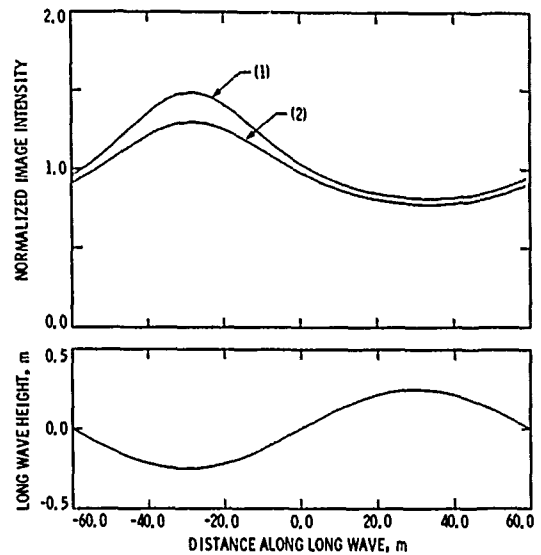


Fig. 2. Simulated image intensity of a 120-m monochromatic ocean wave with a wave amplitude of 0.36 m. Curve 1, optimum focus setting (8 m/s); curve 2, zero focus setting (0 m/s).

and the velocity spread associated with it are given by Beal *et al.* [1983], Tucker [1985b], and Alpers and Bruening [1986]. Owing to the lack of experimental evidence, there is some uncertainty in the accuracy of these expressions. In the simulations that follow the coherence time is varied in the range 0.03–0.2 s, to give suitable agreement with existing SAR field data [Tajirian, 1986].

For the above conditions, (16) is used to generate one-dimensional images of monochromatic ocean waves. Figure 2 shows the image of a 120-m monochromatic wave with a wave amplitude of 0.36 m traveling in the same direction as the aircraft. The magnitude and phase of the modulation transfer function are assumed to be 5 and  $45^\circ$ , respectively. The coherence time is equal to 0.1 s. Curve 1 in Figure 2 is adjusted to give the maximum contrast, with the corresponding optimum focus setting being equal to approximately 8 m/s. The image has been corrected for wave stretching effects. The phase speed of the 120-m-deep water wave is approximately 13.5 m/s. The effective modulation transfer function, which includes the velocity bunching contribution, is approximately 20, clearly indicating that the velocity bunching effect plays an important role in the imaging of a monochromatic wave at an aircraft altitude of 11.5 km. Note how the crest of the image coincides with the trough of the ocean wave, and vice versa. The second harmonic content is approximately 15% of the fundamental, reflecting a reasonably linear imaging process for TOWARD type conditions. Curve 2 in Figure 2 shows the image at zero focus. The magnitude of the fundamental harmonic for zero focus is about 10% smaller than that of optimum focus.

Figure 3 shows similar images for a wave amplitude of 1.08 m. All the other parameters are kept equal. The focus setting is set equal to 8 m/s. For this sea state, the second harmonic is found to be 20% of the fundamental, indicating some nonlinear behavior. The nonlinear effects are induced primarily by velocity bunching. The velocity bunching effects are visually evident. When the coherence time is reduced from 0.1 s to 0.05 s, as would be expected in high sea states, the second harmonic drops to about 2.5% of the fundamental. Therefore in high

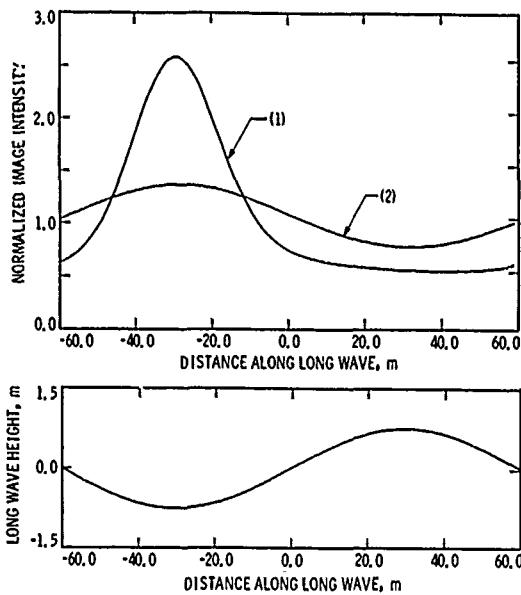


Fig. 3. Simulated image intensity of a 120-m monochromatic ocean wave with a wave amplitude of 1.08 m. Other parameters are as in Figure 2. Curve 1,  $\tau_c = 0.1$  s; curve 2,  $\tau_c = 0.05$  s.

sea states it is anticipated that the nonlinear effects can be diminished, with a corresponding degradation in SAR resolution.

The intensity modulation variations obtained by varying the focusing parameter,  $\chi$ , are shown in Figure 4. These curves are calculated for different values of the radar coherence time. Figure 4 shows focusing curves which correspond to coherence times of 0.05, 0.1 and 0.2 s. The other parameters are the same as indicated for Figure 2. All three curves seem to focus between  $C/4$  and  $C$ . This is consistent with field observations. Furthermore, the curves exhibit broad peaks indicating a weak dependence on the focusing parameter. This is to be expected, as the degradation due to defocusing is small in comparison with the degradation due to the velocity spread. Figure 5 shows the focusing curves for three aircraft altitudes, 11.5 km, 6.1 km, and 2.1 km. The curves demonstrate that the focusing is only weakly dependent on the  $(R/V)$  ratio. This is an important result. It has been suggested by the proponents of the velocity bunching viewpoint that the focusing depends strongly on the  $(R/V)$  ratio. The observations of D. F. Leotta and F. K. Li (Focusing studies of SAR ocean wave images collected during the TOWARD experiment, submitted to *Journal of Geophysical Research*, 1988) confirm in TOWARD a small dependence of focusing on aircraft altitude and hence on the  $(R/V)$  ratio.

Figure 6 shows the focusing curves for two monochromatic waves, one traveling in the same direction as the aircraft (curve 1) and the other traveling in the opposite direction to the aircraft (curve 2). The aircraft altitude, velocity, and integration time are kept the same. Note how the two focusing curves are not symmetric about the ordinate. This is because the velocity bunching effect is dependent on the focusing parameter as shown in (16). When the wave is traveling in the same direction as the aircraft, the velocity bunching effect moves the focus shift to values greater than  $C/2$ , while for waves traveling in the opposite direction it moves the focus shift to values of less than  $C/2$ .

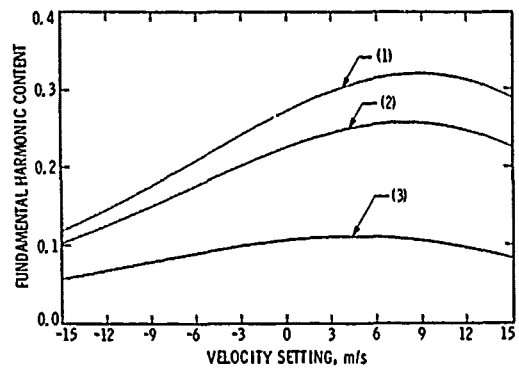


Fig. 4. Focusing curves associated with the simulated image of the monochromatic wave shown in Figure 2, for different coherence times. Curve 1,  $\tau_c = 0.2$  s; curve 2,  $\tau_c = 0.1$  s; curve 3,  $\tau_c = 0.05$  s.

Equation (16) is applicable only to monochromatic waves and is not suitable for spectral analysis. Instead, (12) may be used to study one-dimensional SAR images of simulated random ocean surfaces. In executing the SAR simulations for TOWARD, Monte Carlo simulations are performed on the in situ wave height spectrum of October 31, 1984, as given by Guza [1986]. The latter is converted to an equivalent deepwater wave height spectrum [see Tajirian, 1986] from which  $P(k)$  is calculated and then used in (19) and (20). A 256-point spectrum is used with  $\Delta k$  equal to  $0.0025 \text{ m}^{-1}$ . The coherence time for this simulation is assumed to be 0.1 s. The aircraft altitude is set equal to 11.5 km. Figure 7 shows the wave height spectrum used as the input and the spectrum of the simulated SAR image obtained as the output. It shows a spectral shift in the dominant wavelength of the simulated SAR spectrum to a lower wave number. The SAR image spectrum shows very little higher harmonic content, indicating a low-pass filter action. Figure 8 shows the in situ wave height spectrum and the spectrum of the simulated SAR image when the radar coherence time is 0.04 s. The dominant wavelength of the SAR spectrum has shifted considerably toward the longer wavelengths. The low-pass filter cutoff wave number is much smaller than that in Figure 7. This illustrates the critical importance of the radar coherence time in the imaging process.

Figure 9 shows the image spectrum derived from the field data [Tajirian, 1986] plotted along with the simulated SAR

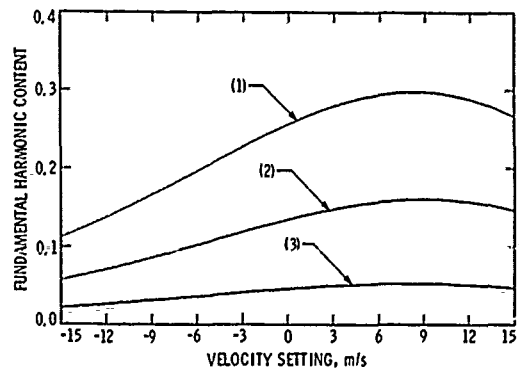


Fig. 5. Focusing curves associated with the simulated image shown in Figure 2 for different  $(R/V)$  ratios. The coherence time is set equal to 0.1 s. Curve 1,  $(R/V) = 62$ ; curve 2,  $(R/V) = 33$ ; curve 3,  $(R/V) = 11.5$ .

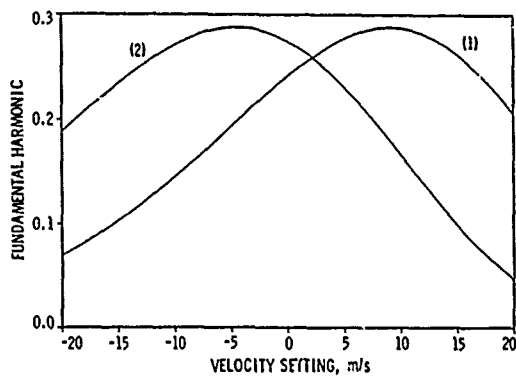


Fig. 6. Focusing curves associated with the simulated images of monochromatic ocean waves traveling in the same direction as the aircraft (curve 1) and in the opposite direction to the aircraft (curve 2). The wave amplitude is 0.36 m, and the coherence time is set equal to 0.2 s.

spectrum. The spectrum of the field image has been corrected for wave stretching effects [Tajirian, 1986]. The two curves show reasonable agreement. The radar coherent time used here is 0.07 s. All the other parameters are kept the same as in Figure 7. The high wave number content in the spectrum of the field data is due to system noise.

#### 4. DISCUSSION OF RESULTS

The aim of this paper has been to delineate the different SAR imaging processes associated with ocean wave imaging. A general description is given in (9), which can be applied to scenes that are correlated in space and time. The SAR image is a map of the covariance of the complex radar reflectivity of the ocean surface. Equation (12) is then specified as the imaging integral for a spatially decorrelated, time-variant ocean surface. It shows that the SAR image is modulated by  $\sigma(X, T)$  and  $U_0(X, T)$  through the radar reflectivity as shown in (10). The SAR system produces an image in one dimension from a scene described by a two-dimensional function of space and time. A closer examination of (12) shows that it is an incoherent integration in  $T$ . The integration does not involve any phase terms like the integration in  $\tau$ . In time-invariant systems the radar cross section is independent of  $T$  and the orbital velocity is zero. Hence one may integrate (12) in  $T$  and obtain

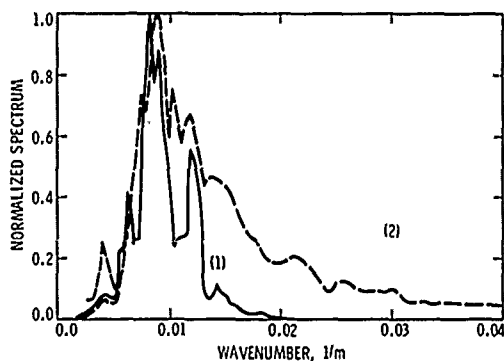


Fig. 7. The normalized spectrum of the simulated SAR image (curve 1, solid line) and the in situ ocean wave height given by Guza [1986] for October 31, 1984, measured in TOWARD (curve 2, dashed line). The SAR coherence time is assumed to be 0.1 s.

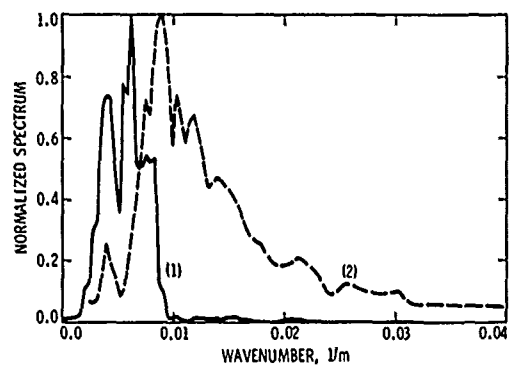


Fig. 8. The normalized spectrum of the simulated SAR image (curve 1, solid line) and the in situ ocean wave height given by Guza [1986] for October 31, 1984, measured in TOWARD (curve 2, dashed line). The SAR coherence time is assumed to be 0.04 s.

the standard SAR imaging integral in  $X$ . This integral yields focused images for  $\chi = 0$ . In the presence of propagating swell, both  $\sigma(X, T)$  and  $U_0(X, T)$  are slowly varying functions of space and time. This dependence on  $T$  is sufficiently strong to produce a nonzero focusing condition. But note that this is unlike the coherent focusing obtained when imaging a rigid target moving at some constant velocity in the azimuth direction. As both  $\sigma(X, T)$  and  $U_0(X, T)$  propagate with the phase velocity of the long wave, one expects the focusing to be related to this quantity. For monochromatic waves this is given by (16). It is easy to show that the image of a monochromatic long wave should focus in the proximity of half the phase speed. It is important to note here that for monochromatic waves, the acceleration effects given by the  $T$  dependence of the orbital velocities may be removed by adjusting the focusing parameter. Alpers and Bruening [1986] include the acceleration as a separate term and use it in computing the SAR resolution in the presence of long waves. This is an artifact of their analysis and not a physical condition.

The modulation of the radar cross section  $\sigma(X, T)$  is due to the tilting and straining of short waves by the long waves. Although tilting is well understood, straining is not. Straining is due to hydrodynamic interactions between the short waves and the long waves [Keller and Wright, 1975]. Extensive experimental evidence on both of these effects has been reported [Plant et al., 1983; Wright et al., 1980; Moore et al., 1986], but

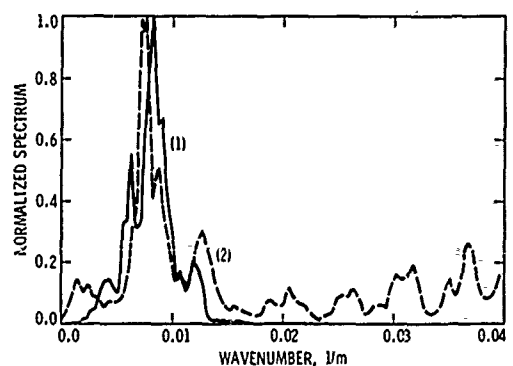


Fig. 9. The normalized spectrum of the simulated SAR image (curve 1, solid line) and the TOWARD field image for October 31, 1984 (curve 2, dashed line). The SAR coherence time is assumed to be 0.07 s.

the spread in the data is considerable and their usefulness can be questioned. The related empirical models assume that the radar cross section modulation is linear and that the nonlinear effects are small and negligible. There is no unanimity among the investigators on this point. But if one is to discern the different imaging processes from field data, it is crucial that this aspect of backscatter modulation be better understood.

The velocity bunching phenomenon associated with  $U_0(X, T)$  is unique to SAR. It is not present in real aperture radars. The Bragg waves are advected by the long waves, and this heaving effect Doppler modulates the radar return signal. It is a nonlinear process and therefore results in distorted images of the ocean surface. Among past investigators, Jain [1981] believed that orbital velocity only produces a smearing process and is not a fundamental imaging process. This view is not valid if the surface orbital velocities are periodically distributed in the azimuth direction. When the latter occurs, the azimuthal shift results in a modulation of the SAR image by the surface orbital velocity.

The simulations discussed in this paper require use of radar coherence time which can be determined from the velocity spread. As was indicated before, coherence time limits the useful integration time. That is, increasing the integration time beyond the coherence time will not improve SAR resolution beyond the limit imposed by the coherence time. Equations (12b) and (12c) reflect this limitation. Jain and Shemdin [1983] reported this effect in the Marine Remote Sensing Experiment (MARSEN). They showed that when the integration time was systematically increased, the image quality improved rapidly at first and then remained constant beyond a certain integration time. One may obtain an estimate of the SAR coherence time from this integration time. From Figure 9 of Jain and Shemdin the coherence time in the MARSEN experiment is estimated to be approximately 0.2 s. It is emphasized here that the smearing due to velocity spread may not be removed by focusing. This spread is due to the intrinsic variability of the short and intermediate surface waves. Plant and Keller [1983] have observed in their measurements both the Doppler shift due to the orbital velocities of the long waves, and the smearing effect due to velocity spread and acceleration of the short waves. It is feasible to obtain good estimates of the coherence time with proper processing of such data.

Equation (12) also reflects the nonlinear nature of the velocity bunching effect. The acceleration effects are also nonlinear. But the simulations show that this effect is small and may be focused out. This is in agreement with Hasselmann *et al.* [1985], who also believe that the nonlinear effects are primarily due to velocity bunching. The nonlinear effects, however, appear only in high sea states where the coherence time is diminished, with the consequence that the SAR resolution is degraded.

The azimuthal resolution in a SAR image is a critical measure of the radar imaging system. In SAR imaging of the ocean surface, the azimuthal resolution is degraded owing to motion effects. The simulations show that the primary degrading influence is the temporal coherence of the radar reflectivity. The coherence time determines the useful integration time and hence the azimuthal resolution of the system. Higher sea states have greater velocity spread and therefore have shorter coherence times and are expected to have higher degradation of azimuthal resolution. The minimum detectable wavelength of ocean waves depends on the azimuthal resolu-

tion of the SAR system and the noise level of the radar receiver. At low noise levels one may assume the minimum detectable wavelength to be twice the resolution. For TOWARD the present analysis suggests that only wavelengths greater than 100 m will be detected with the L band SAR. The orbital acceleration has a minimal effect on azimuthal resolution.

One of the contentious points in previous attempts to formulate the theory for SAR imaging of ocean waves is the question of radar spatial correlation. At incidence angles greater than  $20^\circ$  the primary scattering process is Bragg scattering. For L band radars the scattering is due to a narrow band of the ocean wave height spectrum around 25 cm, at incidence angles near  $30^\circ$ . There is laboratory evidence indicating that these 25-cm short waves decorrelate over distances comparable with their wavelength. For a radar system with an intrinsic resolution of several meters it appears that the radar return will be correlated only over distances considerably shorter than the radar resolution. Hence it appears reasonable to assume that the surface is decorrelated over distances comparable with the radar resolution. These assumptions merit further experimental scrutiny in future field observations.

In the case of specular scattering the focus dependence on the phase velocity of the long wave is anticipated. As specular backscatter does not necessarily decorrelate as fast as the Bragg backscatter, it may be shown that images where the radar return is mainly due to specular scatter are likely to focus at one phase velocity. For incidence angles of less than  $20^\circ$  this scattering process dominates. Therefore if one is to study the complete SAR imaging picture, it is important to investigate the specular scattering mechanism from the ocean surface as well. Wave breaking is another process that is likely to have an impact on the SAR image, as discussed qualitatively by Lyzenga and Shuchman [1983]. It is possible that because of the large orbital velocity, scattering from breaking waves can fall outside the bandwidth of the SAR processor. Finite processor bandwidth may exclude in the SAR image the return from certain parts of the ocean surface, especially in high sea states. This form of image suppression appears as dark spots in the SAR image. In this paper, specular effects are neglected because the incidence angle in TOWARD is approximately  $35^\circ$  in the proximity of the tower.

The simulations given in the previous section show agreement with the results derived from experimentally obtained images. Some of the interesting observations that can be deduced from the analysis of the SAR images obtained in the TOWARD experiment [see Tajirian, 1986] are as follows:

1. The dominant wave number of the image is found to be lower than the dominant wave number of the in situ data.
2. The images are found to focus in the vicinity of the phase velocity of the dominant wave. All the images show broad dependence on the focusing parameter.
3. Nonlinear effects and image distortions are found to be small.
4. Some images, especially at low aircraft altitudes, do not show wavelike patterns with the clarity observed in corresponding high-altitude images.

The first observation is explained by the low-pass filter action of the SAR imaging system. The small coherence times restrict the useful integration time of the SAR. This forces the azimuthal bandwidth of the SAR to be narrow, which in turn results in the image losing its intrinsic resolution. It has been shown in the simulations that as the resolution is degraded the

dominant wave in the SAR images shifts to a lower wave number. The magnitude of the shift is dependent on the radar coherence time.

The second observation has been a source of considerable interest. Initial velocity bunching theories either predicted focusing at zero velocity or gave values that were not related to the direction nor the magnitude of the phase velocity of the dominant wave. But the field images consistently focused in the proximity of the phase velocity of the dominant wave. In the theory presented here, it is shown that both the radar cross section pattern and the velocity bunching pattern may be focused around half the phase velocity. It is also shown that the velocity bunching effect is dependent on the focusing parameter and that this dependence moves the optimum focus setting up to values greater than  $C/2$  when the wave is traveling in the same direction as the aircraft and moves it down to values of less than  $C/2$  when the wave is traveling in the opposite direction to the aircraft, as is shown in Figure 6. Focusing has been an aspect of SAR imaging that appears to benefit from theoretical clarification. It is emphasized that the dependence of SAR on the longwave phase velocity is not due to the effects of coherent integration, but rather is due to that of incoherent integration. This is where the imaging of the ocean surface differs from that of a moving corrugated surface.

The third observation clearly points out that the radar cross section has little if any nonlinear relationship to the wave slope. It also suggests that the nonlinear effects of the velocity bunching effects are small in the TOWARD experiment. This is expected because the sea states encountered in TOWARD were low. It was shown before that in the higher sea states the nonlinear effects increase. It is also known that the coherence time is inversely proportional to the sea state. Therefore there is a reasonable possibility that the nonlinear effects may not be dominant even in high sea states. The important possibility requires more definitive determination of the dependence of coherence time on the sea state. Such a determination may be obtained from near-surface-based radar measurements.

The fourth observation is attributed to two factors. The first is due to the fact that the velocity bunching effect is diminished because the  $(R/V)$  ratio is smaller. The second is due to the radar cross section modulation. At the lower aircraft altitudes, the velocity bunching modulation is comparable in magnitude to the cross section modulation. Therefore it is possible that the two factors eliminate each other. This can be determined by independent analysis of the TOWARD radar backscatter measurements from the tower-based  $L$  band radar. The latter work is in progress.

## 5. CONCLUSION

A one-dimensional theory has been developed to model SAR imaging of the ocean surface. The theory assumes that the radar cross section modulation and the surface orbital velocities have patterns that move with the ocean wave height. The time dependence of these patterns requires a nonzero focus setting to obtain the best image contrast. The simulations indicate that the optimum focus setting is in the proximity of half the phase velocity of the dominant long wave. This dependence on the longwave phase velocity evolves in a different manner compared to the "distributed surface" viewpoint. It is shown that the focus dependence is due to an incoherent integration process and not due to motion induced phase

errors. This integration involves "stacking" independent sub-images incoherently to give the best contrast.

The azimuthal shift due to the slant range directed velocity both modulates the signal and degrades the azimuthal resolution. The statistical nature of the orbital velocities of the intermediate and short waves smear the image in the azimuthal direction. This spread may not be removed by focus adjustment. The radar coherence time is defined as a measure of the velocity spread. Initial theoretical and experimental estimates show the coherence time to be in the range 0.03–0.1 s for the TOWARD data set. It is crucial for SAR simulations purposes to obtain more measurements of this coherence time, as the azimuthal resolution of the SAR imaging system is determined by this factor.

## APPENDIX: DERIVATION OF THE COVARIANCE OF THE COMPLEX RADAR REFLECTIVITY

The complex radar reflectivity is given by

$$\rho(x, t) = \rho_0(x, t) \exp [2ik_0 h(x, t) \cos \theta] \quad (\text{A1})$$

where  $\rho_0(x, t)$  is the reflectivity of the ocean surface,  $h(x, t)$  is the ocean waveheight,  $\theta$  is the incidence angle, and  $k_0$  is the radar wave number. The covariance of this complex reflectivity is

$$\langle \rho(x_1, t_1) \rho^*(x_2, t_2) \rangle = \langle \rho_0(x_1, t_1) \rho_0^*(x_2, t_2) \cdot \exp \{2ik_0 [h(x_1, t_1) - h(x_2, t_2)] \cos \theta\} \rangle \quad (\text{A2})$$

If the dielectric properties of the ocean surface are assumed to be constant, then the surface reflectivity  $\rho_0(x, t)$  will be constant,  $\rho_0$ . Making the substitutions

$$x = x_1 - x_2 \quad (\text{A3a})$$

$$X = \frac{(x_1 + x_2)}{2} \quad (\text{A3b})$$

$$\tau = t_1 - t_2 \quad (\text{A3c})$$

$$T = \frac{(t_1 + t_2)}{2} \quad (\text{A3d})$$

it is shown that the covariance becomes

$$\langle \rho \rho^* \rangle (X, x, T, \tau) = \rho_0^2 \left\langle \exp \left\{ 2ik_0 \left[ h \left( X + \frac{x}{2}, T + \frac{\tau}{2} \right) - h \left( X - \frac{x}{2}, T - \frac{\tau}{2} \right) \right] \cos \theta \right\} \right\rangle \quad (\text{A4})$$

Since the expected value is independent of the initial position and time, (A4) may be rewritten as

$$\langle \rho \rho^* \rangle (X, x, T, \tau) = \rho_0^2 \langle \exp \{ 2ik_0 [h(X, T) - h(X - x, T - \tau)] \cos \theta \} \rangle \quad (\text{A5})$$

The SAR image is a map of the covariance of the complex reflectivity of the ocean surface. The SAR two-scale model is invoked at this stage to represent this covariance function as a product of a longwave term and a shortwave term. The two-scale model gives the ocean wave height as

$$h(x, t) = h_L(x, t) + h_s(x, t) \quad (\text{A6})$$

where  $h_L(x, t)$  and  $h_s(x, t)$  are the longwave and the shortwave components respectively. Implied in the separation of the total

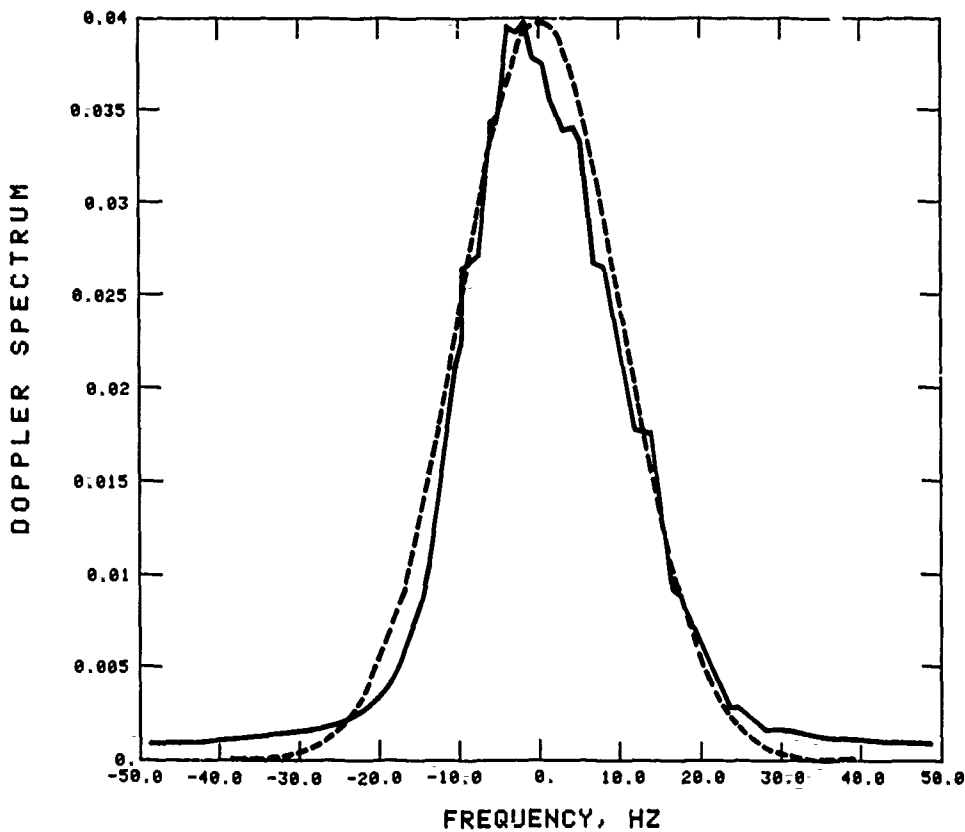


Fig. A1. The Doppler spectrum of the radar return of the NRL L band radar on October 31, 1984. The spectrum is the average of 1-s samples over a period of 100 s. Also shown is the Gaussian (dashed line) that was fitted to the experimental curve to obtain an estimate of the coherence time.

surface displacement into long waves and short waves is a statistical description of the short waves superposed on a deterministic description of the long waves. When (A6) is substituted into (A5), the expected value in (A5) becomes the product of the expected value of the covariance of the shortwave reflectivity and the longwave modulation. The expected value of the covariance of the shortwave reflectivity is obtained using Cramer's [1946] result, which is

$$\left\langle \exp \left[ i \sum_{l=1}^N a_l \eta(\zeta_l) \right] \right\rangle = \exp \left[ -\frac{1}{2} \sum_{l=1}^N \sum_{m=1}^N a_l a_m \psi(\zeta_l - \zeta_m) \right] \tag{A7}$$

where  $a_l$  are constant real coefficients and  $\psi(\zeta_l - \zeta_m)$  is given by

$$\psi(\zeta_l - \zeta_m) = \langle \eta(\zeta_l) \eta(\zeta_m) \rangle \tag{A8}$$

Using (A6) and (A7), (A5) is reduced to

$$\langle \rho \rho^* \rangle (X, x, T, \tau) = \rho_0^2 \exp \left\{ -4k_0^2 \cos^2 \theta [\phi_s(0, 0) - \phi_s(x, \tau)] \right\} \cdot \exp \left\{ 2ik_0 \cos \theta [h_L(X, T) - h_L(X - x, T - \tau)] \right\} \tag{A9}$$

where  $\phi_s(x, \tau)$  is the covariance function of the waveheight of the short waves and is given by

$$\phi_s(x, \tau) = \langle h_s(X, T) h_s(X + x, T + \tau) \rangle \tag{A10}$$

which is assumed to be stationary. Using Taylor series ex-

pansion for the long waves, equation (A9) becomes

$$\langle \rho \rho^* \rangle (X, x, T, \tau) = \rho_0^2 \exp \left\{ -4k_0^2 \cos^2 \theta [\phi_s(0, 0) - \phi_s(x, \tau)] \right\} \cdot \exp \left\{ 2ik_0 \cos \theta \left[ \frac{\partial h_L}{\partial X}(X, T)x + \frac{\partial h_L}{\partial T}(X, T)\tau + \frac{\partial^2 h_L}{\partial X^2}(X, T) \frac{x^2}{2} + \frac{\partial^2 h_L}{\partial T^2}(X, T) \frac{\tau^2}{2} + \dots \right] \right\} \tag{A11}$$

For TOWARD conditions, with an intrinsic SAR resolution of 11 m, calculations using the Pierson-Moskowitz spectrum resulted in a shortwave covariance function with a correlation distance of the order of 1 m and a coherence time of the order of 100 ms. These quantities were obtained from the widths of the covariance function in the space and time domains, respectively. An independent evaluation of radar backscatter at L band obtained during the TOWARD experiment gave radar coherence times of 30 ms. Figure A1 shows the spectrum of the radar return of the Naval Research Laboratory (NRL) L band radar on October 31, 1984. The Doppler shifts due to the longwave orbital velocities have been removed. This curve is the temporal spectrum of the covariance function of the shortwave reflectivity. The bandwidth is inversely proportional to the effective coherence time.

Clearly, the values of the correlation distance and the coherence time are small in comparison with the longwave wavelengths and periods respectively. It follows that the higher-

order terms in the longwave expansion may be neglected in (A11). Hence equation (A11) becomes

$$\langle \rho \rho^* \rangle (X, x, T, \tau) \approx \rho_0^2 \exp \{ -4k_0^2 \cos^2 \theta [\phi_s(0, 0) - \phi_s(x, \tau)] \} \\ \cdot \exp \left\{ 2ik_0 \cos \theta \left[ \frac{\partial h_L}{\partial X}(X, T)x + \frac{\partial h_L}{\partial T}(X, T)\tau \right] \right\} \quad (\text{A12})$$

which is rewritten as

$$\langle \rho \rho^* \rangle (X, x, T, \tau) \approx \rho_0^2 \exp \{ -4k_0^2 \cos^2 \theta [\phi_s(0, 0) - \phi_s(x, \tau)] \} \\ \cdot \exp [2ik_0 \cos \theta S(X, T)x] \exp [2ik_0 \cos \theta U_0(X, T)\tau] \quad (\text{A13})$$

where  $S(X, T)$  is the azimuth-directed component of the longwave slope and  $U_0(X, T)$  is the vertical component of the longwave orbital velocity and are given by the derivatives of  $h_L(X, T)$  with respect to  $X$  and  $T$ , respectively.

The first two terms on the right-hand side of (A13) represent the covariance of the shortwave reflectivity modulated by the longwave tilt. They represent the backscatter seen by real aperture radars and is proportional to the radar cross section,  $\sigma(X, T)$  [see Valenzuela, 1978], of the ocean surface. The last term on the right-hand side of (A13) represents the Doppler modulation induced by the orbital velocities of the long waves. In TOWARD the SAR intrinsic resolution of 11 m is large in comparison with the correlation distance of 1 m. This implies that the total return from a SAR resolution cell may be treated as the incoherent addition of the backscatter from independent scattering elements with dimensions of the order of 1 m. Therefore for imaging purposes the  $x$  dependence in the shortwave covariance function may be replaced by a  $\delta$  function,  $\delta(x)$ . Using the results shown in Figure A1 the time dependence of the covariance of the shortwave reflectivity may be approximated by a Gaussian distribution,  $\exp(-\tau^2/\tau_c^2)$ , where  $\tau_c$  is the radar coherence time. Incorporating the above approximation implies

$$\rho_0^2 \exp \{ -4k_0^2 \cos^2 \theta [\phi_s(0, 0) - \phi_s(x, \tau)] \} \exp [2ik_0 \\ \cdot \cos \theta S(X, T)x] = \sigma(X, T) \exp(-\tau^2/\tau_c^2) \delta(x) \quad (\text{A14})$$

Finally, (A13) becomes

$$\langle \rho \rho^* \rangle (X, x, T, \tau) = \sigma(X, T) \\ \cdot \exp [2ik_0 \tau U_0(X, T) \cos \theta] \exp(-\tau^2/\tau_c^2) \delta(x) \quad (\text{A15})$$

This equation is used as the covariance of the radar reflectivity in equation (10) of the main text.

*Acknowledgments.* This paper is produced in support of the TOWARD experiment, which is sponsored by the Office of Naval Research under their SAR Advanced Research Initiative Program. The oceans element of this program is directed by Hans Dolezalek.

#### REFERENCES

- Alpers, W. R., Monte Carlo simulations for studying the relationships between ocean wave and synthetic aperture radar image spectra, *J. Geophys. Res.*, **88**, 1745-1759, 1983.
- Alpers, W. R., and C. Bruening, On the relative importance of motion-related contributions to the SAR imaging mechanism of ocean waves, *IEEE Trans. Geosci. Remote Sens.*, **GE-24**, 873-885, 1986.
- Alpers, W. R., and C. L. Rufenach, The effect of orbital motions on synthetic aperture radar imaging of ocean waves, *IEEE Trans. Antenna Propag.*, **AP-27**, 685-690, 1979.
- Alpers, W. R., D. B. Ross, and C. L. Rufenach, On the detectability of ocean surface waves by real and synthetic aperture radar, *J. Geophys. Res.*, **86**, 6481-6498, 1981.
- Beal, R. C., D. G. Tilley, and F. M. Monaldo, Large- and small-scale spatial evolution of digitally processed ocean wave spectra from Seasat synthetic aperture radar, *J. Geophys. Res.*, **88**, 1761-1778, 1983.
- Brown, W. M., Synthetic aperture radar, *IEEE Trans. Aerosp. Electron. Syst.*, **AES-3**, 217-229, 1967.
- Cramer, H., *Mathematical Methods of Statistics*, Princeton University Press, Princeton, New Jersey, 1946.
- de Loor, G. P., The radar backscatter of oil spills as measured at platform Noordwijk, *Proj. Noordwijk Rep. 4*, Natl. Defence Res. Organ., 1983.
- Elachi, C., and W. E. Brown, Models of radar imaging of the ocean surface waves, *IEEE Trans. Antennas Propag.*, **AP-25**, 84-95, 1977.
- Guza, R. T., Surface gravity wave measurements, in *Investigation of Physics of Synthetic Aperture Radar in Ocean Remote Sensing, TOWARD Interim Report*, vol. 2, pp. 1-1-1-25, Jet Propulsion Laboratory, Pasadena, Calif., 1986.
- Harger, R. O., *Synthetic Aperture Radar Systems*, Academic, San Diego, Calif., 1970.
- Harger, R. O., The SAR image of short gravity waves on a long gravity wave, in *Wave Dynamics and Radio Probing of the Ocean Surface*, edited by O. M. Phillips and K. Hasselmann, Plenum, New York, 1986.
- Hasselmann, K., et al., Measurements of wind-wave growth and swell decay during the Joint North Sea Wave Project (JONSWAP), *Dtsch. Hydrogr. Z.*, **12**(8), suppl. A, 1973.
- Hasselmann, K., R. K. Raney, W. J. Plant, W. R. Alpers, R. A. Shuchman, D. R. Lyzenga, C. L. Rufenach, and M. J. Tucker, Theory of synthetic aperture radar ocean imaging: A MARSEN view, *J. Geophys. Res.*, **90**, 4659-4686, 1985.
- Ivanov, A. V., On the mechanism of imaging ocean waves by synthetic aperture radar, *IEEE Trans. Antennas Propag.*, **AP-31**, 538-541, 1983.
- Jain, A., Focusing effects in synthetic aperture radar imaging of ocean waves, *Appl. Phys.*, **15**, 323-333, 1978.
- Jain, A., SAR imaging of ocean waves: Theory, *IEEE J. Oceanic Eng.*, **OE-6**, 130-139, 1981.
- Jain, A., and O. H. Shemdin, L band SAR ocean wave observations during MARSEN, *J. Geophys. Res.*, **88**, 9792-9808, 1983.
- Jasik, H., *Antenna Engineering Handbook*, McGraw-Hill, New York, 1961.
- Keller, W. C., and J. W. Wright, Microwave scattering and the straining of wind-generated waves, *Radio Sci.*, **10**, 139-147, 1975.
- Larson, T. R., L. Moskowitz, and J. W. Wright, A note on SAR imagery, *IEEE Trans. Antennas Propag.*, **AP-24**, 393-394, 1976.
- Lyzenga, D. R., and R. A. Shuchman, Analysis of scatterer motion effects in MARSEN X band SAR imagery, *J. Geophys. Res.*, **88**, 9769-9775, 1983.
- Moore, R. K., A Chaudhry, R. Lawner, J. Nice, and J. Boberg, The University of Kansas radar backscatter measurements from the ocean surface during the TOWARD 84/85 experiment, *Tech. Rep. RSL TR-419-4*, Remote Sens. Lab., Univ. of Kansas, Lawrence, 1986.
- Papoulis, A., *Probability, Random Variables, and Stochastic Processes*, McGraw-Hill, New York, 1965.
- Phillips, O. M., *The Dynamics of the Upper Ocean*, Cambridge University Press, New York, 1977.
- Phillips, O. M., The structure of short gravity waves on the ocean surface, in *Spaceborne Synthetic Aperture Radar for Oceanography*, pp. 24-31, Johns Hopkins University Press, Baltimore, Md., 1981.
- Pierson, W. L., and L. Moskowitz, A proposed spectral form for fully developed wind seas based on the similarity theory of S. A. Kitaigorodski, *J. Geophys. Res.*, **69**, 5181-5190, 1964.
- Plant, W. J., and W. C. Keller, The two-scale radar wave probe and SAR imagery of the ocean, *J. Geophys. Res.*, **88**, 9776-9784, 1983.
- Plant, W. J., W. C. Keller, and A. Cross, Parametric dependence of ocean wave-radar modulation transfer functions, *J. Geophys. Res.*, **88**, 9747-9756, 1983.
- Raney, R. K., Synthetic aperture imaging radar and moving targets, *IEEE Trans. Aerosp. Electron. Syst.* **AES-7**, 449-505, 1971.
- Swift, C. F., and L. R. Wilson, Synthetic aperture radar imaging of moving ocean waves, *IEEE Trans. Antennas Propag.*, **AP-27**, 725-729, 1979.
- Tajirian, E., Processing of JPL SAR frame: Azimuthal waves on 31 October 1984, in *Investigation of Physics of Synthetic Aperture*

- Radar in Ocean Remote Sensing, *TOWARD Interim Report*, vol. 2, pp. VI-1-VI-27, Jet Propulsion Laboratory, Pasadena, Calif., 1986.
- Tucker, M. J., The imaging of waves by satelliteborne synthetic aperture radar: The effects of sea surface motion, *Int. J. Remote Sens.*, **6**, 1059-1074, 1985a.
- Tucker, M. J., The decorrelation time of microwave radar echoes from the sea surface, *Intl. J. Remote Sens.*, **6**, 1075-1089, 1985b.
- Valenzuela, G. R., Theories for the interaction of electromagnetic and ocean waves—A review, *Boundary Layer Meteorol.*, **13**, 61-85, 1978.
- Wakasugi, K., N.-F. Kishi, and M. Matsuo, A three-dimensional formulation for synthetic aperture radar images of the ocean waves in orbital motion, *IEEE Trans. Geosci. Remote Sens.*, **GE-24**, 732-738, 1986.
- Wright, J. W., A new model of sea clutter, *IEEE Trans. Antennas Propag.*, **AP-16**, 217-223, 1968.
- Wright, J. W., W. J. Plant, W. C. Keller, and W. L. Jones, Ocean-wave-radar modulation transfer functions from the West Coast Experiment, *J. Geophys. Res.*, **85**, 4957-4966, 1980.

---

D. P. Kasilingam and O. H. Shemdin, Ocean Research and Engineering, 255 S. Marengo Avenue, Pasadena, CA 91101.

(Received September 14, 1987;  
accepted December 18, 1987.)

# Multifocus Processing of L Band Synthetic Aperture Radar Images of Ocean Waves Obtained During the Tower Ocean Wave and Radar Dependence Experiment

E. K. TAJIRIAN

*Ocean Research and Engineering, Pasadena, California*

As part of the Tower-Ocean Wave and Radar Dependence Experiment (TOWARD) objectives, the mechanisms of SAR imaging of ocean waves are investigated using L band SAR data over the Naval Ocean Systems Center tower. This paper provides experimental evidence needed to validate the differing hypotheses. Various processing methods are investigated to generate spectra with large degrees of freedom. The results show that waves traveling in the aircraft direction are most detectable at focus settings in the range 10.0-15.0 m/s, which is consistent with the Marine Remote Sensing Experiment (MARSEN) observations reported by Jain and Shemdin (1983). Waves traveling in the direction opposite to the aircraft are most detectable at settings equal to -5.0 to -15.0 m/s. The SAR imaging system acts as a low-pass filter with the peak of the ocean wave height spectrum occurring at higher wave numbers compared with the peak in the SAR image spectrum.

## 1. INTRODUCTION

Synthetic aperture radar (SAR) provides high-resolution maps of the ocean surface regardless of the time of day and under nearly all weather conditions. This is done by the processing of the radar data collected over a long interval of the aircraft path to improve azimuthal resolution, and by pulse compression to improve the range resolution, as was discussed by Hovanessian [1984]. There is growing interest in SAR imaging of the ocean surface and in theoretical understanding of the mechanisms involved. The work by Larsen *et al.* [1976] and Shemdin *et al.* [1978] marks the beginning of this interest. The modulating mechanisms for azimuthally traveling surface waves have been the subject of much discussion. The modulating mechanisms that are considered to be responsible for imaging surface waves are velocity bunching, hydrodynamic modulation, and tilt modulation.

The velocity bunching effect, discussed by Alpers and co-workers [Alpers and Rufenach, 1979; Alpers *et al.*, 1981] and Plant and Keller [1983] for azimuthally traveling waves, is due to the nonuniform orbital velocity component in the slant range direction. This velocity causes azimuthal shifts of the scattering facets in the SAR image and results in the scatterers being superimposed nonuniformly in the image plane.

The distributed surface viewpoint, discussed by Jain [1978, 1981] and R. Harger (The SAR image of short gravity waves on long gravity waves: An explication, submitted to *IEEE Journal of Oceanic Engineering*, 1985; also private communication, 1985), implicitly assumes that the radar return from the ocean surface is correlated over a distance greater than the intrinsic resolution of the SAR. This assumption results in the radar backscatter being modulated by the longwave slope. Since the longwave features move at the phase speed, this hypothesis gives an optimum focus setting that is equal to the phase speed of the long wave. At present, there is no conclusive data on magnitudes of the spatial correlation distance.

Images of ocean waves have been reported from the Marineland experiment by Shuchman and Shemdin [1983] and

from the Marine Remote Sensing Experiment (MARSEN) by Jain and Shemdin [1983]. These show improved contrast in the peak-to-baseline ratios (PBR; defined in detail by Shuchman and Shemdin [1983] and Jain and Shemdin [1983]) when the focus parameters in the SAR optical processor are adjusted. In these experiments, only optical recording and optical processing were available. Although important results were obtained, it was considered desirable to obtain additional SAR data with higher dynamic range and more precise determination of the ocean wave parameters such as focus setting. The latter can be achieved more easily with digital processing of a SAR image.

In the Tower Ocean Wave and Radar Dependence Experiment (TOWARD), radar data were recorded both optically and digitally and were SAR-processed in both optical and digital modes. Hence large-area coverage could be produced with optical images, and precise determination of the SAR imaging parameters could be achieved with digital processing. The SAR flight pattern shown in Figure 1 was executed over the Naval Ocean Systems Center (NOSC) tower. The flight dates and durations and the SAR characteristics are given in the TOWARD Interim Report [see Shemdin *et al.*, 1986].

Ten SAR frames were selected for focusing studies, as shown in Table 1. In this paper the frames at 11,583-m altitude (38,000 feet), obtained on October 31, 1984, are discussed. These images show the highest contrast for ocean waves and give the clearest contrast improvement for variable focus settings. Because of space limitation, the images obtained at the two lower altitudes will be deferred to a later paper.

Previous experimental results from Shuchman and Shemdin [1983] indicate that the maximum modulation depth occurs when the motion correction in the SAR processor is set at a value equivalent to that required to focus a point target moving in the azimuthal direction with a velocity that is of the order of the wave phase velocity of the dominant surface wave. Jain and Shemdin [1983] investigate this point in the MARSEN data set using both radar and in-situ measurements. They also find that the focus dependence for maximum contrast is that for a point target moving with a velocity that is of the order of the wave phase velocity of the dominant surface wave. They note that azimuthally traveling waves can

Copyright 1988 by the American Geophysical Union

Paper number 88JC03067.  
0148-0227/88/88JC-03067\$05.00

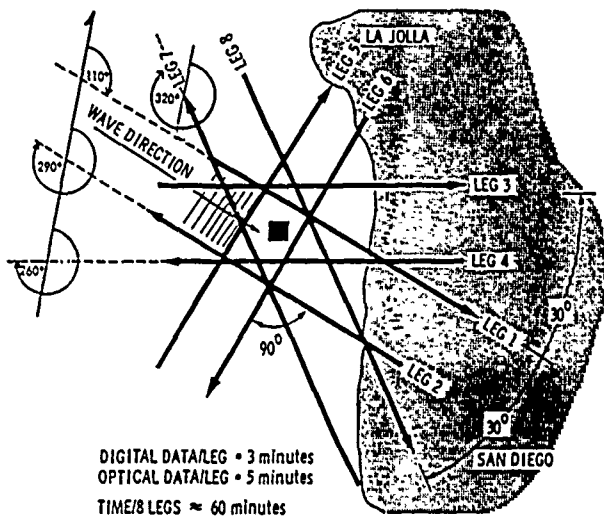


Fig. 1. CV-990 SAR flight paths over the tower.

become as visible as range-traveling waves when the SAR processor is set for optimum focus.

In this paper special processing is used to determine the optimum focus. This is done by examining the energy density at the dominant wave numbers in the SAR spectrum as a function of focus setting. The dominant wave number is chosen because the ocean wave spectrum in the vicinity of the NOSC tower is narrowband. Hence it becomes possible to relate focus shift effects to the dominant wave features. We also explore the total energy variation in the SAR spectra to determine the influence of focus setting on the overall enhancement of the image contrast. In the following, the data processing methods for generating the optimal signal to noise ratio are discussed in section 2, the results of applying the processing methods to the various images are presented in section 3, the comparison of the SAR spectra with the in situ measurements is discussed in section 4, and finally, the conclusions derived are given in section 5.

## 2. DATA PROCESSING METHODS

As was stated before, a key objective in this investigation is to determine the dependence of a SAR spectrum on focus offset. Hence it is necessary to work with data sets that have large signal-to-noise ratios. Initially, one-dimensional data processing is used because of simplicity. The procedure is valid for long waves that are highly directional, as was the case in the TOWARD experiment, where the Channel Islands imposed a directional filter on the swells approaching from the North Pacific Ocean. One-dimensional processing can be applied to small segments of the image, which is useful for studying SAR spectral dependence on range; it also allows spectral determination with large degrees of freedom. The one-dimensional processing method adopted here is based on averaging 31 range resolution cells in the space domain to produce an average azimuthal scan, and is referred to as the space averaging method. This averaging method is found to produce the largest signal-to-noise ratios. The same data were processed by generating power spectra from single resolution azimuthal scans and then adding the different spectra to generate an average spectrum with 62 degrees of freedom. The latter method is referred to as the power spectral averaging method. Results from space versus power spectral averaging

methods were compared as part of the validation effort and were found to yield excellent agreement.

For waves that are traveling at an angle with respect to aircraft heading, geometrical distortions in the SAR image impose inaccuracies that are best dealt with by performing two-dimensional spectral calculations. Such two dimensional spectra yield directionally averaged (omnidirectional) spectra which have high degrees of freedom and yield the directional distribution of waves with respect to the flight direction.

A sample of a digitally processed image is shown in Figure 2, for zero focus setting. A focus setting is defined as the difference between the aircraft ground velocity and the matched filter's velocity setting. For each of 10 frames, 15 such images were processed as focus settings that ranged from  $-25.67$  m/s to  $+25.67$  m/s. The two blocks of data shown in Figure 2 are exhibited in Figure 3 in relation to local bathymetry. Each block is 256 pixels (10.98 m per pixel) in azimuth by 256 pixels (7.5 m per pixel) in slant range. One block (block 2) is in an area where the water depth is 60 m (30 fathoms) at its center point. The second block (block 3) is in an area where the water depth is 26 m (13 fathoms) at its center point. The latter block includes the NOSC tower, shown in Figure 3(b). The location of the data blocks are chosen such that they contain the highest contrast in ocean waves, shown in Figure 2.

Both low dynamic range images (provided in integer numbers) and high dynamic range images (provided in real numbers) were analyzed. The data blocks in the real number data files corresponded to the same locations as in the integer number data blocks. The analysis of the real number data included conversion of data points from amplitude to intensity, and then normalizing the result by the mean intensity to eliminate the dependence on range, as follows:

$$\sigma_0(Az) = \frac{\sigma(R, Az) - M(R)}{M(R)} \quad (1)$$

where  $(Az)$  is the azimuthally modulated radar cross section,  $M(R)$  is the mean value of the cross section at a particular range for azimuth traveling waves, and  $(R, Az)$  is the cross section seen by the SAR. The mean removal produces sharper spectra, since the mean dependence on range acts as a low wave number envelope. The normalized space domain data is broken into four smaller blocks,  $128 \times 128$  points each. A two-dimensional power spectrum is generated for each block and the spectra from the four blocks are summed. Omnidirectional averaging is performed on the summed spectra, from which the dominant wave number and spectral density characteristics are determined.

To increase the degrees of freedom, the normalized space domain data block is broken into 16 smaller blocks each containing  $64 \times 64$  points. A two-dimensional power spectrum is generated for each block, and the 16 power spectra are summed. The latter is omnidirectionally averaged to determine the dependence of the dominant wave energy on focus.

TABLE 1. SAR Frames Especially Processed for Focusing Studies

Altitude, m	Oct. 17	Oct. 31	Nov. 4	Nov. 7
2,134		legs 4, 7		
6,098	leg 2	leg 1	leg 2	leg 2
11,583		legs 1, 2, 4, 7		

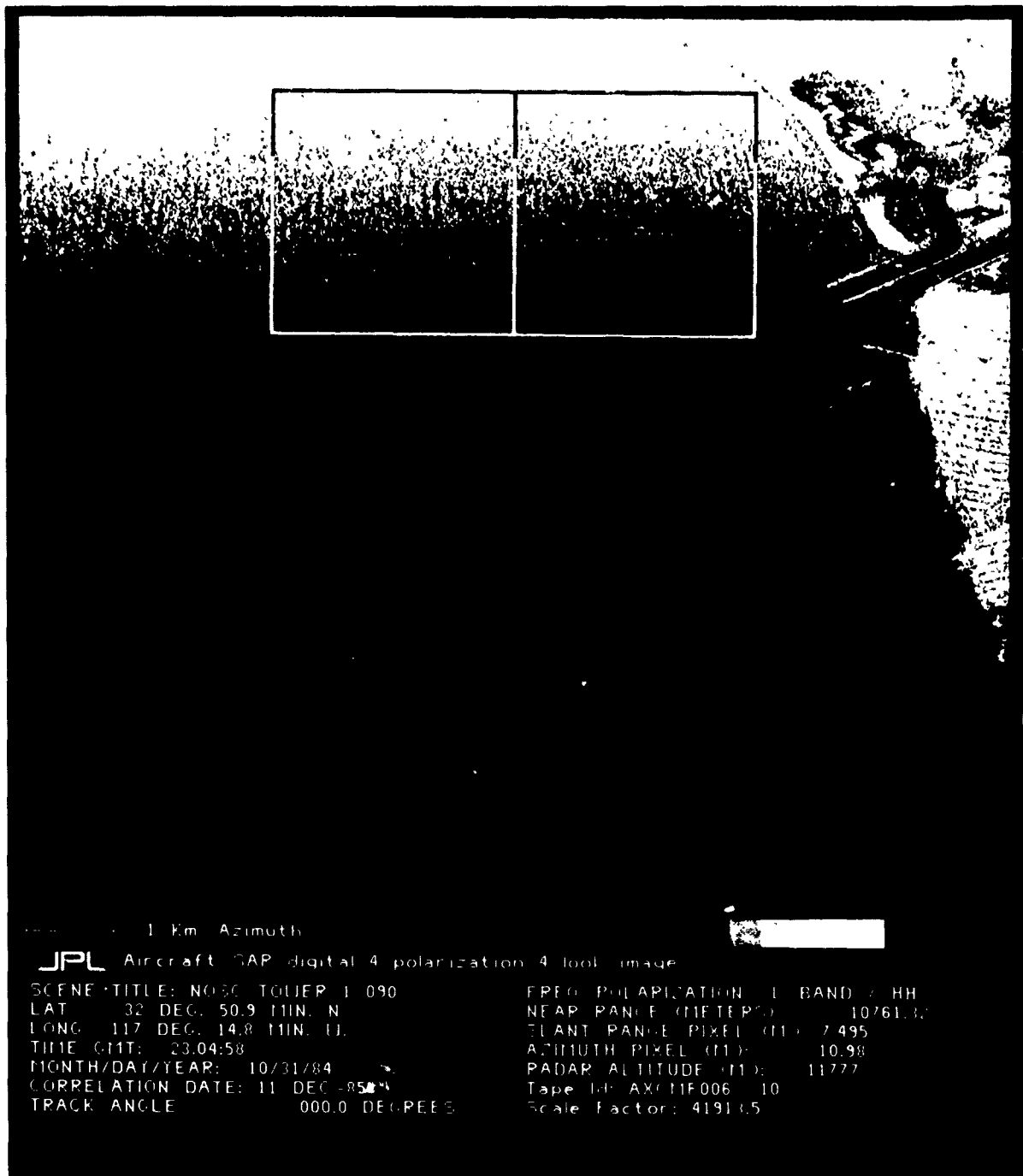


Fig. 2 Sample of digitally processed image used in present analysis. Leg 1, altitude of 11,583 m, heading of 110 deg, and azimuthally traveling waves

In converting the image data to ground range, the relationship between the slant range  $L$  and the ground range  $X$  is given by

$$L = h / \cos(\theta) \tag{2}$$

$$X = (L^2 - h^2)^{1/2} \tag{3}$$

where  $h$  is altitude and  $\theta$  is the incidence angle of the aircraft. The details of the conversion are given by *Laplan* [1987]. Figure 4 shows sample spectra at different focus settings generated from leg 4 images.

### 3. FOCUSING RESULTS

The results presented here are obtained using the processing methods discussed in the preceding section. These include both one-dimensional and two dimensional processings of the SAR images. The aim is to investigate the longwave energy density dependence on focus. Of particular interest is the asymmetry in distribution with respect to flight direction. Leg 1 data (aircraft heading of 110) is discussed first. This is followed by leg 2, 4, and 7 data with aircraft headings corresponding to 290, 260, and 320, respectively. Leg 1 SAR data

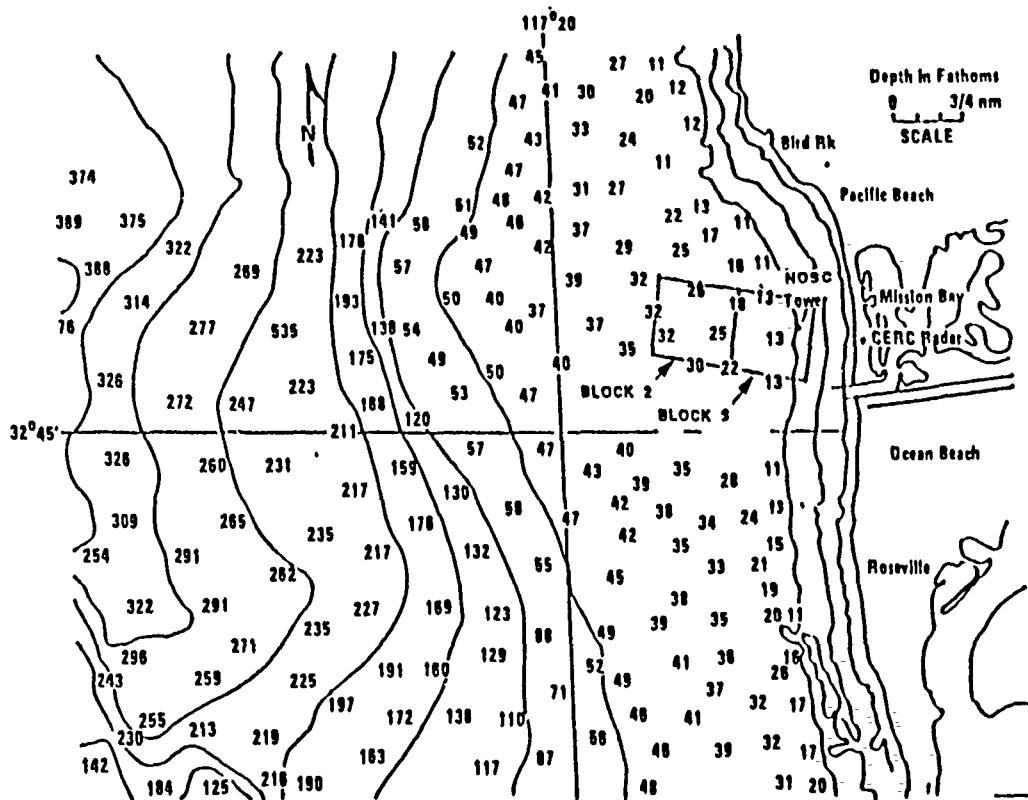


Fig. 3a. Approximate locations of data blocks on the area map for leg 1 (the depth contours are in fathoms).

were processed for 15 different focus settings. Initially, the focus steps were set at 2.75 m/s covering the range  $\pm 19.25$  m/s. The results revealed the asymmetry in the ocean wave contrast versus focus setting, but the location of the peak could not be determined. In the second processing the focus steps were set at 3.67 m/s to extend the range of focus offsets to  $\pm 25.67$  m/s. The latter was found necessary to establish the focus value that corresponds to the maximum wave contrast.

It is useful to examine the dependence of the total energy in the SAR spectrum on range. The total energy obtained using the space averaging method is found to decrease monotonically with range (or incidence angle), as is shown in Table 2. The total energy is also found to be insensitive to focus setting.

If the dc component is removed, the remaining energy exhibits a local maximum at an incidence angle,  $\theta = 26.15^\circ$ , as is shown in Figure 5. The peak at  $\theta = 26.15^\circ$  is found to be sharpest in the optimum focus image, but the trend is detected

for all the focuses. The dependence of total energy (less dc) on focus setting at  $\theta = 26.15^\circ$  is plotted in Figure 6. The latter shows the total energy to vary smoothly as a function of focus setting with the peak corresponding to 11 m/s.

Also of interest is the dependence of the energy density at the dominant wave length on focus setting. The latter is shown

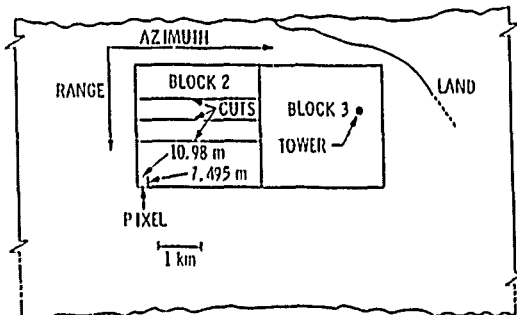


Fig 3b Recorded data blocks and their locations on the image for the leg 1 flight path.

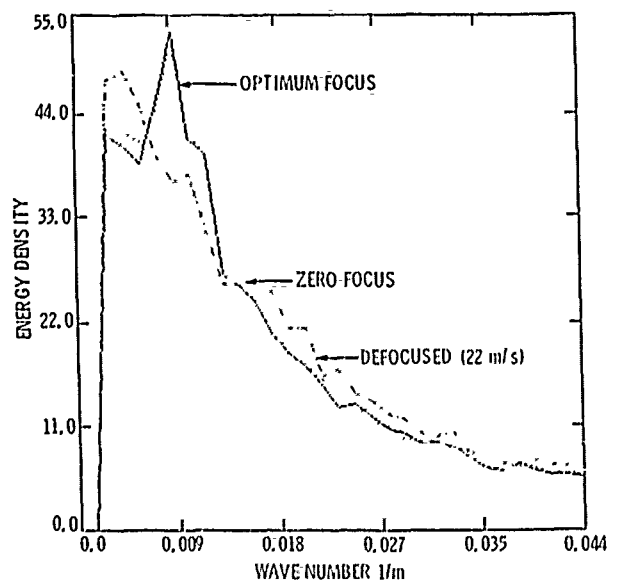


Fig. 4. Power spectra for three focus settings obtained by the omnidirectional averaging of sixteen  $64 \times 64$  two-dimensional spectra for leg 4 real number data. The aircraft heading is  $260^\circ$ , altitude is 11,583 m, and look angle  $\approx 31.4^\circ$ .

TABLE 2. Dependence of Total Energy (Including dc) on Incidence Angle for Leg 1

Focus	Total Energy, $\times 10^6$		
	21.2°	26.1°	29.9°
-7	11.89	6.810	3.572
-6	11.89	6.822	3.580
-5	11.77	6.750	3.531
-4	11.70	6.683	3.509
-3	11.70	6.671	3.524
-2	11.69	6.680	3.529
-1	11.58	6.633	3.509
0	11.45	6.567	3.493
1	11.42	6.550	3.502
2	11.43	6.573	3.523
3	11.40	6.569	3.523
4	11.39	6.564	3.519
5	11.43	6.579	3.525
6	11.49	6.609	3.533
7	11.54	6.643	3.541

in Figure 7 for wave number spectra computed using both the space averaging and power spectral averaging methods. Both methods yield an asymmetry, with the peaks corresponding to an offset equal to 11.0 m/s in the direction of wave propagation. Both methods show the dominant wavelength to be 147.9 m.

A convenient method for presenting the focus offset results shown in Figure 7 is by normalizing the dominant wave energy by the corresponding value in the defocused spectrum. The ratios obtained with this procedure are referred to as the peak-to-baseline ratio. A graphical representation of PBR dependence on focus is shown in Figure 8 for spectra computed using the space averaging method. Here, PBR values corresponding to no wave number averaging and, corresponding to averaging over three contiguous wave numbers are shown. They are compared with similar results obtained by *Jain and*

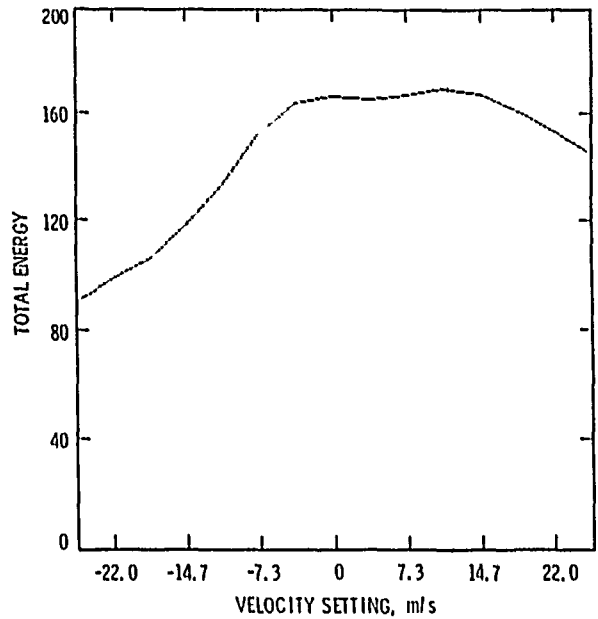


Fig. 6. Total spectral energy less dc versus focus for aircraft heading of 110°, aircraft altitude of 11,583 m, incidence angle of 26.15° (space averaging method); leg 1 data (AXCMF006).

*Shemdin* [1983]. The latter results were derived from optically processed images obtained during the MARSSEN experiment in the North Sea. The agreement between PBR offsets from the TOWARD and MARSSEN experiments confirm that such offsets are real and not a function of optical versus digital processing of SAR images.

The focusing results presented so far are based on spectra derived from line scans in the azimuthal direction. This analysis gives reasonable estimates for azimuth-traveling waves such as those encountered in leg 1 of the TOWARD flight pattern. To test the validity of the one-dimensional analysis,

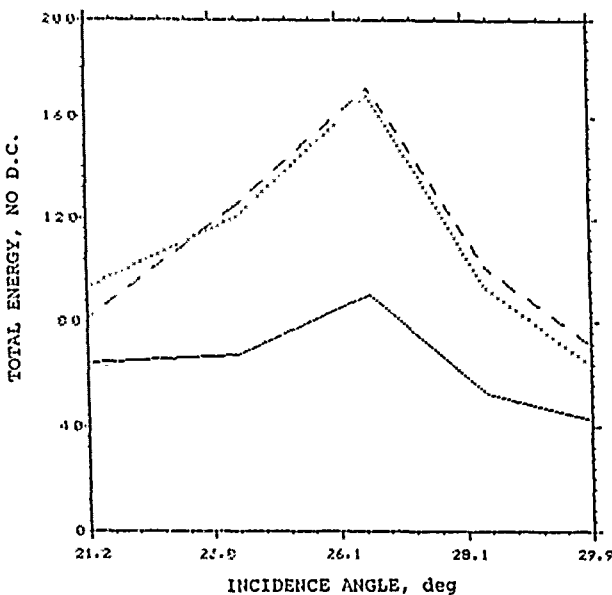


Fig. 5. Total spectral energy less dc versus incidence angle (space averaging method). Aircraft heading is 110°, and aircraft altitude is 11,583 m leg 1 data (AXCMF006). Dashed line, optimum focus; dotted line, zero focus; solid line, defocused.

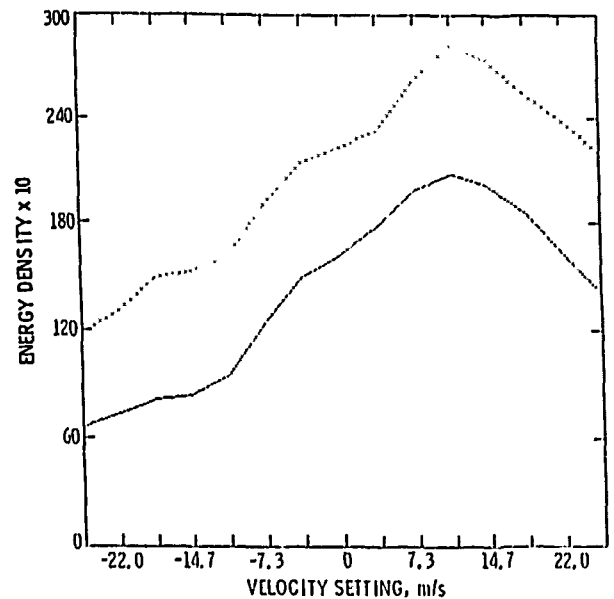


Fig. 7. Energy density at 147.9-m wavelength versus focus, for incidence angle of 26.1°, aircraft heading of 110°,  $N = 0$ , and aircraft altitude of 11,583 m, leg 1 data (AXCMF006). The solid line shows space averaging; the dotted line, power spectral averaging.

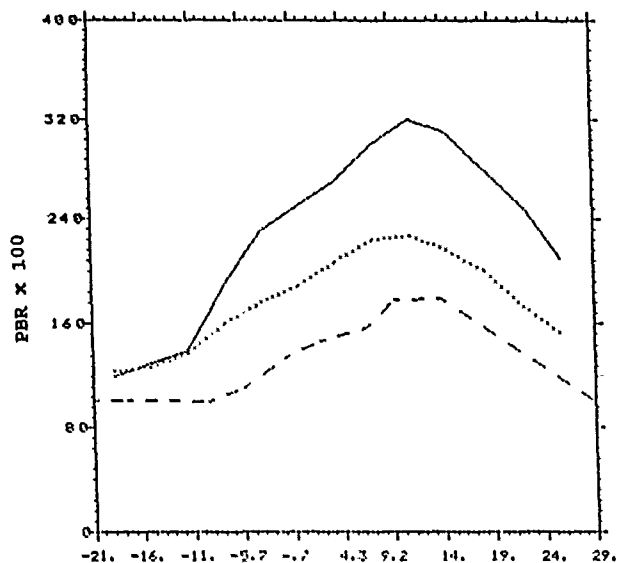


Fig. 8. PBR at 147.9-m wavelength versus focus (space averaging method). Incidence angle is 26.1° and aircraft altitude is 11,583 m; leg 1 data (AXCMF006). The solid line shows results for  $N = 0$ , and the dotted line shows results for  $N = 3$ . The dashed line shows MARSEN results given by Jain and Shemdin [1983].

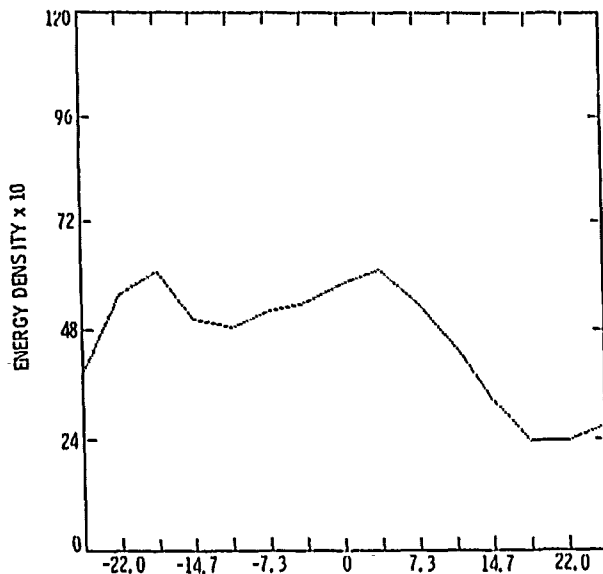


Fig. 10. Energy density at 133.8-m wavelength versus focus, for aircraft heading of 290°, aircraft altitude of 11,583 m; leg 2 data (AXCMF006) (space averaging method).

two-dimensional spectra were generated from the real number image data. First,  $256 \times 256$ -pixel blocks of the space domain data were converted to ground-range and then normalized to remove the dc trend. A directional spectrum with 8 degrees of freedom was generated from four  $128 \times 128$  subblocks. The omnidirectional spectrum, generated by directional averaging of the latter two-dimensional spectrum, shows a dominant wavelength of 127.8 m. The  $128 \times 128$  size blocks are the minimum size necessary to resolve the dominant peaks in the SAR spectrum. If larger data blocks are selected, the area

covers a variable water depth. Increasing the degrees of freedom (without increasing the block size) requires  $64 \times 64$  pixel blocks, which yield 32 degrees of freedom. The latter approach was used to provide more reliable energy estimates at the cost of coarser wave number resolution. The omnidirectional spectra generated from the  $64 \times 64$  pixel, two-dimensional spectra show focus offset with the peak in energy density located at a focus setting equal to 14.7 m/s, as shown in Figure 9.

For leg 2 (aircraft heading of 290°), the plot of dominant energy versus focus is shown in Figure 10. Here, the space averaging method is used, as similar results are found when

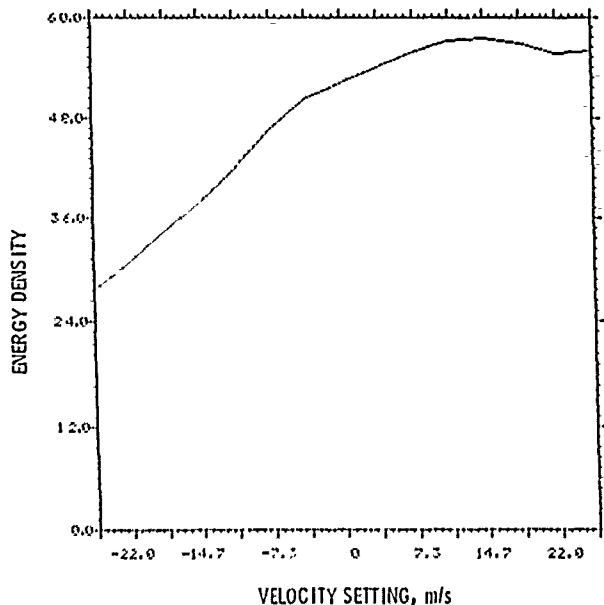


Fig. 9. Dominant wave number energy density dependence on focus, for dominant wavelength of 127.8 m, Aircraft altitude of 11,583 m, aircraft heading of 110°, incidence angle of 22.8°, and 64-point omnidirectional spectra: leg 1-data (AXCMF006), ground range corrected.

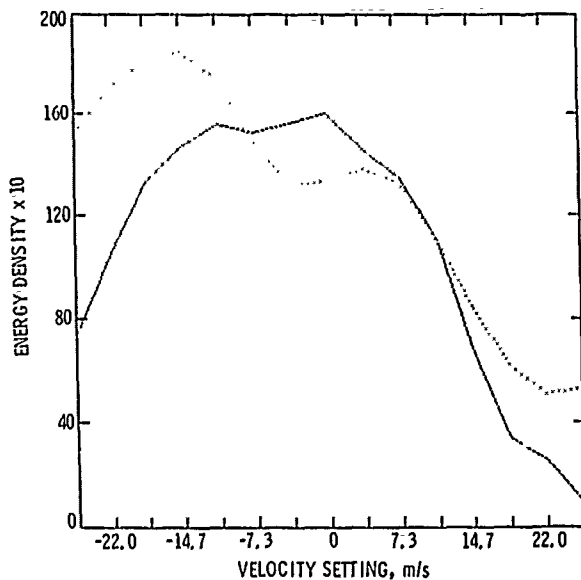


Fig. 11. Energy density at dominant wave versus focus, for aircraft altitude of 11,583 m, incidence angle of 24.6°, aircraft heading of 260°, leg 4 data (AXCMF006). The solid line is for a dominant wave of 117-m (space averaging method), the dotted line is for a dominant wave of 122 m (spectral averaging method).

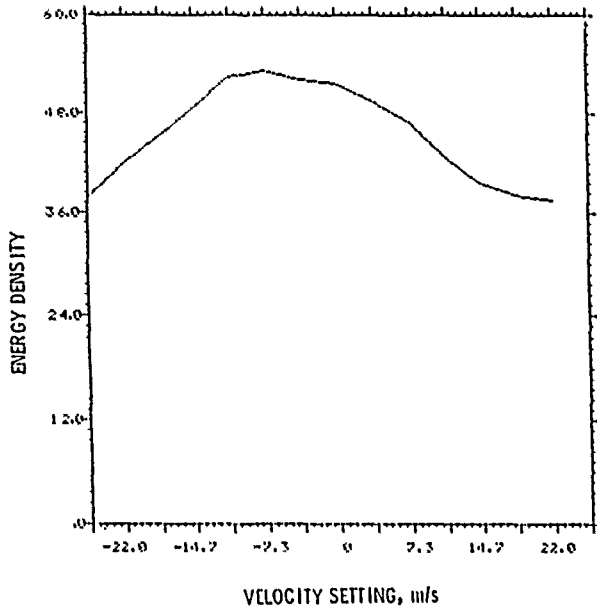


Fig. 12. Dominant wave number energy density dependence on focus, for wavelength of 117 m, aircraft altitude of 11,583 m, incidence angle of 22.9°, aircraft heading of 260°, and 64-point omnidirectional spectra; leg 4 real number data (AXCMF006).

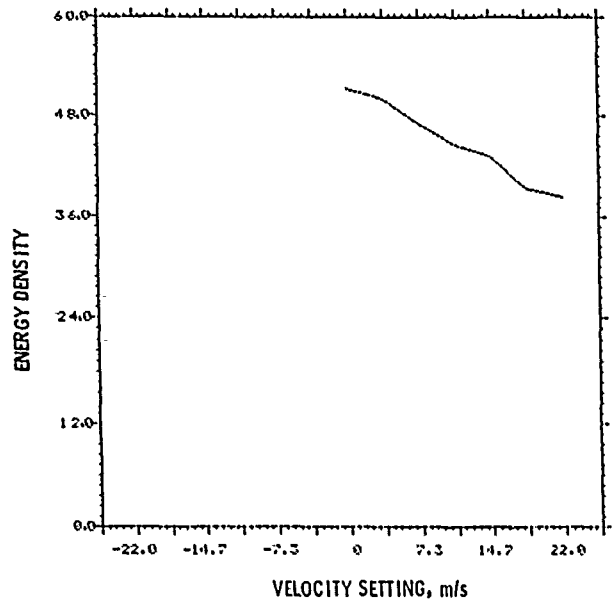


Fig. 14. Dominant wave number energy density dependence on focus, for wavelength of 127.8 m, aircraft altitude of 11,583 m, incidence angle of 28.30°, aircraft heading of 320°, and 64-point omnidirectional spectra; leg 7 real number data (AXCMF006).

using the spectral averaging method. The oscillating shape in Figure 10 is attributed to the low SNR values obtained in this SAR image. The ocean waves here are barely distinguishable from the background.

For leg 4 (aircraft heading of 260°) the variation in energy density of the dominant waves is shown in Figure 11. Here, results from both space averaging and spectral averaging methods are shown. The dominant wave energy dependence on focus offset has a trend that is the reverse of that for leg 1.

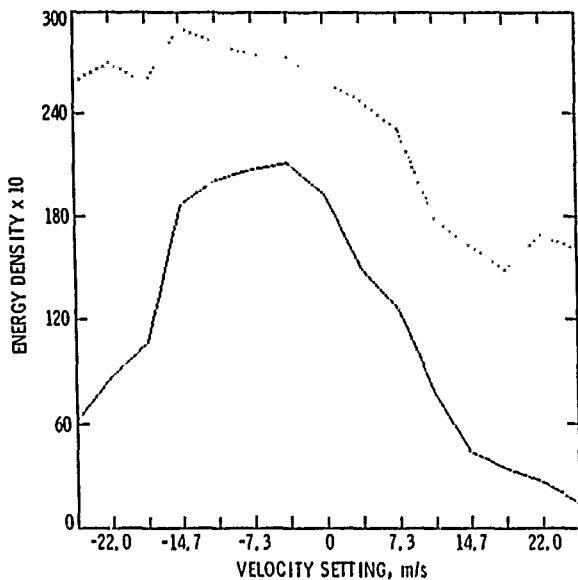


Fig. 13. Energy density at dominant wave versus focus, for aircraft heading of 320°, incidence angle of 24.2°, aircraft altitude of 11,583 m; Leg 7 data (AXCMF006). The solid line shows results for a dominant wave of 117.1 m, space averaging method, and azimuthal angle of 370°; the dotted line shows results for a dominant wave of 140.5 m, power spectral averaging method.

The variation of energy in the dominant wave length (122 m) versus focus setting shows a peak at a focus setting equal to -14.7 m/s when the spectral averaging method is used. The space averaging method gives a dominant wave length of 117 m and shows two focusing peaks, at 0.0 m/s and -11.0 m/s. The difference in establishing the offset for the peak contrast reflects the accuracy with which the peak focus can be determined.

The directional spectra derived from 128 x 128 data blocks show a dominant wavelength of 117.1 m. The omnidirectional spectra generated from 64 x 64 pixel, two-dimensional spectra show a peak energy density for the dominant wave at a focus offset of -7.33 m/s, as shown in Figure 12.

For leg 7 (aircraft heading of 320°), the plot of the energy density as a function of focus setting is shown in Figure 13 for both space averaging and power spectral averaging methods. This figure shows a single peak near -5.5 m/s for the space averaging method. The power spectral averaging method yields a dominant wavelength of 140.5 m and a maximum offset at about -14.7 m/s. For leg 7 the omnidirectional spectra, generated from the 128 x 128 pixel blocks of real number ground-range image data, show a dominant wave length of

TABLE 3. Optimum Focus Settings for the TOWARD SAR Spectra Collected on October 31, 1984

SAR Frame	Aircraft Heading, deg	Optimum Focus, m/s		
		Space Averaging	Spectral Averaging	Directional Averaging
Leg 1	110	+11.0	+11.0	+14.7
Leg 2	290	N.P.	N.P.	N.P.
Leg 4	260	0.0	-14.7	-7.3
Leg 7	320	-5.5	-14.7	I

Notation is as follows: N.P., no clear peaking identified; I, incomplete data set.

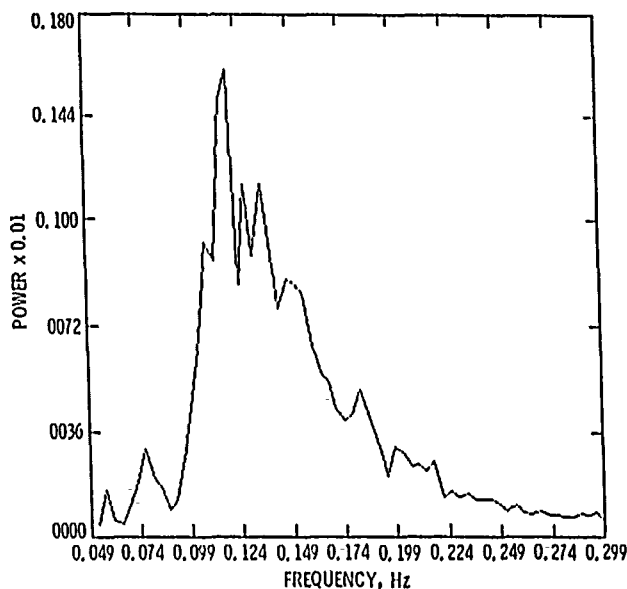


Fig. 15. In situ frequency spectrum obtained by Scripps Institution of Oceanography using pressure sensors on October 31, 1984. The spectrum has 88 degrees of freedom.

127.8 m. The omnidirectional spectra generated from the  $64 \times 64$  two-dimensional spectra show an asymmetric energy density dependence on focus, as shown in Figure 14. The complete curve was not achieved owing to illegal floating point format errors in the data files received. A summary of the focus offset values corresponding to the peak spectral energies is given in Table 3 for the different processing methods employed. This table shows the focus offset to change sign consistently with respect to aircraft heading relative to direction of wave propagation. The variability in leg 1 is estimated to be in the range 10.0 to 15.0 m/s, and that in Legs 4 and 7 is estimated to be in the range  $-5.0$  to  $-15.0$  m/s.

#### 4. SPECTRAL COMPARISONS

In the following, the in situ measurements are compared with the SAR spectra to determine whether the SAR spectra can be related to the ocean surface with a well-defined transfer function. The conversion of the in situ wave frequency spectrum to an equivalent wave number spectrum is discussed first. The correction for aircraft motion is discussed next. The in situ measurements were obtained by R. T. Guza at the tower site using a submerged array of pressure sensors [see Shemdin *et al.*, 1986]. The spectral conversion from the depth-limited tower site to an equivalent deepwater wave height spectrum is treated as a one-dimensional shoaling and-refraction problem. Details of the conversion are discussed by Tajirian [1986]. The in situ frequency spectrum measured at the tower is shown in Figure 15, and the corresponding wave number spectrum in deep water is shown in Figure 16.

To determine if the sloping bottom has an influence on the transformation, the wave height spectrum is also converted to deepwater spectrum by a finite difference procedure that takes into account the slope of the bottom at each interval, as shown by Tajirian [1986]. Both methods give virtually identical spectral values.

In the imaging of ocean waves, the wavelength obtained from a SAR image is not the same as that on the ocean

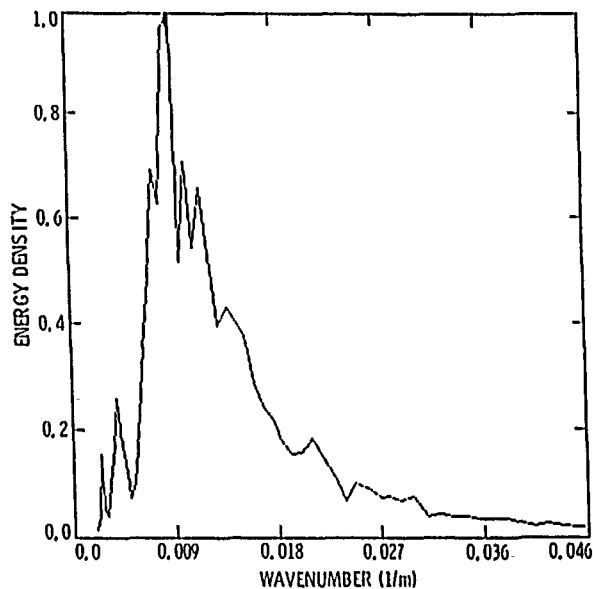


Fig. 16. Normalized in situ wave number spectrum transformed to deep water using the spectrum shown in Figure 15.

surface. For waves traveling in the aircraft direction, the relationship between the actual and observed wave numbers is given by

$$k = k' \left( \frac{v}{v - c} \right) \quad (8)$$

where  $k$  is ocean wave number,  $k'$  is the equivalent SAR image wave number,  $c$  is phase velocity of the ocean wave, and  $v$  is aircraft velocity. Equation (8) is solved for all the SAR  $k'$  values by iteration. The above procedure is used to compare wavelengths obtained from different SAR legs. The dominant

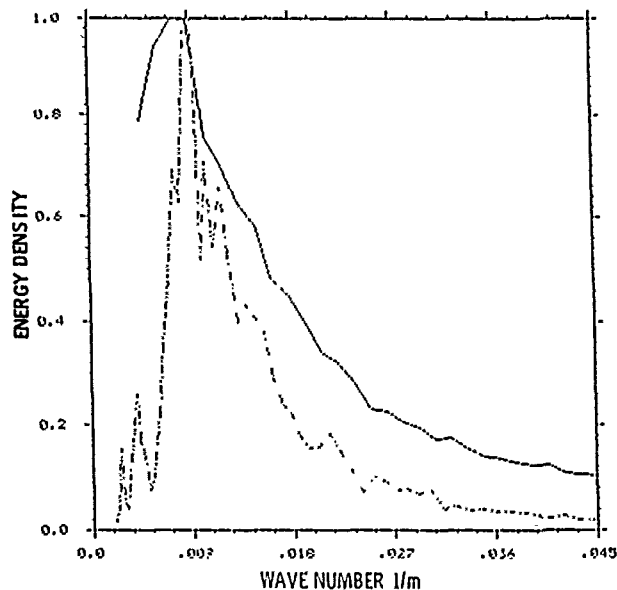


Fig. 17. Spectral comparison between SAR and in situ data. The solid line shows the SAR spectrum in deep water after correction for surface wave motion (Leg 1). The dashed-dotted line shows the in situ spectrum converted to deep water.

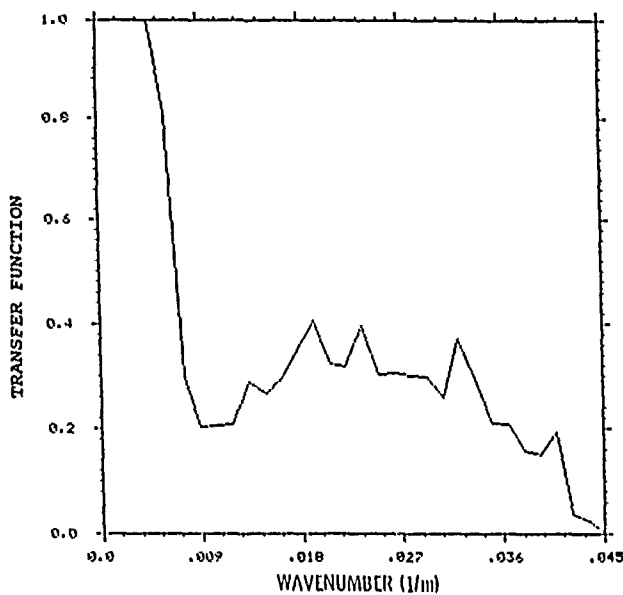


Fig. 18. SAR transfer function (ratio of the SAR spectrum to the in situ spectrum).

wavelength seen by the SAR in the direction of wave motion is 147.9 m, and that in the direction opposite to the ocean wave direction is 133.8 m. When corrected for aircraft motion, the wavelengths become 140.0 and 143.0 m, respectively. The consistency achieved in explaining motion effects from measured SAR dominant wavelengths adds confidence to the analysis employed here. The corrected SAR spectrum for the optimally focused image of leg 1 is shown in Figure 17 and is compared with the equivalent in situ spectrum. The in situ spectrum yields a dominant wavelength of 107.4 m, while the SAR spectrum gives a dominant wavelength of 140.0 m. The latter suggests that the SAR imaging process imposes low-pass filtering on the ocean waves being imaged.

A SAR system transfer function is defined here as the ratio of the SAR image spectrum to the in situ wave height spectrum. The transfer function, obtained from the results given in Figure 17 (after removing the speckle contribution in the SAR spectrum), is shown in Figure 18. The latter exhibits a low-pass filter characteristic with a cutoff wave number at  $k = 0.0075 \text{ m}^{-1}$ .

##### 5. SUMMARY AND CONCLUSIONS

Extensive analysis of SAR image spectra of surface waves reveals an asymmetric behavior in the dependence of the spectral energy of the dominant waves on focus offset. The offset is dependent on the direction of wave propagation relative to aircraft heading. For surface waves traveling in the same direction as the aircraft, the dominant waves in the SAR image are most detectable at offsets in the range of 10.0 to 15.0 m/s. For waves traveling in the opposite direction to the aircraft, the dominant waves are most detectable at offsets in the range of  $-5.0$  to  $-15.0$  m/s. The results obtained for leg 1 indicate a dominant wavelength of 147.9 m. Leg 2 shows a dominant

wavelength of 133.8 m. When corrected for relative aircraft motion, they reduce to 140.0 m and 143.0 m, respectively, which are within one wave number resolution cell. The SAR image spectra show dominant wavelengths longer than those obtained from the in situ spectra. The SAR system transfer function is found to be a low-pass filter with the peak of the ocean wave height spectrum falling in its stop band.

*Acknowledgments.* The SAR images discussed in this paper were processed by the Jet Propulsion Laboratory (JPL). Photographic representations and digital tapes of the SAR images were distributed to the TOWARD SAR investigators. The frames selected for multifocus processing were specified by the SAR Discipline Review Committee. G. DeGeorgio assisted on many occasions by providing details on the JPL SAR processor. The analysis discussed in this paper and the results derived have been obtained in consultation with O. H. Shemdin, principal investigator of the TOWARD Experiment. W. Plant, chairman of the Discipline Review Committee, provided useful information on the SAR imaging mechanisms. D. Lyzenga and Dr. C. Wackerman at the Environmental Research Institute of Michigan supplied the real number image data tapes for phase I of the experiment and provided assistance in reading the tapes. P. Hwang and D. Kasilingam at Ocean Research and Engineering provided useful information on hydrodynamics and SAR imaging aspects of the problem, respectively.

##### REFERENCES

- Alpers, W., and C. Rufenach, The effect of orbital motions on synthetic aperture radar imagery of ocean waves, *IEEE Trans. Antennas Propag.*, 27, 685-690, 1979.
- Alpers, W., D. Ross, and C. Rufenach, On the detectability of ocean surface waves by real and synthetic aperture radar, *J. Geophys. Res.*, 86(C7), 6481-6498, 1981.
- Hovanessian, S., *Radar System Design and Analysis*, Artech, Norwood, Mass., 1984.
- Jain, A., Focusing effects in the synthetic aperture radar imaging of ocean waves, *Appl. Phys.*, 15, 323-333, 1978.
- Jain, A., SAR Imaging of ocean waves: Theory, *IEEE J. Ocean Eng.*, OE-6(4), 130-139, 1981.
- Jain, A., and O. Shemdin, L-band SAR ocean wave observations during MARSEN, *J. Geophys. Res.*, 88, 9792-9808, 1983.
- Larsen, T. R., L. I. Moskowitz, and J. W. Wright, A note on SAR imagery of the ocean, *J. Geophys. Res.*, 81, 2655-2656, 1976.
- Plant, W., and W. Keller, The two-scale radar wave probe and SAR imagery of the ocean, *J. Geophys. Res.*, 88(C14), 9776-9784, 1983.
- Shemdin, O. H., W. E. Brown, Jr., F. G. Staudhammer, R. Shuchman, R. Rawson, J. Zelenka, D. B. Ross, W. McLiesh, and R. A. Berles, Comparison of in-situ and remotely sensed ocean waves off Marmeland, Florida, *Boundary Layer Meteorol.*, 13, 193-202, 1978.
- Shemdin, O. H., et al., *Investigation of Physics of Synthetic Aperture Radar in Ocean Remote Sensing, TOWARD Interim Report*, 2 vols., Jet Propulsion Laboratory, Pasadena, Calif., 1986.
- Shuchman, R., and O. Shemdin, Synthetic aperture radar imaging of ocean waves during the Marineland experiment, *IEEE J. Ocean Eng.*, OE-8(2), 83-90, 1983.
- Tajirian, E., Processing of JPL SAR multifocus ocean wave data collected on October 3, 1984, *Rep. ORE 86-2*, Ocean Res. and Eng., Pasadena, Calif., 1986.
- Tajirian, E., On processing of JPL SAR multifocus ocean wave data collected on October 31, 1984, *Rep. ORE 87-1*, Ocean Res and Eng., Pasadena, Calif., 1987.

E. K. Tajirian, Ocean Research and Engineering, 255 S. Marengo Avenue, Pasadena, CA 91101.

(Received December 28, 1987;  
accepted February 15, 1988.)

# An Analytic Representation of the Synthetic Aperture Radar Image Spectrum for Ocean Waves

DAVID R. LYZENGA

*College of Marine Studies, University of Delaware, Newark*

An analytic expression is derived for the spectrum of a synthetic aperture radar image in terms of the surface reflectivity covariance function. It is shown that within the severe constraints imposed by the short integration time, the third (temporal) dimension of the spectrum can be extracted by varying the processor focus parameter. The results also illustrate the dependence of the image spectrum on the scene coherence time, as well as various nonlinear effects associated with the velocity bunching mechanism. Example calculations are presented for two cases corresponding to data sets collected during the Tower Ocean Wave and Radar Dependence Experiment.

## 1. INTRODUCTION

Although it is widely agreed that ocean waves can be imaged by synthetic aperture radar (SAR) under some conditions, there is less agreement as to the precise relationship between the images and the surface wave conditions. A comprehensive theory for the wave imaging process was presented by *Hasselmann et al.* [1985], including an analytic expression for the ensemble-averaged or expected value of the image intensity in terms of the surface reflectivity spectrum. One prominent feature of this theory is the "velocity bunching" mechanism which was described earlier by several investigators, including *Swift and Wilson* [1979] and *Alpers and Rufenach* [1979]. This mechanism produces image intensity modulations due to the Doppler shifts associated with the orbital velocities of the surface waves.

An expression describing the relationship between the image spectrum and the surface wave height spectrum was also presented by *Alpers et al.* [1981]; but it was recognized that this relationship was valid only for the limited range of conditions under which the velocity bunching mechanism could be considered as a linear process. Because of the importance of nonlinear effects which could not be described analytically, further investigations of the imaging process have been carried out by means of numerical simulations [*Alpers*, 1983; *Alpers and Bruening*, 1986; *Lyzenga*, 1986].

A recurring theme in the investigation of the SAR imaging process has been the debate regarding the effects of refocusing adjustments in the SAR processor. Early observations by *Shuchman and Zelenka* [1978] and *Jain* [1978] indicated that the contrast of wave images could be improved by changing the focus setting in the optical processors that were used to convert the recorded SAR data into images. These focus adjustments were originally interpreted as methods of compensating for the phase velocity of the waves, in analogy with the focus adjustments used to sharpen the images of hard targets moving in the SAR azimuth direction. However, this interpretation was cast into doubt by evidence that the Doppler shifts of the scattered radar signals are related to the orbital motions rather than the phase velocity of the imaged waves. Accordingly, the focus adjustments were considered by many to be

corrections for the radial accelerations associated with the surface-wave orbital motions [e.g., *Alpers and Rufenach*, 1980]. Alternative theories were presented by *Ivanov* [1982] and *Ouchi* [1983] which indicated that the optimum focus setting for ocean waves was equivalent to that required to focus a hard target moving with half the azimuthal phase velocity of the waves. However, this theory was criticized as resulting from a misapplication of the two-scale scattering model [*Plant*, 1983].

The Tower Ocean Wave and Radar Dependence Experiment (TOWARD) of the Office of Naval Research was designed to resolve several outstanding controversies in SAR imaging theory, including the validity of the velocity bunching model and the reason for the apparent focus dependence of SAR images. The present work was carried out in the context of this experiment, having originated as a numerical simulation study to compare the predictions of the velocity bunching theory with the TOWARD observations. The analytical work described in this paper was undertaken in attempt to understand the results of the numerical simulations. This analytical work proved to be more fruitful than had been anticipated and as a result has largely supplanted the numerical simulation studies undertaken in the earlier part of the investigation.

## 2. SAR PROCESSING AND SPECTRAL ESTIMATION

The conventional procedure for estimating wave spectra from SAR images is to Fourier transform the image intensity and then to relate the resulting two-dimensional image spectrum to the wave spectrum using some type of inversion technique. An example of such a procedure, which simplifies the inversion by assuming a linear modulation transfer function, is given by *Monaldo and Lyzenga* [1986].

A modification of this procedure was developed by *Hasselmann* [1980] and further elaborated by *Martin* [1981]. This modified procedure, which was named the SIFT algorithm by *Hasselmann*, was intended to simplify the data processing by calculating the image spectrum directly from the raw SAR signals. The practical utility of this procedure was questioned by *LaHaie et al.* [1984], who showed that it does not provide any significant computational reduction relative to the conventional method of image formation and Fourier transformation. However, the expression developed by *Hasselmann* (which was arrived at independently during the course of this study, by a slightly different route) has proved to be very

useful in providing insight into the SAR imaging process, as was also noted by Ivanov [1983]. A somewhat simplified derivation of this expression is presented in this section, and the result is used as the starting point for the discussion in section 3.

Using a well-known identity, the Fourier transform of the image intensity (defined as the squared magnitude of the complex image) may be written as

$$F_I(K_x, K_y) = \frac{1}{(2\pi)^2} \iint i(x, y) i^*(x, y) \cdot \exp[-j(K_x x + K_y y)] dx dy \\ = \iint F_i(K_x', K_y') F_i^*(K_x' - K_x, K_y' - K_y) dK_x' dK_y' \quad (1)$$

where

$$F_i(K_x, K_y) = \frac{1}{(2\pi)^2} \iint i(x, y) \exp[-j(K_x x + K_y y)] dx dy \quad (2)$$

is the Fourier transform of the complex image  $i(x, y)$ . The complex image is, in turn, obtained by convolving the received signal with the reference function  $h(x, y)$ , i.e.,

$$i(x, y) = \iint s(t, t') h(x - Vt, y - c't) dt dt' \quad (3)$$

where the received signal  $s(t, t')$  has been written in terms of the "slow" time  $t$  between pulses and the "fast" time  $t'$ , which is used to describe the time variation of the signal within each returned pulse. The transformation from temporal to spatial coordinates involves the platform velocity  $V$  in the along-track or azimuth direction ( $x$ ) and the constant  $c' = c/(2 \sin \theta)$  in the cross-track or range direction ( $y$ ), where  $c$  is the speed of light and  $\theta$  is the angle of incidence.

The form of the reference function depends on the transmitted waveform, which is assumed to be a linear FM chirp signal. The motion of the platform produces a similar frequency modulation of the signal in the slow time  $t$ . Hence the appropriate reference function has the form

$$h(x - Vt, y - c't) = C \exp[j\beta(x - Vt)^2 + j\beta'(y - c't)^2] \quad (4)$$

where  $C = (\beta\beta')^{-1/2} i\pi$  is a normalization constant. Normally, the factors  $\beta$  and  $\beta'$  are chosen to match the chirp rate of the signal in order to produce optimum focusing of point targets. However, it is important to note that no assumptions about the values of  $\beta$  and  $\beta'$  need to be made to derive the SIFT algorithm. Thus for the moment these will be considered as free parameters.

Since the complex image is obtained from a convolution of the received signal with the reference function, its Fourier transform can be written as the product of the Fourier transforms of these two quantities, i.e.,

$$F_i(K_x, K_y) = F_s(\omega_x, \omega_y) \exp[-j(K_x^2/4\beta + K_y^2/4\beta')] \quad (5)$$

where

$$F_s(\omega_x, \omega_y) = \frac{1}{(2\pi)^2} \iint s(t, t') \exp[-j(\omega_x t + \omega_y t')] dt dt' \quad (6)$$

is the Fourier transform of the received signal, evaluated at

the frequencies

$$\omega_x = VK_x \text{ and } \omega_y = c'K_y, \quad (7)$$

Substituting (5) into (1) results in the expression

$$F_I(K_x, K_y) = e^{j\psi} \iint F_s(\omega_x, \omega_y) F_s^*(\omega_x - VK_x, \omega_y - c'K_y) \cdot \exp[-j(\omega_x \tau_x + \omega_y \tau_y)] d\omega_x d\omega_y \quad (8)$$

where

$$\tau_x = \frac{K_x}{2\beta V} \quad \tau_y = \frac{K_y}{2\beta' c'} \quad (9)$$

$$\psi = K_x^2/4\beta + K_y^2/4\beta' \quad (10)$$

Equation (8) is similar to Hasselmann's SIFT expression, but it involves the Fourier transform of the received signal rather than the signal itself. However, by substituting (6) into (8) and integrating over  $\omega_x$  and  $\omega_y$ , one readily obtains the result

$$F_I(K_x, K_y) = e^{-j\psi} \iint s(t, t') s^*(t + \tau_x, t' + \tau_y) \cdot \exp[-j(\omega_x t + \omega_y t')] dt dt' \quad (11)$$

which is equivalent to Hasselmann's expression, except for the phase factor  $e^{-j\psi}$  (which, of course does not affect the magnitude of  $F_I$ ) and the tapering functions which Hasselmann includes in order to account for the effect of the Fourier transform window. Note that since the received signal is sampled discretely, the integral in (11) is actually evaluated as a finite sum, and the wave number resolution may be limited by the sample spacing (the resolution may also be influenced by the size of the Fourier transform window, as was shown by Hasselmann). On the other hand, if (8) is used to calculate the image spectrum, the resolution is not limited by the time sample spacing but is determined by the spacing between frequency samples, which depends on the total time interval over which the Fourier transform of the signal is evaluated.

### 3. RELATION OF THE IMAGE SPECTRUM TO THE SURFACE CONDITIONS

Aside from its possible value as a data processing technique, (11) is useful for investigating the relationship between the image spectrum and the surface conditions, as described by the reflectivity statistics. Neglecting for the moment the effects of the finite antenna beam width and pulse length, the signal received by a SAR may be represented by

$$s(t, t') = \iint r(x, t) \cdot \exp[-jk(x - Vt)^2/R - j\gamma(t' - y/c')^2/2] dx dy \quad (12)$$

where  $r(x, t)$  is the complex reflectivity of the surface,  $k$  is the radar wavenumber,  $R$  is the range distance to the surface, and  $\gamma$  is the chirp rate of the transmitted signal. The surface has been assumed to be "frozen" over the fast time scale (i.e., over the duration of each pulse) but to vary from pulse to pulse. Following Hasselmann *et al.* [1985], the complex reflectivity is assumed to have second-order statistics as described by

$$\langle r(x, t) r^*(x', t + \tau) \rangle = \delta(x - x') \sigma_0(x, t) \rho(x, t, \tau) \quad (13)$$

where  $\sigma_0(x, t)$  is the radar cross section per unit area and  $\rho(x, t, \tau)$  is the normalized temporal correlation function. The  $\delta$  correlation property expressed by the term  $\delta(x - x')$  in (13)

represents an important simplifying assumption, as will be seen below. This assumption is supported by the available evidence, as discussed by Hasselmann et al., although it is conceivable that it breaks down under certain conditions. The radar cross section is assumed to vary slowly in time and space, owing to the combined effects of surface tilting and hydrodynamic modulation. In many cases, the temporal and/or spatial spectrum of the radar cross section may be assumed to be proportional to the surface wave height or wave slope spectrum, with the constant of proportionality defined as the radar modulation transfer function. The temporal correlation function is the Fourier transform of the reflectivity variance spectrum, which is commonly assumed to have a Gaussian shape with a center frequency

$$\omega_c = 2kV_r(x, t) \tag{14}$$

and a half width (standard deviation)  $\sigma_\omega$  which may be a function of position and time, but which for the present is considered a constant. The temporal correlation function is then also a Gaussian function, i.e.,

$$\rho(x, t, \tau) = \exp[-\tau^2/2\tau_c^2 + j\omega_c\tau] \tag{15}$$

where  $\tau_c$  is a correlation time, which is defined as the inverse of  $\sigma_\omega$  (in radians per second). Note that the radial velocity  $V_r$  can be calculated from the orbital velocity of the waves, e.g., for a surface wave with amplitude  $a_w$  and wave number  $K_w$ ,

$$V_r(x, t) = a_w\Omega_w g(\theta, \phi) \sin(K_w \cdot x - \Omega_w t) \tag{16}$$

where  $\Omega_w$  is the wave frequency and

$$g(\theta, \phi) = (\cos^2 \theta + \sin^2 \theta \sin^2 \phi)^{1/2} \tag{17}$$

where  $\theta$  is the incidence angle and  $\phi$  is the wave propagation direction relative to the SAR azimuth direction.

Substituting (12) into (11), taking the ensemble average, and using the  $\delta$  correlation property expressed in (13) to reduce two of the spatial integrations, one finds that the fast time dependence of the integrand drops out if the parameter  $\beta'$  is chosen to match the chirp rate of the transmitted signal, i.e.,

$$\beta' = \gamma/(2c^2) \tag{18}$$

With this choice, the integration over  $t'$  becomes trivial, and we obtain the central result

$$\langle F_r(K_x', K_y) \rangle = e^{-j\psi'} \iiint \sigma_0(x, t) \rho(x, t, \tau_x) \cdot \exp[-j(K_x x + K_y y - \Omega t)] dx dy dt \tag{19}$$

where

$$K_x' = (\beta R/k)K_x \quad \Omega = V(K_x - K_x') \quad \tau_x = \frac{R}{2kV} K_x \tag{20}$$

$$\psi' = K_x' \Omega / 4\beta V \tag{21}$$

According to this result, the Fourier transform of the SAR image intensity is equivalent to the three-dimensional Fourier transform of the surface reflectivity covariance function, the third (temporal) dimension being obtained by varying the focus parameter  $\beta$ .

For a stationary surface, the integration over time in (19) yields a maximum value when the parameter  $\Omega$  is equal to zero, or

$$\beta = k/R \tag{22}$$

which corresponds to the nominal focus setting. However, if the surface reflectivity statistics are nonstationary, the integration over time may yield a maximum at  $\Omega \neq 0$ . For example, if the radar cross section is of the form

$$\sigma_0(x, t) = 1 + a_m \cos(K_w \cdot x - \Omega_w t) \tag{23}$$

and the temporal correlation function is assumed to be constant, the integral in (19) has a maximum value for  $\Omega = \Omega_w$ ,  $K_x = K_{wx}$  and  $K_y = K_{wy}$ . This implies that  $\langle F_r(K_x', K_y) \rangle$  is maximized for

$$K_x' = K_{wx} - \Omega_w/V \quad K_y = K_{wy} \tag{24}$$

$$\beta = \frac{k}{R} \left( 1 + \frac{\Omega_w}{VK_y} \right) \tag{25}$$

which is equivalent to the quadratic phase coefficient required to focus a discrete scatterer moving with an azimuthal velocity equal to half the azimuthal phase velocity of the pattern. Note that the focus effect in this case is due not to any actual scene motion (since the temporal correlation function was assumed to be constant) but rather to the translation of the modulation pattern across the scene. The difference between the image wave number  $K_x'$  and the pattern wave number  $K_{wx}$  is due to the scanning distortion discussed by Raney and Lowry [1978].

The effect of a finite pulse length or range bandwidth can be shown to merely weight the spectrum by a roll-off function in  $K_y$ . The effect of a finite azimuth bandwidth, or integration time, is somewhat more complicated. If an antenna weighting function of the form

$$g(x - Vt) = \exp[-(x - Vt)^2/V^2 T^2] \tag{26}$$

is inserted in (12) and carried through into (19), the result is a weighting of the integrand by the function

$$w(x, t) = \exp[-\tau_x^2/2T^2] \exp[-2(x - Vt - V\tau_x/2)^2/V^2 T^2] \tag{27}$$

The first term on the right-hand side of this equation produces a roll-off in  $K_x$  analogous to that caused by a finite range bandwidth. The second term essentially defines the Fourier transform window in the  $x-t$  plane. Thus the resulting Fourier transform is equal to the infinite bandwidth result convolved with the function

$$\tilde{w}(K_x, \Omega) = \exp[-\Omega^2 T^2/8] \delta(K_x - \Omega/V) \tag{28}$$

where the  $\delta$  function is interpreted as a function having a width equal to the inverse of the scene length (i.e., the sample spacing in the digital fast Fourier transform of the image). The effect of this smearing function on the spectrum is sketched in Figure 1. The spectral resolution in either the  $K_x$  direction or the  $\Omega$  direction can be increased by increasing the scene length, but the spectral resolution along the diagonal direction is limited by the integration time  $T$  (assuming that the scene length is greater than  $VT$ ). If the spectral peak is less than this resolution length away from the  $K_x$  axis, i.e.,

$$\Omega_w \lesssim 1/T \tag{29}$$

then the spectral density at  $\Omega = 0$  (i.e., with the nominal focus setting) is nearly equal to the peak value. On the other hand, if the integration time is an appreciable fraction of the period  $T_w = 2\pi/\Omega_w$ , then some increase in the image contrast or spectral density can be obtained by refocusing.

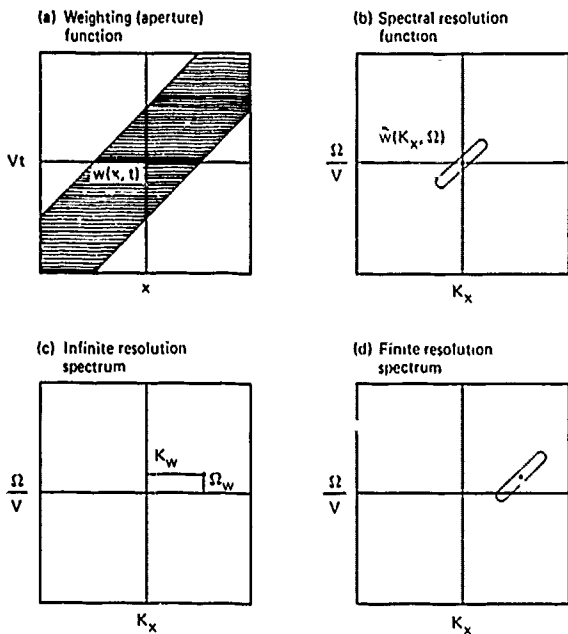


Fig. 1. Sketches of (a) the weighting or aperture function  $w(x, t)$ , (b) the Fourier transform of this aperture function, (c) a hypothetical narrowband spectrum as it would be observed with an ideal (infinite resolution) system, and (d) the same spectrum as observed with an aperture function  $w(x, t)$ .

4. VELOCITY BUNCHING NONLINEARITIES

The velocity bunching effect is caused by spatial variations in the mean radial velocity over length scales larger than the SAR resolution. This effect may be illustrated by assuming that the radial velocity varies as shown in (16). From (14) through (17), the temporal correlation function of the reflectivity is then given by

$$\rho(x, t, \tau_x) = \exp \left[ -\tau_x^2/2\tau_c^2 + j\alpha_w \sin(\mathbf{K}_w \cdot \mathbf{x} - \Omega_w t) \right] \quad (30)$$

where

$$\alpha_w = 2k\tau_x a_w \Omega_w g(\theta, \phi) \quad (31)$$

For simplicity, we will assume in addition that the radar cross section per unit area  $\sigma_0$  is constant. Substituting (30) into (19) and using the Bessel function expansion

$$\exp(ja \sin \Phi) = \sum_{n=-\infty}^{\infty} J_n(a) \exp(jn\Phi) \quad (32)$$

the result (neglecting the phase factor  $e^{-j\psi}$  in (19)) is then

$$\langle F_I(K_x', K_y) \rangle = \sigma_0 \exp(-\tau_x^2/2\tau_c^2) \cdot \sum_{n=-\infty}^{\infty} J_n(\alpha_n) \delta(nK_{wx} - K_x) \delta(nK_{wy} - K_y) \delta(n\Omega_w - \Omega) \quad (33)$$

where

$$\alpha_n = n \frac{R}{V} a_w K_{wt} \Omega_w g(\theta, \phi) \quad (34)$$

The nonlinearity of this mechanism is manifested by the appearance of harmonics in the spectrum. The amplitudes of the harmonics are reduced by the roll-off effect (given by the exponential term in (33)) associated with the finite coherence time  $\tau_c$ . Neglecting this roll-off effect, all of the harmonics would have equal amplitudes when  $\alpha_1 \approx 1$ . The amplitude of

the first harmonic ( $n = 1$ ) increases with the wave amplitude until  $\alpha_1$  reaches a value of approximately 2, after which the amplitude of the first harmonic begins to decline. Note that  $\alpha_1$  is equivalent to the nonlinearity parameter defined by *Alpers et al.* [1981].

Another aspect of the nonlinearity in the velocity bunching mechanism can be illustrated by considering the superposition of two surface waves with amplitudes  $a_w$  and  $a_w'$ , and wave numbers  $\mathbf{K}_w$  and  $\mathbf{K}_w'$ . For this case,

$$\rho(x, t, \tau) = \exp(-\tau_x^2/2\tau_c^2) \cdot \sum_{n=-\infty}^{\infty} J_n(\alpha_n) \exp[jn(\mathbf{K}_w \cdot \mathbf{x} - \Omega_w t)] \cdot \sum_{m=-\infty}^{\infty} J_m(\alpha_m') \exp[jm(\mathbf{K}_w' \cdot \mathbf{x} - \Omega_w' t)] \quad (35)$$

which, when substituted into (19), yields

$$\langle F_I(K_x', K_y) \rangle = \sigma_0 \exp(-\tau_x^2/2\tau_c^2) \cdot \sum_{n=-\infty}^{\infty} \sum_{m=-\infty}^{\infty} J_n(\alpha_{nm}) J_m(\alpha_{nm}') \delta(nK_{wx} + mK_{wx}' - K_x) \cdot \delta(nK_{wy} + mK_{wy}' - K_y) \delta(n\Omega_n + m\Omega_n' - \Omega) \quad (36)$$

where  $\alpha_{nm}$  represents the value of  $\alpha_w$  evaluated at  $K_x = nK_{wx} + mK_{wx}'$  and  $\alpha_{nm}'$  represents the value of  $\alpha_w'$  evaluated at the same wave number. In addition to the appearance of false responses at the sum and difference frequencies (e.g., for  $n = 1, m = 1$  and for  $n = 1, m = -1$ , respectively), this equation indicates that the spectral response to each wave component can be reduced by the presence of the other. Specifically, the spectral amplitude at the wave number of the first component ( $n = 1, m = 0$ ) is reduced by the factor  $J_0(\alpha_{10}')$ , while the amplitude at the second wave number ( $n = 0, m = 1$ ) is reduced by the factor  $J_0(\alpha_{01})$ . Note that this effect causes a larger suppression of the wave component with the smaller amplitude and would therefore appear to be capable of producing an apparent narrowing of the spectral peak under certain conditions. On the other hand, the false responses at the sum and difference frequencies would appear to have the opposite effect of broadening the spectrum. The formalism presented here allows these nonlinear effects to be investigated analytically, at least to second order in the wave amplitude. However, such an investigation is beyond the scope of the present paper.

5. A LINEAR APPROXIMATION FOR THE IMAGE SPECTRUM

If the radial velocity  $V_r$  and/or the time lag  $\tau$  is sufficiently small, so that  $2kV_r\tau \ll 1$ , the reflectivity covariance function may be approximated as

$$\sigma_0(x, t) \rho(x, t, \tau) = \sigma_0(x, t) [1 + j2kV_r(x, t)\tau] \cdot \exp(-\tau^2/2\tau_c^2) \quad (37)$$

If, in addition, the variations in the radar cross section consist of small perturbations about a mean value  $\bar{\sigma}_0$ , i.e.,

$$\sigma_0(x, t) = \bar{\sigma}_0 [1 + f(x, t)] \quad (38)$$

where  $f(x, t) \ll 1$ , the covariance function can be further approximated by

$$\sigma_0(x, t) \rho(x, t, \tau) = \bar{\sigma}_0 [1 + f(x, t) + j2kV_r(x, t)\tau] \cdot \exp(-\tau^2/2\tau_c^2) \quad (39)$$

The three-dimensional Fourier transform of this covariance function may be written as

$$F_c(K_x, K_y, \Omega) = \bar{\sigma}_0 \{ \delta(K_x) \delta(K_y) \delta(\Omega) + [mK + 2k\tau\Omega(\cos \theta + j \sin \theta \sin \phi)] \cdot F_z(K_x, K_y, \Omega) \} \exp(-\tau^2/2\tau_c^2) \quad (40)$$

where

$$F_z(K_x, K_y, \Omega) = F_w(K_x, K_y) \delta[\Omega - (gK)^{1/2}] \quad (41)$$

is the Fourier transform of the surface elevation,  $K = (K_x^2 + K_y^2)^{1/2}$ , and  $m$  is a dimensionless radar modulation transfer function [e.g., *Plant et al.*, 1983].

The expected value of the Fourier transform of the SAR image intensity is then given by the convolution of  $F_c(K_x, K_y, \Omega)$  with the Fourier transform of the antenna weighting function, as given in (28). Neglecting the d.c. term, this convolution yields the result

$$\langle F_i(K_x', K_y) \rangle = \bar{\sigma}_0 G(\Omega - \Omega_k) [R_m + R_r] F_w(K_x, K_y) \cdot \exp(-\tau_x^2/2\tau_c^2) \quad (42)$$

where

$$G(\Omega) = \exp(-\Omega^2 T^2/8) \quad (43)$$

$$\Omega = VK_x'(\alpha - 1) \quad (44)$$

$$R_m = mK \quad (45)$$

$$R_r = 2k\tau_x \Omega_k (\cos \theta + j \sin \theta \sin \phi) \quad (46)$$

$$\tau_x = \frac{K_x' R}{2kV} \alpha \quad (47)$$

and  $K_x' = K_x - \Omega_k/V$  is the image wave number,  $\Omega_k = (gK)^{1/2}$  is the wave frequency,  $T$  is the integration time, and  $\alpha = k/\beta R$  is a dimensionless focus parameter which is equal to 1 for the nominal focus setting. Note that  $R_m$  and  $R_r$  are both complex quantities and can add constructively or destructively depending on their relative phases. Except for the dependence on the focus parameter  $\alpha$ , the linear approximation given in (42) is similar to the results obtained by previous investigators. For example,  $R_r$  is equivalent (except for the dependence on  $\alpha$ ) to the velocity bunching transfer function discussed by *Alpers et al.* [1981], and the exponential term in (42) is equivalent to the azimuth falloff function discussed by *Monaldo and Beal* [1986].

Since the Fourier transform is a complex quantity whose phase is not generally of interest, the usual procedure is to compute and display the squared magnitude of the Fourier transform of the image. The resulting quantity is referred to as the image spectrum. Using the Gaussian moment theorem [Reed, 1962], the expected value of this quantity can be shown to be equal to the squared magnitude of  $\langle F_i(K_x, K_y) \rangle$  plus a constant, which may be interpreted as the contribution of coherent speckle to the image spectrum. The value of this constant can be derived by noting that speckle is a multiplicative white noise process whose variance is equal to the square of the mean image intensity, for one-look or fully coherent processing [Alpers and Hasselmann, 1982]. The resulting expression for the expected value of the image spectrum can be written as

$$\langle S_i(K_x', K_y) \rangle = \bar{\sigma}_0^2 G^2(\Omega - \Omega_k) |R_m + R_r|^2 S_w(K_x, K_y) \cdot \exp(-\tau_x^2/\tau_c^2) + \bar{\sigma}_0^2 \rho_x \rho_y \quad (48)$$

where  $S_w(K_x, K_y)$  is the wave height spectrum,  $\rho_x$  is the azimuth resolution, and  $\rho_y$  is the range resolution of the SAR. The term  $G^2(\Omega - \Omega_k)$  is maximized for  $\Omega = \Omega_k$ , or

$$\alpha = 1 + \Omega_k/VK_x' \quad (49)$$

which produces the dominant focus effect. However,  $R_r$  and  $\tau_x$  also depend on the focus parameter, and this dependence can cause the optimum focus to differ from the value given in (49). Two conditions appear to be necessary for the focus effect to be observable. First, the integration time  $T$  must be an appreciable fraction of the wave period (as discussed in section 3), so that  $G^2(0)$  is significantly larger than  $G^2(\Omega_k)$ . Second, the azimuthal phase velocity  $\Omega_k/K_x$  of the waves must be an appreciable fraction of the platform velocity  $V$ , so that the optimum value of  $\alpha$  differs significantly from 1. These conditions are generally met for L band data collected from aircraft platforms but are not met for radars operating at higher frequencies (such as X band) or from satellite platforms.

6. EXAMPLE RESULTS FOR TOWARD

The TOWARD experiment data sets which have been most completely analyzed to date are those collected on October 31, 1984. The data segments considered here were collected with an  $R/V$  ratio of 52 s, at an incidence angle of 35°, and with the flight direction parallel (and antiparallel) to the dominant wave propagation direction.

The wave spectrum obtained from the in-situ data collected for this case contains a fairly narrow peak at a wave number of approximately 0.047 rad/m (i.e., a wavelength of 134 m), with a significant waveheight of 1.23 m. If all of the height variance were associated with a single wave component, the amplitude of this component would be approximately 0.44 m. This amplitude, combined with the data collection parameters listed above produces a value of 0.6 for the parameter  $\alpha_1$  defined in (34). Therefore nonlinear effects are not expected to be very important for this case. The coherence time was calculated from

$$\tau_c = 1/(2k\sigma_r) \quad (50)$$

where  $\sigma_r$  is the standard deviation of the radial velocities within a SAR resolution cell. This standard deviation was assumed to be 0.20 m/s, based on a Pierson-Moskowitz-type spectrum for the subresolution-scale waves and a resolution cell size of 11 m. This results in a coherence time of about 0.1 s. However, because of the uncertainty in this parameter, calculations were also made with  $\tau_c$  reduced to half this value, i.e., 0.05 s.

The SAR spectrum was calculated from (48) at the peak wave number, as a function of the focus parameter  $\alpha$ , for two SAR passes flown in opposite directions (during leg 1 the aircraft heading was in the wave propagation direction, and during leg 2 the aircraft heading was opposite to the wave propagation direction). The radar cross section was assumed to be constant for these calculations, and the integration time was taken to be 1.43 s for leg 1 and 1.79 s for leg 2, based on a nominal azimuthal resolution of 4.6 m. The results of these calculations are shown in Figures 2 and 3. The focus setting is expressed in these plots in terms of the equivalent azimuthal target velocity or platform velocity correction

$$V_a = (\alpha - 1)V/2 \quad (51)$$

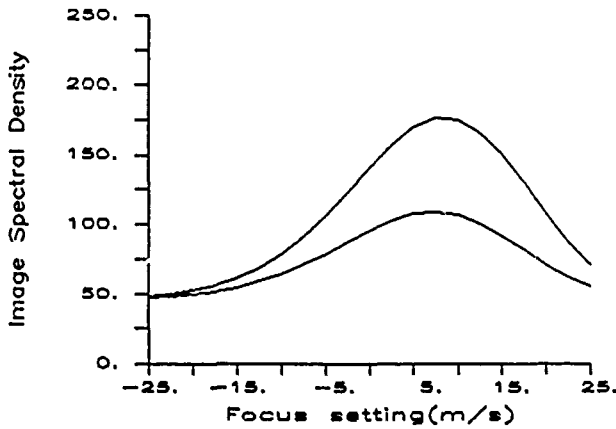


Fig. 2. Calculated image spectrum versus focus setting for the TOWARD data set collected during leg 1 on October 31, 1984. The top curve is for a coherence time of 0.1 s, and the bottom curve is for a coherence time of 0.05 s.

where  $V$  is the platform velocity, which was 273 m/s for leg 1 and 218 m/s for leg 2. Note that the optimum focus setting corresponds to approximately half the phase velocity of the waves (i.e., about 7.5 m/s), and has opposite signs for the two flight directions. The optimum focus settings reported by Tajirian [this issue] are of the order of 5–15 m/s, with opposite signs for the data sets collected with opposite headings. These observations agree qualitatively with the predictions shown in Figures 1 and 2, although the magnitudes of the observed focus shifts tend to be somewhat larger than the predictions. More detailed comparisons with the TOWARD data are in progress and will be reported separately.

## 7. CONCLUSIONS

The central conclusion presented in this paper is that the SAR image spectrum is essentially equivalent to the three-dimensional spectrum of the surface reflectivity covariance function, evaluated at a time lag which depends on the wave number and the  $R/V$  ratio of the SAR. The third (temporal) dimension of this spectrum is obtained, within the limits imposed by the short integration time of most SAR systems, by varying the processor focus setting.

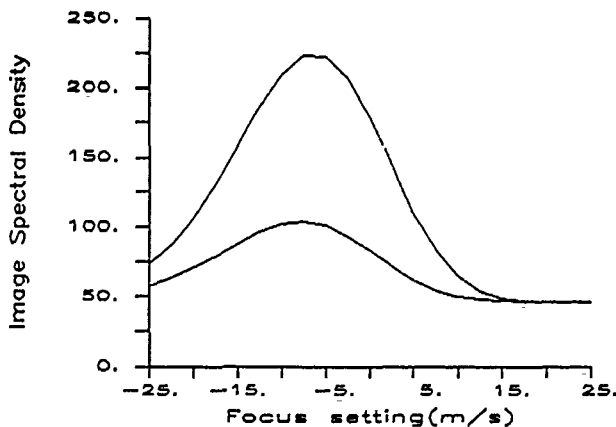


Fig. 3. Calculated image spectrum versus focus setting for the TOWARD data set collected during leg 2 on October 31, 1984. The top curve is for a coherence time of 0.1 s, and the bottom curve is for a coherence time of 0.05 s.

By modeling the reflectivity covariance function in terms of the surface motion statistics, an expression for the image spectrum is obtained which agrees with previous descriptions of the velocity bunching process, except for the inclusion of focus effects. This expression also illustrates various effects resulting from the nonlinearity of the velocity bunching process and allows analytical investigations of these nonlinearities to be carried out.

Predicted image spectra for two TOWARD data sets indicate that the optimum focus setting corresponds to a velocity correction of the order of half the longwave phase velocity, and reverses sign depending on the direction of motion of the SAR platform. These predictions agree qualitatively with the TOWARD observations, although the magnitude of the focus shift seems to be slightly smaller than has been observed in the data sets analyzed to date.

*Acknowledgments.* This work was carried out under the sponsorship of the Office of Naval Research. The technical monitor for this activity was Hans Dolezalek.

## REFERENCES

- Alpers, W. R., Monte Carlo simulations for studying the relationship between ocean wave and synthetic aperture radar image spectra, *J. Geophys. Res.*, **88**, 1745–1759, 1983.
- Alpers, W. R., and C. Bruening, On the relative importance of motion-related contributions to the SAR imaging mechanism of ocean surface waves, *IEEE Trans. Geosci. Remote Sens.*, **GE-24**, 873–885, 1986.
- Alpers, W. R., and K. Hasselmann, Spectral signal to clutter and thermal noise properties of ocean wave imaging synthetic aperture radars, *Int. J. Remote Sens.*, **3**, 423–446, 1982.
- Alpers, W. R., and C. L. Rufenach, The effect of orbital motions on synthetic aperture radar imagery of ocean waves, *IEEE Trans. Antennas Propag.*, **AP-27**, 685–690, 1979.
- Alpers, W. R., and C. L. Rufenach, Image contrast enhancement by applying focus adjustment in synthetic aperture radar imagery of moving ocean waves, *Eur. Space Agency Spec. Publ.*, **ESA SP-154**, 25–30, 1980.
- Alpers, W. R., D. B. Ross, and C. L. Rufenach, On the detectability of ocean surface waves by real and synthetic aperture radar, *J. Geophys. Res.*, **86**, 6481–6498, 1981.
- Hasselmann, K., A simple algorithm for the direct extraction of the two-dimensional surface image spectrum from the return signal of a synthetic aperture radar, *Int. J. Remote Sens.*, **1**, 219–240, 1980.
- Hasselmann, K., R. K. Raney, W. J. Plant, W. Alpers, R. A. Shuchman, D. R. Lyzenga, C. L. Rufenach, and M. J. Tucker, Theory of synthetic aperture radar ocean imaging: A MARSEN view, *J. Geophys. Res.*, **90**, 4659–4686, 1985.
- Ivanov, A. V., On the synthetic aperture radar imaging of ocean surface waves, *IEEE J. Oceanic Eng.*, **OE-7**, 96–103, 1982.
- Ivanov, A. V., On the mechanism for imaging ocean waves by synthetic aperture radar, *IEEE Trans. Antennas Propag.*, **AP-31**, 538–541, 1983.
- Jain, A., Focusing effects in the synthetic aperture radar imaging of ocean waves, *Appl. Phys.*, **15**, 323–333, 1978.
- LaHaie, I. J., A. R. Dias, and G. D. Darling, Digital processing considerations for extraction of ocean wave imaging spectra from raw synthetic aperture radar data, *IEEE J. Oceanic Eng.*, **OE-9**, 114–120, 1984.
- Lyzenga, D. R., Numerical simulation of synthetic aperture radar image spectra for ocean waves, *IEEE Trans. Geosci. Remote Sens.*, **GE-24**, 863–872, 1986.
- Martin, P. J., Direct determination of the two-dimensional image spectrum from raw synthetic aperture radar data, *IEEE Trans. Geosci. Remote Sens.*, **GE-19**, 194–203, 1981.
- Monaldo, F. M., and R. C. Beal, Limitations of the Seasat SAR in high sea states, in *Wave Dynamics and Radio Probing of the Sea Surface*, edited by O. M. Phillips and K. Hasselmann, pp. 423–442, Plenum, New York, 1986.
- Monaldo, F. M., and D. R. Lyzenga, On the estimation of wave slope- and height-variance spectra from SAR imagery, *IEEE Trans. Geosci. and Remote Sens.*, **GE-24**, 543–551, 1986.

- Ouchi, K., Effect of defocusing on the images of ocean waves, in *Satellite Microwave Remote Sensing*, edited by T. D. Allen, pp. 209-222, Wiley-Interscience, New York, 1983.
- Plant, W. J., Comment on "On the synthetic aperture radar imaging of ocean surface waves," *IEEE J. Oceanic Eng.*, OE-8, 300, 1983.
- Plant, W. J., W. C. Keller, and A. Cross, Parametric dependence of ocean wave-radar modulation transfer functions, *J. Geophys. Res.*, 88, 9747-9756, 1983.
- Raney, R. K., and R. T. Lowry, Oceanic wave imagery and wave spectra distortions by synthetic aperture radar, in *Proceedings of the 12th International Symposium on Remote Sensing of Environment*, pp. 683-702, Environmental Research Institute of Michigan, Ann Arbor, 1978.
- Reed, I. S., On a moment theorem for complex Gaussian processes, *IRE Trans. Inf. Theory*, IT-8, 194-195, 1962.
- Shuchman, R. A. and J. S. Zelenka, Processing of ocean wave data from a synthetic aperture radar, *Boundary Layer Meteorol.*, 13, 181-191, 1978.
- Swift, C. T., and L. R. Wilson, Synthetic aperture radar imaging of moving ocean waves, *IEEE Trans. Antennas Propag.*, AP-27, 725-729, 1979.
- Tajirian, E. K., Multifocus processing of L band synthetic aperture radar images of ocean waves obtained during the Tower Ocean Wave and Radar Dependence Experiment, *J. Geophys. Res.*, this issue.
- 
- D. R. Lyzenga, College of Marine Studies, University of Delaware, Newark, DE 19716.

(Received September 7, 1987;  
accepted March 11, 1988.)

## Comparisons of Simulated and Actual Synthetic Aperture Radar Gravity Wave Images

ROBERT O. HARGER AND CAN E. KORMAN

*Electrical Engineering Department, University of Maryland, College Park*

The synthetic aperture radar (SAR) images obtained with the Jet Propulsion Laboratory's L-band system in the Tower Ocean Wave and Radar Dependence (TOWARD) oceanographic experiment are compared with images generated by a simulation program implementing a SAR ocean imaging model based on two-scale hydrodynamic and electromagnetic scattering approximate models. A critically regarded test of a theory of SAR ocean imaging is its prediction of the best image focus dependence on surface motion. The primary means of comparison here is an estimate of the best focus parameter that uses a subimage cross-correlation technique. The focus parameter estimates for both the actual and simulated images show (1) a reversal in sign with reversal in dominant longwave direction relative to the SAR direction, (2) a magnitude increase with an increase in magnitude of the angle between the dominant long wave and SAR axes, and (3) an independence of the altitude and also the range-to-velocity ratio. All equivalent velocity estimates are of the order of the dominant longwave phase velocity, normalized by the SAR vehicle velocity, and agree well qualitatively though there are some quantitative differences. These behaviors are in agreement with a related analytical prediction. The "visibility" of the long waves' SAR image artifacts, for this TOWARD data set, increased with increased altitude and also with increased range-to-velocity ratio for both the actual and simulated images, as was predicted by a related analysis. Agreement of spectral density estimates of the actual and simulated SAR images generally required an order of magnitude increase in the strength of the hydrodynamic interaction of the long and short waves. This may indicate, as have surface measurements in TOWARD and other experiments, that the two-scale model does not fully describe this nonlinear interaction. With this interaction adjustment, a comparison of actual and simulated images using an alternative focus criterion showed very close agreement in some cases.

### INTRODUCTION

A comparison is presented of predictions of a theoretical model for synthetic aperture radar (SAR) imagery of two-scale ocean gravity waves with actual imagery obtained by the L-band SAR of the Jet Propulsion Laboratory (JPL) during the Tower Ocean Wave and Radar Dependence Experiment (TOWARD). The comparison will be made employing a simulation program, realizing the theoretical model, that can produce SAR images. A specific comparison is the measurement of an "optimal focus parameter," applied to both the simulated and actual SAR complex, high-resolution imagery for imaging runs of October 31, 1984. It was felt that in particular, the image behavior with respect to focus parameter variation in these selected runs, with their variation in relative direction and altitude, could be a discriminator and/or validator, in part, of proposed theories.

The theoretical model under discussion here is an extension of that due to Harger [1981, 1986] which synthesized three basic models. (1) The hydrodynamic model employed is based on a two-scale, or WBK, theory discussed by Phillips [1981a, b]. (2) The electromagnetic scattering model employed is that appropriate to a two-scale surface as discussed by Bass *et al.* [1968], Bass and Fuks [1979], Wright [1966, 1968], Valenzuela [1968], and others. (3) The SAR imaging model is that for an extended, time-varying scene due to Harger [1980]. For application here it was desirable to extend that theory to allow a nonmonochromatic long wave; because such a hydrodynamic theory is only now under development [Longuet-Higgins, 1987], an ad hoc generalization was used that is reasonable for the narrowband longwave fields encountered in the TOWARD experiment on this date.

The resulting model, given in the appendix, is somewhat involved; its attributes can be discovered by analytic means seemingly only with difficulty, even approximately. Therefore a simulation program embodying it was written to produce high-resolution, complex SAR images of sufficient extent. One may then perform rather arbitrary comparisons between the simulated and actual SAR images.

Examples of the simulated images are shown in Figures 1 to 6 corresponding to the six actual runs to be discussed here. The general parameters of these runs are given in Table 1. In each figure, the right-hand image is the actual SAR image and the center image is the corresponding simulated SAR image; the left-hand image is the underlying long wave at one instant, realized by the simulation from the longwave directional frequency spectrum measured roughly contemporaneously by the Scripps Institute of Oceanography (SIO), assuming a zero mean, normal random field.

These SAR images are "four-look" image magnitudes, generated by adding together incoherently four reduced resolution images. The actual SAR images have an azimuth and a ground range resolution of 11 m and 13 m, respectively, and an extent of about 1.3 km and 1.66 km in azimuth and ground range. The simulated SAR images have azimuth and ground range resolutions equal to 8 m and an extent of about 1 km in both azimuth and ground range; additive noise was adjusted to agree with the estimated actual signal-to-noise ratio, and as will be discussed later, the hydrodynamic interaction strength was adjusted for improved agreement in its estimated spectral density with that of the actual data.

### BACKGROUND

The sea surface height varies in time, of course, and it is well known that a scatterer's motion can belie its azimuth, or along-track, position to a SAR. The along-track coordinate of

Copyright 1988 by the American Geophysical Union.

Paper number 8C0187.  
0148-0227/88/008C-0187\$05.00

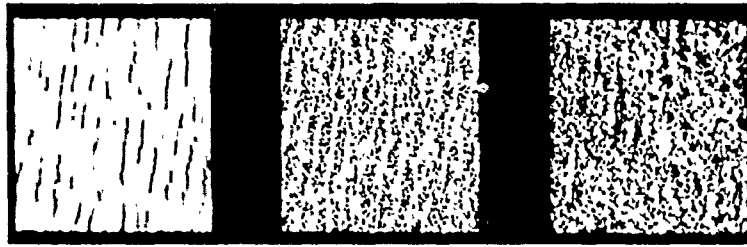


Fig 1 (left) Simulated long wave, (middle) simulated SAR image, and (right) actual SAR image, run 006.

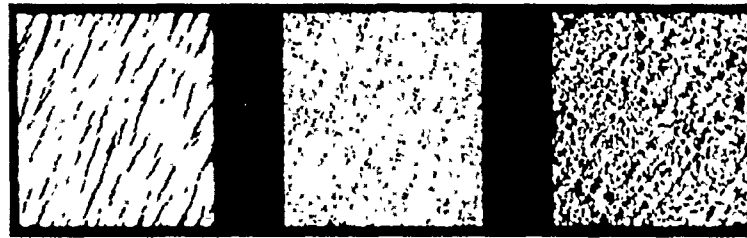


Fig 2 (left) Simulated long wave, (middle) simulated SAR image, and (right) actual SAR image, run 007.

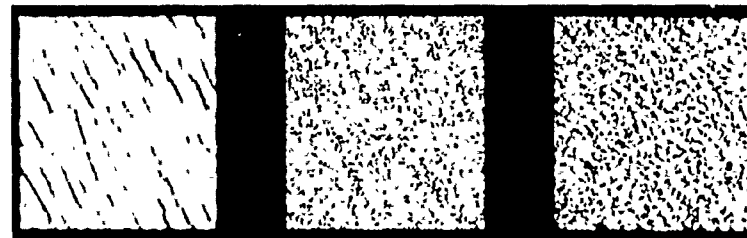


Fig 3 (left) Simulated long wave, (middle) simulated SAR image, and (right) actual SAR image, run 008.

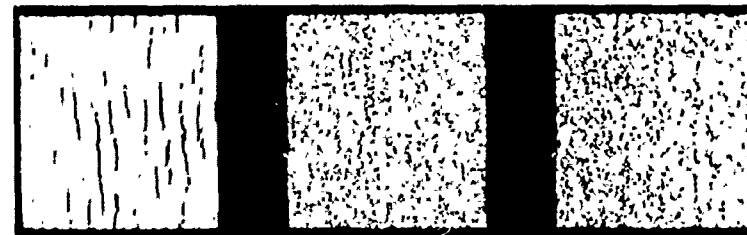


Fig 4 (left) Simulated long wave, (middle) simulated SAR image, and (right) actual SAR image, run 009.

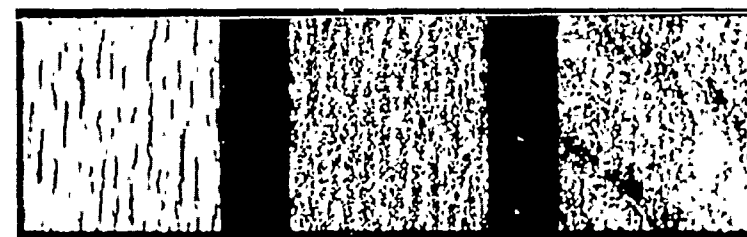


Fig 5 (left) Simulated long wave, (middle) simulated SAR image, and (right) actual SAR image, run 010.



Fig. 6. (left) Simulated long wave, (middle) simulated SAR image, and (right) actual SAR image, run 012.

a scatterer is noted by the instant its returned signal frequency changes from "up Doppler" to "down Doppler," giving its time abeam (in the conventional SAR). For typical SAR systems, this Doppler-induced modulation on the scattered signal, generated as the scatterer passes through the antenna beam, is a linear frequency modulation (FM) characterized by its rate of change, denoted here by  $K_{SAR}$ . To achieve an image of the scatterer with a resolution typically small in relation to that normally set by the antenna pattern, the SAR processor "compresses" this "Doppler history" using a "matched," or conjugate, filter whose linear FM rate is  $-K_{SAR}$ . (For a review of the ideas of SAR see, for example, Harger [1970].)

The two-scale electromagnetic scattering model employed here approximates the scattered field as a perturbation of the field scattered at the air-sea boundary formed by the large-scale height structure, that is, the long wave. The perturbed part of the scattered field is due to the boundary perturbation caused by the small-scale height structure (the short gravity waves here).

The long wave, in the monochromatic case, moves at its phase velocity, and it is reasonable to expect that (for example) if the long wave is directed with the SAR-bearing vehicle (i.e., "with the SAR"), then the compression of its image, relative to a stationary wave, would be degraded but restored with an appropriate decrease in the processor's linear FM rate (i.e., by an appropriate refocusing) corresponding to the decreased relative velocity. In the oppositely directed case, the relative velocity is greater, and an increase in the processor's linear FM rate would be expected to refocus the image.

Generally speaking, observations in major oceanographic experiments over a decade (see, for example, reports by Shuchman and Zelenka [1978] and Shuchman and Shemdin [1983] on the Marineland experiment and Jain and Shemdin [1983] on the MARSEN experiment) and also in the TOWARD experiment have confirmed this prediction. While the experimental methods and the proportionality constant were subject to debate, it is fair to say that the best focus correction was

always found to be of the order of the longwave phase velocity. In fact, this can be concluded merely by observing a set of SAR images processed with various focus parameter values, as has been done with the TOWARD SAR images by Shemdin. As an example, shown in Figure 7 are actual SAR images, processed with best focus, no focus, and worst focus, for focus corrections taken in a set defined below.

Detailed consideration of the motion effects is rather complicated. For example, the small-scale height structure perturbing the large-scale height structure (the short gravity waves which are needed for backscatter at intermediate incidence angles) also have their intrinsic motion and motion due to their residence on the long wave. Other points of view have been advanced which ascribe the basic motion to scattering "facets" which have the orbital motion of Lagrangian parcels of the long wave; in particular, it has been asserted [Alpers *et al.*, 1981, p. 6481] that "...The phase velocity of the long waves does not enter into the SAR imaging process...."

Thus the ability of any theoretical model to predict the best focus for actual SAR images has appeared to be an important test of that theory, and the TOWARD experiment devised conditions under which competing theories were expected to make differing predictions.

In the following, the refocused linear FM rate of the SAR processor will be denoted

$$K_{pr} = (1 + c)^2 K_{SAR}$$

where  $c$  will be termed the focus parameter. The best  $c$  is expected to be, in magnitude, of the order of the ratio of the phase velocity  $V_{ph}$  of the dominant long wave to the SAR vehicle velocity  $V_{SAR}$ , and hence  $c$  is a small parameter. As the latter velocity varies in the imaging runs, it is convenient to present some of the results using a velocity parameter  $U$ , also called a focus parameter, which is  $c$  multiplied by the SAR velocity:

$$U = V_{SAR} c$$

The actual SAR images for each selected run were routinely processed, in the four-look mode, by JPL with  $U$  in the set  $\{l * v_{ph}/3, l = -7, \dots, +7\}$  where  $v_{ph} = 11$  m/s, is the phase velocity of the dominant long wave at the tower of the Naval Ocean Systems Center (NOSC) where the longwave directional frequency spectrum was measured. For example, in Figure 1, the values of  $U$  are  $-v_{ph}$ , 0, and  $+(7/3) * v_{ph}$ .

While a correctly implemented simulation program gives directly the "predictions" of the theoretical model, it is very useful to have available analyses that can yield insight into the nature of the SAR ocean imaging process. A related analysis, when the long wave is monochromatic, gives the best focus correction to yield zero quadratic phase error due to the long-wave motion and, though this is not the sole effect of surface

TABLE 1. SAR Direction, Altitude, and Velocity for Selected Runs of October 31, 1984

Run	Direction, deg	$\cos(\theta)$	Altitude, m	Velocity, m/s	$R_0/v_{SAR}$ , s
006	110	0.985	14,640	273	94
007	260	-0.940	14,630	214	119
008	320	-0.766	14,640	220	116
009	290	-0.985	14,640	218	117
010	110	0.985	7,759	229	59
012	260	-0.940	2,690	133	35

The dominant long wave's direction was  $100^\circ$ ; the cosine of the (least) angle to the SAR direction's axis is also given, along with the nominal slant range-to-velocity ratio.

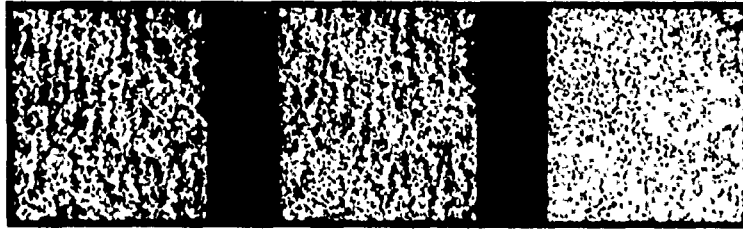


Fig. 7. The actual SAR image for run 006, processed for (left) best, (middle) no, and (right) worst focus.

motion, provides a guide to the behavior of this parameter that may be expected for a narrowband long wave.

The following assertion is established in the appendix. Suppose that the (monochromatic) long wave's direction, relative to the SAR direction, is at an angle  $\theta$ . Also, suppose that the shortwave ensemble is represented, as it often is, by a Fourier summation of wavelets of the form  $\exp(ik \cdot x - i\sigma(k)t)$ . Since in this two-scale model the SAR image depends linearly on the short waves, this image consequently has a representation as a summation of subimages, each uniquely corresponding to a wavelet. Then

*Theorem.* A SAR processor linear FM rate  $K_{pr} = (1 + c)^2 K_{SAR}$  with

$$c = -\left(\frac{V_{ph}}{V_{SAR}}\right) \frac{1}{\cos(\theta)} \quad \cos(\theta) \neq 0$$

yields a scaled and translated version of the wavelet's subimage when  $V_{SAR}$  is infinitely large.

That is, as there are no observable effects of the sea's motion with an arbitrarily large SAR scanning velocity  $V_{SAR}$ , this focus correction negates (aside from a scaling and translation) the effects of motion, specifically defocusing, on the wavelet's subimage. Remarkably, this focus correction does not depend on the wavelet's wave number and hence holds for all subimages. As is shown in the appendix, the scaling, but not the translation, is also independent of the wavelet's wave number.

This result gives four predictions with regard to the best focus parameter (BFP) expressed as a velocity: (1) the BFP is the order of the longwave phase velocity, (2) the BFP reverses sign with a reversal of  $V_{SAR}$ , (3) the BFP magnitude increases with decreasing  $|\cos \theta|$ , and (4) the BFP magnitude is independent of the altitude of the SAR-bearing vehicle.

The asserted dependence of the wavelet's image contribution translation on its wave number leads, in this TOWARD data set, a fifth prediction, that the visibility of the images's longwave artifacts increases with increasing altitude of the SAR-bearing vehicle. This prediction will be discussed later in this paper.

#### SUBIMAGE CROSS-CORRELATION FOCUS COMPARISON

Focus will be estimated here with a technique that has been used for some time with SAR images and has been recently applied to SAR ocean imagery by *Li et al* [1985] and also to TOWARD SAR data by *Leotta and Li* [1987]. It is based on a simple and clear idea. If there is a quadratic phase error in a scatterer's Doppler history (due to a linear FM rate that does not match that assumed by the SAR processor, for example), then in each half of the history, the phase errors have best linear approximations that are nonzero and of opposite slope. If each half is separately processed to form two subimages,

each subimage will be displaced in azimuth as its zero Doppler times is belied, and their displacements will have opposite signs. A subsequent cross correlation of these (random) subimage intensities can then yield an estimate of their displacement and hence of the original quadratic phase error.

If the quadratic phase error is expressed as  $(2c + c^2)K_{SAR}x^2/2$ , then the resulting subimage translation magnitudes are given approximately by

$$D = (2c) * [l_0 R_0 / 4 * D_h] \quad c \ll 1$$

where  $l_0$ ,  $R_0$ , and  $D_h$  are, the SAR mean RF wavelength, the mean slant range, and the along-track dimension of the SAR's antenna aperture, respectively. In the TOWARD experiment on October 31, 1984, for the high-altitude runs,

$$l_0 R_0 / D_h = 400 \text{ m}$$

and  $c$  will take on values of the order of

$$V_{ph} / V_{SAR} = 11/250 = 0.044.$$

Therefore  $D = 9$  m in magnitude. At the medium and low altitude runs,  $D$  is 5 m, and 1.7 m, respectively. The JPL SAR used in TOWARD had an azimuth resolution of about 4.5-m. Thus a careful measurement, with a sufficiently large number of independent measurements, is required to attain good accuracy.

For each run, the following procedure was carried out: for each of a set of corrections  $c$ , the algorithm just described was applied to 1024 azimuth points, at a given range, of the complex, full-resolution SAR image, actual or simulated. The resulting cross correlations were averaged for 64 ranges. For each  $c$ , the estimated location  $D_c(c)$  of the maximum was then determined, typically using a quadratic fit based on seven points. Then, with  $D_c(c)$  viewed as a function of  $c$ , a least squares error linear fit  $D_l(c)$  to  $D_c(c)$  was made and the intercept  $D_l(c_0) = 0$  determined the best focus parameter estimate  $c_0$  for that run.

This measurement technique was applied to the set of runs listed in Table 1. For the actual images, these cross correlations yielded a well-defined maximum on about 85% of the trials: see, for example, Figure 8. However, on about 15% of the trials there was a less well defined maximum: see, for example, Figure 9. For the simulated images, almost all the trials yielded a well-defined maximum.

In Figures 10-15 are shown direct comparisons of the focus tests for the actual and simulated data for these runs. The estimated displacement values and their linear fits  $D_l(c)$  are shown, with the focus parameter expressed as a velocity. The results are summarized in Table 2. Clearly, these best focus parameter values are all of the order of the dominant long wave's phase velocity, verifying the first prediction.

With regard to the second prediction, the comparisons of

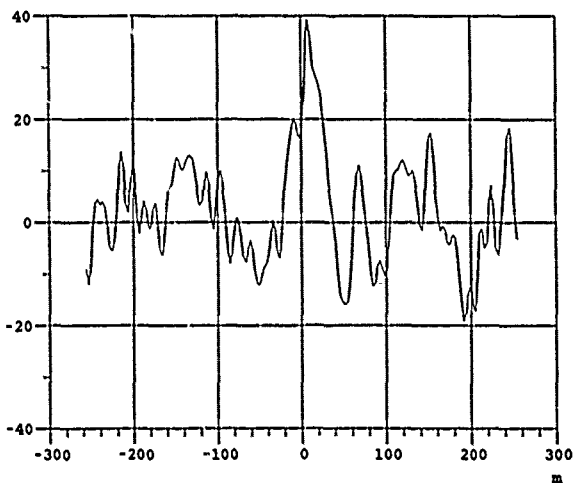


Fig. 8. An example of a cross correlation of subimages with a well-defined maximum (arbitrary ordinate scaling).

runs 006 and 009, for both the actual and simulated data, are shown in Figures 16 and 17. Clearly, there is a reversal of the sign of the best focus correction with reversal of the SAR direction, establishing the second prediction. When the directions are opposing, the value of the best focus correction for the actual imagery is unexpectedly low. In part, this may be due to the selection of a somewhat anomalous region in the image: *Leotta and Li* [1987] get a larger value (about one-half the dominant long wave's phase velocity) with averages over a larger region. The values of the best focus correction for the simulated images are nearly equal in magnitude but are about one-half the dominant long wave's phase velocity.

The comparisons of Figures 18 and 19 show that the results for runs 007, 008, and 009 are ordered according to the third prediction for the actual data and, within the expected accuracy of the measurement, also for the simulated data.

Finally, Figures 20 and 21 show the predicted independence of altitude of the best focus correction for runs 006 and 010 (at 14,640 m and 7759 m, respectively) for both the actual and simulated SAR images. This is also shown in Figures 22 and 23 for runs 007 and 012, at 14,630 m and 2690 m, resp.

As is shown in Table 3, the slope of the displacement versus

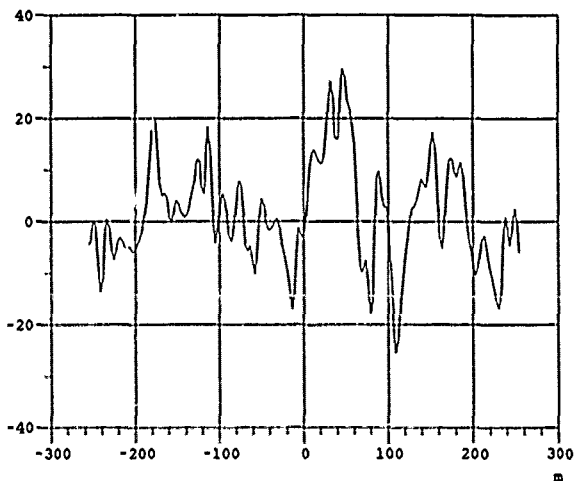


Fig. 9. An example of a cross correlation of subimages with a poorly defined maximum (arbitrary ordinate scaling).

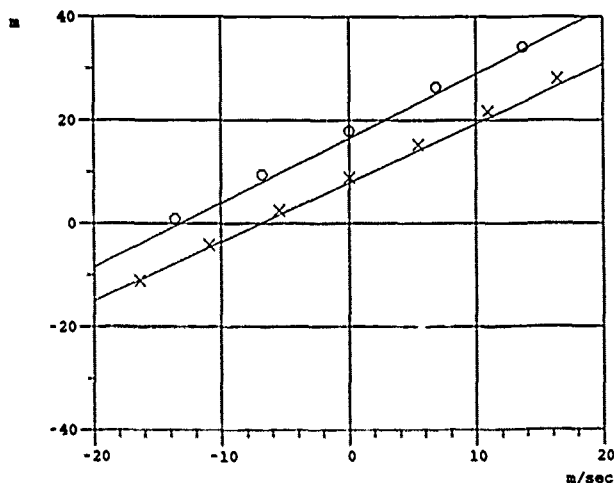


Fig. 10. The displacement of the cross-correlation maximum versus the focus parameter, for the actual (circles) and simulated (crosses) SAR images of run 006.

focus correction predicted by the theorem, assuming a sinusoidal long wave, agrees well with those of the best linear fits derived from both the simulated and actual SAR images and especially well for the latter. This suggests the possibility of estimating the best focus correction using just the correlation measurement with the normally focused image and the theoretical slope prediction. However, observing the deviation of the measurements from the best linear fit, it is preferable to make multiple measurements to reduce errors.

IMAGE LONGWAVE ARTIFACT VISIBILITY  
VERSUS HEIGHT

A detailed analysis of the image contribution of one wavelet of the short waves shows that when the slope of an azimuth-directed, sinusoidal long wave is sufficiently large, the nature of this image is well approximated in the azimuth coordinate by pairs of SAR system azimuth impulse responses repeated at the longwave-wavelength. These image artifact pairs, which are associated with the extrema of the long wave, have a relative translation that depends upon the wavelet's wave number. There exists a condition, partly incumbent on nature,

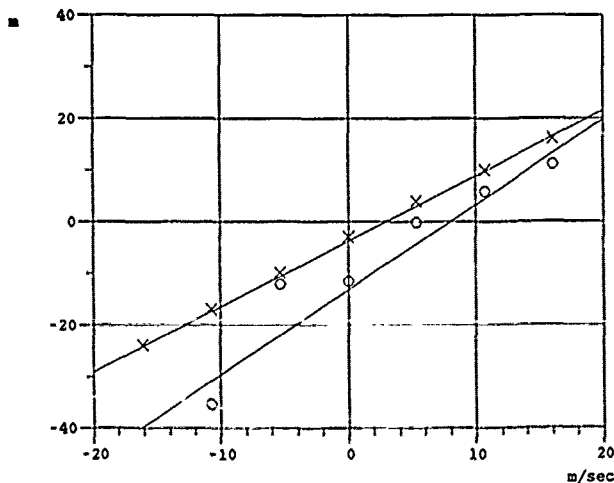


Fig. 11. The displacement of the cross-correlation maximum versus the focus parameter, for the actual (circles) and simulated (crosses) SAR images of run 007.

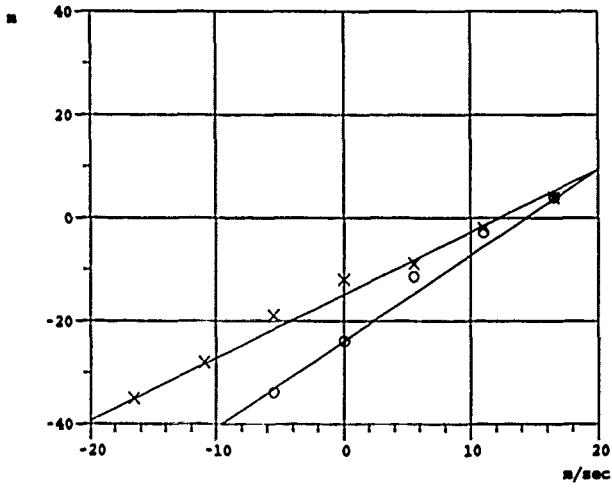


Fig. 12. The displacement of the cross-correlation maximum versus the focus parameter, for the actual (circles) and simulated (crosses) SAR images of run 008.

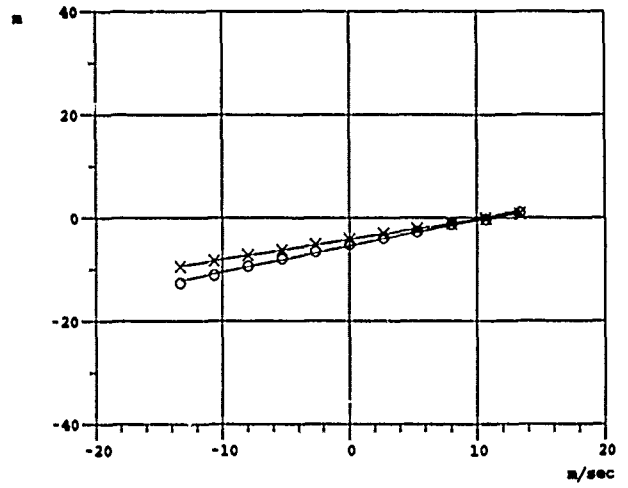


Fig. 15. The displacement of the cross-correlation maximum versus the focus parameter, for the actual (circles) and simulated (crosses) SAR images of run 012.

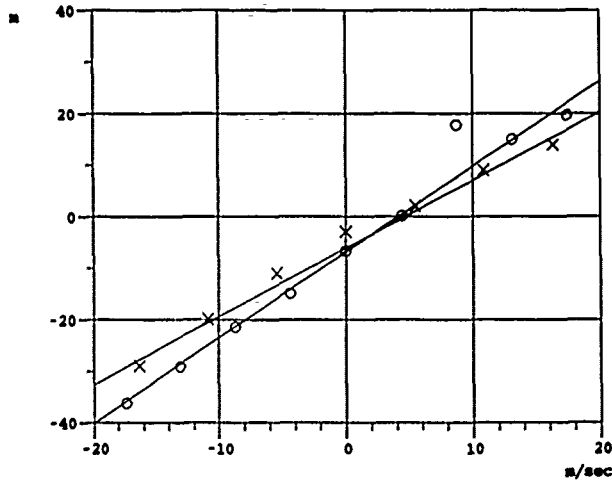


Fig. 13. The displacement of the cross-correlation maximum versus the focus parameter, for the actual (circles) and simulated (crosses) SAR images of run 009.

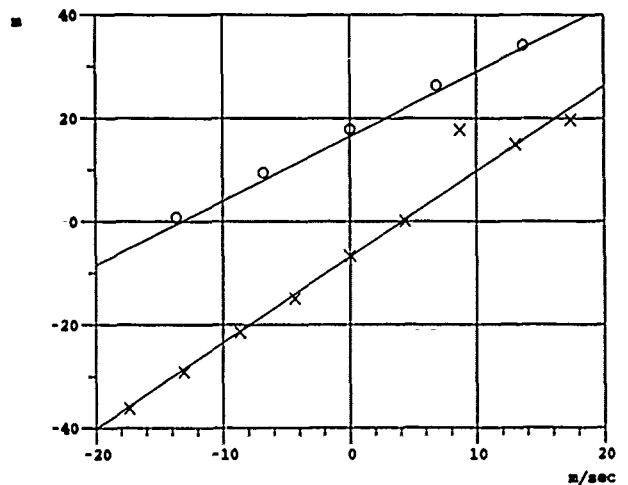


Fig. 16. The displacement of the cross-correlation maximum versus the focus parameter for the actual SAR images for run 006 (circles) and run 009 (crosses).

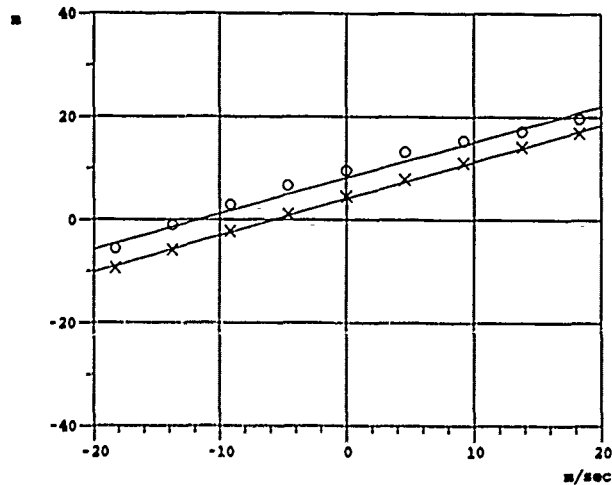


Fig. 14. The displacement of the cross-correlation maximum versus the focus parameter, for the actual (circles) and simulated (crosses) SAR images of run 010.

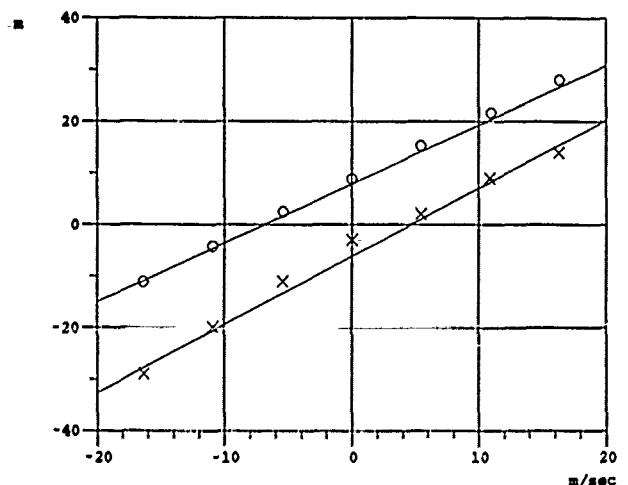


Fig. 17. The displacement of the cross-correlation maximum versus the focus parameter for the simulated SAR images for run 006 (circles) and run 009 (crosses).

TABLE 2. Comparison of the Best Focus Parameters, Expressed as a Velocity, Based on the Subimage Cross-Correlation Technique

Run	$U_{sinc}$	$U_{sim}$	$U_{SAR}$
006	-12.9	-6.01	-13.1
007	+13.5	+3.85	+8.67
008	+16.6	+11.8	+14.4
009	+12.9	+5.01	+4.18
010	-12.9	-5.65	-11.6
012	+13.5	+10.9	+10.8

$U_{sinc}$  is by an analytic prediction for a monochromatic long wave,  $U_{sim}$  is from the SAR simulated images, and  $U_{SAR}$  is from the actual TOWARD SAR images.

that ensures that the artifacts associated with the crests will have equal translations while those artifacts associated with the troughs will have unequal translations. This condition, which presumably therefore enhances the likelihood of well-resolved, or "visible," artifacts associated with the crests of the long wave, is, assuming best focusing,

$$HAK\sigma(K)/V_{SAR} = 1$$

where  $A$ ,  $K$ , and  $\sigma(K)$  are the long wave's amplitude, wave number, and frequency, respectively, and  $(H, V_{SAR})$  are the SAR vehicle's altitude and speed, respectively. This condition is better met with increasing altitude on the SAR runs of this date: the left side takes on the values (0.91, 0.52, 0.34) at the altitudes (14.6, 7.8, 2.7) thousand meters.

The actual and simulated SAR images of these three altitudes are shown in Figures 24 and 25, respectively: the increasing visibility of the longwave artifacts with  $H$  and  $H/V_{SAR}$  is evident in both, supporting the fifth and last prediction.

AN OBSERVATION ON THE HYDRODYNAMIC INTERACTION STRENGTH

According to the present SAR imaging theory, a fundamental image-forming mechanism is the "filtering" (i.e., wave number bandwidth restriction) of the reflectivity density as it is sensed by the SAR. The reflectivity density has a phase factor, due to the round-trip ray path to the unperturbed, large-scale surface: the long wave here, which, for sufficiently large long-wave amplitudes, causes maxima in the SAR image intensity at the extrema of the long wave (as is explained at length by Harger [1981, 1986]). In itself, this phenomenon would cause, for example, a second harmonic of the longwave dominant wave number to appear in the spectral density estimate of the SAR image intensity. This theory identifies three mechanisms that suppress alternate maxima, which together

TABLE 3. The Predicted and Measured (From Simulated and Actual SAR Images) Slope of the Linear Dependence of Image Displacement on Focus Correction

Run	Predicted Slope	Measured Slope	
		Simulated Data	Actual Data
006	1.3	1.2	1.2
007	1.7	1.3	1.7
008	1.6	1.1	1.7
009	1.6	1.1	1.7
010	0.8	0.7	0.7
012	0.5	0.4	0.5

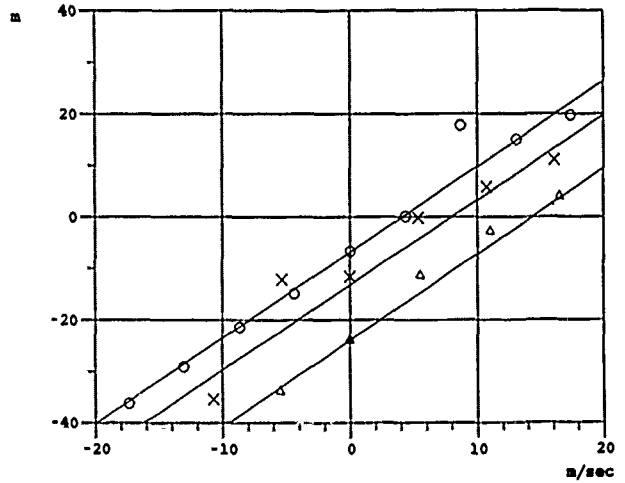


Fig. 18. Displacement of cross-correlation maximum versus focus parameter for actual SAR images, runs 007 (crosses), 008 (triangles), and 009 (circles).

lead toward an image intensity spectral density estimate with only one dominant wave number: that of the long waves.

1. These image extrema tend, with increasing longwave amplitude, to a collection of degraded SAR system impulse responses, one associated with each extremum of the long wave. An evaluation, by the method of stationary phase, of the image nature near each such extremum shows that the degradation is due to two quadratic phase error contributions, one due to the longwave motion and the other which is of opposite sign at the crest and trough of the long wave. Thus this latter quadratic phase error can, at the crest, partially cancel the quadratic phase error due to motion, thereby "sharpening" the maxima associated with longwave crests, while adding to the quadratic phase error due to motion at the troughs, thereby "blurring" the maxima associated with the troughs of the long wave.

2. As already discussed, there is seen to be a differing translation, at the crest and trough, of the image contributions of each wavelet of the small-scale ensemble. In the TOWARD experiment, the parameters were such that at the crests, the

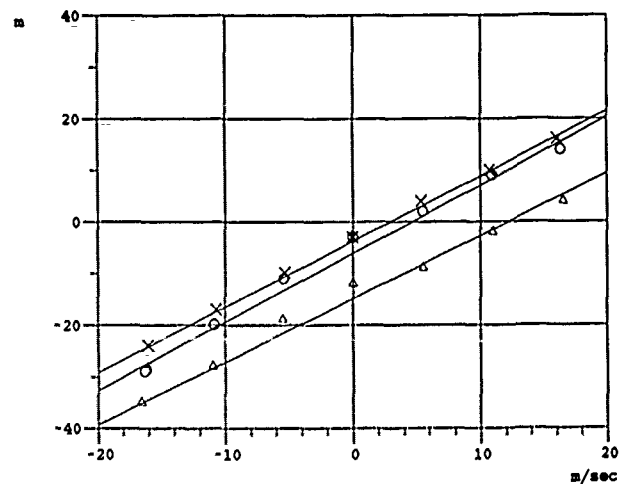


Fig. 19. Displacement of cross-correlation maximum versus focus parameter for simulated SAR images, runs 007 (crosses), 008 (triangles), and 009 (circles).

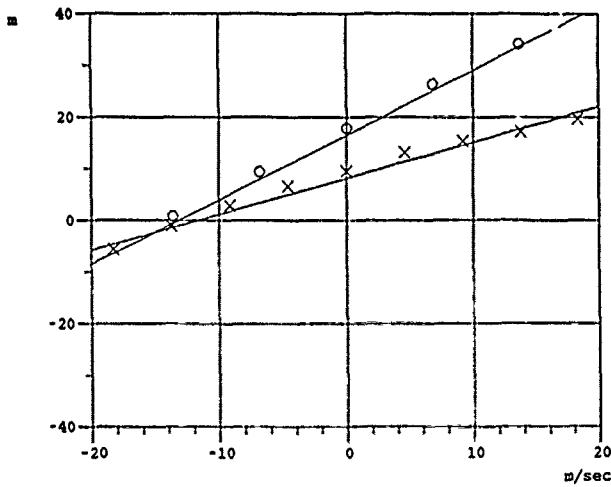


Fig. 20. Displacement of cross-correlation maximum versus focus parameter for actual SAR images, runs 006 (circles), 010 (crosses).

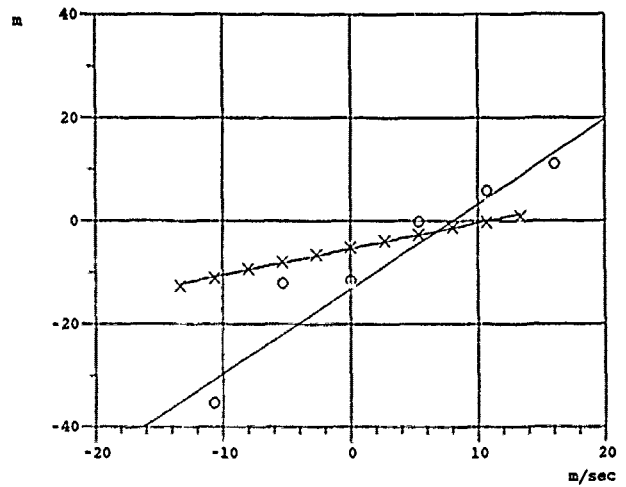


Fig. 22. Displacement of cross-correlation maximum versus focus parameter for actual SAR images, runs 007 (circles) and 012 (crosses).

translations were less dependent on the wavelet's wave number (especially so at the highest altitude) so that the maximum at the crest were less "dispersed"; however, at the troughs, the translations caused a greater "dispersal" of the contributions. To repeat, this leads to a prediction that the artifacts of the long wave will increase in visibility with increasing altitude (as in fact was observed), with an artifact spacing equal to period that of the long wave.

3. As is well known [Phillips, 1981b], the two-scale, or WKB, theory predicts that the amplitude of a small-scale wavelet is increased at the crests, and decreased at the troughs, of the long wave.

It was noticed in comparing the spectral density estimates (sde) of the simulated and actual SAR images that these three effects were not always sufficient to suppress the second harmonic. But it was observed that increasing the strength of the interaction described in the preceding paragraph led to much closer agreement and, in particular, suppressed the second-harmonic maxima. In Figures 26 and 27 are shown the simulated SAR images for runs 006 and 008 for three multiples,

$f = (1, 10, 20)$ , of the WKB interaction strength, HDF: the simulated images for  $f = 20$  more closely resemble the actual image (for example, see again Figures 1 and 3). More dramatically, the corresponding spectral density estimates are shown in Figures 28 and 29. The disappearance of the second harmonic with increasing interaction strength is clearly seen. The interplay here, in this simulated "computer experiment", with oceanographic experiments and evolving hydrodynamic theory, is regarded as quite interesting.

With this increase in the hydrodynamic interaction strength, the sde of the simulated SAR image is compared with the corresponding sde of the actual SAR image in Figures 30 and 31 for runs 006 and 008. In each of these figures, the left-hand image is the sde of the long waves whose directional frequency spectrum was measured by SIO, the middle image is the sde of the simulated SAR image, and the right-hand image is the sde of the actual SAR image. (The degrees of freedom in the estimates are 70, 32, and 32, respectively). They agree quite well in their dominant parts. Their spectral maximum is located at the "white" pixel locations imbedded in the spectra.

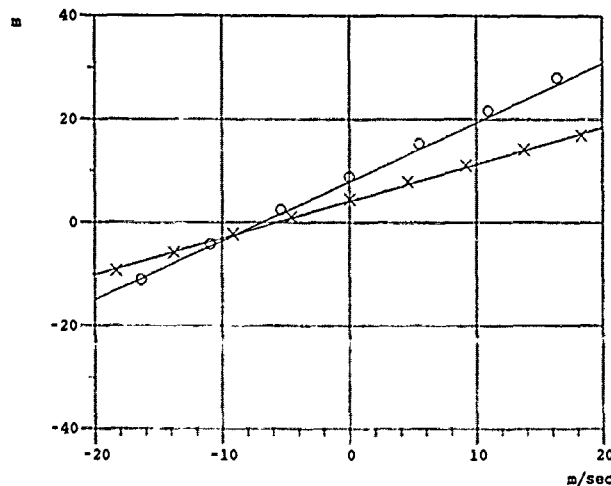


Fig. 21 Displacement of cross-correlation maximum versus focus parameter for simulated SAR images, runs 006 (circles) and 010 (crosses).

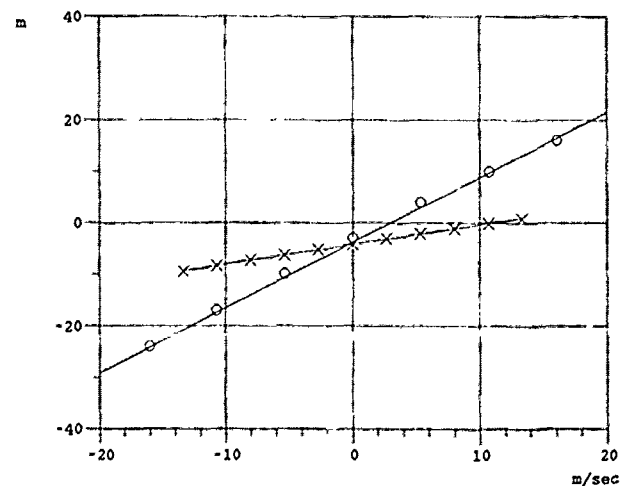


Fig. 23. Displacement of cross-correlation maximum versus focus parameter for simulated SAR images, runs 007 (circles) and 012 (crosses).

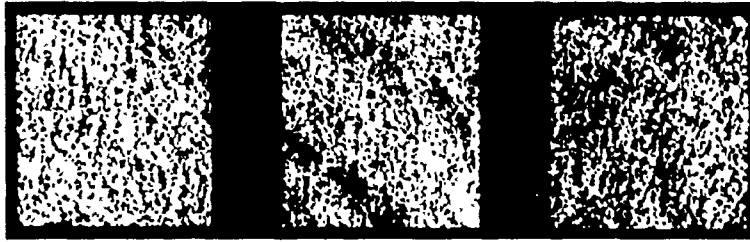


Fig. 24. Actual SAR images at three altitudes for runs (left) 006, (middle) 010, and (right) 012. (Image parameters as in Figure 1.)

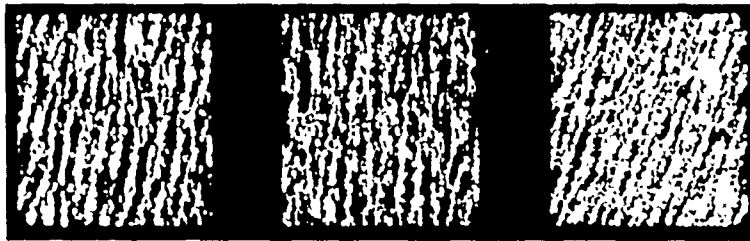


Fig. 25. Simulated SAR images at three altitudes, runs (left) 006, (middle) 010, and (right) 012. (Image parameters as in Figure 1.)



Fig. 26. Simulated SAR images for run 006 at three HDFs. (left) 1, (middle) 10, and (right) 20. (Image parameters as in Figure 1.)

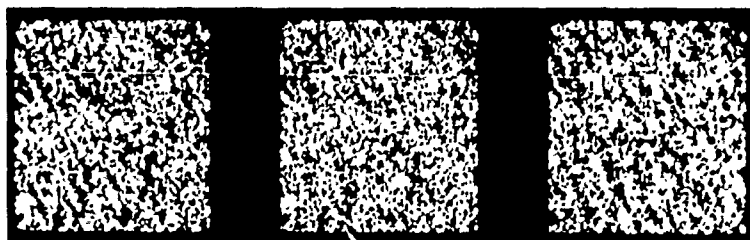


Fig. 27. Simulated SAR images for run 008 at three HDFs. (left) 1, (middle) 10, and (right) 20. (Image parameters as in Figure 1.)

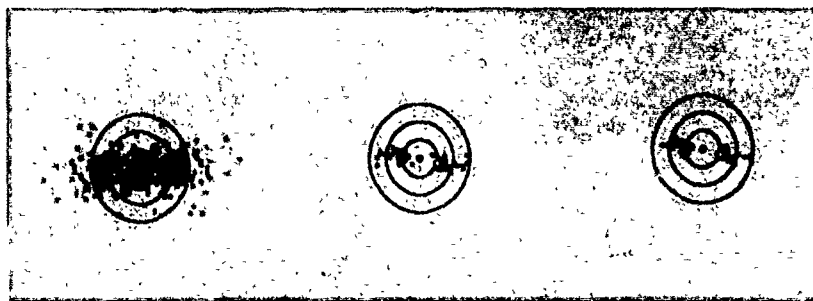


Fig. 28. Estimated spectral densities of simulated SAR images for run 006 at three HDFs: (left) 1, (middle) 10, and (right) 20.



Fig. 29. Estimated spectral densities of simulated SAR images for run 008 at three HDFs. (left) 1, (middle) 10, and (right) 20.

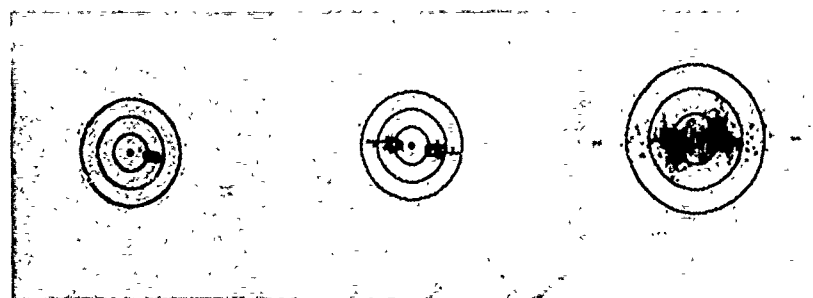


Fig. 30. Estimated spectral densities of the (left) long wave, (middle) simulated SAR image, and (right) actual SAR image for run 006.

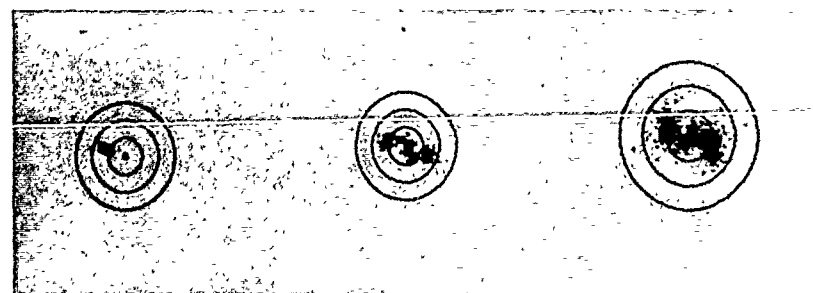


Fig. 31. The estimated spectral densities of the (left) long wave, (middle) simulated SAR image, and (right) actual SAR image for run 008.

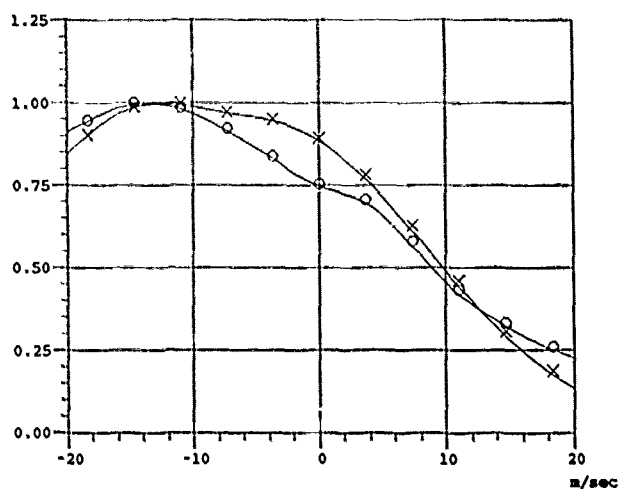


Fig. 32. Normalized maximum of sde versus focus parameter for actual (circles) and simulated (crosses) SAR images, run 006.

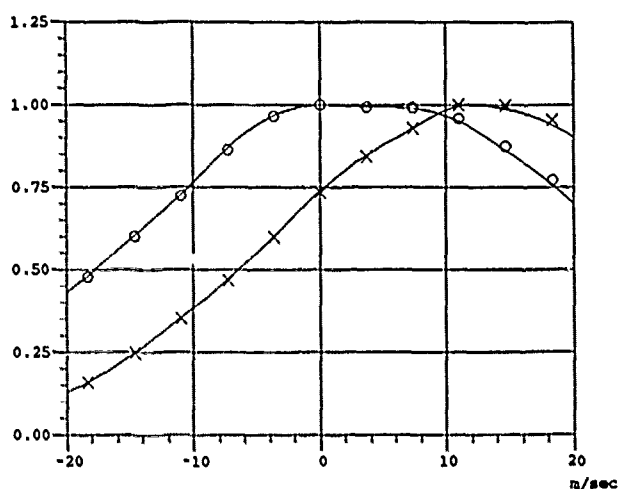


Fig. 34. Normalized maximum of sde versus focus parameter for actual (circles) and simulated (crosses) SAR images, run 008.

Remarkably, it has been observed that a second harmonic does indeed appear in SAR images of ice fields under which a long wave is propagating [Freeman *et al.*, 1987]). While such an imaging problem has interesting detail in itself worthy of study, we do observe that of course there is no "hydrodynamic interaction" of the various scales of the frozen ice surface height; therefore the image intensity maxima associated with the troughs of the ice field height are not as strongly suppressed as they would be for a corresponding ocean wave!

It has been observed in direct measurements of the ocean surface by a "wave follower" laser device (by Tang and Shemdin [1983] and also in TOWARD) that the two-scale WKB theory may well underpredict the strength of the interaction of the long and short waves. Indeed, one specific such measurement in TOWARD conforms nearly exactly with the nature and magnitude of the interaction adjustment described previously. As other such measurements may indicate, the matter could be more complicated: there may be nonlinear interactions of significance not included in the present model. Two candidates are the interaction of the small waves, not only with the long wave as modeled here but also among themselves and with intermediate waves.

A visual examination of a set of simulated SAR images indicated that when the hydrodynamic interaction strength was increased above the two-scale theory's value by an order of magnitude, the amplitude "straining" became the dominant image artifact-forming mechanism. However, the presence of the phase factor due to the round-trip ray path to the long-wave surface was still required for an accurate estimate of best focus; otherwise, the latter estimate is small.

#### A FOCUS COMPARISON BASED ON SPECTRAL DENSITY ESTIMATES

Another technique, a two-dimensional version of one that has been used to estimate the best focus parameter [Shuchman and Zelenka, 1978; Shuchman and Shemdin, 1983; Jain and Shemdin, 1983] is based on an examination of the estimated spectral density of the image intensity. For example, one may process SAR complex data for a set of focus parameters, find the sde for each image so processed, and then find, over the set, the wave number of the largest response; the associated focus parameter is said to be the optimal one of the set. Typically, the response at said wave number is plotted versus the focus parameter.

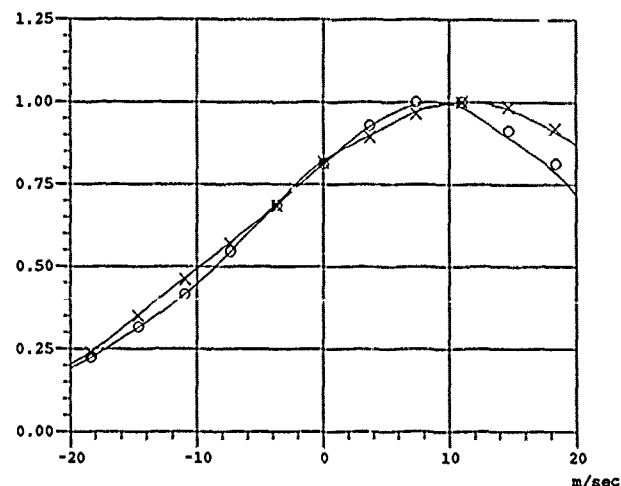


Fig. 33. Normalized maximum of sde versus focus parameter for actual (circles) and simulated (crosses) SAR images, run 007.

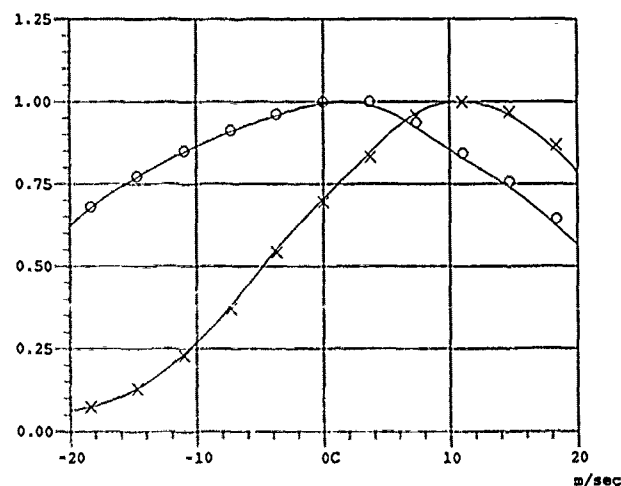


Fig. 35. Normalized maximum of sde versus focus parameter for actual (circles) and simulated (crosses) SAR images, run 006.

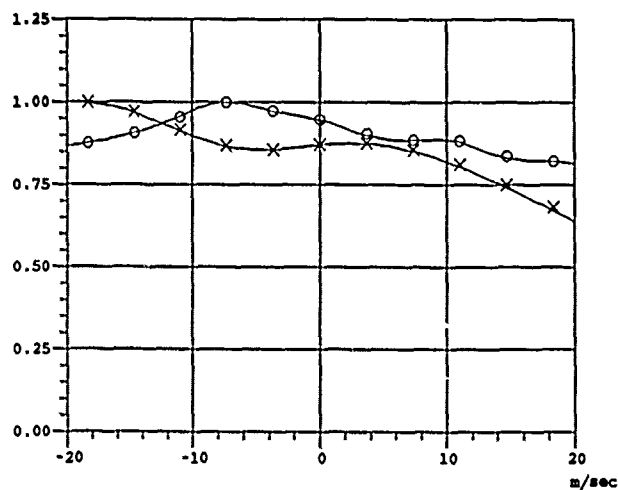


Fig. 36. Normalized maximum of sde versus focus parameter for actual (circles) and simulated (crosses) SAR images, run 010.

This optimality criterion seems to be more difficult to relate precisely to artifacts in the SAR image due to motion than is that of the subimage cross-correlation technique, and hence predictions from models are more tenuous. However, one can compare the actual and simulated images in this manner.

These dominant spectral responses, as a function of the focusing parameter and normalized by their maximum value, are compared for the actual and simulated SAR images in Figures 32-37. These responses show remarkably close agreement for runs 006 and 007 but agree less well in (for example) run 009.

The location of their maxima were estimated using cubic spline fits, and the focus parameters best according to this spectral criteria are listed in Table 4. All values are of the order of the longwave phase velocity, and a reversal in sign is shown with reversal in SAR direction.

#### COMMENTS AND CONCLUSIONS

The best focus parameter estimated by the subimage cross-correlation technique, has shown agreement in four important behaviors between actual TOWARD and simulated SAR images. First, all BFPs are of the order of the phase velocity of the long wave. Second, the reversal of sign of the BFP with

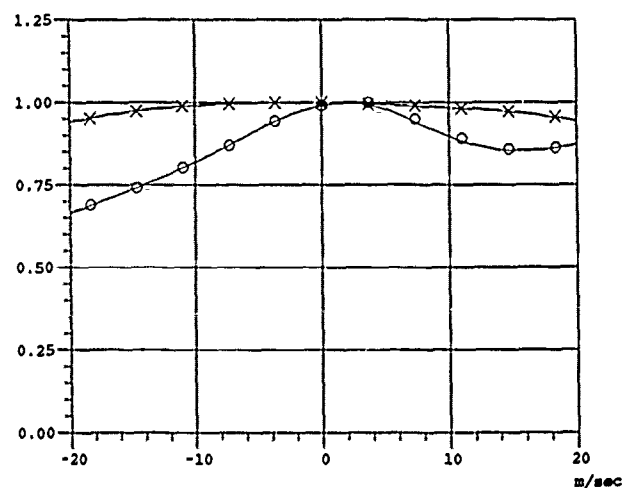


Fig. 37 Normalized maximum of sde versus focus parameter for actual (circles) and simulated (crosses) SAR images, run 012.

TABLE 4. Comparison of the Best Focus Parameter, Expressed as a Velocity, Based on the Spectral Density Estimates' Maxima

Run	$U_{sim}$	$U_{SAR}$
006	-12.6	-15.6
007	+9.42	+9.42
008	+12.8	+3.08
009	+14.4	+3.48
010	-19.9	-10.1
012	0.0	+2.62

$U_{sim}$  is from the SAR simulated images, and  $U_{SAR}$  is from the actual TOWARD SAR images.

reversal of the longwave direction is observed in both. Third, the increase in the BFP magnitude with increase in magnitude of the angle between the dominant long wave and SAR axes is observed in both. Fourth, the independence of the BFP of vehicle altitude and on range-to-velocity ratio is observed in both. Agreement on these attributes was, at the time of planning of the TOWARD experiment, believed to be a discriminator of SAR ocean wave imaging theories.

The quantitative agreement of these measurements between the actual and simulated images may be less than is desired in some cases. There could be several contributing reasons. It was observed that the TOWARD SAR images produced apparently stable but different estimates of the focus parameter in different regions of the images. This could be indicative of a spatial inhomogeneity of the longwave field. Perhaps related, the longwave directional frequency spectrum measured by SIO and used in the simulation program was averaged over about 3 hours to achieve about 70 degrees of freedom: the SAR gathered its image of any given point in roughly 1 s. Temporal inhomogeneity of the longwave field could then contribute to differences between the measurements on the actual and simulated images. The implementation of the theory in the simulation program necessarily involved approximations and was a fairly large code; some improvements could be made but at the cost of even more computation. The simulations cited here assumed that over the quite narrow wave number band that can affect the SAR image, the short waves are of constant, or "white," spectral density: this approximation is believed to be accurate but could easily be checked. The simulations cited here assumed an 18-m depth (appropriate to the NOSC tower location), but the actual SAR data was in effectively deep water: the difference in phase velocity for this dominant wave is about 10% and could therefore lead to an observable error. Finally, two ensembles of short waves can affect the SAR image: one propagating toward and the other propagating away from the SAR: the major effect in the TOWARD experiment is to produce two displaced images, separated by about 40 m and of unknown relative intensity; some numerical experimentation on such weighting and angle relative to the wind direction could prove interesting.

The comparison between the estimated spectral densities of the actual and simulated SAR images showed that good agreement generally required an ad hoc increase, of about an order of magnitude, in the strength of the hydrodynamic interaction of the long and short waves. While these differences might be attributed to some of the sources of error just listed, it may be, in view of direct surface measurements made heretofore and in the TOWARD experiment, that the two-scale WKB approximation as applied here neglects other observ-

able, nonlinear interactions (such as among the short waves and with intermediate scale waves) and that a more accurate model could have consequences more complicated than those of a simple scalar adjustment.

In summary, these comparisons of actual TOWARD and simulated SAR images, containing remarkably close agreement in some cases, are regarded as supportive of this integrated theoretical model, especially its treatment of the extended scene's temporal behavior, although improvement of the constituent two-scale hydrodynamic model may be necessary. These results were given in preliminary form by Harger [1987] and Harger and Korman [1987].

#### APPENDIX

The two-scale SAR imaging theory derived by Harger [1981, 1986] is recalled. Assume that the undistorted short waves "at mean water" are represented by

$$\xi_0(\mathbf{x}, t) = \text{Re} \frac{1}{4\pi^2} \iint d\mathbf{K} \exp(i\mathbf{x} \cdot \mathbf{K} - i\sigma(\mathbf{K})t) E(\mathbf{K}) \quad (1)$$

a sum of wavelets  $\exp[i\mathbf{x} \cdot \mathbf{K} - i\sigma(\mathbf{K})t]$  with random complex amplitude  $E(\mathbf{K})$ , and that the long wave is, for the moment, the sinusoid

$$h(\mathbf{x}, t) = A_{1w} \cos \varphi(\mathbf{x}, t) \quad (2)$$

where

$$\varphi(\mathbf{x}, t) = \mathbf{K}_{1w} \cdot \mathbf{x} - \sigma(\mathbf{K}_{1w})t \quad (3)$$

$\sigma$  is the gravity wave dispersion relation,  $\mathbf{x}$  is a point in the mean plane of the sea, and  $\mathbf{K}$  is the associated (Fourier) wave number.

According to the two-scale, or WKB, theory [Phillips, 1981a, b], when  $K_{1w} \ll K$ , a short wavelet of wave number  $\mathbf{K}$ , propagating freely on the large wave, will experience, in effect, a current and altered acceleration of gravity varying slowly according to the orbital motion and inclination of the long wave. To first order in the longwave slope  $A_{1w}K_{1w}$ , the wavelet's amplitude and phase vary as  $[1 + A_{1w}K_{1w} \cos \varphi]$  and  $[\varphi + K_x A_{1w} \sin \varphi]$ , respectively, where the coordinate  $x$  is aligned with the longwave direction. The phase thus contains the form  $K_x(x + A_{1w} \sin \varphi)$  which accounts for the "to-and-fro" translation of the wavelet by the orbital motion of the long wave: the  $x$  coordinate of a Lagrangian parcel on the surface of the long wave varies as  $[-A_{1w} \sin \varphi]$ . Assuming that each such wavelet interacts only with the long wave, the (linear) summation (1) of the modified wavelets gives a description of the short waves as they vary over the long wave. (The possibility that this assumption ignores observable nonlinear interactions is discussed here.)

The two scale electromagnetic scattering theory [Bass et al., 1968, 1979; Wright, 1966, 1968; Valenzuela, 1968] gives the reflectivity density (the ratio of scattered to incident scalar fields referred to the mean sea plane) as

$$g_1 = g_0(1 - i\beta\xi) \left[ 1 + \left( \frac{\partial h}{\partial y} \right) \tan \delta_0 \right] \quad (4)$$

for horizontal transmit and receive polarizations, where  $y$  is the ground range coordinate and  $\beta \equiv 2k_0 \cos \delta_0$ ,  $k_0$  is the mean SAR radiated wave number, and  $\delta_0$  is the incidence angle. The received scattered field also has the phase shift  $(2k_0 r - \beta h)$  accounting for the round-trip ray path to the large-scale (longwave) surface;  $r = y \sin \delta_0$  is the slant range

coordinate. At intermediate incidence angles, the phase  $\exp i2k_0 r$  performs a wave number translation that in effect means the "1" in the form  $(1 - i\beta\xi)$  may be ignored and only those wave numbers in  $\xi$  near  $(0, -2k_0 \sin \delta_0)$  can influence the SAR image. Denote the ensemble of influential short-scale wavelets by  $\xi_{(-)}$ ; its wave number bandwidth depends upon the long wave because of the nonlinear multiplication of (4) with  $\exp(-i\beta h)$ .

The SAR system, in effect, scans a scene with a "beam"  $[A(x)F(r)]$ , where the amplitude of  $A$  is determined by the physical antenna pattern and its phase is determined by the Doppler modulation due to relative motion and where  $F$  is determined by the modulation of the SAR system's transmitted pulse. For a stationary scene, this scanning operation is a convolution of this beam with the scene's reflectivity density (as modified by the round-trip ray path). However, for a time-varying scene, as the scanning velocity  $V_{\text{SAR}}$  in azimuth is significantly slow, the time ( $t$ ) dependence of the modified reflectivity density is replaced by  $x/V_{\text{SAR}}$ , destroying the convolution property of the scanning operation; here  $x$  is the azimuth coordinate of the resultant complex data. The processor of the SAR system is assumed here to be linear with impulse response  $A_{\text{pr}}(-x)^* F(-r)^*$ , the conventional matched filter, except  $A_{\text{pr}}(-x)^*$  is necessarily modified when the image is refocused.

Combining these three models, the complex image of a two-scale sea is then given by

$$I(x, r) = I_0 \int dx_1 A_{\text{pr}}[-(x - x_1)]^* \int dx_2 A(x_2 - x_1) \int dr_2 q_F(r - r_2) G(x_2, r_2, x_1) \quad (5a)$$

As there are no significant motion effects on range scanning (range scanning is effected at half the velocity of light) the SAR system range impulse response  $q_F$ , the convolution of  $F(r)$  with  $F^*(-r)$ , appears explicitly. Also,

$$G(x_2, r_2, x_1) = A_G(h) \xi_G(x_2, r_2; x_1) \exp(i2k_0 r_2 - i\beta h) \quad (5b)$$

where  $h$  is expressed in slant range coordinates  $(x, r)$  with  $t$  replaced by  $x_1/V_{\text{SAR}}$  ( $\mathbf{k}$  is a wave number associated with the  $(x, r)$  slant range plane).  $A_G$  contains the amplitude strain and tilt modulations due to nonlinear hydrodynamics and the scattering from the long wave, respectively, to first order in these small effects,

$$A_G(h) = a_0 [1 + f A_{1w} K_{1w} \cos \phi - A_{1w} K_{1w} \sin \theta \sin \phi \tan \delta_0] \quad (5c)$$

where  $\theta$  is the angle between the SAR and longwave directions. The hydrodynamic interaction strength parameter  $f$ , nominally unity, is introduced as a result of comparisons of predictions with actual SAR imagery, as variously discussed. The modified short waves

$$\xi_G(x_2, r_2, x_1) = \xi_{(-)} \left[ \left( \frac{x_2}{r_2 \sin \delta_0} \right) + \left( \frac{K_{1w}}{K_{1w}} \right) A_{1w} \sin \phi, \frac{x_1}{V_{\text{SAR}}} \right] \quad (5d)$$

exhibit the to-and-fro translation due to the orbital motion of the long wave. The phase  $\phi$  is also expressed in  $(x, r)$  coordinates with  $t$  replaced by  $x_1/V_{\text{SAR}}$ ; thus the dispersion relation  $\sigma$  enters normalized by  $V_{\text{SAR}}$ .

To formally generalize (5) for a narrowband longwave ensemble, one may use a spectral representation for  $h$ , similar in form to (1), and modify each appearance of  $h$  in (5) appropriately. To ease the computational load in the simulation, the narrowband property of the long wave's directional frequency spectrum was used to simplify these modifications. Thus, in the phase of (5b),  $h$  explicitly appears, and no functional change is formally required. In the strain term of (5c),  $K_{1w}(A_{1w} \cos \phi)$  is replaced by  $K_{dom}h$ , where  $K_{dom}$  is the magnitude of the wave number of the dominant long wave. The tilt term of (5c) is  $(\partial h/\partial y) \tan \delta_0$ , directly from (4). And the displacement of (5d) may be approximated as  $h_d \approx \nabla h/K_{dom}$ . These approximations were used in the simulations discussed here.

Even though the shortwave ensemble is nonlinearly modified in its interaction with the longwave, the modified ensemble  $\xi_G$  still enters (5) linearly, and therefore the Fourier representation (equation (1)), a sum of (modified) wavelets, remains useful as an analytic decomposition. The image contribution due to each wavelet is then

$$I(x, r; K) = I_0 \int dx_1 A_{pr}[-(x-x_1)]^* \exp\{-i\sigma_v(K)x_1\} \\ \cdot \int dx_2 A(x_1-x_2) \int dr_2 q_F(r-r_2) \\ \cdot A_G(h) \exp\{ik_x[x_2+h_d \cos(\theta)] + ik_r[r_2+h_d \sin(\theta) \\ \cdot \sin(\delta_0)] + i2k_0r_2 - i\beta h\} \quad (6)$$

For such an image contribution, the following result holds: Let the (monochromatic) long wave, of phase velocity  $V_{ph}$ , have direction  $\theta$ ,  $\cos \theta \neq 0$ , relative to the SAR direction and set

$$V_{N\theta} = -\frac{V_{ph}}{V_{SAR}} \frac{1}{\cos \theta}$$

Then a choice of processor impulse response  $A_{pr}$ , with modulus

$$\left| A_{pr}\left(\frac{x}{1-V_{N\theta}}\right) \right| = |A(x)|$$

and quadratic phase with linear FM rate

$$K_{pr} = (1+V_{N\theta})^2 K_{SAR}$$

yields a wavelet image (equation (6)) that is a scaled and translated version of that image when  $V_{SAR}$  is infinite. That is, as there are no motion effects when  $V_{SAR}$  is infinite, the choice of processor impulse response in effect negates the motion effects. Note that perhaps surprisingly, this processor-choice is independent of the wavelet's wave number—that is, all wavelet image contributions are thus, so to speak, rendered stationary. As will be seen, the image contribution's translation does depend on the wavelet's wave number. This result will be established by a series of simple change of variables of integration in the integrals representing the SAR scanning and processing operations.

Noting that  $x_1$  enters the integrand (characterizing the motion of the sea and preventing a convolution evaluation of the  $dx_1$  integral, as carried out implicitly in the  $r_1$ -coordinate) only as the form

$$\mathbf{k}_{1w} \cdot (x_2, r_2) - \sigma_v(K_{1w})x_1$$

a transformation of the "dummy variables of integration" is suggested to "render stationary" this form: replace  $(x_2, r_2)$  by  $(n_2, r_2)$  such that

$$\mathbf{k}_{1w} \cdot (n_2, r_2) = \mathbf{k}_{1w} \cdot (x_2, r_2) - \sigma_v(K_{1w})x_1$$

That is,

$$n_2 = x_2 - [\sigma_v(K_{1w})/k_{1wx}]x_1 \quad k_{1wx} \neq 0$$

and  $r_2$  is unchanged. Note that

$$\sigma_v(K_{1w})/k_{1wx} = [\sigma_v(K_{1w})/K_{1wx}][K_{1w}/k_{1w}] \\ = [V_{ph}/V_{SAR}]/\cos(\theta) = V_{N\theta}$$

where  $V_{ph}$  is the phase velocity of the long wave and  $\theta$  is the long wave's direction in the SAR-oriented coordinates.

With such a transformation, one has the subimage representation

$$I(x, r; \mathbf{K}) = I_0 \int dx_1 A_{pr}[-(x-x_1)]^* \\ \cdot \exp\{i[k_x V_{N\theta} - \sigma_v(K)]x_1\} \\ \cdot \int dn_2 A(x_1-n_2-V_{N\theta}x_1) \\ \cdot \int dr_2 q_F(r-r_2) G_{inf}(n_2, r_2)$$

where  $G_{inf}$  is the transformed reflectivity density

$$G_{inf}(n_2, r_2) = A_G(h_1) \exp\{i[k_x(n_2+h_1 \cos \theta) \\ + k_r(r_2+h_1 \sin \theta \sin \delta_0) + 2k_0r_2 - \beta h_1]\} \quad (7)$$

and where

$$h_1(n_2, r_2) = A_{1w} \cos[\mathbf{K}_{1w} \cdot (n_2, r_2)]$$

Note that  $G_{inf}$  does not depend on  $x_1$  and is in fact the scene's reflectivity density  $G$  when  $V_{SAR}$  is infinite.

The further changes of dummy variables

$$n_1 = (1-V_{N\theta})x_1$$

$$n = (1-V_{N\theta})x$$

lead to the form

$$(1-V_{N\theta})I[n/(1-V_{N\theta}), r; \mathbf{K}] = I_0 \int dn_1 A_{pr}[-(n-n_1)/(1-V_{N\theta})]^* \\ \cdot \exp\{iPn_1\} \int dn_2 A(n_1-n_2) \int dr_2 q_F(r-r_2) G_{inf}(n_2, r_2) \quad (8)$$

where

$$P = [V_{N\theta}k_x - \sigma_v(K)]/(1-V_{N\theta}) \quad (9)$$

It remains to choose the SAR processor impulse response and interpret its multiplying phase factor. Suppose  $A_{pr}$  is chosen so that

$$|A_{pr}[n/(1-V_{N\theta})]| = |A(n)|$$

and its phase is a linear FM with rate

$$K_{pr} = (1-V_{N\theta})^2 K_{SAR}$$

$K_{SAR}$  being the linear FM rate of  $A$ . Note that these choices do not depend upon the wavelet's wave number  $\mathbf{K}$ . Then (8)

becomes

$$(1 - V_{N0})I[n/(1 - V_{N0}), r; \mathbf{K}] = I_0 \int dn_1 A[-n - n_1]^* \cdot \exp\{iPn_1\} \int dn_2 A(n_1 - n_2) \int dr_2 q_f(r - r_2) * G_{inf}(n_2, r_2) \quad (10)$$

Note that no approximations have been made to this point, given (6).

The right-hand side of (10) is the conventionally processed SAR image of a stationary scene, characterized by the reflectivity density  $G_{inf}(n_2, r_2; \mathbf{K})$ , except that the scanned SAR data (or if we choose, the processing filter) is "on a carrier" of wave number  $P$ . It is well known that this results in an image shift, or translation, of amount  $n_d = P/K_{SAR}$ ; the image is otherwise undistorted, to a good approximation, when this translation is small in relation to the support of  $A$ , that is, the azimuth extent of the SAR antenna's "footprint" on the mean sea. Omitting these well-known details (see, for example, Harger [1970]) here, to a good approximation,

$$(1 - V_{N0})I[(n - n_d)/(1 - V_{N0}), r; \mathbf{K}] = \exp\{iPn\}I_0 \int dn_2 q_A(n - n_2) * \int dr_2 q_f(r - r_2) G_{inf}(n_2, r_2) \quad (11)$$

The  $n_1$  integration has been implicitly carried out in (11);  $q_A(n)$ , the convolution of  $A(x)$  with  $A(-x)^*$ , is the SAR system's impulse response in the along-track direction. The magnitude-squared of the right-hand side of (11) has the form of the image intensity of the conventional SAR image of a scene with reflectivity density  $G_{inf}$ , which is the reflectivity density of the temporally varying scene scanned with infinite  $V_{SAR}$ .

Thus the assertion is established. Note that as the wavelets are uncorrelated in the representation in (1), the phase  $\exp iPn$  in (11) does not affect, for example, the average intensity of the refocused image.

It remains of interest to further analyze the nature of the image defined by (11). The nature of  $G_{inf}$ , given by (7), suggests an approximation by the method of stationary phase. Omitting the details of this calculation, it results that, when  $\rho_{SAR} K_{iw} (A_{iw} \beta)^{1/2} \gg 1$ , the SAR image is well approximated by pairs of SAR impulse responses, of resolution  $\rho_{SAR}$ , one associated with the crest of the long wave and the other with the trough, each degraded by a quadratic phase error, translated, and repeated at the period of the long wave. The phase error and the translation are of opposite sign for each member of the pair; again, the phase error is independent of, and the translation dependent on, the wavelet's wave number.

Thus it can happen that the phase error and translation due to the longwave motion can be reduced at the crests and increased at the troughs of the long wave. The focus correlation for the combined phase error is, in TOWARD, little altered from that due to motion alone. Given such a focus correction, the translations of the wavelets' image artifacts associated with the longwave crests will all be equal provided

$$A_{iw} K_{iw} \sigma(K_{iw}) H / V_{SAR} = 1 \quad (12)$$

where  $H$  is the SAR vehicle's altitude.

Relation (12) explains why the artifacts of only long waves with a restricted set of parameters seem to be visible to a specific SAR system [Beal et al., 1983].

**Acknowledgments.** The complex high-resolution SAR imagery gathered by the JPL L band SAR was provided by Dan Held and Howard Zebker of JPL; the distribution was effected by the Environmental Research Institute of Michigan under the direction of David Lyzenga. The longwave directional frequency spectrum was measured and provided by Robert Guza of SIO. Lower-resolution TOWARD SAR imagery in a format especially convenient for initial orientation was provided by Edmund Tajirian of Ocean Research and Engineering, under the direction of Omar Shemdin, the TOWARD experiment leader whose general guidance has been very helpful. This research was supported by the Office of Naval Research.

#### REFERENCES

- Alpers, W. R., D. B. Ross, and C. L. Rufenach, On the detectability of ocean surface waves by real and synthetic aperture radar, *J. Geophys. Res.*, **86**, 6481-6498, 1981.
- Bass, F. G., and I. M. Fuks, *Wave Scattering From Statistically Rough Surfaces*, Pergamon, Elmsford, New York, 1979.
- Bass, F. G., I. M. Fuks, A. I. Kalmykov, I. E. Ostrovsky, and A. D. Rosenberg, Very high frequency radio wave scattering by a disturbed sea surface, *IEEE Trans. Antennas Propag.*, **AP-16**, 554-568, 1968.
- Beal, R. C., D. G. Tilley, and F. M. Monaldo, "Large- and small-scale spatial evolution of digitally processed ocean wave spectra from Seasat synthetic aperture radar, *J. Geophys. Res.*, **88**, 1761-1778, 1983.
- Freeman, N. G., P. W. Vachon, and C. E. Livingstone, Airborne SAR imaging of azimuthally traveling ocean surface waves: The LEWEX experiment, in *International Geoscience and Remote Sensing Symposium Digest*, vol. 2, 1393-1398, IEEE, New York, 1987.
- Harger, R. O., *Synthetic Aperture Radar Systems*, Academic, San Diego, Calif., 1970.
- Harger, R. O., The side-looking radar image of time-variant scenes, *Radio Sci.*, **15**, 749-756, 1980.
- Harger, R. O., SAR ocean imaging mechanics, in *Spaceborne Synthetic Aperture Radar for Oceanography*, edited by R. C. Beal, P. S. DeLeonibus, and I. Katz, pp. 41-52, Johns Hopkins University Press, Baltimore, Md., 1981.
- Harger, R. O., The SAR image of short gravity waves on a long gravity wave, in *Wave Dynamics and Radio Probing of the Ocean Surface*, edited by O. M. Phillips and K. Hasselmann, pp. 371-392, Plenum, New York, 1986.
- Harger, R. O., Simulated vs. actual SAR images: Focus and spectrum estimates, in *International Geoscience and Remote Sensing Symposium Digest*, vol. 2, pp. 1571-1574, IEEE, New York, 1987.
- Harger, R. O., and C. E. Korman, A comparison of simulated and actual SAR images, paper presented at the URSI Radio Science Meeting, Int. Union of Radio Sci., Blacksburg, Va., 1987.
- Jain, A., and O. H. Shemdin, L-band SAR ocean wave observations during MARSEN, *J. Geophys. Res.*, **88**, 9792-9808, 1983.
- Leotta, D. F. and F.-K. Li, Focussing studies of SAR ocean wave images collected during the TOWARD experiment, Digest of IGARSS '87, Vol. 2, p. 1389 (abstract), in *International Geoscience and Remote Sensing Symposium-Digest*, vol. 2, p. 1389, IEEE, New York, 1987.
- Li, F.-K., D. N. Held, J. C. Curlander, and C. Wu, Doppler parameter estimation for spaceborne synthetic-aperture radars, *IEEE Trans. Geosci. Remote Sens.*, **GE-23**, 47-56, 1985.
- Longuet-Higgins, M., A stochastic model of sea-surface roughness, I, Wave crests, *Proc. R. Soc. London, Ser. A*, **410**, 19-34, 1987.
- Phillips, O. M., The structure of short gravity waves on the ocean surface, in *Spaceborne Synthetic Aperture Radar for Oceanography*, edited by R. C. Beal, P. S. DeLeonibus, and I. Katz, pp. 24-31, Johns Hopkins University Press, Baltimore, Md., 1981a.
- Phillips, O. M., The dispersion of short wavelets in the presence of a dominant long wave, *J. Fluid Mech.*, **107**, 465-485, 1981b.
- Shuchman, R. A., and O. M. Shemdin, Synthetic aperture radar imaging of ocean waves during the Marineland experiment, *IEEE J. Oceanic Eng.*, **OE-8**, 83-90, 1983.
- Shuchman, R. A., and J. S. Zelenka, Processing of ocean wave data from a synthetic aperture radar, *Boundary Layer Meteorol.*, **13**, 181-192, 1978.
- Tang, S., and O. H. Shemdin, Measurement of high-frequency waves using a wave follower, *J. Geophys. Res.*, **88**, 9830-9840, 1983.

Valenzuela, G. R., Scattering of electromagnetic waves from a tilted, slightly rough surface, *Radio Sci.*, 3, 1057-1066, 1968.

Wright, J. W., Backscattering from capillary waves with application to sea clutter, *IEEE Trans. Antennas Propag.*, AP-14, 749-754, 1966.

Wright, J. W., A new model for sea clutter, *IEEE Trans. Antennas Propag.*, AP-16, 217-223, 1968.

---

R. O. Harger and C. E. Korman, Electrical Engineering Department, University of Maryland, College Park, MD 20742.

(Received October 5, 1987;  
accepted January 4, 1988.)

# Comparison of Measured and Predicted Sea Surface Spectra of Short Waves

O. H. SHEMDIN<sup>1</sup>

*Jet Propulsion Laboratory, Pasadena, California*

P. A. HWANG

*Ocean Research and Engineering, Pasadena, California*

Reliable sea surface slope time series, using a laser-optical receiver system deployed on a wave follower, are analyzed to yield slope frequency spectra of the ocean surface up to 300 Hz. The results show significant differences when compared with the Pierson and Stacy (1973) model. An empirical model is proposed in this paper that is consistent with the observed slope spectra. The newly proposed model is compared with other more recently advanced shortwave spectral models.

## 1. INTRODUCTION

Considerable interest in short surface waves has evolved in recent years with the advent of microwave remote sensing techniques. Previous emphasis has been on long ocean wave measurements with frequencies of less than 0.3 Hz, and corresponding wavelengths greater than 15 m. Present interest in shortwave measurements extends in frequencies to 300 Hz and in wavelengths down to 0.2 cm.

Early interest in wave spectral properties focused on the forward face of the spectrum denoted by the "equilibrium range." Phillips [1958] suggested, on the basis of dimensional arguments, that the form of the spectrum is  $f^{-5}$ , where  $f$  is frequency. The equivalent wave number form corresponds to  $k^{-4}$ , where  $k$  is wave number. The equilibrium range, in the form proposed by Phillips [1958], is independent of wind speed. The above spectral forms have been incorporated in such wave prediction models as the Joint North Sea Wave Project (JONSWAP) model (see Hasselmann *et al.* [1973], Pierson *et al.* [1966], Barnett [1968], and Ewing [1971], among others).

The concept of the equilibrium range, as proposed by Phillips [1958], has been questioned by a number of investigators on the basis of experimental evidence and theoretical arguments [see Phillips, 1985]. The dependence of the high-frequency region of the spectrum on wind speed was shown by Shemdin *et al.* [1972]; it was further corroborated by Mitsuyasu and Honda [1974], Mitsuyasu [1977], Leonart and Blackmann [1980], Tang and Shemdin [1983], Leykin and Rozenberg [1983], and Atakturk and Katsaros [1987]. Alternative forms of the equilibrium range have been advanced that are primarily valid in the region  $f < 0.3$  Hz. These spectra exhibit power law forms  $f^{-4}$  or  $k^{-3.5}$  and a dependence on wind speed. Among those subscribing to these characteristics are Kitaigorodskii [1983], Phillips [1985], and Donelan *et al.* [1985], among others.

The determination of the spectral shape of short waves in the range  $0.3 < f < 300$  Hz or  $0.2 \text{ cm} < \lambda < 15$  m, where  $\lambda$  is wavelength, has become a subject of interest in order to un-

derstand radar backscatter processes. The spectral form given by Pierson and Stacy [1973] is based on a mix of data sets obtained in the laboratory and in the field. The data sets on short waves were obtained by investigators using capacitance wave gauges [Sutherland, 1968] which are now known to be limited in frequency response ( $< 10$  Hz) and by optical sensors [Cox, 1958] which are known to have high-frequency response. The model has been used extensively in many applications and, in the absence of detailed verification, has produced reasonable results.

The present paper focuses on analysis of slope time series obtained with a laser-slope sensor deployed from a wave follower. Two data sets, obtained in the Marine Remote Sensing Experiment in the Tower Ocean (MARSEN) and in Wave and Radar Dependence Experiment (TOWARD), are analyzed at various wind speeds  $u$ . The results obtained provide a basis against which the Pierson and Stacy [1973] model is evaluated. The experimental results are used to produce an empirical model that is consistent with the TOWARD and MARSEN observations. The proposed model is compared with those suggested by other investigators, such as that proposed by Donelan and Pierson [1987].

## 2. EXPERIMENTAL SETUP AND DATA ANALYSIS PROCEDURE

The surface slope measurements were obtained using a laser-optical sensor [see Tober *et al.*, 1973] mounted on a wave-following C frame. The wave follower structural system is shown in Figure 1, and the C frame is shown in Figure 2 [see Hwang and Shemdin, this issue]. The results of sensor calibration are given by Hwang and Shemdin [this issue]. The sensor measures surface slopes in the range  $0^\circ$ - $30^\circ$ , with an accuracy of 0.5 and/or 13% of the surface slope, whichever is smaller. More than 100 hours of slope data were acquired at various wind speeds and swell conditions. Of these, approximately 20 hours of data were selected for detailed analysis.

In this paper the slope spectra are computed using 15-min time series following two procedures. The first procedure is to compute a spectrum from each 1-s time series and then average over 900 such spectra to achieve high statistical reliability. The second is to compute one spectrum from each 64-s time series in a 15-min record and then average 14 independently determined spectra to achieve high frequency resolution. A combination of these two procedures is used to present

<sup>1</sup>Now at Ocean Research and Engineering, Pasadena, California.

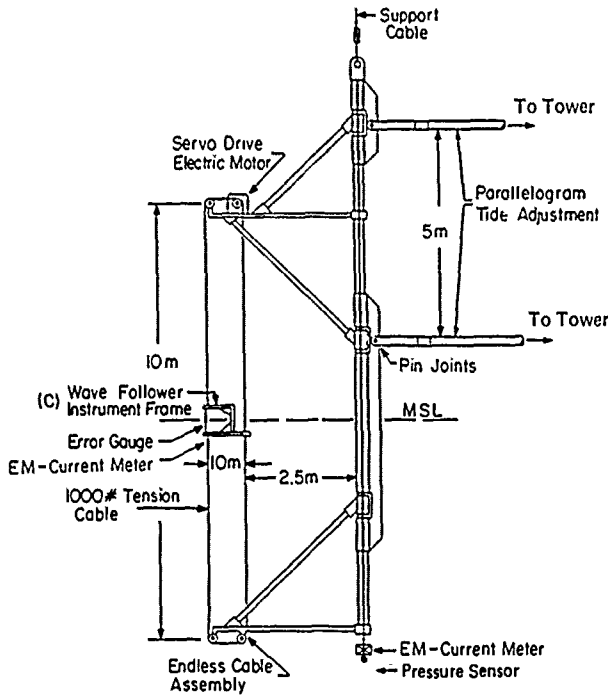


Fig. 1. Wave follower structural assembly.

the experimental results. Typical such spectra at  $u_* = 6$  and 21 cm/s are shown in Figure 3. The slope spectra are presented in terms of frequency times the slope spectrum versus frequency. An amplitude spectrum that has  $f^{-5}$  shape in the gravity range would show as a flat distribution (parallel to the frequency axis) in Figure 3.

The spectra shown in Figure 3 suggest that in the vicinity of  $f = 1.0$  Hz the wave height spectrum with form  $f^{-n}$  corresponds to  $n = 5$ . At lower frequencies it is shown that  $n < 5$ , and at higher frequencies there are regions where  $n > 5$ . A comparison between the measured spectra, shown in Figure 3, and predicted spectra based on the *Pierson and Stacy* [1973] model is shown in Figure 4. Differences are observed between the model (hereinafter referred to as the P-S model) and the

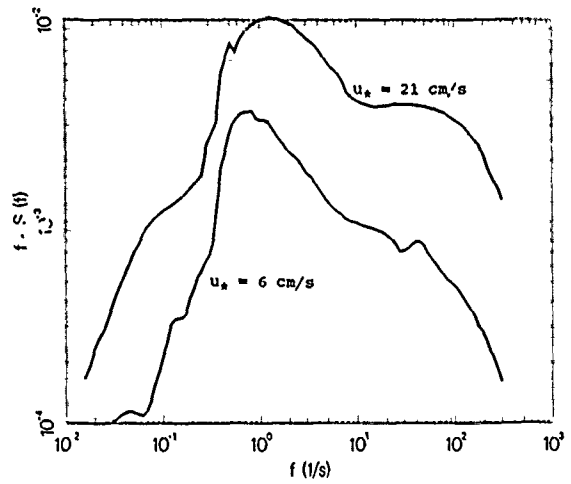


Fig. 3. Measured slope spectra at  $u_* = 6$  and 21 cm/s.

TOWARD measurements. These include (1) A region  $0.2 < f < 2.0$  Hz where the P-S model shows no wind speed dependence whereas the measured spectra do and (2) A region  $2.0 < f < 20.0$  Hz where the P-S model predicts higher spectral values than the measurements.

*Donelan and Pierson* [1987] have recently proposed a wave spectral model utilizing radar backscatter measurements. This model is hereinafter referred to as the D-P model. The D-P model is specified as a directional wave number spectrum in terms of environmental parameters such as wind speed and sea surface temperature. Comparison with the TOWARD measurements requires either conversion of the D-P model to the frequency domain or conversion of the TOWARD data to the wave number domain. The latter requires assumptions on the directional distribution of waves in addition to local measurement of the current field. To minimize the need for assumptions and to make the comparison more valid, it was decided to convert the D-P spectral model to the frequency domain for comparison with the TOWARD frequency spectra. This was achieved by using the locally measured current field and adopting the transformation equations given by *Hughes* [1978]. The Doppler influence of the orbital current

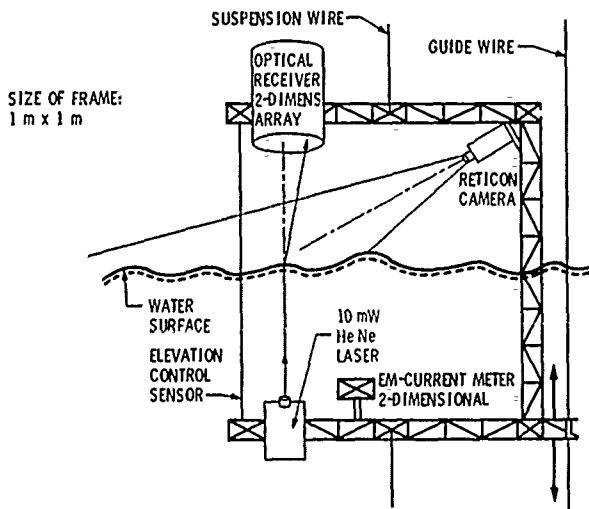


Fig. 2. C frame structural assembly.

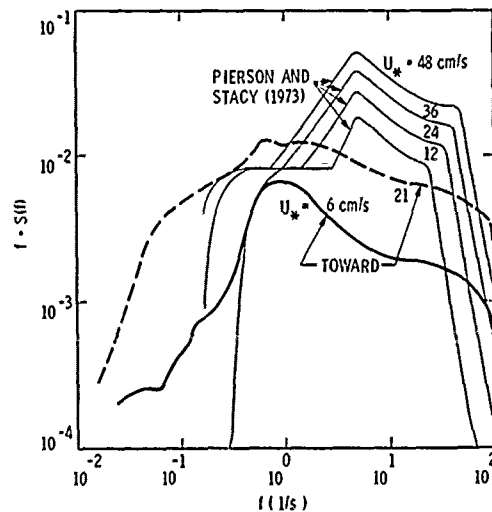


Fig. 4. Comparison of measured slope spectra with predictions of *Pierson and Stacy* [1973].

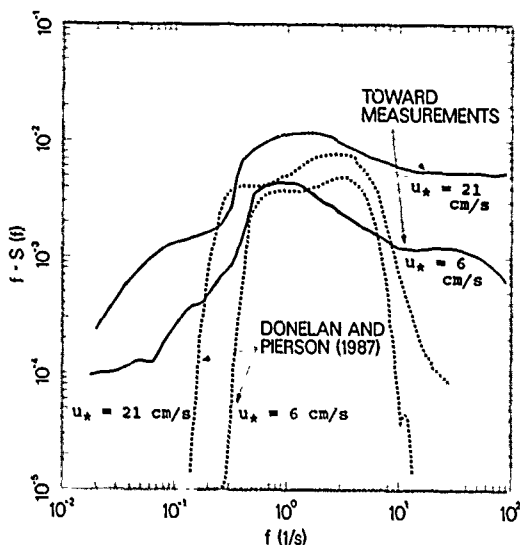


Fig. 5. Comparison of measured spectra with predictions of Donelan and Pierson [1987].

associated with long waves on the intrinsic frequency of short waves has been addressed by Evans and Shemdin [1980] and more recently by Atakturk and Katsaros [1987]. The wave number spectra and associated directional distributions specified in the D-P model were converted into frequency wave height spectra for the wind speeds, water temperatures, and current fields measured in TOWARD. A slope frequency spectrum is obtained by multiplying the wave height-frequency spectrum by  $k^2$ , where  $k$  is the wave number. The converted D-P model is shown in Figure 5 for two wind speeds,  $u_* = 6$  cm/s and 21 cm/s. The orbital velocity of long waves and the ambient current have the effect of broadening the bandwidth of the intrinsic frequency spectrum. Without the Doppler effect due to current, the D-P converted frequency spectra would have narrower bandwidths compared with those shown in Figure 5.

The frequency spectra derived from the TOWARD measurements are also shown in Figure 5 for  $u_* = 6$  cm/s and 21 cm/s. Substantial differences are observed between the model and measurements in the region  $f < 0.5$  Hz and  $f > 8$  Hz. An order of magnitude agreement is observed in the region  $0.5 < f < 8$  Hz.

3. DELINEATION OF WAVE HEIGHT SPECTRAL DOMAINS

Since the introduction of the equilibrium range by Phillips [1958], other dynamical influences on the high-frequency slope of the wave height spectrum have been considered. The influence of surface drift on wave breaking and hence on the high-frequency face of the spectrum has been examined. The influence of surface drift is found to be important in a domain that corresponds to  $2\pi f \sim 2g/u_*$ , where  $g$  is gravitational acceleration and  $u_*$  is wind shear velocity [see Phillips, 1977]. Both Kitaigorodskii [1983] and Phillips [1985] have concluded recently, on the basis of theoretical arguments, that the forward face of the spectrum can have  $f^{-4}$  distribution in certain frequency bands and  $f^{-5}$  distribution in others. Building on the above arguments, it is postulated here that five spectral domains in the forward face of the wave height spectrum may be specified as follows (see Figure 6).

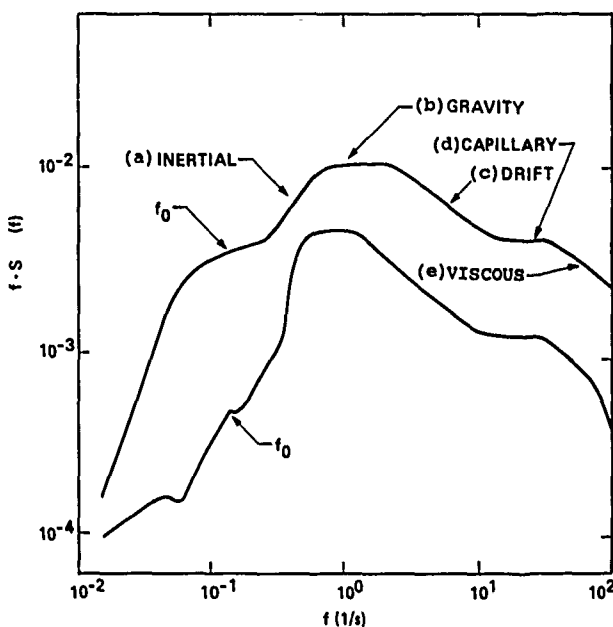


Fig. 6. Delineation of five wave spectral regions ( $f_0$  is the frequency corresponding to peak energy in the wave height spectrum).

1. The inertial range (domain-a in Figure 6) is given by

$$\phi(\sigma) = \alpha u_* g \sigma^{-4} \quad \sigma_0 < \sigma < \sigma_g \quad (1)$$

where  $\phi$  is wave height spectrum,  $\sigma = 2\pi f$ ,  $\sigma_0$  is the frequency corresponding to peak energy in the wave height spectrum,  $\alpha$  is a dimensionless spectral constant, and  $\sigma_g$  is the frequency bound that separates the inertial range from the gravity range, shown in normalized form as  $\tilde{\sigma}_1 = \sigma_g u_* / g$  in Figure 7.

2. The gravity range (b in Figure 6) is given by

$$\phi(\sigma) = \beta g^2 \sigma^{-5} \quad \sigma_g < \sigma < \sigma_d \quad (2)$$

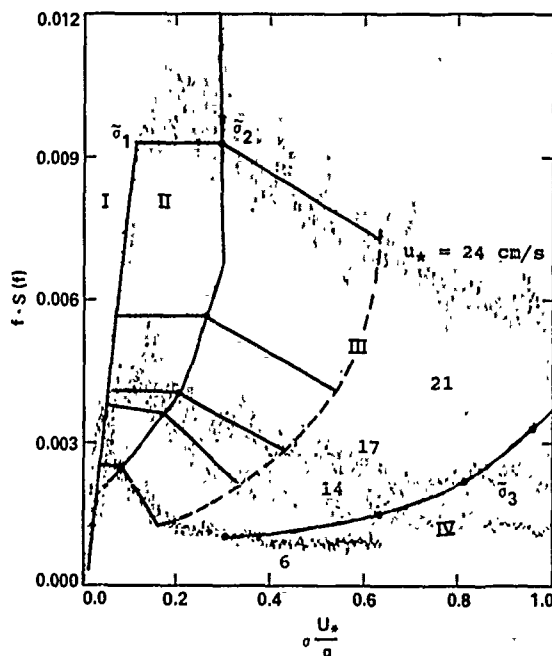


Fig. 7. Dimensionless graph of four spectral regions. Regions I-IV correspond to the inertial, gravity, drift, and capillary domains, respectively. The boundaries  $\tilde{\sigma}_1$ ,  $\tilde{\sigma}_d$  are specified in the text

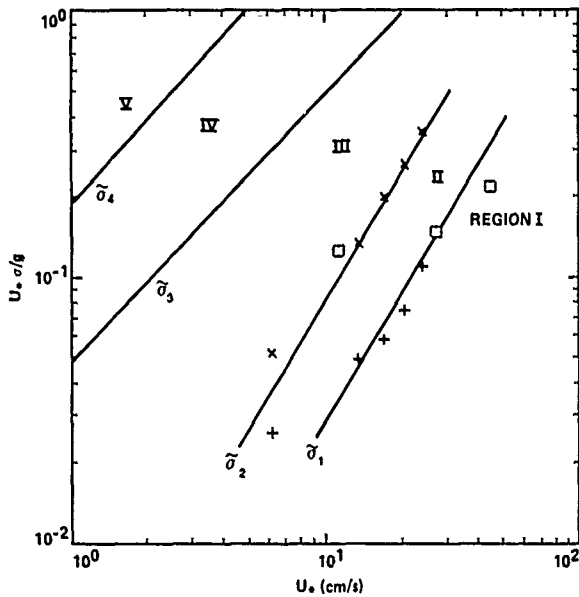


Fig 8 Graphical description of the frequency bounds of regions I-V.

where  $\beta$  is a dimensionless spectral constant defined for this range and  $\sigma_d = 2g/u_*$  is the frequency that separates the gravity range from the surface drift range, shown in normalized form as  $\bar{\sigma}_2$  in Figure 7.

3. The surface drift range (c in Figure 6) is given by

$$\phi(\sigma) = f_1\left(\frac{\sigma u_*}{g}\right) g^2 \sigma^{-5} \quad \sigma_d < \sigma < \sigma_c \quad (3)$$

where  $f_1(\sigma u_*/g)$  is a function, whose form is yet to be defined, that specifies the influence of surface drift in the high-frequency slope of the wave height spectrum, and  $\sigma_c$  is the frequency that separates the surface drift range from the capillary range, shown in normalized form as  $\bar{\sigma}_3$  in Figure 7.

4. The capillary range (d in Figure 6) is given by

$$\phi(\sigma) = f_2\left(\frac{u_* v}{\gamma}\right) \gamma^{2/3} \sigma^{-7/3} \quad \sigma_c < \sigma < \sigma_v \quad (4)$$

where  $f_2$  is a function, whose form was defined by *Leonart and Blackmann* [1980], that determines the influence of wind speed, surface-tension, and viscosity in this range,  $\gamma = T/\rho$ ,  $T$  is surface tension,  $\rho$  is water-density,  $v$  is kinematic viscosity and  $\sigma_v$  is the frequency bound that separates the capillary range from the viscous range, shown in normalized form as  $\bar{\sigma}_4$  in Figure 7.

5. The final spectral range is the viscous range, whose functional form is not well understood because of the overwhelming influence of ambient current (e.g., surface drift) and orbital velocities of the long waves, as was shown by *Leonart and Blackmann* [1980]. Further measurements of the short wave number spectra in this domain are required to properly characterize this region.

In examining the measured slope spectra in TOWARD, shown in Figure 6, it is possible to discern the above five ranges. Specifying the above wave height spectra in terms of wave slope spectra,  $S(\sigma)$ , where  $S(\sigma) = k^2 \phi(\sigma)$ ,  $k$  is wave number, the corresponding spectral forms for the wave slope spectra become

Inertial range

$$S(\sigma) = \alpha g^{-1} u_* \quad \sigma_0 < \sigma < \sigma_g \quad (5)$$

Gravity range

$$S(\sigma) = \beta \sigma^{-1} \quad \sigma_g < \sigma < \sigma_d \quad (6)$$

Surface drift range

$$S(\sigma) = f_1\left(\frac{\sigma u_*}{g}\right) \sigma^{-1} \quad \sigma_d < \sigma < \sigma_c \quad (7)$$

Capillary range

$$S(\sigma) = f_2\left(\frac{u_* v}{\gamma}\right) \sigma^{-1} \quad \sigma_c < \sigma < \sigma_v \quad (8)$$

Viscous range

$$S(\sigma) = \text{unspecified} \quad (9)$$

In equating the above ranges with those shown in Figure 6 (noting that the vertical axis in this figure is frequency times the slope spectrum) it is seen that the spectrum is wind speed dependent in all five ranges. In the inertial range this dependence is indicated in (5). For (6) to be valid, the constant  $\beta$  must assume a functional form that is wind speed dependent. Equation (7) correctly suggests that  $f_1$  is wind-speed dependent. This holds true for (8), suggesting that  $f_2$  is wind speed dependent.

#### 4. AN EMPIRICAL SHORTWAVE SPECTRAL MODEL BASED ON TOWARD AND MARSEN DATA SETS

Past investigations by *Mitsuyasu* [1977], *Forristal* [1981], *Kahama* [1981], and *Kitaigorodskii* [1983] have all shown that in the spectral region up to  $3\sigma_0$  the wave height spectrum shows dependence on wind speed. Furthermore, spectra measured at different wind speeds cluster together in this range when the frequency axis is normalized with respect to  $(u_*/g)$  [see *Geernaert et al.*, this issue]. When the slope spectra obtained in TOWARD are normalized in this manner, as shown in Figure 7, they also cluster together in this range (denoted by region-I in Figure 7). The TOWARD spectra in Figure 7 demonstrate the high-frequency response of the laser-optical sensor. Whereas reliable spectra are achieved with conventional sensors only in region I, where  $\sigma u_*/g = 0.1$ , the TOWARD data give reliable spectra that go beyond  $\sigma u_*/g = 1.0$ . From the data set shown in Figure 7 it is possible to delineate four regions (I-IV) which correspond to the first four ranges discussed previously. In Figure 7,  $\bar{\sigma} = \sigma u_*/g$ ; the lines denoted by  $\bar{\sigma}_1$ ,  $\bar{\sigma}_2$ ,  $\bar{\sigma}_3$ , and  $\bar{\sigma}_4$  specify the border frequencies  $\sigma_g$ ,  $\sigma_d$ ,  $\sigma_c$ , and  $\sigma_v$ , respectively. The border frequencies  $\bar{\sigma}_1$ - $\bar{\sigma}_4$  are plotted in Figure 8 as functions of  $u_*$ . Figure 8 graphically defines the five regions I-V.

The spectra in region I are uniquely defined by normalization with respect to  $u_*/g$  and specification of  $\alpha$  in (5). Here,  $\alpha$  is found to be

$$\alpha = (7.2 \pm 1) \times 10^{-2} \quad (10)$$

The boundary frequency  $\bar{\sigma}_1$  is specified as (in centimeters per second)

$$\bar{\sigma}_1 = 9.17 \times 10^{-4} u_*^{3/2} \quad (11)$$

In region II the slope spectra multiplied by frequency are all parallel to the frequency axis. The spectral level is wind speed dependent, as is shown in Figure 9. The latter, in conjunction with  $\bar{\sigma}_1$  and  $\bar{\sigma}_2$ , define region II. Here, the empirical values for  $\bar{\sigma}_2$  and the slope spectrum are, respectively,

$$\bar{\sigma}_2 = 2.9 \times 10^{-3} u_*^{3/2} \tag{12}$$

$$fS(f) = \sigma S(\sigma) = 7.0 \times 10^{-5} u_*^{3/2} \tag{13}$$

The MARSEN data set, shown in Figure 9, indicates a tendency toward saturation at the high wind speeds encountered ( $u_* > 50$  cm/s). Hence a saturation level is adopted empirically in this region.

In region III the upper bounding frequency  $\bar{\sigma}_3$  is defined as

$$f_c = 7.5 \text{ Hz}$$

or

$$\sigma_c = 47.1 \text{ rad/s}$$

which corresponds to

$$\bar{\sigma}_3 = \sigma_c \frac{u_*}{g} = 4.8 \times 10^{-2} u_* \tag{14}$$

In Figure 7 the slopes of the  $fS(f)$  spectra in region III are found to be wind speed dependent. When the spectra are normalized with respect to the levels in region II and the frequencies are normalized with respect to  $\bar{\sigma}_2$ , the slope dependence on  $u_*$  is shown in Figure 10a for the TOWARD data set and in Figure 10b for the MARSEN data set. The empirical relationships of the slopes with respect to wind speed are shown in Figure 11 for the above two data sets. Here, the TOWARD data set exhibits a different variation compared to the MARSEN data set. The empirical relationships are

$$\frac{\sigma_2 S(\sigma)}{\sigma S(\sigma_2)} = \frac{fS(f)}{f_2 S(f_2)} = \left(\frac{f}{f_2}\right)^y \tag{15}$$

where

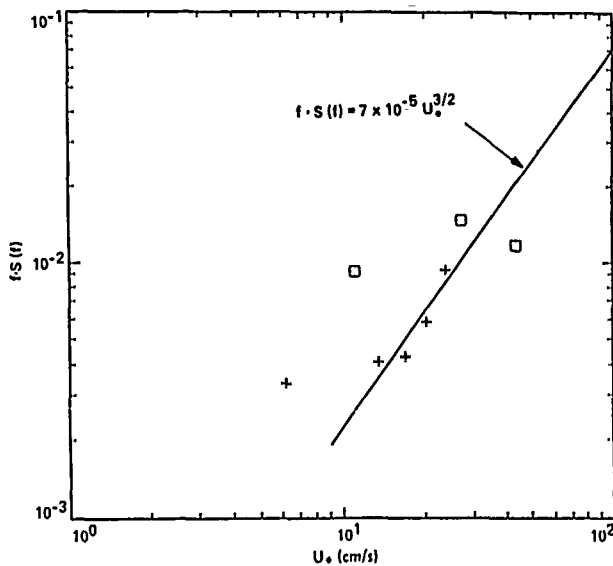


Fig. 9. Peak spectral values in region II—versus  $u_*$ . Pluses denote TOWARD data; squares, MARSEN data.

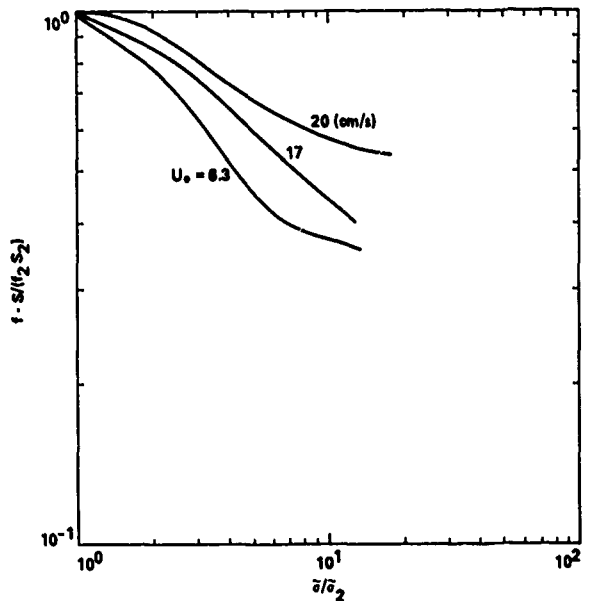


Fig. 10a

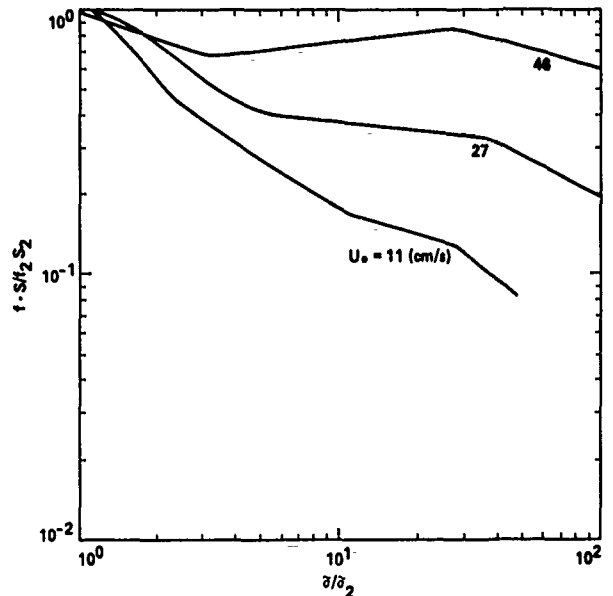


Fig. 10b

Fig. 10. Slopes of region III for (a) TOWARD and (b) MARSEN.

$$y = \log \left( \frac{u_*}{u_{*c}} \right)^B \tag{16}$$

The constants  $u_{*c}$  and  $B$  for the TOWARD and MARSEN data sets are as follows:

	TOWARD	MARSEN
$u_{*c}$	158	57.9
$B$	0.5	1.18

In region IV the boundary frequency  $\sigma_4$  is specified by  $f_c = 30$  Hz, which yields

$$\sigma_4 = 19.2 \times 10^{-2} u_* \tag{17}$$

The spectral level in region IV is selected on the basis of the value of  $fS(f) = \sigma S(\sigma)$  at  $f = 7.5$  Hz. The slope of  $fS(f)$  is flat, i.e., parallel to the frequency axis in this region.

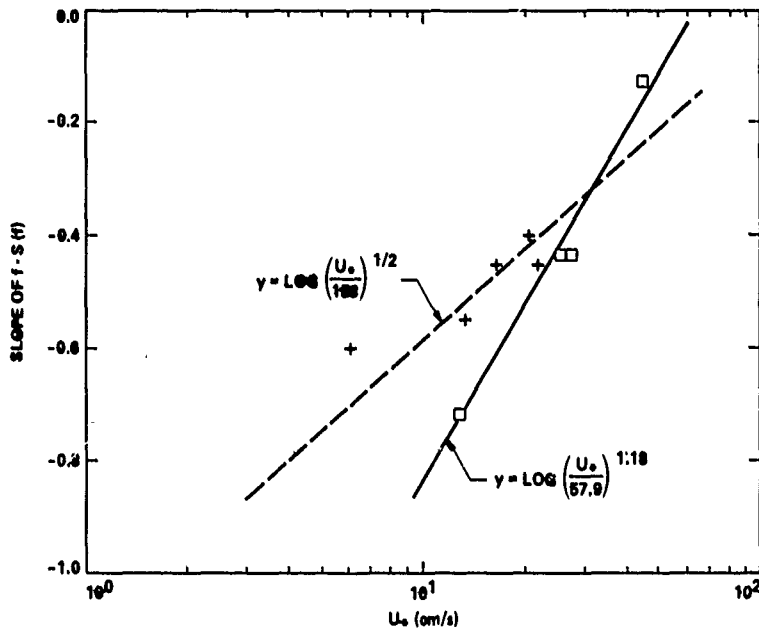


Fig. 11. Slopes of spectra in region III versus  $u_*$ . Pluses denote TOWARD data; squares, MARSEN data.

As can be observed in Figure 3, region V occupies the domain  $f > 80$  Hz. Here, the influences of viscous dissipation and ambient current are dominant [see *Leonart and Blackmann, 1980*]. The slope of the  $fS(f)$  spectrum in this region ( $100 < f < 300$ ) is determined from the TOWARD measurements to be  $-1$ . This corresponds to a wave slope spectrum of  $-2$  and a wave height spectrum of  $-3.33$ . The available measurements from TOWARD do not allow a complete determination of the functional form relevant to this region. Hence it is left unspecified in the empirical model proposed here until additional data become available.

The model proposed in this paper is presented graphically in Figure 12. A comparison with the TOWARD data is shown in Figure 13 for two different wind speeds. The model ap-

proximates the data rather well in the region where  $f > 0.5$  Hz. In this domain, only the TOWARD and MARSEN data sets provide measurements that are free of sensor response limitations. In the frequency domain  $f < 0.5$  Hz, an abundance of measurements collected by numerous investigators have been utilized to specify the model proposed. In Figure 13 the model deviates from the TOWARD data in this region because the model in this domain is shaped by the extensive data sets available in the literature.

5. MODEL COMPARISONS

A comparison between the model developed in this paper and that given by *Pierson and Stacy [1973]* is shown in Figure 14. As expected, the two models differ in the region  $0.2 < f < 2.0$  Hz in their dependencies on wind speed. The model proposed here does exhibit the observed wind speed dependence, whereas the P-S model does not. The two models

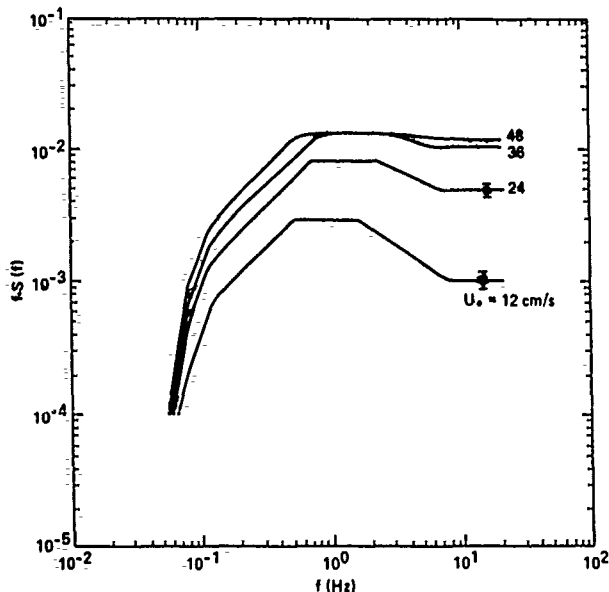


Fig. 12. Predicted spectra of the model at  $u_* = 12, 24, 36,$  and  $48$  cm/s.

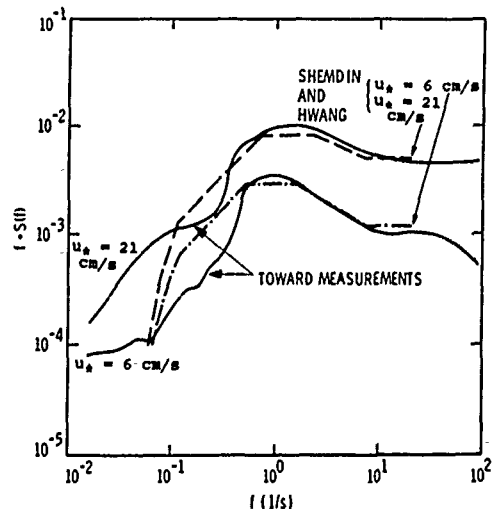


Fig. 13. Comparison of the proposed model with TOWARD data.

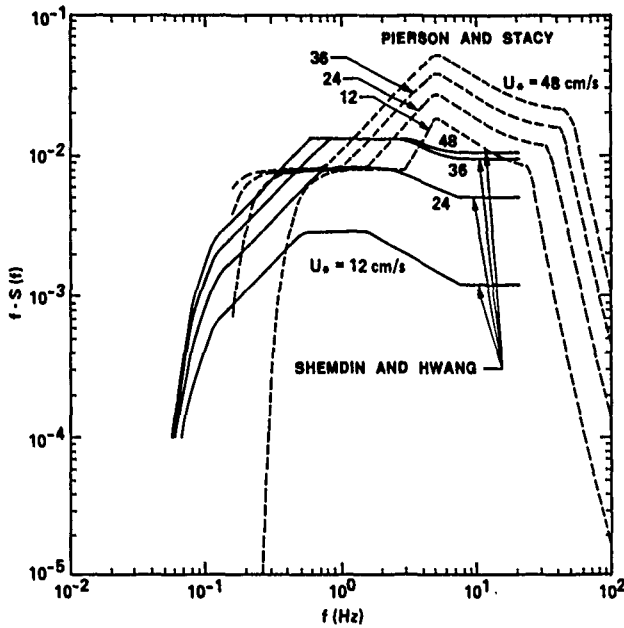


Fig. 14. Comparison of the proposed model with the Pierson and Stacy [1973] model.

also differ in the range  $2.0 < f < 20.0$  Hz, where the P-S model predicts significantly higher spectral levels compared with the model proposed here.

Finally, the model proposed by Donelan and Pierson [1987] is compared with the model developed here in Figure 15. These two models also show substantial differences, although both exhibit the wind speed dependence in the region  $0.2 < f < 2.0$  Hz. The D-P model, however, shows a sharp spectral cutoff at frequencies  $f > 8.0$  Hz. The latter is not substantiated by the TOWARD and MARSEN observations. At the lower frequencies (proximity of  $f = 0.1$  Hz) the D-P model also deviates from the model proposed here.

6. SUMMARY AND CONCLUSIONS

An empirical frequency-spectral model is developed using the TOWARD and MARSEN wave slope observations. The

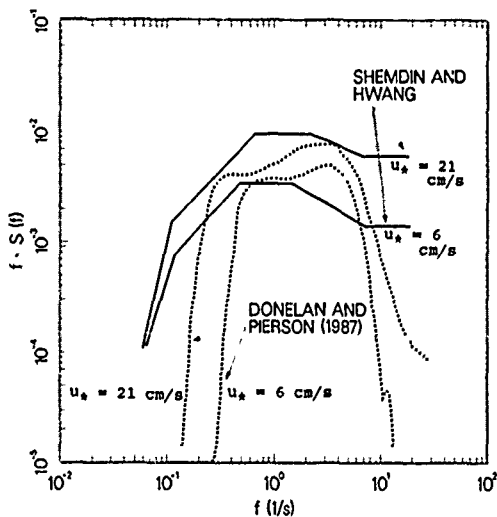


Fig. 15. Comparison of the proposed model with the Donelan and Pierson [1987] model.

same laser-optical sensor used in MARSEN was used in TOWARD and was deployed from the same wave follower. The frequency response of this sensor allows accurate measurement of the sea surface slope to 300 Hz. The two data sets, obtained in different environments, are sufficiently consistent to allow development of a coherent model, as proposed here. This model shows significant differences when compared with the P-S model and also when compared with the D-P model. The P-S model was developed in 1973 and is based on a collection of data sets, some acquired in the laboratory and some in the field. The frequency responses of the sensors used in acquiring some of the data sets were limited to  $< 10$  Hz. Hence it is inferred that the present model is based on more representative data compared with the P-S model. The lack of accurate shortwave measurements had prevented verification of the P-S model until now.

The D-P model specifies shortwave spectral levels based on in situ wave measurements and on radar backscatter measurements. While in principle the approach is sound, the lack of better agreement between the D-P model and TOWARD/MARSEN data sets leaves questions to be answered regarding the correlation between shortwave and radar backscatter. The latter is the subject of considerable interest recently.

REFERENCES

Ataturk, S. S., and K. B. Katsaros, Intrinsic frequency spectra of short gravity-capillary waves obtained from temporal measurements of wave height on a lake, *J. Geophys. Res.*, 92, 5131-5141, 1987.

Barnett, T. P., On the generation, dissipation, and prediction of wind waves, *J. Geophys. Res.*, 73, 513-550, 1968.

Cox, C. S., Measurement of slopes of high-frequency wind waves, *J. Mar. Res.*, 16, 199-225, 1958.

Donelan, M. A., and W. J. Pierson, Jr., Radar scattering and equilibrium ranges in wind-generated waves with application to scatterometry, *J. Geophys. Res.*, 92, 4971-5029, 1987.

Donelan, M. A., J. Hamilton, and W. H. Hui, Directional Spectra of Wind-Generated Waves, *Philos. Trans. R. Soc. London, Ser. A*, 315, 509-562, 1985.

Evans, D. D., and O. H. Shemdin, An investigation of the modulation of capillary and short gravity waves in the open ocean, *J. Geophys. Res.*, 85, 5019-5024, 1980.

Ewing, J. A., A numerical wave prediction method for the North Atlantic Ocean, *Deutsche Hydrogr. Fr.*, 24, 241-261, 1971.

Forristal, G. Z., Measurements of a saturated range in ocean wave spectra, *J. Geophys. Res.*, 86, 8075-8084, 1981.

Geernaert, G. L., K. L. Davidson, S. E. Larsen, and T. Mikkelsen, Wind stress measurements during the Tower Ocean Wave and Radar Dependence Experiment, *J. Geophys. Res.*, this issue.

Hasselmann, K., et al., Measurements of wind-wave growth and swell decay during the Joint North Sea-Wave Project (JONSWAP), *Dtsch. Hydrogr. Zeitung*, 12(8), suppl. A, 95 pp., 1973.

Hughes, B. A., The effect of internal waves on surface wind waves, 2, Theoretical analysis, *J. Geophys. Res.*, 83, 455-465, 1978.

Hwang, P. A., and O. H. Shemdin, The dependence of sea surface slope on atmospheric stability and swell conditions, *J. Geophys. Res.*, this issue.

Kahama, K. K., A study of the growth of the wave spectrum with fetch, *J. Phys. Oceanogr.*, 11, 1503-1515, 1981.

Kitaigorodskii, S. A., On the theory of the equilibrium range in the spectrum of wind generated gravity waves, *J. Phys. Oceanogr.*, 13, 816-827, 1983.

Leykin, I. A., and A. D. Rozenberg, Sea-tower measurements of wind-wave spectra in the Caspian Sea, *J. Phys. Oceanogr.*, 14, 168-176, 1983.

Leonart, C. T., and D. R. Blackmann, The spectral characteristics of wind-generated capillary waves, *J. Fluid Mech.*, 97, 455-479, 1980.

Mitsuyasu, H., Measurement of the high-frequency spectrum of ocean surface waves, *J. Phys. Oceanogr.*, 7, 882-891, 1977.

Mitsuyasu, H., and T. Honda, The high frequency spectrum of wind-generated waves, *J. Oceanogr. Soc. Jpn.*, 30, 185-198, 1974.

- Pierson, W. J., Jr., and R. A. Stacy, The elevation, slope and curvature spectra of a wind-roughened sea surface *NASA Contract. Rep., CR-2247*, 126 pp., 1973.
- Phillips, O. M., The equilibrium range in the spectrum of wind-generated waves, *J. Fluid Mech.*, *4*, 426-434, 1958.
- Phillips, O. M., *The Dynamics of the Upper Ocean*, 2nd ed., 336 pp., Cambridge University Press, New York, 1977.
- Phillips, O. M., Spectral and statistical properties of the equilibrium range in wind-generated gravity wave, *J. Fluid Mech.*, *156*, 505-531, 1985.
- Shemdin, O. H., R. J. Lai, A. Reece, and G. Tober, Laboratory investigation of whitecaps, spray and capillary waves, *Tech. Rep. 11*, Coastal and Oceanogr. Eng. Lab. of Fla., Gainesville, 1972.
- Sutherland, A., Growth of spectral components in a wind-generated wave train, *J. Fluid Mech.*, *33*, 545-560, 1968.
- Tang, S., and O. H. Shemdin, Measurement of high frequency waves using a wave follower, *J. Geophys. Res.*, *88*, 9832-9840, 1983.
- Tober, G., R. C. Anderson, and O. H. Shemdin, Laser instruments for detecting water ripple slopes, *Appl. Opt.*, *12*, 788-794, 1973.
- 
- P. A. Hwang and O. H. Shemdin, Ocean Research and Engineering, 255 S. Marengo Avenue, Pasadena, CA 91101.

(Received September 14, 1987;  
accepted February 9, 1988.)

# Directional Measurement of Short Ocean Waves With Stereophotography

OMAR H. SHEMDIN<sup>1</sup>

*Jet Propulsion Laboratory, Pasadena, California*

H. MINH TRAN

*Ocean Research and Engineering, Pasadena, California*

S. C. WU

*U.S. Geological Survey, Flagstaff, Arizona*

Stereophotographs of the sea surface, acquired during the Tower Ocean Wave and Radar Dependence experiment (TOWARD), are analyzed to yield directional wave height spectra of short surface waves in the 6- to 80-cm range. The omnidirectional wave height spectra are found to deviate from the  $k^{-4}$  distribution, where  $k$  is the wave number. The stereo data processing errors are found to be within  $\pm 5\%$ . The omnidirectional spectra yield 514 degrees of freedom for 30-cm-long waves. The directional distribution of short waves is processed with a directional resolution of  $30^\circ$ , so as to yield 72 degrees of freedom for 30-cm-long waves. The directional distributions show peaks that are aligned with the wind and swell directions. It is found that dynamically relevant measurements can be obtained with stereophotography, after removal of the mean surface associated with long waves.

## 1. INTRODUCTION

The advent of microwave remote sensing has emphasized interest in short surface waves with wave lengths in the range 1-1000 cm. There is need for spatial measurements of the sea surface using photographic, remote sensing, and in-situ scanning techniques.

Early interest in wave height spectral properties focused on the shape of the forward face of the spectrum. This region has been referred to in the literature as the "equilibrium range." Phillips [1958] proposed, on the basis of dimensional arguments, that the wave height spectrum should have frequency dependence  $f^{-5}$ , which for linear gravity waves corresponds to wave number dependence  $k^{-4}$ . This form has been commonly incorporated in wave spectral models such as those proposed by Pierson *et al.* [1966], Barnett [1968], Ewing [1971], Hasselmann *et al.* [1973], and more recently, Donelan and Pierson [1987].

The concept of the equilibrium range, as proposed by Phillips [1958], has been reevaluated by a number of investigators on the basis both of experimental evidence and of theoretical arguments. The high-frequency region of the wave height spectrum is found to depend on wind speed, as reported by investigators such as Shemdin *et al.* [1972], Mitsuyasu and Honda [1974], Mitsuyasu [1977], Leonart and Blackman [1980], Tang and Shemdin [1983] and more recently, Shemdin and Hwang [this issue]. Alternative forms of the equilibrium range have been advanced based on theoretical arguments, and are shown to be valid when compared to measurements in the range  $f < 0.3$  Hz. These exhibit a dependence on wind speed

and follow a power law of the form  $f^{-4}$  or  $k^{-3.5}$ . Among those subscribing to this form are Kitaigorodskii [1983], Phillips [1985], and Donelan *et al.* [1985]. The advance of new techniques to directly measure the wave number spectrum in the range 1-100 cm will have a profound impact on understanding radar backscatter mechanisms. It is also crucial for determining the dynamical processes governing the equilibrium of short waves and their modulation by long waves. The traditional in situ techniques provide time series from which wave height and slope frequency spectra are computed. Conversion of frequency spectra to wave number spectra has been attempted by investigators using the linear wave dispersion relationships and suitable directional distributions [see Steele *et al.*, 1985]. The assumptions associated with such a conversion require verification and hence in themselves generate the need for direct measurement of the spatial properties of surface waves.

The use of stereophotography to measure sea surface topography was demonstrated by Cote *et al.* [1960] for long ocean waves. The labor intensive requirement for processing stereo images from pairs of photographs has prevented wide use of this technique for oceanographic applications.

Alternatively, a method developed by Stillwell [1969], based on single photographs of the sea surface, is demonstrated to provide a measure of the slope wave number spectrum, subject to presence of uniform sky illumination. This method is investigated in detail by Gotwols and Irani [1980] and Monaldo and Kasevich [1981], who found it to yield reasonable results under ideal sky conditions. They also note that the technique is limited in accuracy when such conditions are not present. The technique does not provide the directional distribution of the wave height spectrum. Rather, it provides the directional slope component spectrum as measured through a  $\cos^2(\theta - \theta_0)$  filter, where  $\theta_0$  is the camera look direction. Presumably, the directional slope spectrum can be extracted using the above filter, subject to signal attenuation at high azimuthal angles relative to the camera look direction.

<sup>1</sup>Now at Ocean Research and Engineering, Pasadena, California

Copyright 1988 by the American Geophysical Union.

Paper number 88JC03064,  
0148-0227/88/88JC-03064\$05.00

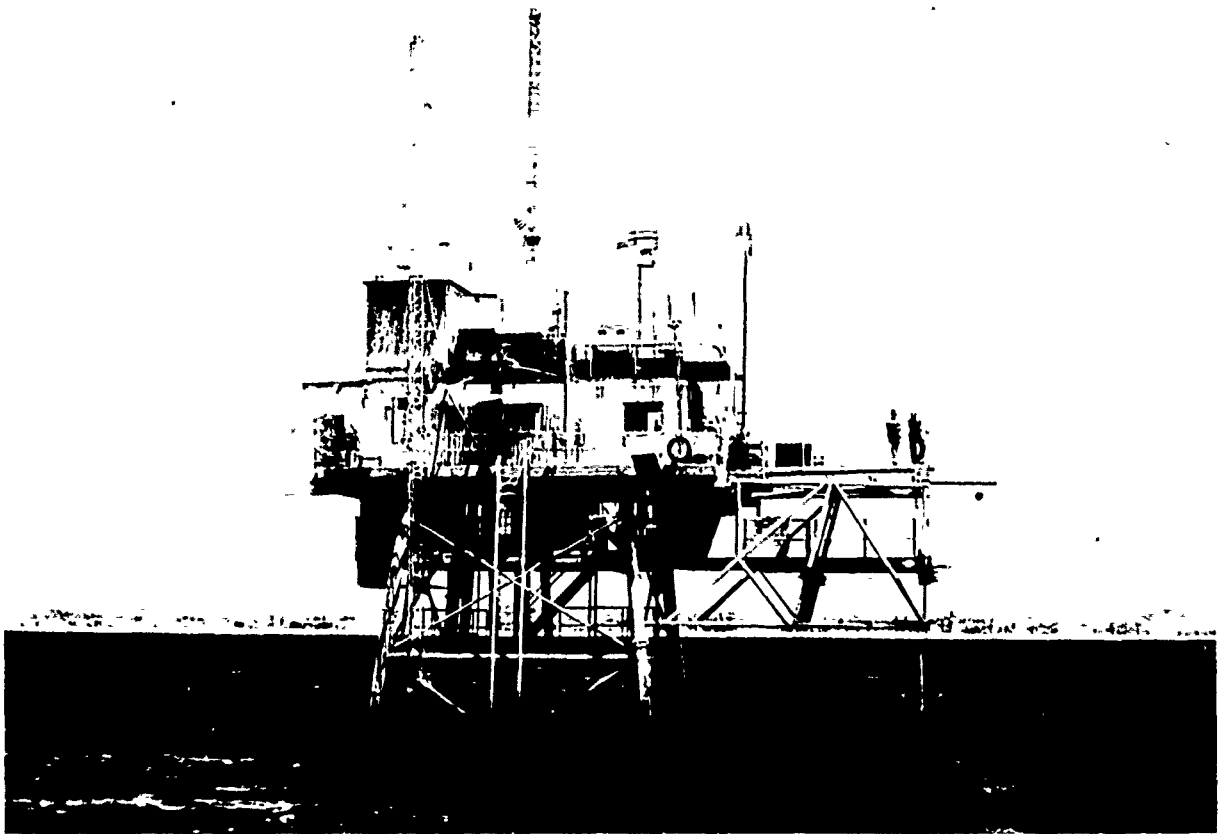


Fig. 1. Recent photograph of the NOSC tower seen from the west.

Because of the limitations associated with the Stillwell technique, interest in stereophotography has persisted, as is evidenced by the studies of Sugimori [1975] and Holthuijsen [1983].

The present investigation is part of the Tower Ocean Wave and Radar Dependence experiment (TOWARD) conducted during 1984–1986 from the Naval Ocean Systems Center (NOSC) tower offshore of Mission Beach, San Diego, California. An overview of this experiment and early results are given by Shemdin *et al.* [1986]. The present paper is part of a collection of papers representing the first segment of the scientific output from the TOWARD experiment.

## 2. EXPERIMENTAL SETUP AND PROCEDURE

Two 70-mm Hasselblad cameras with 150-mm focal-length lenses were used in March 1985, and 80-mm lenses were used in December 1985 and January 1986. They were deployed on the NOSC tower, shown in Figure 1, at an altitude of approximately 9.5 m (subject to tidal fluctuations) and horizontal baseline separation of 5.0 m. A baseline-to-height ratio of 0.4 was selected for the experiment. The two cameras were set to view a common area on the sea surface in the westerly direction by setting the incidence angle of each camera to approximately  $30^\circ$  and the azimuthal angle so that the overlapped area in the view of both cameras is maximized. A schematic diagram of the stereo setup is shown in Figure 2. A horizontal

T bar was deployed from the tower at an elevation of 3.0 m above the sea surface, also extending in the westerly direction, as shown in Figure 2b. The T bar was used (1) to define the area of overlap on the sea surface, and (2) to provide control

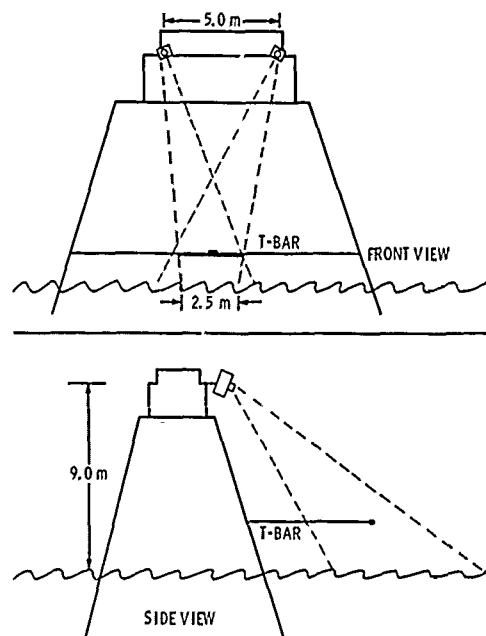


Fig. 2. Schematic of stereo geometry. The camera and T bar view direction is toward west.

CONTOURS: ELEVATION OF LARGE SCALE WATER SURFACE  
 GREY TONES: AMPLITUDE OF SMALL SCALE WAVES

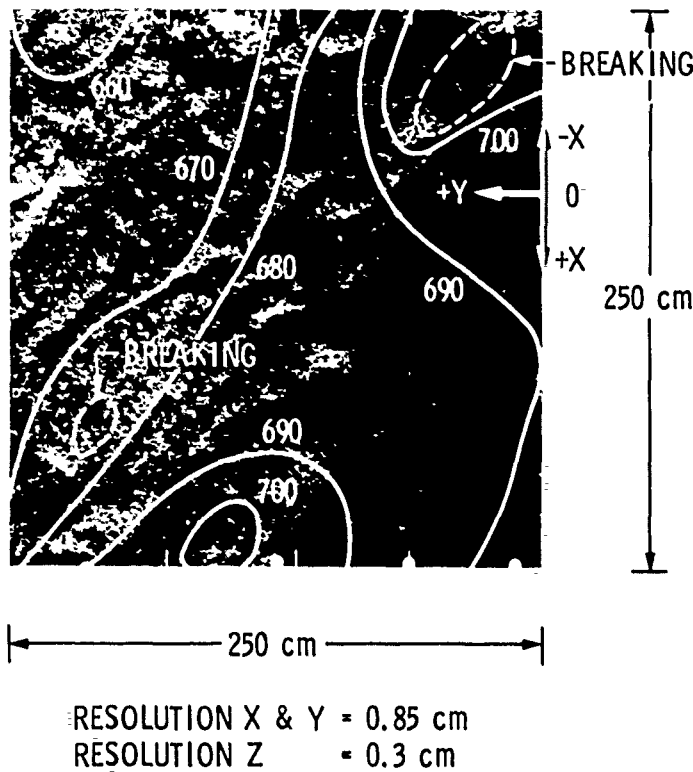


Fig. 3a. Map of surface elevation determined from stereo pair frame 24 acquired on March 27, 1985. The contours represent the mean surface elevation above an arbitrary datum. Intensity in the frame represents small-scale surface elevation  $Z$  at each point in the  $X$ - $Y$  plane.

points for establishing the stereo processing model. The latter defines the incidence angle and range to the ocean surface patch being surveyed. The stereophotographic correlating facilities of the U.S. Geological Survey in Flagstaff, Arizona, were used for stereo processing of all the data acquired in TOWARD. The camera  $f$ -stops were selected in the range 8-16, with  $1/250$  s as a minimum shutter speed. The depth of field was kept in the range 5-10 m to insure continuous focus for the short waves at all phase points of the long waves. The selected frame rate was one per 1.5 s. A high-speed film, 400 ISO, was used.

A typical stereo image is shown in Figure 3a, where contours of the mean sea surface elevation (due to long waves) are superposed. The contour lines are established from the absolute elevation above the datum provided by the stereo analysis. They show the area being viewed in relation to the surface elevation associated with the long surface waves. The area of the sea surface viewed by the cameras in Figure 3 is 250 cm  $\times$  250 cm. The corresponding horizontal resolution in both the  $X$  and  $Y$  directions is 0.85 cm, and the estimated vertical resolution is 0.3 cm. The  $X$  axis is aligned in the east-west direction, and the  $Y$  axis is aligned in the north-south direction.

The photograph obtained with the left camera is shown in Figure 3b. This photograph shows the position of the T bar, which is aligned horizontally by two carpenter leveling bubbles. The photograph also shows wave breaking patches (white water). The contours superposed on this photograph

are obtained from the stereo image shown in Figure 3a. They are superposed on Figure 3b to show positions of the breaking patches in relation to elevation and slopes of the mean sea surface. Conversely, the breaking patches shown in Figure 3a are obtained from their locations in the photograph shown in Figure 3b. The combination of stereo image and a photograph provides useful information on elevation and slope of the mean sea surface, superposed ripples, and regions of breaking waves. Such information, over a 250 cm  $\times$  250 cm patch, is precisely what is needed for testing models of radar backscatter from the sea surface and comparing outputs of such models with radar backscatter measurements.

### 3. DATA PROCESSING AND ERROR ANALYSIS

From the outset of this stereophotographic investigation it was clear that extensive data processing would be required to extract surface elevation and directional wave height spectra of short waves. A typical stereo image, without special processing, is shown in Figure 4a. Its two-dimensional Fourier transform is shown in Figure 4b. The bright cross at the origin reflects the strength of the mean surface on which the ripples are superposed. The mean surface masks the height and directional properties associated with the short waves. It was found, following several initial trials, that the mean surface must be removed before meaningful measurements of short waves can be obtained.

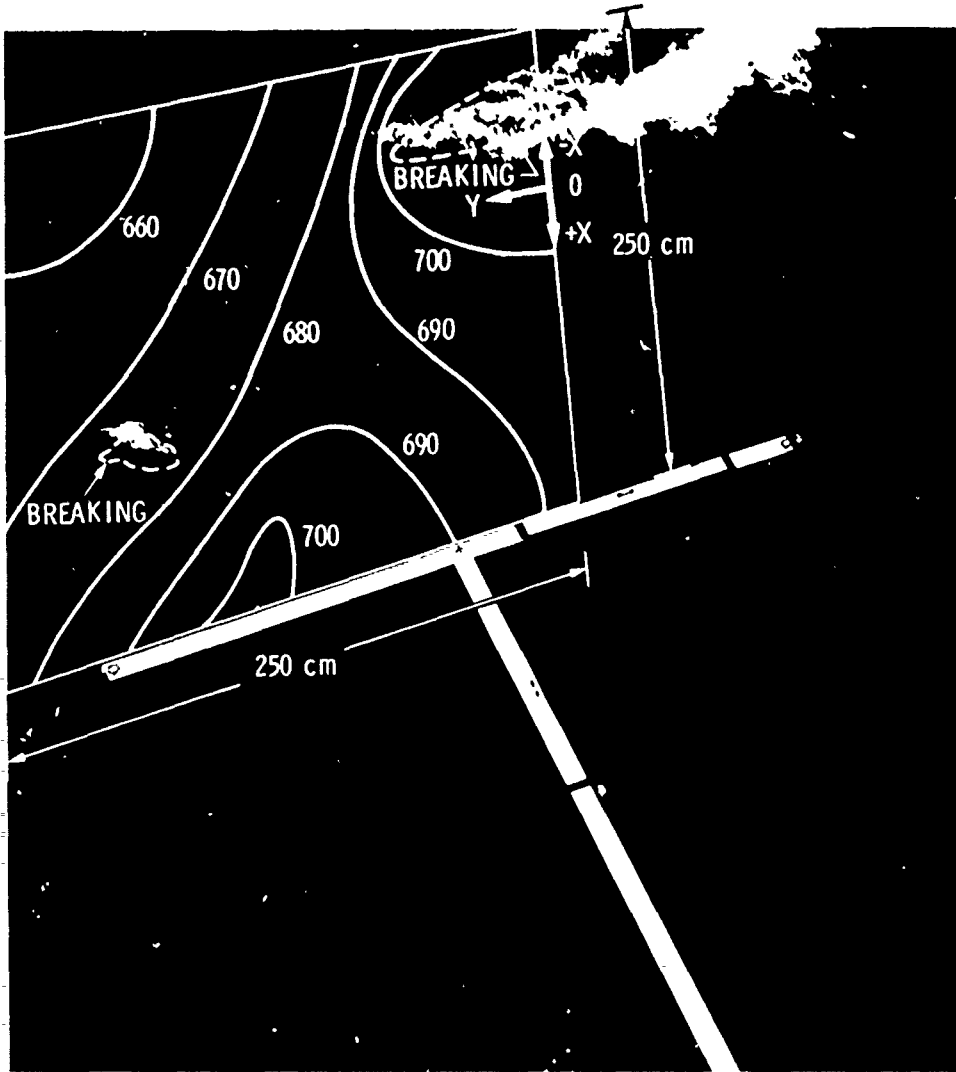


Fig 3b Photograph of the sea surface showing wave breaking. Superposed surface elevation contours are derived from the stereo image shown in Figure 2a.

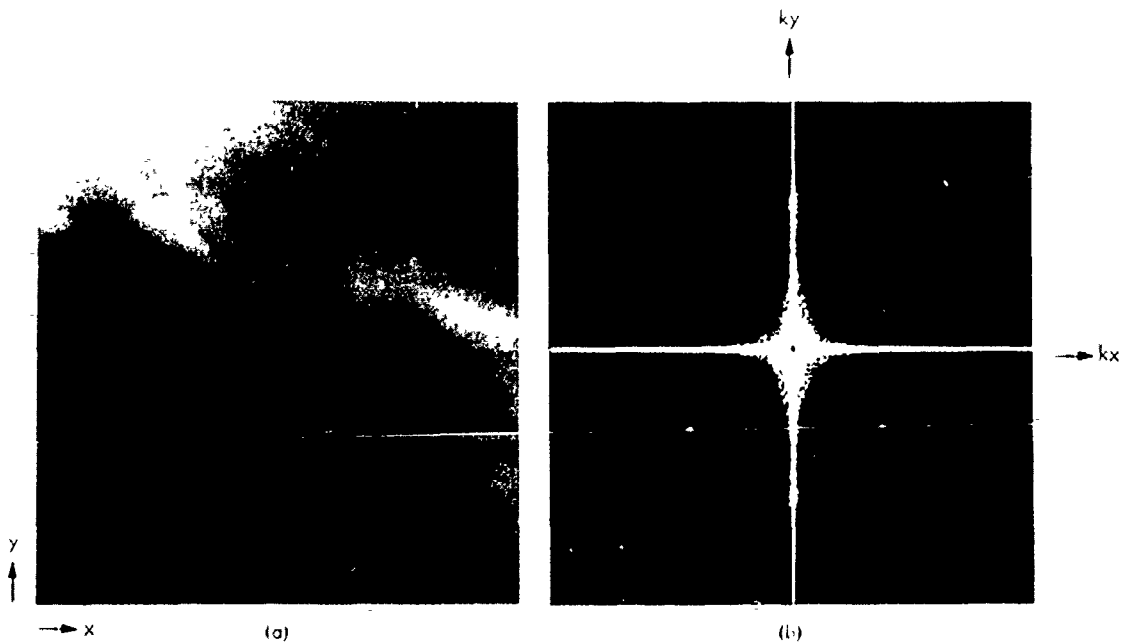


Fig 4 (a) Unfiltered stereo image and (b) its two-dimensional Fourier transform of October 31, 1984, 1520.34 Pacific standard time (PST).

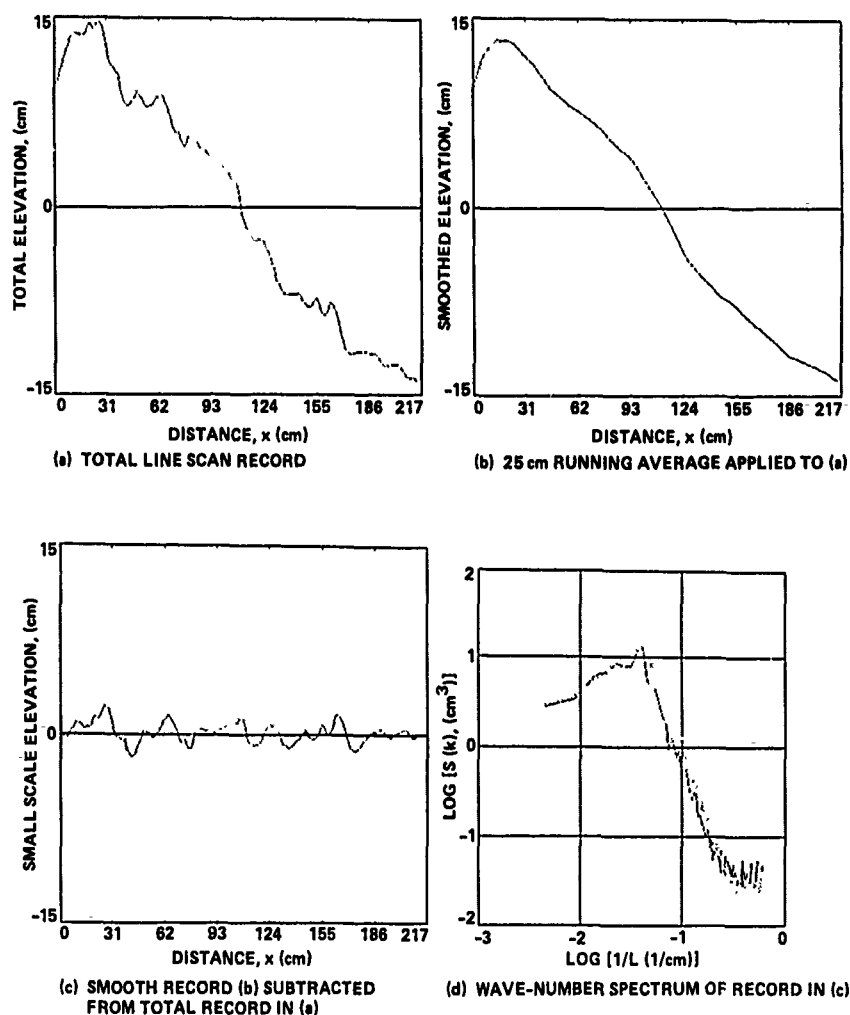


Fig. 5. Line scan analysis of stereo frame shown in Figure 4a. (a) Total record, (b) 25-cm running average, (c) total record minus mean, and (d) wave number spectrum of Figure 5c.

A line scan, in the  $X$  direction, of the image shown in Figure 4a is given in Figure 5a. The scan shows a 30-cm vertical relief across the frame, with the short waves superposed. A 25-cm running average over this line scan is shown in Figure 5b. The latter represents the mean trend associated with the line scan. Subtraction of the mean elevation in Figure 5b from the total elevation in Figure 5a yields the surface displacements associated with the short waves, shown in Figure 5c. A one-dimensional Fourier transform of the space series given in Figure 5c is presented in Figure 5d.

This one-dimensional procedure is presented to provide a simple illustration of the high-pass filtering that is required. In reality, two-dimensional high-pass filtering must be applied. The latter is achieved by least squares fitting a mean surface to the stereo image. The elevation  $Z$  for such a surface is defined by a second-order polynomial of the form

$$Z = a_0 + a_1x + a_2y + a_3xy + a_4x^2 + a_5y^2 \quad (1)$$

where  $a_1 - a_5$  are coefficients defined by the least squares fit. Subtracting the mean surface from the total image on a pixel by pixel basis provides topography of the short surface waves. A two dimensionally high-passed surface using this method is shown in Figure 6a. The surface shown here is a square with

256  $\times$  256 grid points, and with corresponding horizontal resolution in both the  $X$  and  $Y$  directions equal to 1.6 cm. The total length of the surface is 410 cm on each side. A boxcar window is applied in Figure 6a. The same surface is shown in Figure 6b after a cosine taper window [see Harris, 1978] is applied with 10% tapering around the edges.

The Fourier transform of the windowed surface in Figure 6b is shown in Figure 6c. The latter has 2 degrees of freedom (DOF) but highest possible wave number resolution. Increasing the degrees of freedom can be achieved by dividing the surface in Figure 6a into 16 subblocks each containing 64  $\times$  64 grid elements. The Fourier transform of each subblock yields 2 degrees of freedom but with a degraded wave number resolution. In Figure 6d the average of the 16 Fourier transforms is shown, it corresponds to 32 degrees of freedom. The statistical reliability of the spectral estimates will be discussed in greater detail below. The high-pass filter function applied in Figure 6 is shown in Figure 7. Here, only waves longer than 80 cm are significantly attenuated by this filter.

The conversion of a two-dimensional Fourier transform into an omnidirectional spectrum is achieved by converting the wave number spectrum from Cartesian to polar coordinates. For each wave number  $k = (k_x^2 + k_y^2)^{1/2}$ , the spectral

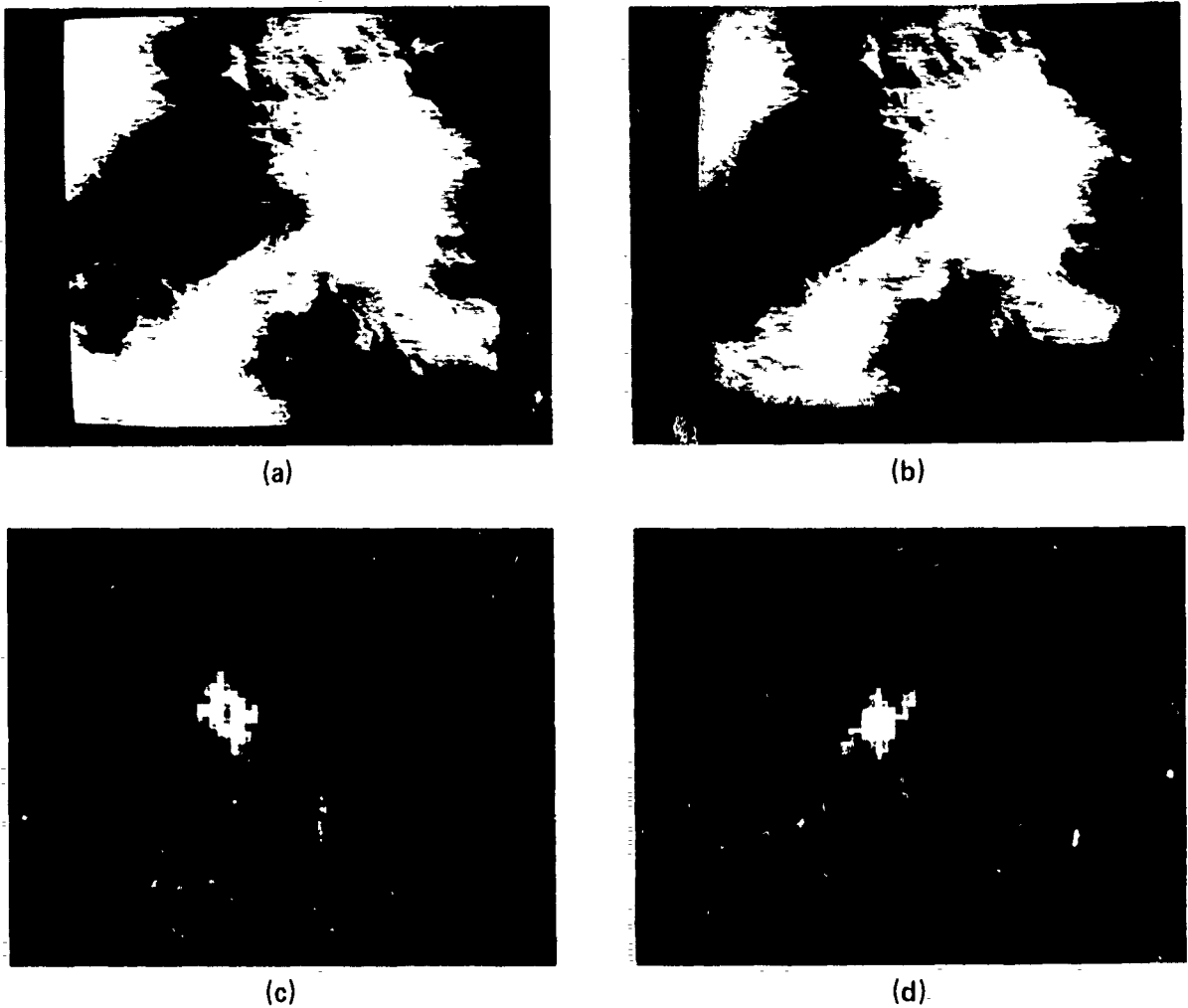


Fig. 6. Two dimensionally high-pass filtered stereo image: (a) boxcar window, (b) 20% cosine taper window applied, (c) two-dimensional Fourier transform of Figure 6b with 2 degrees of freedom, and (d) average of 16 Fourier transforms of subblocks of Figure 6a with 32 degrees of freedom.

energy is summed directionally, over a ring with a width  $dk = dk_x = dk_y$ , from 0 to  $2\pi$ . The portion of energy included is weighed in proportion to the area of overlap between the square pixel and the ring. Hence only 50% of the spectral energy in a pixel is included if 50% of the pixel area overlaps the ring. The total spectral energy in both Cartesian and polar coordinates is conserved.

In computing the degrees of freedom for omnidirectional spectra, each pixel element  $dk_x$  by  $dk_y$  is considered to have 2 degrees of freedom. Hence the total number of elements in a ring is used to compute the ring DOF. Averaging over neighboring rings is used to increase DOF. A typical value for a ring centered at 30-cm wavelength and averaging over three contiguous wave numbers, yields 514 DOF. The latter corresponds to  $\pm 8\%$  in statistical variability for 80% confidence limits.

Another source of error in stereo processing is attributed to the stereo operator. This source is investigated in this study by scanning the same stereo pair four independent times with different operators. Applying the two-dimensional high-pass filtering procedure discussed above to each of the five scans,

performing the two-dimensional Fourier transforms, and computing the directionally averaged spectra on each, yield four independent spectra of the same frame. A comparison of these is given in Figure 8. The agreement between the four spectra is considered very good, error bands specifying the operator error are also shown in Figure 8. These error bands are similar in magnitude to the bands of statistical variability for 30-cm-long waves.

#### 4. RESULTS

From the discussion of stereo processing errors and statistical variability in the previous section, it is clear that useful dynamical and statistical measurements can be obtained with stereophotography. In this section, the early scientific results are presented. They focus on the equilibrium range in the wave number spectrum, and the modulation of short waves by long waves.

A two-dimensional wave number spectrum  $\psi(k)$  is defined for a sea surface displacement  $\eta(x)$  in terms of the covariance

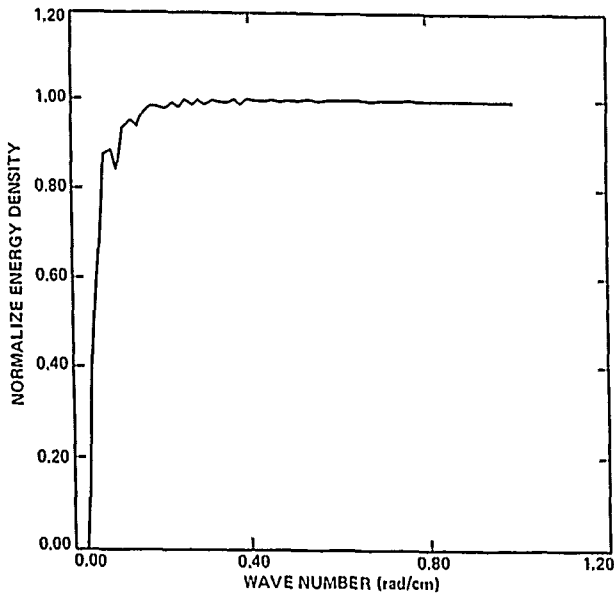


Fig. 7. The high-pass filter function applied to the image in Figure 6.

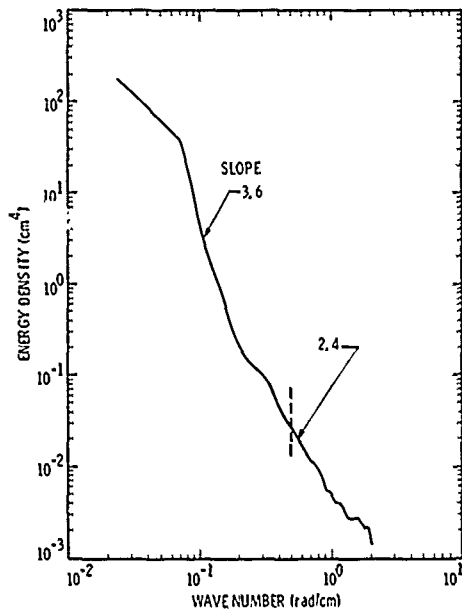


Fig. 9. Averaged omnidirectional spectrum from 23 frames in sequence 1.

function,  $\phi(\mathbf{r})$

$$\phi(\mathbf{r}) = \langle \eta(\mathbf{x})\eta(\mathbf{x} + \mathbf{r}) \rangle \quad (2)$$

where  $\mathbf{x}$  is the vector position of a point on the sea surface and  $\mathbf{r}$  is the separation vector between two neighboring points. It can be shown that [see Phillips, 1977]

$$\phi(\mathbf{r}) = \int_{-\infty}^{+\infty} \int_{-\infty}^{+\infty} \psi(\mathbf{k}) \exp(i\mathbf{k} \cdot \mathbf{r}) d\mathbf{k} \quad (3)$$

where the mean squared surface,  $\langle \eta^2 \rangle$ , is given by

$$\langle \eta^2 \rangle = \phi(0) = \int_{-\infty}^{+\infty} \int_{-\infty}^{+\infty} \psi(\mathbf{k}) d\mathbf{k} \quad (4)$$

Here,  $\mathbf{k}$  is the wave number vector given by  $\mathbf{k} = k_x i + k_y j$ . Equation (4) may be expressed in polar coordinates, so that

$$\langle \eta^2 \rangle = \phi(0) = \int_0^{2\pi} \int_0^\infty \psi(k, \theta) k dk d\theta \quad (5)$$

An omnidirectional spectrum,  $F(k)$ , is defined

$$F(k) = \int_0^{2\pi} \psi(k, \theta) d\theta \quad (6)$$

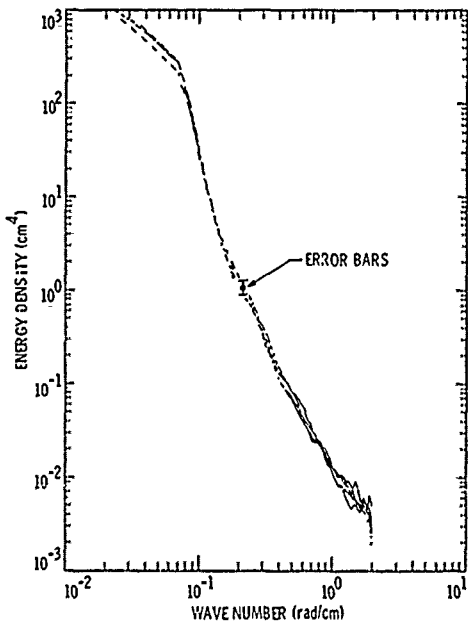


Fig. 8. Four omnidirectional spectra derived from five independent stereo scans of the same frame.

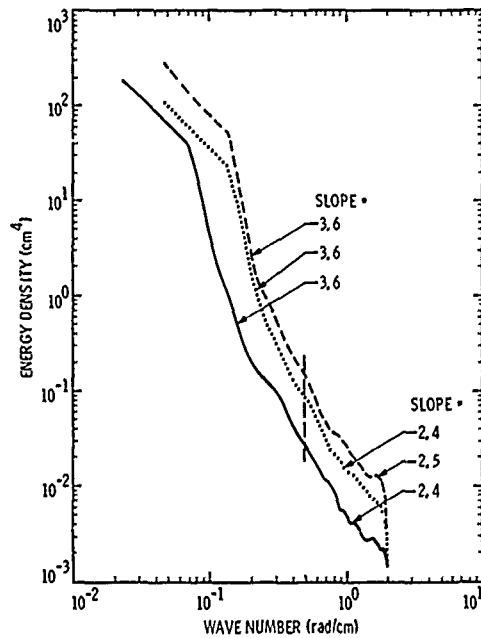


Fig. 10. Average omnidirectional spectra from sequences 1-3. Wind speeds are 1.5-2.0 m/s (solid line), 2.5-3.0 m/s (dotted line), and 4.5-5.0 m/s (dashed line).

TABLE 1. Summary of Stereo Image Sequences

Sequence	No. of Frames	Date	Time, PST	Wind Speed, m/s	Upper Slope $-n$	Lower Slope $-n$
1	10	Jan. 22, 1986	1545:00	1.5-2.0	3.6	2.4
2	8	Jan. 24, 1986	1320:00	2.5-3.0	3.6	2.5
3	10	Jan. 24, 1986	1402:00	4.5-5.0	3.6	2.4

so that

$$\langle \eta^2 \rangle = \int_k F(k) k \, dk \quad (7)$$

where  $F(k)$  is referred to in the graphical presentations to follow as the energy density with units of  $\text{cm}^4$ . The directional energy density,  $\psi(k, \theta)$ , has units of  $(\text{cm}^4/\text{deg})$ , as noted in the graphical presentation.

#### 4.1. Wind Wave Spectra in the Equilibrium Range

The results presented here are based on analysis of 28 stereo pairs in three sequences (Table 1). The average omnidirectional spectrum derived from the 10 spectra in sequence 1 is shown in Figure 9. Here, extremely narrow statistical variability bands corresponding to  $\text{DOF} = 5140$  can be achieved for 30-cm-long waves. The Nyquist length for these spectra is 3.2 cm.

The omnidirectional spectrum can be assumed to have the form

$$F(k) = Ak^{-n} \quad (8)$$

where  $A$  is the equilibrium range constant and  $n$  is the slope magnitude. From Figure 9 it is found that  $n = 3.6$  for waves longer than 30 cm, and 2.4 for waves shorter than 30 cm. A noise floor is approached at waves shorter than 8.0 cm. It is noted that in other stereo-processed frames, where the Nyquist wave length is 1.7 cm, the noise floor extended to waves shorter than 5.0 cm and the  $n = 3.6$  slope region extended to wave lengths longer than 10 cm.

The  $n = 3.6$  slope supports the recent theoretical arguments introduced by *Kitaigorodskii* [1983] and *Phillips* [1985]. The slope  $n = 2.4$  in the higher wave number range is presently unexplainable in dynamical terms. It can represent the transition from the  $n = 3.6$  range to the noise deck,  $n = 0$ , at the limit of the high wave numbers measured.

It is noted that results similar to those in Figure 9 are obtained from the other two sequences analyzed. A summary of slopes examined is shown in Table 1.

The equilibrium range distribution proposed by *Kitaigorodskii* [1983] and *Phillips* [1985] can be expressed in the form

$$F(k) = B_1 g^{1/2} U_a k^{-3.5} \quad (9)$$

or

$$F(k) = B_2 g^{1/2} U_* k^{-3.5} \quad (10)$$

where  $B_1$  and  $B_2$  are constants,  $U_a$  and  $U_*$  are the wind speed at the reference altitude and wind friction velocity, respectively, and  $g$  is gravitational acceleration. The above forms suggest that wave height spectra having slopes of 3.5 should also exhibit wind speed dependence. The average spectra from each of the three sequences 1-3 are shown in Figure 10. A

systematic wind speed dependence is detected for all wave lengths in the omnidirectional spectra.

The omnidirectional spectrum shown in Figure 9 is compared with the recent model of *Donelan and Pierson* [1987] in Figure 11.

#### 4.2. Modulation of Short Waves by Long Waves

A sequence of seven consecutive frames obtained on March 27, 1985, 1048:22 Pacific standard time (PST), are processed to yield the two-dimensional spectra of short waves at different phase points along a long wave. The frames are obtained in time-lapse mode at 1.5-s intervals. The high-pass-filtered images and their two-dimensional Fourier transforms are shown in Figure 12. The corresponding omnidirectional spectra are shown in Figure 13. Here the 80% confidence limit bands correspond to  $\pm 8\%$ .

In Figure 13 the bands associated with stereo processing errors and statistical variability are both shown. It is clear from this figure that the variability of the omnidirectional spectra at different phase-points along the long waves are due to dynamical interactions between the short waves and long waves and to statistical variability inherent in surface wave measurements. The highest shortwave spectral intensities are observed on the trough of the long waves, while relatively low shortwave intensities appear on the crest of the long wave. These results are not inconsistent with the recent observations of *Strizhkin et al.* [1985].

The directional modulation of short waves by long waves is of considerable interest. In Figure 14 the directions of the wind and dominant swell are noted with respect to true north.

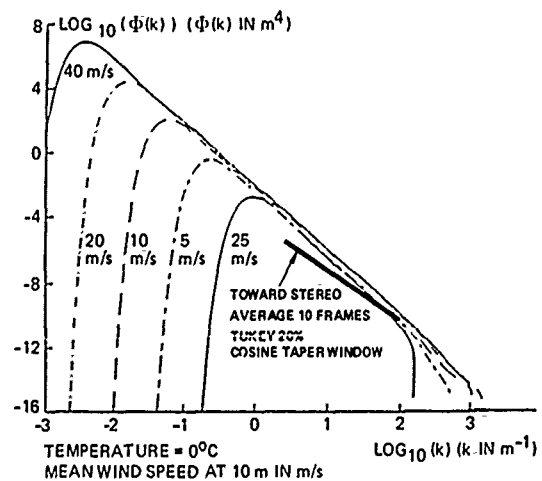


Fig. 11. Comparison of omnidirectional spectrum in Figure 9 with the model of *Donelan and Pierson* [1987].

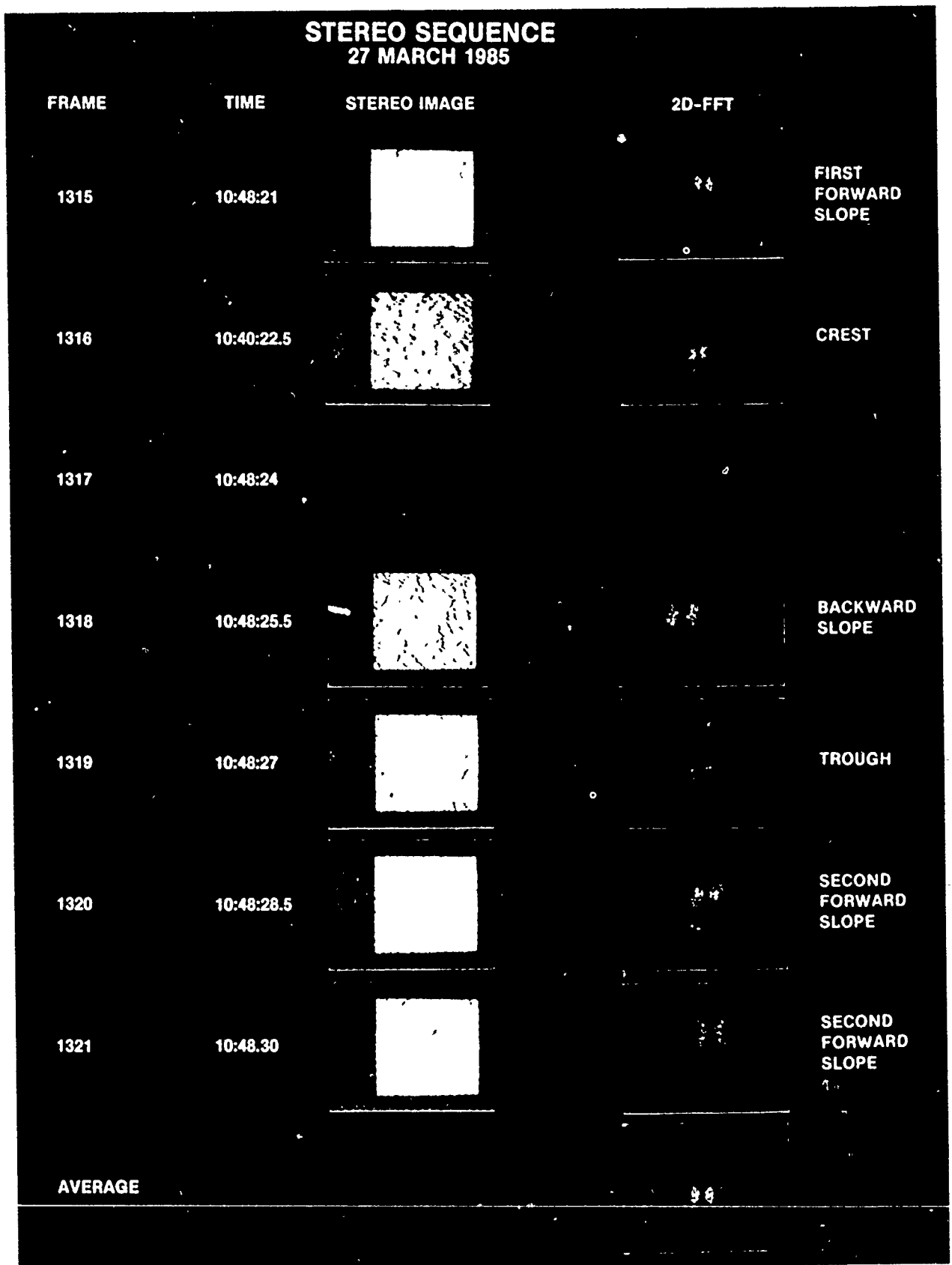


Fig. 12. Sequence of stereo images and corresponding two-dimensional spectra of short waves modulated by long waves

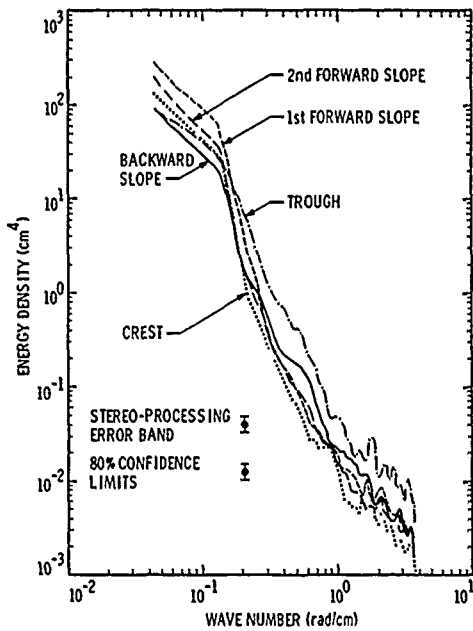


Fig. 13. Omnidirectional spectra at different phase points along the long wave. Processing error bands and statistical variability bands for 80% confidence limits are shown.

The directional modulation of the 30-cm-long waves is shown in Figure 15 at different phase positions along the long wave. The results in Figure 15 correspond to 30° directional resolution, averaging over five wave numbers with  $DOF = 72$ . The statistical variability band for 80% confidence limits are also noted in Figure 15. The modulated energy density levels exceed the bands of statistical variability, indicating that the modulation is due to the dynamical processes. Here again, the trough energy density levels are greater than those at other phase locations along the long wave.

A complete dynamical description of the modulations shown in Figure 15 is beyond the scope of this paper. What is clear is that stereophotography offers a unique measurement technique that is needed to investigate the directional modulation of short waves by long waves.

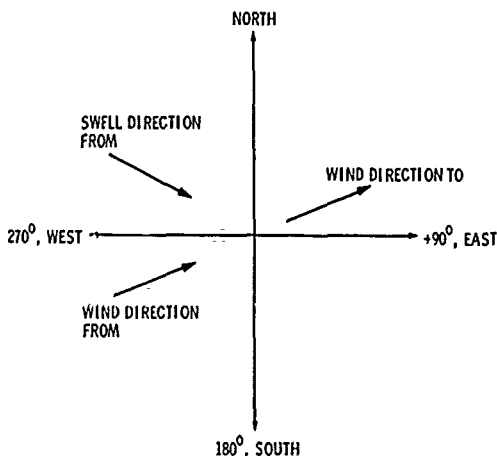


Fig. 14 Schematic of wind and wave orientations for images shown in Figure 12.

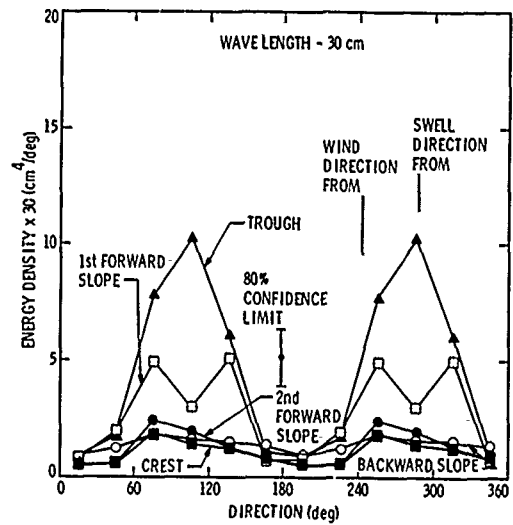


Fig. 15. Directional distributions of 30-cm-long waves at different phase points along the long wave. Directional resolution is 30°;  $DOF = 72$ . The statistical variability bands are shown.

5. SUMMARY AND CONCLUSIONS

Stereophotography was incorporated in the TOWARD experiment to validate the assumptions used in the transformation of wave frequency spectra to wave number spectra. A careful analysis of stereo images to date reveals the following conclusions.

1. Two-dimensional high-pass filtering is required before useful information on short waves can be obtained.
2. The errors associated with standard stereo processing are small (within  $\pm 5\%$ ) in comparison with the signatures associated with the physical processes affecting the short waves.
3. The slopes of the omnidirectional wave number spectra are found to deviate from the familiar  $k^{-4}$  distribution.
4. The stereophotographic observations of centimeter waves are not inconsistent with the theoretical concepts advanced by Kitaigorodskii [1983] and Phillips [1985] for the equilibrium range.
5. The directional distribution of the centimeter waves is highly directional, with the peaks generally aligned in the wind and swell directions.
6. Significant directional modulation of the centimeter waves is observed at different phase points along the long waves. The short wave energy densities in the trough of the long wave exceed those at other phase locations.

*Acknowledgments.* The initiative for using stereophotography to investigate short surface waves in the TOWARD experiment was promoted by W. Brown, Jr., and O. H. Shemdin. The initial set of photographs was obtained by W. Brown, Jr., and S. Skotniki of the Jet Propulsion Laboratory. The stereophotographic processing was executed by a team at the U.S. Geological Survey (Flagstaff, Arizona) under the supervision of S. C. Wu and F. J. Schafer. P. A. Hwang of Ocean Research and Engineering provided valuable input in the analysis phase. W. J. Pierson, Jr., of City University of New York reviewed the paper and provided helpful comments on statistical processing of the data. The effort was sponsored by the Office of Naval Research, SAR Research Program, under the technical cognizance of H. Dolezalek.

REFERENCES

Barnett, T. P., On the generation, dissipation, and prediction of wind waves, *J. Geophys. Res.*, 73, 513-550, 1968.

- Donelan, M. A., and W. J. Pierson, Jr., Radar scattering and equilibrium ranges in wind-generated waves with application to scatterometry, *J. Geophys. Res.*, **92**, 4971-5029, 1987.
- Donelan, M. A., J. Hamilton, and W. H. Hui, Directional spectra of wind-generated waves, *Philos. Trans. R. Soc. London, Ser. A*, **315**, 509-562, 1985.
- Cote, L. F., J. O. Davis, W. Marks, R. F. McGough, E. Mehr, W. J. Pierson, Jr., J. F. Ropek, G. Stephenson, and R. C. Vetter, The directional spectrum of a wind generated sea as determined from data obtained by the stereo wave observation project, *Meteorological Papers, Vol. 2, No. 6*, 88 pp., N. Y. Univ., New York, 1960.
- Ewing, J. A., A numerical wave prediction method for the North Atlantic Ocean, *Dtsch. Hydrogr. Fernz. 24*, 241-261, 1971.
- Gotwols, B. L., and G. B. Irani, Optical determination of the phase velocity of short gravity waves, *J. Geophys. Res.*, **85**, 3964-3970, 1980.
- Harris, F. J., On the use of windows for harmonic analysis with the discrete Fourier transform, *Proc. IEEE*, **66**, 51-83, 1978.
- Hasselmann, K., et al., Measurements of wind-wave growth and swell decay during the Joint North Sea Wave Project (JONSWAP), *Dtsch. Hydrogr. Zeitung*, **12(8)**, suppl. A, 95 pp., 1973.
- Holthuijsen, L. H., Observations of the directional distribution of ocean-wave energy in fetch-limited conditions, *J. Phys. Oceanogr.*, **13**, 191-207, 1983.
- Kitagorodskii, S. A., On the theory of the equilibrium range in the spectrum of wind generated gravity waves, *J. Phys. Oceanogr.*, **13**, 816-827, 1983.
- Leonart, C. T., and D. R. Blackman, The spectral characteristics of wind-generated capillary waves, *J. Fluid Mech.*, **97**, 455-479, 1980.
- Mitsuyasu, H., Measurement of the high-frequency spectrum of ocean surface waves, *J. Phys. Oceanogr.*, **7**, 882-891, 1977.
- Mitsuyasu, H., and T. Honda, The high frequency spectrum of wind generated waves, *J. Oceanogr. Soc. Jpn.*, **30**, 185-198, 1974.
- Monaldo, F. M., and R. S. Kasevich, Daylight imagery of ocean surface waves for wave spectra, *J. Phys. Oceanogr.*, **11**, 272-283, 1981.
- Pierson, W. J., L. J. Tick, and L. Baer, Computer based procedures for preparing global wave forecasts and wind field analysis capable of using wave data obtained by a spacecraft, in *Proceedings of the 6th Symposium on Naval Hydrodynamics*, Office of Naval Research, Washington, D. C., 1966.
- Phillips, O. M., The equilibrium range in the spectrum of wind generated waves, *J. Fluid Mech.*, **4**, 426-434, 1958.
- Phillips, O. M., *The Dynamics of the Upper Ocean*, (2nd ed.), 336 pp., Cambridge University Press, New York, 1977.
- Phillips, O. M., Spectral and statistical properties of the equilibrium range in wind-generated gravity waves, *J. Fluid Mech.*, **156**, 505-531, 1985.
- Shemdin, O. H., and P. A. Hwang, Comparison of measured and predicted sea surface spectra of short waves, *J. Geophys. Res.*, this issue.
- Shemdin, O. H., R. J. Lai, A. Reece, and G. Tober, Laboratory investigation of white caps, spray, and capillary waves, *Tech. Rep. 11*, Coastal and Oceanogr. Eng. Lab., Univ. of Fla., Gainesville, 1972.
- Shemdin, O. H., et al., *Investigation of Physics of Synthetic Aperture Radar in Ocean Remote Sensing, TOWARD Interim Report*, 2 vols., 113 pp., Jet Propulsion Laboratory, Pasadena, Calif., 1986.
- Steele, K. E., J. C. Lau, and Y. L. Hsu, Theory and application of calibration techniques for an NDBC directional wave measurements buoy, *IEEE J. Oceanic Eng.*, **OE-10**, 382-396, 1985.
- Stillwell, D., Directional energy of sea waves from photographs, *J. Geophys. Res.*, **74**, 1974-1986, 1969.
- Strizhkin, I. I., M. P. Lapchinskaya, Yu. A. Il'in, and V. A. Malinnikov, Spatial structure of high-frequency wind waves on the sea for different meteorological conditions, *Izv. Acad. Sci. USSR Atmos. Oceanic Phys.*, Engl. Transl., **21**, 342-344, 1985.
- Sugimori, Y., A study of the application of the holographic method to the determination of the directional spectrum of ocean waves, *Deep Sea Res.*, **22**, 339-350, 1975.
- Tang, S., and O. H. Shemdin, Measurement of high-frequency waves using a wave follower, *J. Geophys. Res.*, **88**, 9832-9840, 1983.

O. H. Shemdin and H. M. Tran, Ocean Research and Engineering, 255 S. Marengo Avenue, Pasadena, CA 91101.  
S. C. Wu, U.S. Geological Survey, Flagstaff, AZ 86001.

(Received October 14, 1987;  
accepted March 14, 1988.)

# The Dependence of Sea Surface Slope on Atmospheric Stability and Swell Conditions

PAUL A. HWANG

*Ocean Research and Engineering, Pasadena, California*

OMAR H. SHEMDIN<sup>1</sup>

*Jet Propulsion Laboratory, Pasadena, California*

A tower-mounted optical device is used to measure the two orthogonal components of the sea surface slope. The results indicate that an unstable stratification at the air-sea interface tends to enhance the surface roughness. The presence of a long ocean swell system steers the primary direction of shortwave propagation away from wind direction, and may increase or reduce the mean square slope of the sea surface.

## 1. INTRODUCTION

The characteristics of short wind-generated waves in the ocean can be easily modified by environmental parameters as wind, long surface waves, internal waves, currents, surface slicks and atmospheric stability, among others. Such sensitivity of the short waves allows remote sensing of these same oceanographic parameters (see, for example, *Hasselmann et al.* [1985], *Huang* [1979], *Chelton and McCabe* [1985] for related literature). While the importance of short waves in remote sensing is widely recognized, the dynamical response of the short waves to these parameters is still not completely understood, partly owing to the complexity and nonlinearities involved in the theoretical analysis and partly because of the difficulties involved in making in situ measurements of such short waves in the ocean. Only a handful of field programs have been reported over a span of about 30 years [*Cox and Munk*, 1954, 1956; *Hughes et al.*, 1977; *Lubard et al.*, 1980; *Evans and Shemdin*, 1980; *Tang and Shemdin*, 1983]. Some of the important observations from the sun-glitter experiment of Cox and Munk are as follows: (1) The probability distribution of the cross-wind slope component is nearly Gaussian. The distribution of the upwind component sea surface slopes is skewed. The skewness increases with wind speed. The peakness factor is found to be slightly higher than Gaussian distribution, but only barely above the limit of observation error. (2) The primary axis of the slope distribution is closely aligned with the wind direction. (3) The ratio between the variance of cross-wind and upwind slope components (an indicator of the directional distribution of short waves) ranges from 0.54 to 1.0 with a mean value of 0.75. (4) The mean square slope increases linearly with wind speed. (5) Oil slicks, which tend to suppress the shorter waves, reduce the mean square slope by a factor of 2 to 3 and reduce skewness but leave peakness unchanged.

*Hughes et al.* [1977] used a different technique that derives the sea surface slope from the refraction of a light beam passing through the air-water interface. Their results, obtained from an instrument mounted on a moving ship, are essentially

in agreement with the observations of Cox and Munk. The detailed statistical characteristics and wind dependence of short waves derived from their study are similar to what is summarized above for Cox and Munk.

More recently, and in support of remote sensing of the ocean surface, a series of wave follower sea surface slope experiments were executed to compare with radar return from the sea surface. Among these were the West Coast [*Lubard et al.*, 1980], Marineland [*Evans and Shemdin*, 1980], and Marine Remote Sensing (MARSEN) [*Tang and Shemdin*, 1983] experiments, as well as the Tower Ocean Wave and Radar Dependence Experiment (TOWARD) being reported on here. The optical devices for slope measurements used in those experiments were based on a similar design [*Tober et al.*, 1973] which was improved in the years that followed. The optical slope meter was mounted on a wave follower device designed to maintain the instrument at a fixed distance above the instantaneous ocean surface. The first two experiments mentioned provided only preliminary results. There was no discussion on the statistical properties of the wave slope. The MARSEN data [*Tang and Shemdin*, 1983] provided interesting results. Of special relevance to this paper is the classification of the mean square slope data into two distinctive groups in relation to sea state, identified as "mixed sea" and "well-defined peak" conditions. The dependence on wind speed of the data in the second group is similar to that of Cox and Munk, but there is significant deviation from the established wind dependence in the first group of data. Tang and Shemdin also observed that the probability distributions of the upwind and cross-wind slope components are nearly identical and approximately Gaussian. The lack of skewness in the upwind slope distribution is quite different from the observation of *Cox and Munk* [1954, 1956] and *Hughes et al.* [1977].

It may be concluded from the preceding review that although many of the earlier observations of the shortwave characteristics are confirmed by the newer experiments, modification of certain fundamentals seems to be necessary to account for the dependence of short waves on the environmental conditions. Recognizing the sensitivity of short waves in responding to changes in the environmental parameters, the TOWARD Experiment included in its suite of measurements a complete set of hydrodynamic parameters such as speed and

<sup>1</sup>Now at Ocean Research and Engineering, Pasadena, California

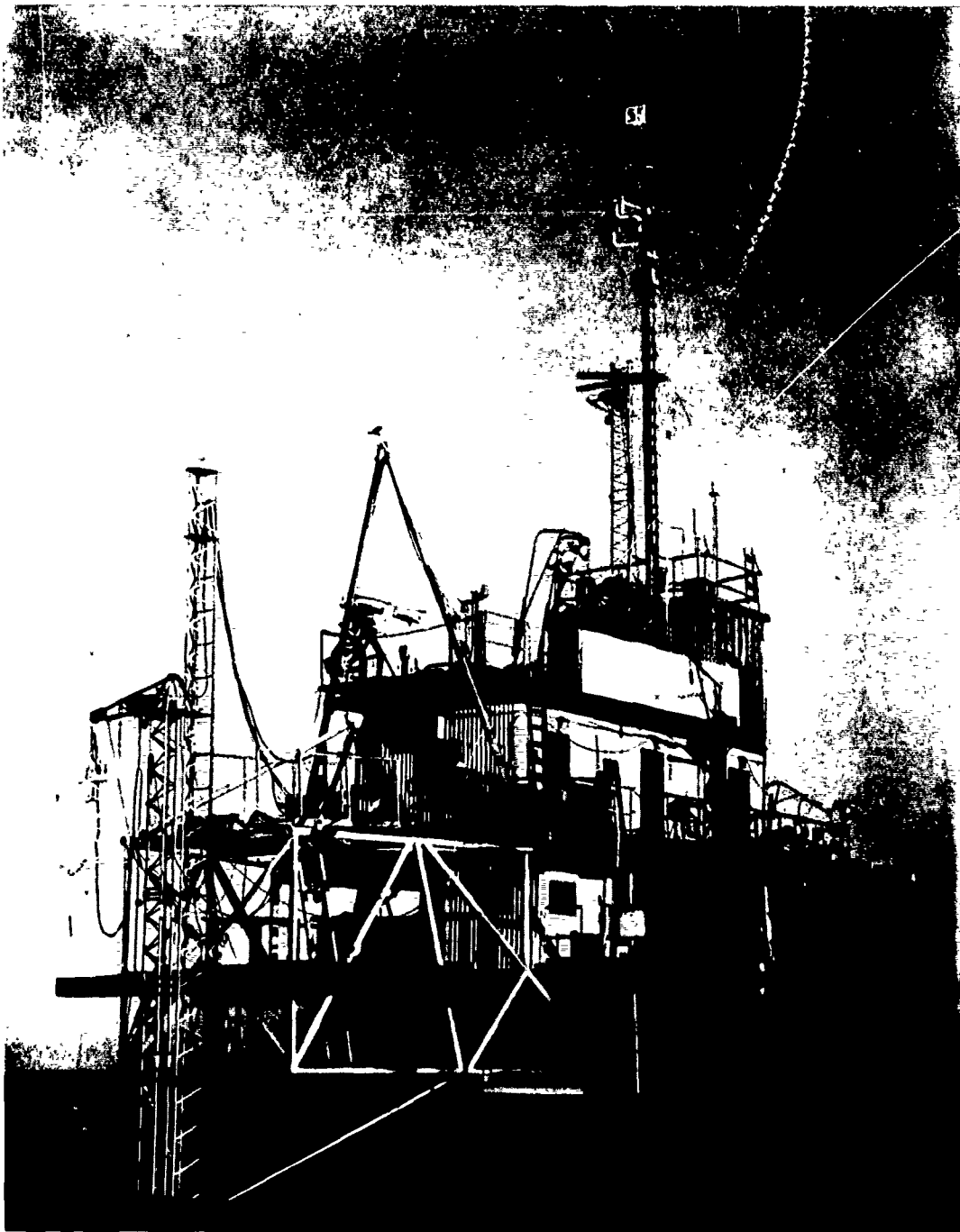


Fig. 1. Photographic view of the wave follower structure.

direction of wind, turbulence properties of air flow, temperatures of air and water, and directional properties of swell and internal waves in addition to the sea surface slopes. This data set proves to be the most complete so far and provides a valuable addition to the existing data base needed for investigating shortwave dynamics and related processes that form the foundation of remote sensing of the ocean surface.

In the next section, the experimental program and the instruments used for the measurements are described. Section 3 shows the effects of swell on the probability distribution of the slope components. Section 4 discusses the effects of wind stress, atmospheric stability, and swell parameters on the mean square slope. Additional discussion and concluding re-

marks are given in section 5. The results related to the slope spectrum and modulation of short waves by long waves are given in separate papers by *Shemdin and Hwang* [this issue] and *Hwang and Shemdin* (Modulation of short waves by long surface waves, submitted to *Journal of Fluid Mechanics*, 1988, also Modulation of short waves by surface currents, A numerical solution, submitted to *Journal of Geophysical Research*, 1988).

## 2. THE EXPERIMENTAL PROGRAM AND INSTRUMENTATION

The TOWARD Experiment was designed to provide experimental verification of the mechanisms involved in radar

remote sensing of the ocean surface, especially those related to the synthetic aperture radar (SAR). The optical slope measurements discussed in this paper are a part of the extensive data sets acquired to provide information on the modulation of short ocean waves. For a complete description of the TOWARD plan and preliminary results, the reader is referred to Shemdin et al. [1986a, b].

To facilitate measurements of shortwave quantities in the oceanic environment, the relevant sensors were mounted on a wave follower. The wave follower assembly was installed on the south extension structure of the Naval Ocean Systems Center (NOSC) tower (Figure 1). The assembly was placed 7.0 m away from the tower structure and was connected to it by a catwalk (see Figure 2). A set of instruments (a pressure transducer, denoted by a in Figure 2, and a two-dimensional electromagnetic (em) current meter shown by b in Figure 2) were installed at the bottom of the fixed structure of the wave follower assembly to provide long wave directional measurements.

On the moving frame (also referred to as the C frame), four instruments were mounted, as shown in Figure 3. A capacitance gauge, denoted by c in Figure 3, was used as an elevation control sensor. This sensor provided the feedback signal to the servo system to maintain the C frame at a fixed elevation with respect to the instantaneous water level. A two-dimensional em current meter (d in Figure 3) was mounted on the lower arm of the C frame to provide information of the near-surface current. The two-dimensional optical wave slope sensor (e in Figure 3) and the optical wave height sensor (Reticon camera, f in Figure 3) were used to measure the slopes and height of the short waves. The light source for both

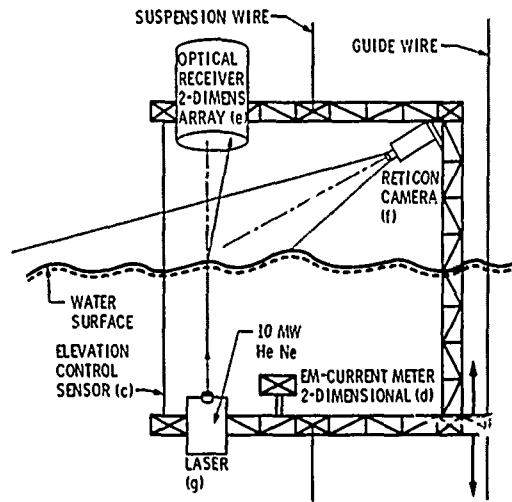


Fig. 3. Wave follower instrument frame. A capacitance gauge is used as elevation control sensor (labeled c). A two-dimensional current meter (d) is used for measuring two horizontal current components near the water surface. An optical receiver (e) records two surface slope components. A Reticon camera (f) records vertical displacement of water surface, using a He-Ne laser (g) as light source.

optical sensors was the 10-mW laser (g in Figure 3) mounted on the lower arm of the C frame.

The wave slope sensor was calibrated in the laboratory before and after each experiment. Refraction of light at the air-water interface was simulated by light refraction at the air-glass interface (see top inset of Figure 4). The magnitude of the refracted angle was varied by moving the glass lens horizontally. Changes in azimuthal angle  $\psi$  were obtained by rotating the glass lens on the horizontal plane (see bottom inset in Figure 4). A typical calibration result is shown in Figure 4. Averaged over the azimuthal angles, Figures 5a and 5b show the calibration curves for phase I (fall 1984) and phase II (spring 1985), respectively. The uncertainty is estimated to be the lesser of  $\pm 0.5^\circ$  or  $\pm 13\%$  in water surface slope, in the range  $0^\circ$  to  $30^\circ$  based on phase II calibration data (eight calibration repetitions in phase II compared with two repetitions in phase I). The design and the operating principles of the slope sensor are well documented [Tober et al., 1973; Palm, 1975; Palm et al., 1977; Tang and Shemdin, 1983] and will not

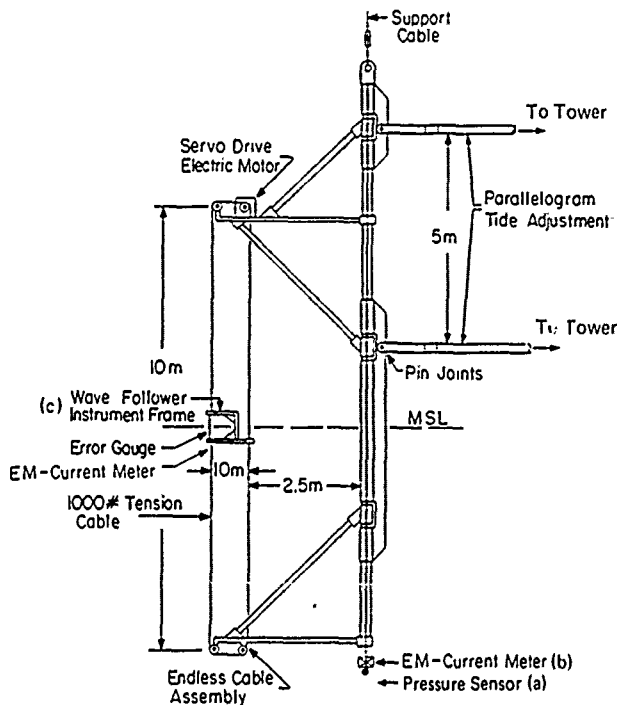


Fig. 2. Wave follower structural assembly. A pressure sensor (labeled a) and a two dimensional em current meter (b) are mounted on the fixed frame to measure long swell information. Other instruments mounted on wave follower instrument frame (c) are shown in Figure 3.

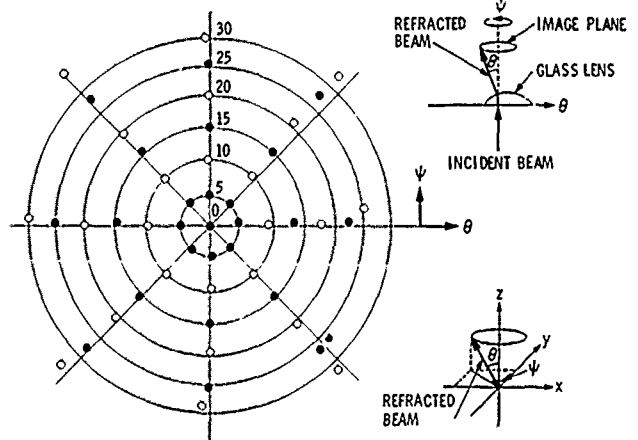


Fig. 4. Laboratory calibration of the wave slope instrument used in TOWARD 1984-1986.

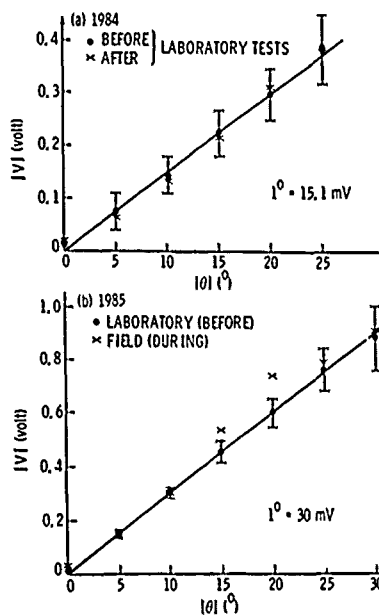


Fig. 5. Calibration of the wave slope instrument in (a) 1984 and (b) 1985.

be further elaborated on here. More than 100 hours of slope, current, wave, and wind time series were recorded on analog tapes from both phases of the experiment. From these recordings about 20 hours of prime data were digitized. The criteria for selection of the data segments to be digitized were based on periods of aircraft flights, periods of stereophoto sessions and ranges of wind, wave, and temperature conditions [Hwang, 1986a, b]. The data sets presented in this paper represent a typical subset of the digitized data but cover the range of the environmental conditions measured. A total of 36 data segments, each 5 min long, were processed. Table 1 lists the related parameters. The symbols used in this table are as follows:  $U_{10}$  is wind velocity in meters per second at 10 m above mean water surface;  $u_*$  is wind friction velocity in centimeters per second measured by the dissipation method;  $\theta_w$  is wind direction in degrees relative to true north;  $z/L$  is the dimensionless Monin-Obukhov stability parameter;  $T_a$  is air temperature and  $T_w$  is water surface temperature, both in degrees Celsius (the wind and temperature data were supplied by G. Geernaert in tabulated form; for further information on the measurements of the atmospheric parameters, see Geernaert *et al.* [this issue];  $\theta_{sw}$  is the angle between swell and wind, and  $\theta_{pw}$  is the angle between principal axis of slope vector and wind, both in degrees;  $\langle \eta^2 \rangle$  is the mean square surface elevation in square centimeters;  $\langle \eta_u^2 \rangle$ ,  $\langle \eta_c^2 \rangle$  are the mean square slope components in the principal (discussed in section 3) and cross-axis direction, respectively;  $C/U_{10}$  is wave age, or the ratio between the phase velocity of the peak component of the elevation-spectrum and wind speed; and  $KA$  is the longwave steepness.

### 3. OBSERVATIONS FROM THE PROBABILITY DISTRIBUTION FUNCTION

It was observed by Cox and Munk [1954, 1956] and Hughes *et al.* [1977] that there is little difference between the orientation of the wind direction and the principal axis of the slope

probability distribution; however, inspection of the present data shows that such is not the case for the TOWARD environment. Figure 6 gives an example of the joint probability density function (pdf) of wave slopes decomposed in the upwind and cross-wind directions. Deviation of the principal axis from the wind direction is obvious. Figure 6 further shows clearly the asymmetric characteristics of the along (principal) axis component compared with the relatively symmetric distribution in the cross-axis direction. Using these characteristics, it is easy to find the angle  $\alpha$  between the principal axis and the  $x$  axis of any orthogonal coordinate system ( $x, y$ ) from the following equation,

$$\alpha = \frac{1}{2} \tan^{-1} \frac{2\langle \eta_x \eta_y \rangle}{\langle \eta_y^2 \rangle - \langle \eta_x^2 \rangle} \quad (1)$$

where  $\langle \eta_x^2 \rangle$ ,  $\langle \eta_y^2 \rangle$  are the variance and  $\langle \eta_x \eta_y \rangle$  is the covariance of slope components in the ( $x, y$ ) directions. The covariance in the new principal axis coordinate system ( $u, c$ ), is zero by definition of cross-axis symmetry. The variance of the slope components in the ( $u, c$ ) coordinates are related to  $\langle \eta_x^2 \rangle$ ,  $\langle \eta_y^2 \rangle$  and  $\langle \eta_x \eta_y \rangle$  as follows

$$\langle \eta_u^2 \rangle = \langle \eta_x^2 \rangle \cos^2 \alpha + \langle \eta_y^2 \rangle \sin^2 \alpha - \langle \eta_x \eta_y \rangle \sin 2\alpha \quad (2)$$

$$\langle \eta_c^2 \rangle = \langle \eta_x^2 \rangle \sin^2 \alpha + \langle \eta_y^2 \rangle \cos^2 \alpha + \langle \eta_x \eta_y \rangle \sin 2\alpha \quad (3)$$

where  $\alpha$  is the angle between  $x$  and  $u$  axes.

Figure 7 plots  $\theta_{pw}$  vs.  $\theta_{sw}$ , where  $\theta_{pw}$  is the angular deviation of the principal axis of the joint pdf from the wind direction and  $\theta_{sw}$  is the swell direction relative to wind direction. The information of the orientation of the principal axis of the joint pdf was not available from Tang and Shemdin [1983], and therefore the MARSÉN data were not included in this figure. Based on the data shown in Figure 7, one observes a tendency toward increasing  $\theta_{pw}$  with  $\theta_{sw}$ . This tendency is somewhat weaker in the data set of Cox and Munk compared with TOWARD. It is possible that the wave age,  $C/U_{10}$ , may have some effects on the degree of shortwave reorientation from the wind direction. As is shown in Table 2, the well-developed swell system in TOWARD, with  $C/U_{10}$  in the range 2.5–6.6, is distinctively different from the local sea conditions that prevailed in the other two experiments. Furthermore, there appears to be a trend of symmetry about  $\theta_{sw} = \pm 90^\circ$ , i.e., a maximum reorientation of short waves occurs when the swell is perpendicular to the wind direction. Since radar backscatter is sensitive to the direction of short waves, it is important to know the principal direction of short waves. The available data suggest that swell modification is not small.

### 4. MEAN SQUARE SLOPE, EFFECTS OF ATMOSPHERIC STABILITY AND SWELL CHARACTERISTICS

The mean square slope generally increases with wind speed. Cox and Munk [1954, 1956] suggested the following linear relationship based on their sun glitter measurements.

$$s = 0.003 + 5.12 \times 10^{-3} U \pm 0.04 \quad (4)$$

The wind speed  $U$  (meters per second) in (4) was measured at 12.5 m above the mean sea level. The environmental conditions they tabulated indicated neutral to stable atmospheric stratification, and a (short fetch) locally generated wind sea. Hughes *et al.* [1977] used a laser optical instrument mounted on a ship's bow to measure the surface slope and obtained a

TABLE 1. Summary of the Experimental Conditions

File	Start Time	$U_{10}$ , m/s	$u_*$ , cm/s	$\theta_{sw}$ , deg	$z/L$	$T_a - T_{sw}$ , °C	$T_{sw}$ , °C	$\theta_{sw}$ , deg	$\theta_{pw}$ , deg	$10^3 \langle \eta^2 \rangle$ , cm <sup>2</sup>	$10^4 \langle \eta_u^2 \rangle$	$10^3 \langle \eta_c^2 \rangle$	$C/U_{10}$	KA	
<i>March 21, 1985</i>															
1	S04230a	1500	3.01	6.0	299	0.31	1.2	13.4	-26	-45.2	53.40	6.719	4.210	6.32	0.0155
2	S04230b	1505	2.91	6.1	303	0.33	1.2	13.4	-24	-37.1	32.70	5.793	3.294	6.22	0.0121
3	S04230c	1510	3.06	6.5	306	0.35	1.4	13.2	-28	-51.9	46.02	5.802	4.775	6.43	0.0144
4	S04232a	1520	2.72	5.2	316	0.44	1.5	13.1	-40	-59.6	37.46	6.477	4.048	5.85	0.0130
5	S04232b	1525	2.74	7.2	315	0.42	1.5	31.1	-41	-64.7	41.48	6.311	3.656	6.88	0.0137
6	S04232c	1530	2.52	6.6	314	0.47	1.5	13.1	-40	-54.1	45.98	6.984	4.262	6.83	0.0144
<i>March 25, 1985</i>															
7	S10003a	1630	5.70	17.3	218	0.01	0.0	13.6	41	4.4	34.05	19.46	12.61	2.94	0.0178
8	S10003b	1635	5.51	20.3	220	0.00	0.0	13.6	57	-9.0	38.83	27.70	13.75	2.84	0.0190
9	S10003c	1640	5.83	25.0	217	-0.01	-0.1	13.6	55	-7.1	38.80	28.52	13.75	2.40	0.0190
10	S10013a	1730	5.51	22.0	234	-0.02	-0.2	13.6	47	5.0	34.74	27.56	12.90	2.66	0.0180
11	S10013b	1735	5.44	22.1	231	-0.01	-0.2	13.6	41	11.0	45.30	25.42	13.36	2.83	0.0206
12	S10013c	1740	5.62	25.3	229	-0.01	-0.1	13.6	44	9.0	34.84	29.71	13.66	2.87	0.0180
13	S10015a	1750	5.57	23.0	228	-0.01	-0.1	13.6	47	1.0	43.15	28.26	13.10	2.84	0.0201
14	S10015b	1755	5.47	22.5	232	-0.01	-0.1	13.6	47	3.4	45.59	30.38	14.84	2.80	0.0206
15	S10015c	1800	5.13	17.7	239	-0.01	-0.1	13.6	45	5.0	40.17	27.57	13.68	2.85	0.0193
16	S10034a	1940	4.07	17.0	170	0.00	-0.1	13.7	100	47.1	41.36	15.35	11.46	3.80	0.0196
17	S10034b	1945	3.90	17.5	171	0.00	-0.1	13.7	105	47.8	35.80	16.39	11.94	3.83	0.0183
18	S10034c	1950	4.02	17.5	171	0.00	-0.1	13.7	104	44.6	50.41	10.09	12.23	4.00	0.0217
19	S10040a	2000	5.00	17.8	155	0.00	0.0	13.7	120	26.3	37.19	17.19	11.76	3.54	0.0188
20	S10040b	2005	4.53	20.5	151	0.00	0.0	13.7	120	26.3	42.63	15.59	11.04	3.12	0.0199
21	S10040c	2010	4.59	16.8	168	0.00	0.0	13.7	114	32.3	37.74	16.11	11.02	3.47	0.0188
<i>March 27, 1985</i>															
22	S17213a	1330	5.36	17.6	221	0.13	1.3	13.9	50	26.5	34.78	9.998	6.200	3.75	0.0149
23	S17213b	1335	5.12	16.9	223	0.14	1.2	13.9	59	28.7	22.26	8.776	5.014	3.39	0.0119
24	S17213c	1340	4.81	16.1	224	0.16	1.3	13.9	57	31.1	34.84	9.615	6.258	3.54	0.0119
25	S17220a	1400	5.25	19.9	247	0.06	0.8	13.9	26	-5.3	30.61	17.09	5.398	3.21	0.0140
26	S17220b	1405	6.60	20.8	243	0.04	0.6	14.0	33	1.6	35.43	23.66	7.471	2.90	0.0150
27	S17220c	1410	6.59	20.8	230	0.04	0.5	14.0	37	5.7	25.99	25.05	8.172	2.75	0.0129
28	S17223a	1630	5.26	17.0	254	0.08	0.8	14.0	35	-4.3	38.53	16.25	6.197	3.52	0.0157
29	S17223b	1655	5.04	16.6	256	0.10	0.9	14.0	26	2.2	27.20	17.31	6.203	3.45	0.0132
30	S17223c	1680	5.48	16.8	260	0.01	1.0	14.0	24	6.3	21.60	15.04	5.899	3.58	0.0117
31	S17230a	1500	5.71	19.1	255	0.12	1.3	14.0	32	8.0	25.65	12.91	5.710	3.32	0.0128
32	S17230b	1505	5.13	16.9	258	0.14	1.3	14.0	35	4.4	33.71	15.55	5.900	3.31	0.0147
33	S17230c	1510	5.16	15.3	259	0.14	1.3	14.0	32	8.3	30.28	13.46	5.665	3.18	0.0139
34	S17233a	1530	4.58	12.8	254	0.20	1.5	13.9	27	0.0	31.27	8.578	5.606	3.54	0.0141
35	S17233b	1535	4.42	14.8	259	0.18	1.5	13.9	26	-1.8	34.13	8.936	5.198	3.98	0.0147
36	S17233c	1540	4.82	12.9	259	0.19	1.5	13.9	21	-6.2	22.48	8.848	5.675	3.69	0.0120

similar linear relationship. The conditions of long waves was not listed in their study. They noted, however, that the fetch was generally short (mostly less than 17 km except for one case with a fetch of 77.5 km). Further, the air-sea temperature difference during their experiment was consistently positive and stable. Tang and Shemdin [1983] used a laser optical instrument mounted on a wave follower to measure surface slope from the Noordwijk tower, Netherlands. They found that there is a group of data with wind speed between 4 and 6 m/s with mean square slope 2 to 3 times higher than the results from other experiments in the same range of wind speed. Tang and Shemdin stated that the swell condition may be contributing to the observed differences. Notably, they found that in the presence of a swell-system (wherever double peaks were noted in the surface elevation spectra they identified them as "mixed sea" condition) the measured mean square slopes were much higher than those shown by Cox and Munk. On the other hand, in a wind-sea condition (single peak in the displacement spectrum, which they identified as "well-defined peak" condition) the mean square slope was found to be in good agreement with the data set of Cox and Munk.

Figure 8 presents the mean square slope versus wind friction velocity. Data from all four field experiments cited above are included. Whenever  $u_*$  was not reported in the original

report, the following equation for the drag coefficient  $C_{10}$  was used to convert wind velocity to  $u_*$  [Wu, 1980, 1982]:

$$C_{10} = (0.8 + 0.65 U_{10}) \times 10^{-3} \quad (5)$$

The data set collected during the TOWARD Experiment displays a different trend of wind dependence (inset, Figure 8). The mean square slope increases gradually with wind friction velocity at low wind, followed by a rapid growth near  $u_* = 20$  cm/s and beyond. Interestingly, the large deviation of MARSSEN data from those of Cox and Munk and Hughes et al. also occurred near  $u_* = 20$  cm/s.

In the following, we discuss the effects of swell and stability on the surface roughness. Since the data set of Hughes et al. did not give quantitative swell and stability information, it is excluded from the subsequent presentation. The data set of Cox and Munk, collected under the condition of wind-generated sea, is used as the reference relationship between mean square slope  $s_0$  and  $u_*$  under neutral and wind-sea conditions. The following equation was obtained from the least squares fit of their data:

$$s_0 = 10^{-3} (11.0 + 1.10 u_*) \quad (6)$$

where  $u_*$  is in centimeters per second.

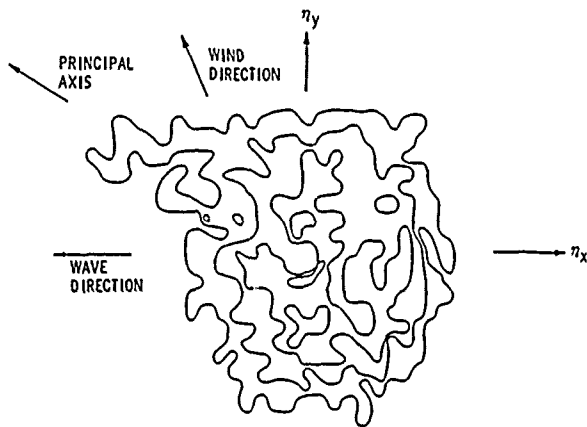


Fig. 6. An example of the joint probability distribution of wave slopes. Deviation of the principal axis from wind direction is not trivial when wind and swells are not colinear (case S17220).

We have assumed that the surface tension was similar in all the data sets considered, since surface tension of clean water varies from 7.23 N/m at 26°C (typical of Cox and Munk's experiment) to 7.48 N/m at 10°C (the lower limit of the other two data sets). We further assume that the deviation of  $s$  from  $s_0$  is from the effects of swell, atmospheric stability, and other factors, and that the different effects are linearly additive, i.e.,

$$s = s_0 + f_1'( \text{stability} ) + f_2'( \text{swell} ) + \dots \quad (7)$$

or normalizing by  $s_0$

$$s_r = s/s_0 = 1 + f_1( \text{stability} ) + f_2( \text{swell} ) + \dots \quad (8)$$

Our knowledge of the functions  $f_1$  and  $f_2$  is only qualitative. For the first function,  $f_1$ , we expect that an unstable stratification at the air-water interface enhances the momentum exchange and therefore increases the surface roughness. For the second function,  $f_2$ , conflicting results are reported in the literature. Analytical studies suggest that the wave-induced current and wind drift tends to suppress the short waves by breaking the small waves prematurely [Banner and Phillips,

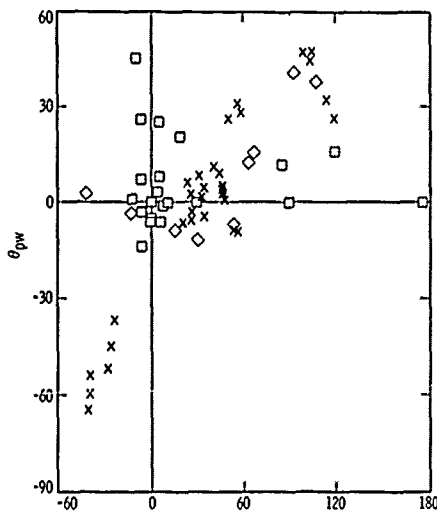


Fig. 7. Dependence of the angle between principal axis and wind,  $\theta_{pw}$ , on the angle between wind and swell,  $\theta_{ws}$ . Symbols are crosses, TOWARD; squares, Cox and Munk [1954], diamonds, Hughes et al. [1977].

TABLE 2. A Summary of the Representative Environmental Conditions for the Experiments Cited in This Paper

	Cox and Munk	Hughes et al.	Tang and Shemdin	TOWARD
$U$ , m/s <sup>a</sup>	0.7-13.8	3.6-8.2	3-12.7	2.5-6.6
$u_*$ , cm/s	...	10.6-28.9	...	5.2-25.3
$C/U_{10}$	0.4-6.5 <sup>b</sup>	...	0.7-3.0	2.4-8.3
$KA$	0.10-0.34	...	0.03-0.08	0.01-0.02
Fetch, km	...	4-16 <sup>c</sup>	...	...
$R$	-0.03-12.5	stable	...	-0.01-2.58
$z/L$	...	...	...	-0.02-0.47

<sup>a</sup>Elevation of wind speed is as follows: Cox and Munk, 41 feet (12.5 m); Hughes et al., 19.5 m; Tang and Shemdin, not specified; TOWARD, 10 m, calculated from  $U$  (18 m).

<sup>b</sup>Eighteen out of 23 of Cox and Munk's data points have  $C/U_{10} < 1$ .

<sup>c</sup>Except one case with fetch of 77.5 km.

1974; Phillips and Banner, 1974]. However, the analysis of Tang and Shemdin implied increased roughness in the mixed sea condition in the presence of swell. The microwave measurement of Plant and Wright [1977] did not show any significant effects of drift current on the short wave amplitude. On the other hand, laboratory experiments of Mitsuyasu [1966] and Donelan [1987] provided convincing evidence that shortwave variance is reduced by addition of a mechanical wave train to the wind-wave system. In the following we carry out correlation studies of the normalized mean square slope with the swell and atmospheric stability parameters.

#### 4.1. Swell as the Primary Modifying Factor

First, we consider the swell to be the primary factor that modifies the relationship between the mean square slope and wind friction velocity  $u_*$ . Expecting  $s_r$  to be closely related to certain swell parameters, we plot in Figure 9  $s_r$  versus  $C/U_{10}$ , the wave age of the dominant swell. It is customary to classify  $C/U_{10} < 1$  as the wind-generated sea and  $C/U_{10} > 1$  as swelled condition. The measurement of surface slope (which is

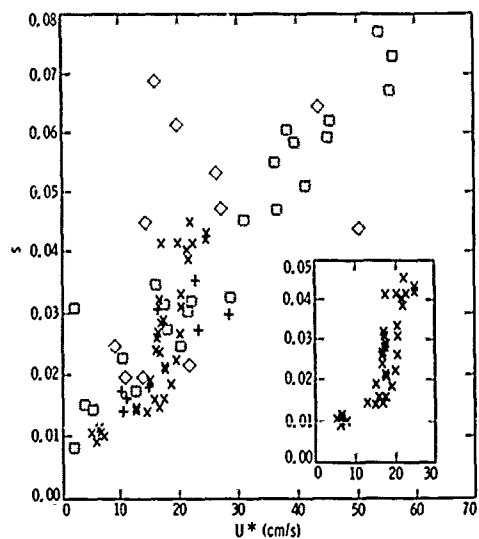


Fig. 8. Mean square slope versus wind friction velocity for TOWARD data (crosses), Cox and Munk [1954] (squares), Hughes et al. [1977] (pluses), and Tang and Shemdin [1983] (diamonds). Note the rapid growth in the range of  $u_* = 16-22$  cm/s of TOWARD data as shown in inset.

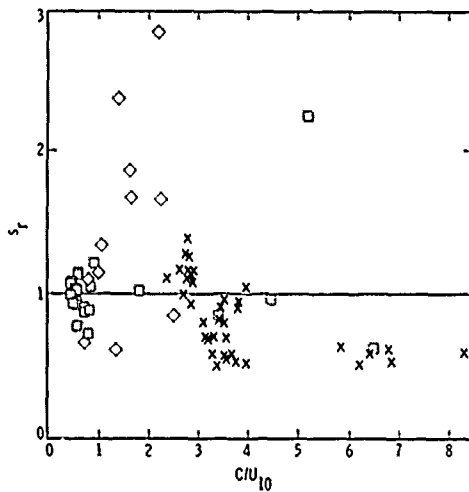


Fig. 9. Plot of the normalized mean square slope  $s_r$  versus wave age  $C/U_{10}$ . Symbols are the same as in Figure 8.

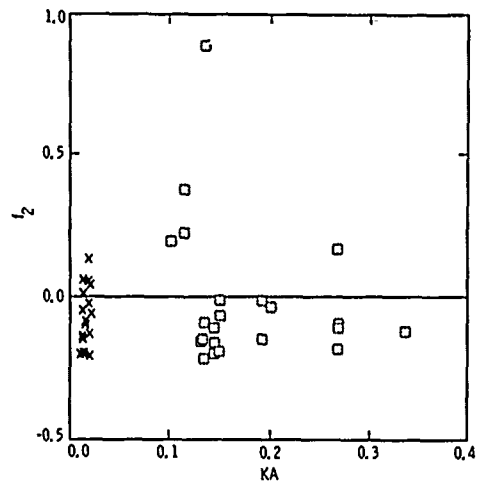


Fig. 10. Same as Figure 9 but for  $s_r$  versus the swell steepness  $KA$ . Symbols are the same as in Figure 8.

primarily contributed by short waves) presented in Figure 9 indicates that the presence of a swell system can either enhance or reduce the surface roughness. In particular, when the wind speed is low,  $C/U_{10} > 3$ , the observations indicate a reduction of mean square slope up to 40%. There is, however, a narrow region,  $1 < C/U_{10} < 3$ , where the mean square slope is significantly higher than that of a wind-generated sea.

A complete analysis of the swell and wind wave system must involve not only the interactions of the air and water boundary layers, but also interactions of long and short waves. Although there are repeated reports on the reduction of short waves in the presence of a swell, there is little agreement on the mechanisms that contribute to such an effect. *Plant and Wright* [1977] disputed the small-scale breaking mechanism induced by wind drift and orbital velocity suggested by *Phillips and Banner* [1974]. *Donelan* [1987] found the growth rate of wind-generated short waves in the laboratory to be insensitive to mechanically generated long waves. He suggested that the reduction in shortwave energy may be due to a detuning of the resonant condition between the short waves and the wind. Such a mechanism, while plausible, has to be verified. The suggestion from Figure 9 that the surface roughness can increase in the presence of waves has not been observed under laboratory conditions. *Hwang* [1986b] estimated the enhancement in surface roughness to be to the domain where  $C_g = U_{10}$ , where  $C_g$  is the group velocity of swell.

Figure 10 plots  $s_r$  versus  $KA$ , the swell steepness. Comparing Figures 10 and 9, it is clear that these two parameters ( $C/U_{10}$  and  $KA$ ) are not statistically independent in the three data sets available. There does not appear to be a clear trend of the data in Figure 10 other than the feature discussed previously. Future experiments, carried out in a controlled environment with a wide range of  $C/U_{10}$  and  $KA$  values, are desirable to identify the role of swell in the modulation and modification of the statistics of short surface waves.

#### 4.2. Stability as the Primary Factor

Next to the wind friction velocity, here we consider atmospheric stability to be the primary factor influencing the mean square slope. Atmospheric stability is generally expressed in

terms of the Monin-Obukhov parameter,

$$\frac{z}{L} = \frac{gKz\langle w'T_a' \rangle}{u_*^3\langle T_a \rangle} \quad (9)$$

where  $L$  is the Monin-Obukhov length scale,  $K$  is the von Kármán constant,  $w'$  is the fluctuation component of the vertical velocity,  $T_a'$  is air temperature fluctuation, and  $\langle T_a \rangle$  is the mean air temperature. When only the air and water temperatures are reported, we use the following expression (a reduced Richardson's number) to characterize atmospheric stability

$$R = \frac{g(\langle T_a \rangle - \langle T_w \rangle)}{u_*^2\langle T_w \rangle} \quad (10)$$

where  $\langle T_w \rangle$  is water temperature. Equations (9) and (10) allow intercomparisons among the different data sets when only temperature data are available. The TOWARD data show the relationship between  $R$  and  $z/L$  to be monotonic and smooth, as is shown in Figure 11. The normalized mean square slope  $s_r$  (equation (8)), calculated from the TOWARD data set, is plotted versus  $z/L$  in Figure 12. A reduction in the mean square

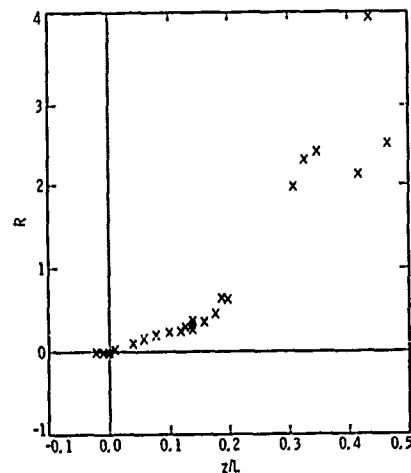


Fig. 11. Comparison of the two stability factors,  $R$  and  $z/L$ . Data from TOWARD show smooth and monotonic relationship between the two parameters.

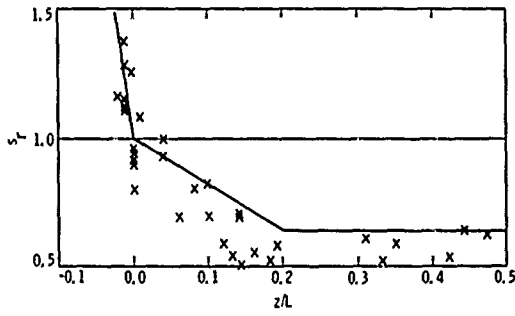


Fig. 12. Same as Figure 9, but for  $s_r$  versus  $z/L$ ; data are from TOWARD.

slope ( $s_r$  of less than 1) for stable conditions ( $z/L$  positive) is evident. The reduction is approximately linear for mildly stable conditions but reaches a limit at  $(z/L)_c = 0.20$ . For  $z/L > (z/L)_c$ ,  $s_r$  does not decrease any more. For unstable conditions there is a sharp increase in the mean square slope. The range of  $z/L$  in the data set is very limited, however. Figure 13 plots  $s_r$  versus  $R$ . In this figure both data sets of TOWARD and Cox and Munk are presented. Both data sets display similar stability effects on the mean square slope. From these data sets, the following corrections are proposed:

$$\begin{aligned} f_1(z/L) &= -24 z/L & -0.02 < z/L < 0 \\ f_1(z/L) &= -1.8 z/L & 0 < z/L < 0.2 \\ f_1(z/L) &= -0.32 & z/L > 0.2 \end{aligned} \quad (11)$$

or in terms of  $R$ ,

$$\begin{aligned} f_1(R) &= -15 R & -0.03 < R < 0 \\ f_1(R) &= -0.72 R & 0 < R < 0.5 \\ f_1(R) &= -0.32 & 0.5 < R < 3.5 \end{aligned} \quad (12)$$

The solid curves in Figures 12 and 13 correspond to equations (11) and (12), respectively. These trends are similar to the effect of stability on momentum transfer at the air-water (or air-land) interface [Lemon and Yaglom, 1971].

The dependence of radar backscatter on atmospheric stability has been noted [Guinard et al., 1971; Keller et al., 1985]. Guinard et al. [1971, p. 1535] compared radar measurements at high sea states for various air-sea stability conditions and found that "the effect on the [radar] cross section of the tem-

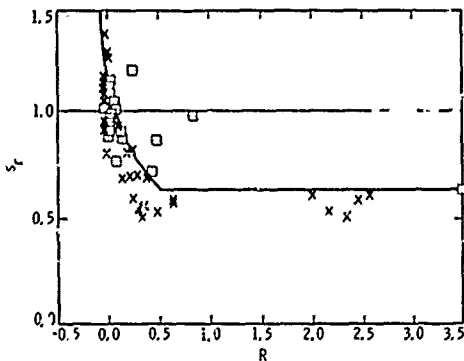


Fig. 13. Same as Figure 12, but for  $s_r$  versus  $R$ . Symbols are the same as in Figure 8.

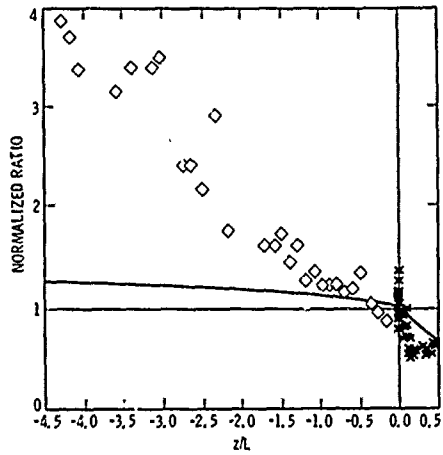


Fig. 14. The effect of unstable air-sea interface on mean square slope (crosses), compared with the effects on the radar cross section (diamonds) and wind stress (solid curve) reported by Keller et al. [1985].

perature difference is equivalent to a change in wind speed from 5 to 20 m/s." Unfortunately, there were no quantitative temperature measurements in that mission. Keller et al. obtained a unique set of radar measurements under unstable conditions simultaneously with wind and temperature measurements. They found the (relative) radar cross-section to increase with wind speed (or wind friction velocity), and to display a distinctive dependence on the air-sea temperature difference. Their results show that the cross section, normalized by the reference cross-section (i.e., radar cross section corresponding to near-neutral condition) increases steadily with decreasing  $z/L$ . They also showed the increase in cross section with negative  $z/L$  to be stronger than the corresponding increase due to wind stress (Figure 14). These observations are consistent with the observed effects of stability on the mean square slope noted in Figure 14.

When applying the atmospheric stability correction (equations (11) and (12)) to the mean square slope data, the swell effect ( $f_2$  in equation (8)) is found to have a weak dependence on  $C/U_{10}$  (Figure 15) and on  $KA$  (Figure 16). The large in-

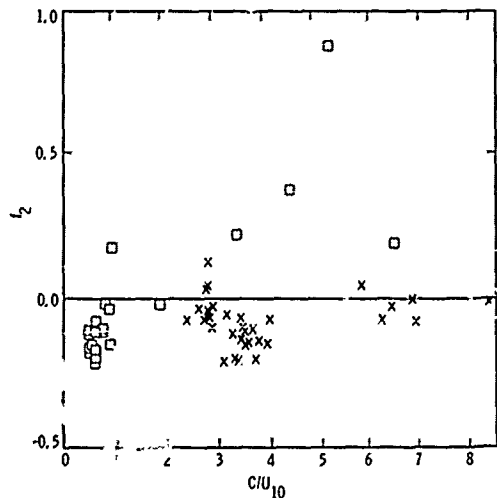


Fig. 15. Normalized residual mean square slope after stability adjustment versus  $C/U_{10}$ . Symbols are the same as in Figure 8.

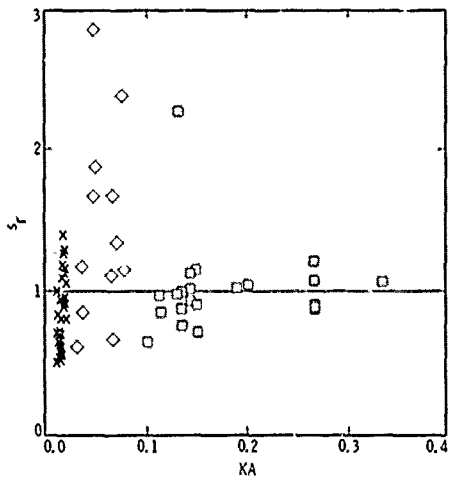


Fig. 16. Same as Figure 15, but for  $s_0$  versus  $KA$ . Symbols are the same as in Figure 8.

crease in surface roughness in the MARSEN Experiment [Tang and Shemdin, 1983] under "mixed sea" conditions may have coincided with unstable atmospheric conditions. However, since air and water temperatures were not reported, this point can not be verified.

#### 4.3. Other Wind Speed Dependence of Mean Square Slope

Wu [1972] reanalyzed the data of Cox and Munk [1956]. By arguing that the wind wave spectrum is at equilibrium in the shortwave range, he suggested that the dependence of the mean square slope on wind speed is logarithmic and can be approximated by

$$\begin{aligned} s_0 &= 0.01 \ln U_{10} + 0.6 \quad U_{10} < 7 \text{ m/s} \\ s_0 &= 0.085 \ln U_{10} - 0.145 \quad U_{10} > 7 \text{ m/s} \end{aligned} \quad (4')$$

The division of data into two separate regions is believed to be caused by the change of the flow regimes from hydrodynamically smooth and transitional to hydrodynamically rough at 7-m/s wind. Replotting the mean square slope versus wind friction velocity, we find the following approximation to be reasonable:

$$\begin{aligned} s_0 &= 0.010 \ln u^* - 0.0010 \quad u^* < 26.7 \text{ cm/s} \\ s_0 &= 0.116 \log u^* - 0.132 \quad u^* > 26.3 \text{ cm/s} \end{aligned} \quad (6')$$

The computational procedure in sections 4.1 and 4.2 were repeated using (6') instead of (6) in the normalizing process. The dependence of the mean square slope on atmospheric stability and sea state parameters are found in this procedure to be similar to the results already presented in sections 4.1 and 4.2. This lends support to the conclusions derived in this paper as being insensitive to the detailed form of mean square slope dependence on wind speed used.

## 5. CONCLUSIONS

Recent field data on short waves from the optical slope measurement indicate deviation from the linear (or logarithmic) dependence of the mean square slope on wind speed established previously [Cox and Munk, 1956; Wu, 1972]. The deviation is found to be correlated with the stability condition

at the air-water interface and, to a lesser degree, with the swell conditions at the experimental sites. On the basis of the available data, it appears that the surface roughness increases significantly whenever a slightly unstable stratification prevails. There appears to be a lower bound for wave suppression due to positive atmospheric stability. The enhancement of surface roughness under unstable conditions and the suppression under stable conditions appear to exceed the corresponding enhancements and suppressions of wind stress and radar return under equivalent stability conditions. The presence of a swell system appears to reduce the sea surface roughness, but the effect is small compared with the influence of atmospheric stability. The direction of the slope vector deviates from the direction of wind owing to the presence of long waves. The larger the wave age, the more effective is the steering of short waves away from wind direction by the long waves.

*Acknowledgments.* The support for this work by the Ocean Science Division, Office of Naval Research (project N00014-86-C-0303) is gratefully acknowledged. The Instrumentation Group of the Jet Propulsion Laboratory provided technical support for operating the wave following system. Here particular credit goes to R. Martin and D. Hoff, Ken Davidson, Gary Geernaert, and Bob Guza provided data defining the atmospheric and oceanic environmental parameters.

## REFERENCES

- Banner, M. L. and O. M. Phillips, On the incipient breaking of small scale waves, *J. Fluid Mech.*, 65, 647-656, 1974.
- Chelton, D. B., and P. J. McCabe, A review of satellite altimeter measurement of sea surface wind speed: With a proposed new algorithm, *J. Geophys. Res.*, 90, 4707-4720, 1985.
- Cox, C., and W. Munk, Slope of sea surface derived from sun glitter, *J. Mar. Res.*, 13, 198-227, 1954.
- Cox, C., and W. Munk, Slope of the sea surface deduced from photographs of sun glitter *Bull. Scripps Inst. Oceanogr.*, 6, 401-488, 1956.
- Donelan, M. A., The effect of swell on the growth of wind waves, *APL Tech. Dig.*, 8, 18-23, 1987.
- Evans, D. D., and O. H. Shemdin, An investigation of modulation of capillary and short gravity waves in the open ocean, *J. Geophys. Res.*, 85, 5019-5024, 1980.
- Geernaert, G. L., K. L. Davidson, S. E. Larsen, and T. Mikkelsen, Wind stress measurements during the Tower Ocean Wave and Radar Dependence Experiment, *J. Geophys. Res.*, this issue.
- Gunard, N. W., J. T. Rosson, Jr., and J. C. Daley, of the NRCS of the sea with increasing roughness, *J. Geophys. Res.*, 76, 1525-1538, 1971.
- Hasselmann, K., R. K. Rancey, W. J. Plant, W. Alpers, R. A. Shuchman, D. R. Lyzenga, C. L. Rufenach, and M. J. Tucker, Theory of synthetic aperture radar ocean imaging: A MARSEN view, *J. Geophys. Res.*, 90, 4659-4686, 1985.
- Huang, N. W., New development in satellite oceanography and current measurements, *Rev. Geophys.*, 17, 1558-1568, 1979.
- Hughes, B. A., H. L. Grant, and R. W. Chappell, A fast response surface-wave slope meter and measured wind-wave moments, *Deep Sea Res.*, 24, 1211-1223, 1977.
- Hwang, P. A., Wave follower measurements during TOWARD 84/85, *Rep. ORE 86-1*, 43 pp., Ocean Research and Engineering, Pasadena, Calif., 1986a.
- Hwang, P. A., Surface slope measurement with a wave follower in TOWARD 84/86, *Rep. ORE 86-3*, 67 pp., Ocean Research and Eng., Pasadena, Calif., 1986b.
- Keller, W. C., W. J. Plant, and D. I. Weissman, The dependence of X band microwave sea return on atmospheric stability and sea state, *J. Geophys. Res.*, 90, 1019-1029, 1985.
- Lubard, S. C., J. E. Krimmel, L. R. Thebaud, D. D. Evans, and O. H. Shemdin, Optical image and laser slope meter intercomparisons on high-frequency waves, *J. Geophys. Res.*, 85, 4996-5002, 1980.
- Mitsuyasu, H., Interactions between water waves and wind, 1, *Rep. Res. Inst. Appl. Mech. Kyushu Univ.*, 14, 67-88, 1966.
- Monin, A. S., and A. M. Yaglom, *Statistical Fluid Mechanics: Mechanics of Turbulence*, vol. 1, translated from Russian, MIT Press, Cambridge, Mass., 1971.

- Palm, C. S., An instrument to measure the two-dimensional wave-slope spectrum of ocean capillary waves, Ph.D. dissertation, Univ. of Fla., Gainesville, 1975.
- Palm, C. S., R. C. Anderson, and A. M. Reece, Laser probe for measuring 2-D wave slope spectra of ocean capillary waves, *Appl. Opt.*, *16*, 1074-1081, 1977.
- Phillips, O. M. and M. L. Banner, Wave breaking in the presence of wind drift and swell, *J. Fluid Mech.*, *66*, 625-640, 1974.
- Plant, W. J., and J. W. Wright, Growth and equilibrium of short gravity waves in a wind-wave tank, *J. Fluid Mech.*, *82*, 767-793, 1977.
- Shemdin, O. H., and P. A. Hwang, Comparison of measured and predicted sea surface spectra of short waves, *J. Geophys. Res.*, this issue.
- Shemdin, O. H., et al., *TOWARD Field Experiment Interim Report*, vol. I, *Data Summary and Early Results*, Jet Propulsion Laboratory, Pasadena, Calif., 1986a.
- Shemdin, O. H., et al., *TOWARD Field Experiment Interim Report*, vol. II, *Contributions of Individual Investigators*, Jet Propulsion Laboratory, Pasadena, Calif., 1986b.
- Tang, S., and O. H. Shemdin, Measurement of high frequency waves using a wave follower, *J. Geophys. Res.*, *88*, 9832-9840, 1983.
- Tober, G., R. C. Anderson, and O. H. Shemdin, Laser instrument for detecting water ripple slopes, *Appl. Opt.*, *12*, 788-794, 1973.
- Wu, J., Sea surface slope and equilibrium wind-wave spectrum, *Phys. Fluids*, *15*, 741-747, 1972.
- Wu, J., Wind-stress coefficients over sea surface near neutral conditions—A revisit, *J. Phys. Oceanogr.*, *10*, 727-740, 1980.
- Wu, J., Wind-stress coefficients over sea surface from breeze to hurricane, *J. Geophys. Res.*, *87*, 9704-9706, 1982.
- 
- P. A. Hwang and O. H. Shemdin, Ocean Research and Engineering, 255 S. Marengo Avenue, Pasadena, CA 91101.

(Received September 7, 1987;  
accepted January 27, 1988.)

# Wind Stress Measurements During the Tower Ocean Wave and Radar Dependence Experiment

G. L. GEERNAERT

*Naval Research Laboratory, Washington, D. C.*

K. L. DAVIDSON

*Department of Meteorology, Naval Postgraduate School, Monterey, California*

S. E. LARSEN AND T. MIKKELSEN

*Riso National Laboratory, Roskilde, Denmark*

During the Tower Ocean Wave and Radar Dependence Experiment (TOWARD), near-continuous measurements of the wind drag were conducted using the dissipation technique. An intercomparison between these measurements and direct stress magnitudes using a sonic anemometer was performed over 3 days of the experiment. The results indicated that the dissipation technique compared well to the directly determined values when conditions were steady and neutral; otherwise, the dissipation method performed poorly. When neutrally stratified data were used, the drag coefficient exhibited a systematic dependence on both surface tension and wave age.

## 1. INTRODUCTION

The determination of the wind stress over the sea on fine spatial and temporal scales is fundamental to operational air-sea modeling. Wave state, boundary layer depth, turbulence intensity, waveguide predictions, and signal propagation both above and below the interface all depend to some degree on the magnitude of the wind stress. The physical problem of determining the wind stress, however, is not dependent only on the surface layer wind shear and thermal stratification; information on the state of the surface wave development must also be known. The interplay between the waves and the wind stress which generates and maintains the energy and slope of the waves is both complex and far from understood.

Since the wind stress  $\tau$  is the primary momentum source for surface wave growth, the scatterometer model function, which relates the wind speed to the radar cross section  $\sigma_0$ , requires a physical model of the air-sea energetics. The cross section, in fact, is more directly related to the wind stress [Keller *et al.*, 1985], and it is both a theoretical and experimental problem to relate the stress to the overlying wind. It therefore follows that for any given wind speed, variations in  $\sigma_0$  are due, at least in large part, to variations in the drag coefficient. By definition, the wind stress (or momentum flux) is related to the wind speed through a drag coefficient  $C_D$  such that

$$\tau = \rho C_D |U|U \quad (1)$$

where  $U$  is the mean wind velocity and  $\rho$  is air density. The drag coefficient has been observed by many investigators to depend on wind speed, stratification, and wave state [Businger *et al.*, 1971; Geernaert *et al.*, 1986].

Measurements of the drag coefficient have been reported by many experimentalists, and there are currently large differ-

ences between the suggested  $C_D$  values at any given wind speed [Geernaert, 1987] (see Figure 1). The differences between the drag coefficient regression equations of Figure 1 are thought to be most likely due to sea states that consistently differ between the measurement sites. It is therefore desirable for current field investigations of the wind stress to include detailed characteristics of the surface wave field. Characterizing the wind stress in terms of bulk weather information and a drag coefficient is a practical method for providing wind stress estimates, and as Figure 1 implies, the drag coefficient must be parameterized with bulk wave information as well. It is the intent of many field investigators to determine both theoretically and experimentally the nature of the wave state dependence.

Direct measurements of the stress require that the covariance between the turbulent fluctuations of horizontal and vertical wind velocity be obtained. However, in order to conduct such a direct measure, the platform must be steady and free of flow distortion, and as a consequence, most direct drag coefficient calculations are based from low-flying airplanes, coastal masts, and/or towers firmly mounted to the seafloor. Since the most practical platform is a moving ship, an alternative method, the dissipation technique, is often employed. For neutral stratifications and moderate to high wind speeds over the open ocean, Fairall and Larsen [1986] and Large and Pond [1981] have shown close agreement between the dissipation technique and the direct covariance method. Measurements over arctic ice floes in the marginal ice zone by Guest and Davidson [1987] have similarly shown close agreement. However, for largely nonneutral stratifications, little data have so far been collected over the sea to validate the dissipation technique.

During the autumn of 1984 and the spring of 1985, the Tower Ocean Wave and Radar Dependence Experiment (TOWARD) was conducted on a tower 2 km offshore of San Diego, California. Because the wind stress is a key element in describing sea surface energetics, both a sonic anemometer

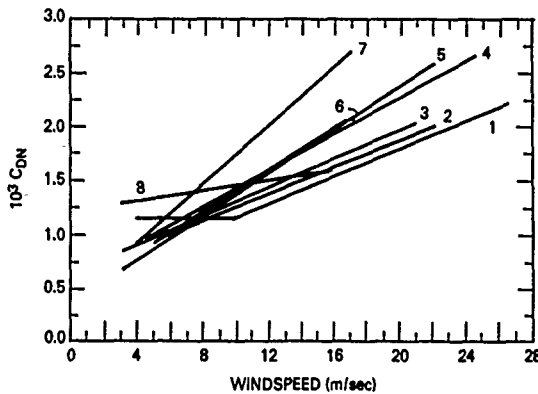


Fig. 1. Distribution of the neutral drag coefficient with wind speed from the following investigations: 1, *Large and Pond* [1981]; 2, *Smith* [1980]; 3, *Smith and Banke* [1975]; 4, *Geernaert et al.* [1987b]; 5, *Geernaert et al.* [1986]; 6, *Sheppard et al.* [1972]; 7, *Donelan* [1982]; 8, *Kondo* [1975].

and a hot-film system were included in the data collection package. The sonic provided direct wind stress measurements, while the hot film was used to obtain estimates of the stress by the dissipation technique. In the next section, a summary of the basic turbulence theory applicable to the surface layer is presented. In section 3, the experiment is described. The results, which include both the comparison between the sonic and hot film data and the dependence of the drag coefficient on wave state will be presented in section 4, while in section 5 we summarize the results in light of recommendations for further research.

## 2. BASIC THEORY

The vertical profiles of the surface layer wind speed, temperature, and humidity over the sea can be described by the vertical turbulent fluxes of momentum, sensible heat, and latent heat. These fluxes, being the primary mechanism for atmosphere-ocean momentum and energy exchange and wind wave generation, may be evaluated directly by performing the covariance between fluctuating variables or indirectly by the use of energy and variance budgets or with vertical profiles of mean quantities.

By assuming stationarity and an averaging time long enough so that the vertical velocity approaches zero and the ensemble mean is approached, the flux of momentum,  $\tau$ , sensible heat  $H$ , and latent heat  $E$ , may be represented directly by the following relations:

$$\tau/\rho = -\langle u'w' \rangle \hat{i} - \langle v'w' \rangle \hat{j} \quad (2)$$

$$H = \rho c_p \langle w'T' \rangle \quad (3)$$

$$E = \rho L_v \langle w'q' \rangle \quad (4)$$

where  $c_p$  is the specific heat of air at constant pressure,  $L_v$  is the latent heat of vaporization,  $T$  is the potential temperature,  $q$  is the specific humidity, and  $u$ ,  $v$ , and  $w$  are the instantaneous longitudinal, lateral, and vertical wind velocity components. Primed quantities indicate perturbations about a mean value. By convention, the wind stress is defined to be positive downward, while the heat fluxes are positive upward. Devices such as sonic and Gill propeller anemometers and fast response temperature and humidity sensors are capable of directly measuring these fluxes.

In a coordinate system defined where  $V = 0$  while remaining at the bottom of the Ekman layer, the lateral stress,  $\langle v'w' \rangle$  is small relative to the longitudinal stress  $\langle u'w' \rangle$ . However, since the atmospheric boundary layer is three-dimensionally turbulent and baroclinic terms are often important, especially near storms, we will define an angle  $\theta$  such that

$$\theta = \arctan(-\langle v'w' \rangle / \langle u'w' \rangle) \quad (5)$$

We will assume for the purposes of this analysis that in the long-term average, the angle  $\theta$  is close to 0.

Primarily because numerical modelers need estimates of surface fluxes based on available weather data, the bulk aerodynamic formulations were introduced, i.e.,

$$|\tau/\rho| = \rho C_D U_{10}^2 \quad (6)$$

$$H = \rho c_p C_H U_{10} (T_0 - T_{10}) \quad (7)$$

$$E = \rho L_v C_E U_{10} (q_0 - q_{10}) \quad (8)$$

The subscripts 0 and 10 represent measurement heights in meters above the surface. The bulk exchange coefficients are  $C_D$  for wind drag (the drag coefficient),  $C_H$  (the Stanton number) for the sensible heat flux, and  $C_E$  (the Dalton number) for the latent heat flux. The surface humidity is assumed to be saturated with respect to the sea surface temperature. All three coefficients have magnitudes of the order of  $10^{-3}$ .

### 2.1. Surface Layer Scaling

Within the lowest part of the boundary layer, the vertical gradients in the wind speed, temperature, and humidity are much larger than the corresponding gradients in the fluxes. As a consequence, scaling relations were developed where the fluxes may be treated as "constant." The "constant flux layer," or surface layer, may be characterized by a wind speed gradient which is defined as

$$\partial U / \partial z = u^* / kz \phi_M(z/L) \quad (9)$$

where the function  $\phi_M$  has been evaluated by *Businger et al.* [1971] in the form.

$$\phi_M(z/L) = (1 - \alpha z/L)^{-1/4} \quad z/L < 0 \quad (10)$$

$$\phi_M(z/L) = 1 + \beta z/L \quad z/L > 0$$

*Panofsky and Dutton* [1984] suggest values for  $\alpha$ ,  $\beta$ , and  $k$  to be 16, 5, and 0.4, respectively. The friction velocity  $u^*$  is defined according to

$$|\tau| = \rho u_*^2 \quad (11)$$

The function  $\phi_M$  requires a measure of the stratification which is conventionally defined as a nondimensional quantity based on the height above the surface,  $z$ , and the Monin-Obukhov length  $L$  such that

$$z/L = -\frac{gkz \langle w'T_v' \rangle}{T_v u_*^3} \quad (12)$$

where  $g$  is the acceleration due to gravity. For unstable stratifications,  $z/L < 0$ , and for stable flow,  $z/L > 0$ . When the atmosphere is neutrally stratified,  $z/L = 0$ . The virtual temperature  $T_v$  is related to the air temperature  $T$  according to

$$T_v = T(1 + 0.61q) \quad (13)$$

By integrating the wind profile between a lower limiting

height  $z_0$ , which is also called the roughness length, to a height  $z$ , the wind speed profile is obtained:

$$U = u^*/k(\ln z/z_0 - \psi) \tag{14}$$

The stratification function  $\psi$  is an adjustment to the profile and has been derived by Paulson [1970] for unstable conditions to be

$$\psi = 2 \ln \left( \frac{1 + \phi_M^{-1}}{2} \right) + \ln \left( \frac{1 + \phi_M^{-2}}{2} \right) - 2 \tan^{-1} (\phi_M^{-1}) + \pi/2 \tag{15}$$

For stable stratifications, an empirical parameterization has been suggested by Lo and McBean [1978] to be

$$\psi = -5 z/L \tag{16}$$

By combining (2) and (11), the drag coefficient may be determined directly according to

$$C_D = (u_*/U_{10})^2 \tag{17}$$

By considering the wind profile, one may also write

$$C_D = [k/(\ln z/z_0 - \psi)]^2 \tag{18}$$

Variations in  $C_D$  due to wave state are usually modeled by relating the roughness length  $z_0$  to particular characteristics of the local wave field, for example, wave slope, height, or age.

For the purposes of the analysis presented herein, the heat fluxes were estimated according to the bulk method by defining

$$10^3 C_H = 1.08 \quad z/L < 0 \tag{19}$$

$$10^3 C_H = 0.83 \quad z/L > 0$$

$$10^3 C_E = 1.3 \tag{20}$$

where the values for  $C_H$  and  $C_E$  are based, on data reported by Smith [1980] and Anderson and Smith [1981], respectively.

Since the measurements of the drag coefficient must be compared with the results from other investigations, a neutral stratification counterpart to the measured drag coefficient has been defined, i.e.,  $C_{DN}$ , where  $C_{DN}$  is related to  $C_D$  according to

$$C_{DN} = (C_D^{-1/2} + \psi/k)^{-2} \tag{21}$$

2.2. The Wave Influence

The evidence for a wave state influence on the drag coefficient may be classified into two general areas: variations in  $C_D$  due to wave age, where wave age may be defined either as  $C_0/U$  or  $C_0/u^*$ , or variations due to short wave slope and energy, the latter of which is dependent on the surface tension. Given that  $C_0$  is the phase speed of the dominant wind wave, many data sets [DeLeonibus and Simpson, 1986; Graf et al., 1984; Davidson, 1974; Geernaert et al., 1986, 1987a, b] have shown that  $C_D$  is larger for a growing sea (young wave age) than for a decaying sea (old wave age). No widely accepted functional dependence of  $C_D$  on wave age has yet been derived.

Measurements of the drag coefficient in the presence of an artificial slick [Barger et al., 1970] indicated that the attenuation of high-frequency waves by the reduction of surface tension acts to dramatically decrease the magnitude of the wind profile's roughness length and consequently reduce the drag coefficient. Naturally occurring surface tension variations over such regions as the North Sea have been investigated by

Hühnerfuss et al. [1975], who implied that especially during low wind speeds, large excursions in the drag coefficient from typical bulk estimates could be expected.

Models developed to explain the variations of  $C_D$  with spectral wave parameters have been reviewed by Geernaert et al. [1986]. Theoretical approaches that consider primarily the characteristics of the dominant long wave include models proposed by Hsu [1974] and Byrne [1982]. Kitaigorodskii [1973] derived a dependence of the roughness length on higher-frequency wind waves, and Donelan [1982] assumed that the drag coefficient could be partitioned into two components, one due to the form drag over the primary ocean surface gravity wave and the second component due to the roughness induced by shorter wind waves. The models of Kitaigorodskii [1973], Hsu [1974], and Byrne [1982] each reduce for steady state conditions to the simple Charnock relation, where the relation proposed by Charnock [1955] is

$$z_0 = au^{*2}/g \tag{22}$$

and the Charnock coefficient  $a$  has a value of the order of  $10^{-2}$ .

2.3. The Dissipation Method

While the direct method measures the fluxes by definition from the covariance between fluctuating variables, it is a practical problem to conduct measurements from either unsteady or moving platforms. Since ships have motions with frequencies that are significantly lower than the frequencies in the turbulent wind's inertial subrange, the dissipation technique was introduced as a viable alternative to the operational measurement of the wind stress over the sea.

Neglecting molecular diffusion, the turbulent kinetic energy (TKE) equation may be written as

$$\frac{\partial e}{\partial t} = -\langle u'w' \rangle \frac{\partial u}{\partial z} - \langle v'w' \rangle \frac{\partial v}{\partial z} + \frac{g}{T} \langle w'T' \rangle - \frac{1}{\rho} \frac{\partial \langle w'p' \rangle}{\partial z} - \frac{\partial \langle w'e \rangle}{\partial z} - \epsilon \tag{23}$$

where  $\epsilon$  is the dissipation rate of TKE, and TKE is defined as

$$\text{TKE} = e = \frac{1}{2}(\langle u'u' \rangle + \langle v'v' \rangle + \langle w'w' \rangle) \tag{24}$$

Assuming that the angle  $\theta$  is small, and noting that  $\partial e/\partial t$  is insignificant when compared to other terms, (22) may be simplified to become

$$\langle u'w' \rangle \partial u/\partial z = g/T_r \langle w'T_r' \rangle - \epsilon - I \tag{25}$$

where the imbalance term  $I$  is

$$I = \frac{\partial}{\partial z} \left( \frac{1}{\rho} \langle w'p' \rangle + \frac{\partial}{\partial z} \langle w'e \rangle \right) \tag{26}$$

In (26), the first term on the right-hand side is the pressure transport, while the second term is the turbulent energy divergence. The quantities  $\langle w'e \rangle$  and  $\langle w'p' \rangle$  were measured at a single height over land by McBean and Elliott [1975]; their results indicated that from unstable through slightly stable stratifications,

$$\langle w'p' \rangle / \rho u_*^3 = 2.3 z/L - 0.20 \tag{27}$$

$$\langle w'e \rangle / u_*^3 = -2.3 z/L + \text{const} \tag{28}$$

[after Large, 1979]. Over a wider range of stratifications, Wyngaard and Cote [1971] found a nearly identical depen-

dence of the divergence term on buoyancy, i.e.,

$$\langle w'e \rangle / u_*^3 = -2.5 z/L + \text{const} \quad (29)$$

Subtracting (29) or (28) from (27) and differentiating, the imbalance term in the near-neutral regime over land is near zero. It is on the basis of this assumption that the imbalance term is often ignored and current operational calculations of the wind stress based on the dissipation method may proceed [Large and Pond, 1981; Boyle et al., 1987]. For the sake of our discussion, we will retain the imbalance term in the TKE budget and treat the errors in the dissipation-derived stresses in terms of  $I$ .

By combining (25) with (9), (10), and (11), one may easily write:

$$u_*^3 = kz(\epsilon + I)/\phi_\epsilon \quad (30)$$

where  $\phi_\epsilon = \phi_M - z/L$ .

Although the function  $\phi_\epsilon$  provides a reasonable correction to the stress for diabatic conditions, particularly when the stratifications are near-neutral, Kaimal et al. [1972] determined a stability function based on experimental data, such that

$$\begin{aligned} \phi_\epsilon^* &= (1 + 0.5|z/L|^{3/5})^{3/2} & z/L < 0 \\ \phi_\epsilon^* &= (1 + 2.5(z/L)^{2/3})^{3/2} & z/L > 0 \end{aligned} \quad (31)$$

where they assumed that (30) could be rewritten as

$$u_*^3 = kz \epsilon / \phi_\epsilon^* \quad (32)$$

It is easy to see by combining (30) and (32) that the term  $I$  must exhibit a weak dependence on stratification in the near-neutral regime:

$$I(z/L) = \epsilon(\phi_\epsilon / \phi_\epsilon^* - 1) \quad (33)$$

It must be pointed out that the stratification functions for the wind profile and for the dissipation technique have never been determined from measurements over the sea, and all of these relations are based on experiments conducted over land. An important difference between a land and water surface is that while a land surface remains stationary, water waves are generated by the wind stress. Water waves additionally propagate and interact with the wind by producing pressure perturbations that vary over the phase of the moving waves. We used (31) and (32) to operationally determine the wind stress during TOWARD.

The dissipation rate is determined by assuming that for frequencies within the inertial subrange, i.e., for frequencies above 2 Hz and a sampling height of 20 m, the spectral energy  $S$  is related to wave number  $k_\lambda$  and dissipation according to:

$$S(k_\lambda) = \alpha \epsilon^{2/3} k_\lambda^{-5/3} \quad (34)$$

where  $\alpha$  has a value of 0.52 [Wyngaard and Cote, 1971].

In (34), we used Taylor's hypothesis, i.e.,

$$k_\lambda = 2\pi f/U \quad (35)$$

where  $f$  is eddy frequency in hertz. Equation (35) may then be written

$$S(f) = \alpha(2\pi/U)^{-5/3} \epsilon^{2/3} f^{-5/3} \quad (36)$$

Although the spectral decomposition of the horizontal wind speed will yield  $S$  and  $f$  and consequently  $\epsilon$ , the method applied to our data analysis was to integrate (36) over eddy frequencies within the inertial subrange (bounded by 5 Hz and

50 Hz in our case), resulting in a band-passed variance,  $\sigma_u^2$ , described by

$$\sigma_u^2 = \frac{3\alpha}{2} (\epsilon U / 2\pi)^{2/3} (f_1^{-2/3} - f_2^{-2/3}) \quad (37)$$

Since  $\sigma_u^2$  represents the filtered wind variance from a spectrum analyzer,  $\epsilon$  may be easily calculated and  $u^*$  determined from (32). Given that the quality of the data is heavily dependent on the existence of the  $-5/3$  slope in the spectral power over frequency, each data record included a plotted spectrum so as to guarantee that the 5- and 50-Hz sampling limits were well within the inertial subrange. In those cases where this criterion was not satisfied, the record was deleted from the data set.

### 3. THE WIND STRESS MEASUREMENT PROGRAM

The meteorological measurements were collected on the Naval Ocean Systems Center (NOSC) tower, located 2 km offshore of Mission Beach, near San Diego, California. The tower has its highest level at approximately 11 m, and during TOWARD, an 11-m mast was mounted above the tower on its north end and was rigidly held with guide wires. Both the wind stress measurements with the sonic and the stress estimates from the hot film were based on instrument locations of 22 m above the surface. Both the cup anemometer for mean wind speed and the air and dew point temperature sensors were mounted at 18 m above the surface. The wind vane was located at 17 m. See Figure 2 for a diagram of the tower with the respective locations of each instrument.

The sonic and hot film systems were horizontally mounted on a rotor atop the mast which gave remote capability of pointing the sensors into the wind. Predominant winds at the NOSC tower were from the northwest (associated with the sea breeze), and maximum wind speeds were generally 7 or 8 m/s. Owing to the possibility of flow distortion, southerly and southeasterly winds were deleted from the data set. At the location of the tower, the water column depth was approximately 15 m, and wind waves generated by the sea breeze could therefore be characterized as deepwater waves. Large swell propagating from North Pacific storms, on the other hand, was a common occurrence and could generally be characterized as steep, shallow water waves. Calibration of the hot film required mean output voltages as a function of wind speed. The procedure was conducted many times during the field experiment and is reviewed by Geernaert et al. [1987a].

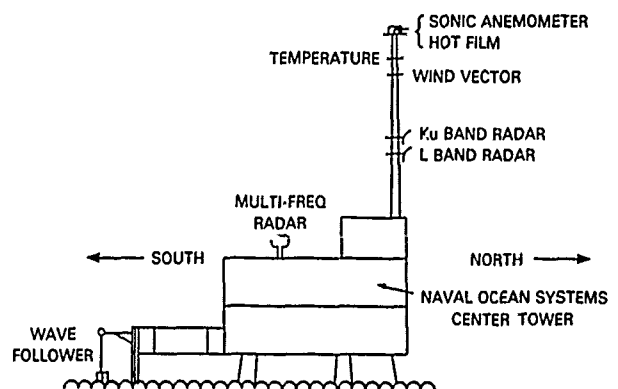


Fig. 2 Orientation of the Naval Ocean Systems Center tower with the location of the meteorological instruments on the vertical mast.

The data collection was conducted in two phases: the first phase from mid-September through early November 1984; and the second phase from mid-March through April 1985. A detailed summary of the meteorology conditions and the accompanying dissipation-derived stress estimates may be found in the work of Geernaert *et al.* [1987a].

The data acquisition system included a Hewlett-Packard 9825 computer, which was used to record 5-minute averages of the following quantities: wind speed and direction, air and dew point temperatures, sea temperature (at 3-m depth), and the variance of the voltage corresponding to the band-passed wind speed variance within the chosen inertial subrange frequency limits (5 and 50 Hz). Plots of the wind energy spectrum insured that the  $-5/3$  power law in the inertial subrange was not contaminated by either noise or nonstationary conditions. The sonic data were recorded on a 14-track Honeywell tape recorder. While the dissipation measurements were nearly continuous during both phases of the TOWARD experiment, the sonic data were collected only during selected period of interest. The compilation of the stress estimates by both methods, in addition to all meteorological variables, was based on an averaging time of 30 min.

4. RESULTS

In the first subsection of the results, we present the intercomparison between the  $u^*$  estimates from the sonic anemometer (the direct method) to those  $u^*$  estimates derived from the dissipation technique (using equations (31), (32), and (34)). The second subsection will describe only the dissipation  $u^*$  data, and finally, in the third subsection, inferences of wave effects on the drag coefficient will be presented using TOWARD data.

4.1. Intercomparison Between Sonic and Hot Film

The compilation of 3 days of  $u^*$  estimates by both the eddy correlation (sonic anemometer) and dissipation (hot film) techniques is presented in Figure 3. At a first glance, it would seem that a bias is evident, i.e.,  $u^*$  by dissipation method is smaller than the  $u^*$  by the direct method; however, under closer inspection, the environmental conditions associated with much of the data were far from ideal.

We have compiled in Table 1 the time series of the wind speeds, stratifications, and  $u^*$  estimates; in addition, we have calculated the ratio of the  $u^*$  values by the two techniques with the corresponding normalized imbalance terms for each data record. The measured imbalance has been calculated by rearranging (30) into the form

$$I(\text{meas}) = u_*^3 \phi_z/kz - \epsilon \tag{38}$$

Since  $I(\text{meas})$  contains an inherent stratification dependence which has been described in (33), we may examine the effect of nonstationarity in the atmospheric surface layer and/or wave field on the dissipation method by defining a residual imbalance as

$$I(\text{res}) = I(\text{meas}) - I(z/L) \tag{39}$$

For the purposes of this study,  $I(\text{res})$  has been normalized against the mechanical production term (of the TKE equation), i.e.,

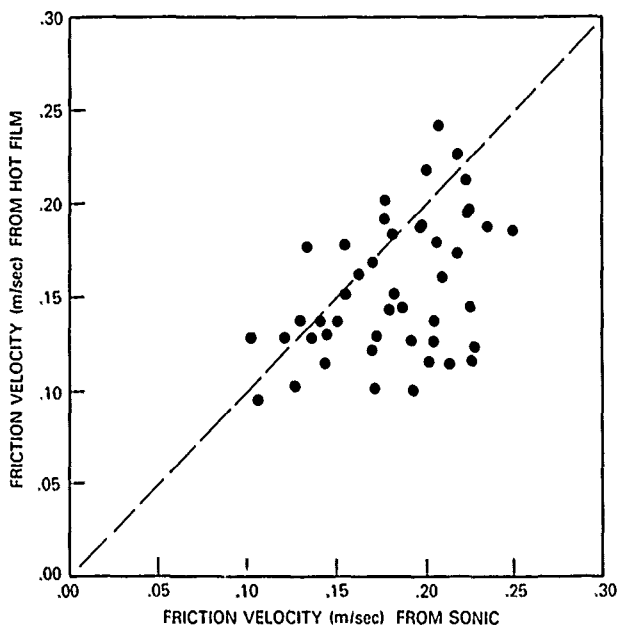


Fig. 3. Intercomparison between directly measured  $u^*$  values from the sonic anemometer to calculated  $u^*$  values using the hot film dissipation technique.

$$I_r = I(\text{res})/(u_*^3 \phi_M/kz) \tag{40}$$

The perfect correlation between the direct and dissipation techniques should then be associated with a value of  $I(\text{res})$  of 0.

The 3 days of simultaneous sonic and dissipation data were unique in terms of the differing environmental conditions. On the first day (March 25, 1985), stratifications were in general near neutral. The wind direction was additionally observed to gradually shift from southwest to south-southeast during the course of the afternoon. With no major changes in the weather conditions, the dissipation technique produced  $u^*$  estimates that were in close agreement with the directly measured  $u^*$  from the sonic anemometer.

On the second day (March 26, 1985), the environmental conditions were characterized by mostly stable stratifications, and large variations in the magnitude of  $z/L$  were observed within the time series of 30-min records. There was additionally observed a large variation in the wind direction. This second day is generally characterized by dissipation  $u^*$  estimates of as much as 30% less than the direct  $u^*$  measurements.

On the last day of the intercomparison (March 27, 1985), the stratifications were again very stable, but the wind speed and direction were both steady. The comparison yielded dissipation-derived  $u^*$  estimates underestimated by between 15% and 40%. See Figures 4, 5, and 6 for the time series of these results.

Although it appears that the dissipation-derived  $u^*$  estimates are of high quality during neutral, steady conditions, which is in agreement with the results of Large and Pond [1981], a stability dependence is exhibited in both the resulting  $I(\text{res})$  and also the ratio of  $u^*(\text{diss})$  to  $u^*(\text{direct})$ , i.e., a consistently small value for the ratio during stable flow. The full set of  $u^*$  estimates from the TOWARD experiment will be presented in the next section in order to illustrate the stratification bias.

TABLE 1. Compilation of Statistics for the Intercomparison Between the Sonic and Hot Film Techniques

Record	Stop Date	Hour	$U_{10}$	Wind Direction, deg	$z/L$	$u^*$		$R$	$I_r$
						Direct	Dissipation		
1	March 25	1300	6.48	243	0.068	0.228	0.216	0.947	0.137
2	March 25	1330	5.82	240	0.144	0.159	0.165	1.038	-0.103
3	March 25	1430	5.78	240	0.270	0.135	0.153	1.133	-0.388
4	March 25	1530	6.19	230	0.042	0.223	0.229	1.027	-0.078
5	March 25	1730	6.20	225	0.000	0.209	0.246	1.177	-0.631
6	March 25	1800	5.89	230	-0.024	0.202	0.221	1.094	-0.329
7	March 25	1830	4.33	216	-0.007	0.180	0.194	1.078	-0.256
8	March 25	1900	3.34	186	0.000	0.179	0.183	1.022	-0.069
9	March 25	1930	3.86	175	0.000	0.170	0.170	1.000	0.000
10	March 25	2000	4.59	155	0.005	0.221	0.180	0.814	0.455
11	March 25	2030	5.04	153	0.016	0.200	0.191	0.955	0.125
12	March 25	2100	5.18	154	0.014	0.213	0.200	0.939	0.168
13	March 25	2130	5.71	150	0.061	0.182	0.197	1.082	-0.247
14	March 25	2200	5.78	155	0.053	0.208	0.181	0.870	0.316
15	March 25	2230	5.91	156	0.109	0.167	0.152	0.910	0.219
16	March 26	730	3.59	210	0.013	0.126	0.131	1.040	-0.121
17	March 26	830	3.75	233	0.020	0.207	0.143	0.691	0.646
18	March 26	930	3.89	215	0.018	0.229	0.154	0.672	0.673
19	March 26	1000	3.71	214	0.009	0.183	0.145	0.792	0.493
20	March 26	1030	3.29	224	0.006	0.148	0.134	0.905	0.255
21	March 26	1100	3.63	221	0.023	0.133	0.135	1.015	-0.044
22	March 26	1200	4.56	215	0.013	0.194	0.130	0.670	0.682
23	March 26	1230	4.67	220	0.040	0.173	0.139	0.803	0.452
24	March 26	1300	4.58	227	0.015	0.212	0.168	0.792	0.488
25	March 26	1330	4.76	244	0.060	0.176	0.134	0.761	0.514
26	March 26	1400	4.96	252	0.058	0.219	0.148	0.676	0.638
27	March 26	1430	5.12	260	0.060	0.230	0.133	0.578	0.742
28	March 26	1500	4.27	270	0.094	0.173	0.108	0.624	0.680
29	March 26	1530	3.95	260	0.196	0.133	0.097	0.729	0.528
30	March 26	1630	3.78	260	0.332	0.110	0.084	0.764	0.468
31	March 26	1700	4.91	275	0.214	0.145	0.107	0.738	0.514
32	March 26	1730	6.39	290	0.154	0.188	0.134	0.713	0.558
33	March 26	1800	5.64	280	0.085	0.184	0.149	0.810	0.424
34	March 26	1830	4.35	280	0.020	0.205	0.122	0.595	0.761
35	March 26	1900	4.55	275	0.108	0.110	0.120	1.091	-0.266
36	March 26	1930	3.58	272	0.005	0.173	0.128	0.749	0.589
37	March 26	2000	3.24	250	0.000	0.141	0.129	0.915	0.234
38	March 26	2030	3.92	230	0.000	0.155	0.137	0.884	0.309
39	March 27	1430	6.28	255	0.110	0.253	0.193	0.763	0.495
40	March 27	1500	6.32	256	0.208	0.212	0.182	0.858	0.316
41	March 27	1530	5.49	260	0.372	0.158	0.135	0.854	0.316
42	March 27	1700	5.29	265	0.126	0.230	0.129	0.561	0.728
43	March 27	1730	5.36	263	0.215	0.195	0.106	0.544	0.721

$R$  is the ratio between the friction velocities determined by the hot film and sonic techniques, while  $I_r$  is the normalized imbalance term.

#### 4.2. TOWARD Drag Coefficients Using the Dissipation Technique

A wide variety of conditions were encountered during the TOWARD experiment. Three cold fronts with good meteorological coverage passed through the San Diego region on October 15-16, 1984; March 18, 1985; and March 25, 1985. A large range in atmospheric stratifications was additionally encountered. Unfortunately, only a small portion of the 486 30-min data records collected during TOWARD were associated with wind speeds exceeding 5 m/s.

The results of all the neutral drag coefficient measurements were determined by calculating an equivalent 10-m height wind speed, and adjustments were made for the surface layer stratification. The calculated  $C_{DN}$  values are plotted as a function of the 10-m height wind speed in Figure 7, where the range in stability was limited to  $|10 \text{ m}/L| < 0.8$ . For wind speeds above 5 m/s, the encountered stabilities spanned the range  $-0.3 < 10 \text{ m}/L < 0.5$ .

Because the residual imbalance terms (in section 4.1) seemed to exhibit a dependence on stratification, we chose to examine the dependence of the dissipation method on the stratification by plotting the neutral drag coefficient  $C_{DN}$  against the stability parameter  $z/L$ . Theoretically,  $C_{DN}$  should exhibit no stability dependence, and any resulting stability dependence would imply that the functions  $\phi_M$ ,  $\phi_e^*$ ,  $\phi_e$ , and  $\psi$  may be in question. In order to avoid any  $C_{DN}$  dependence on wind speed, we examined the  $C_{DN}$  dependence on  $z/L$  over narrow 1-m/s wind speed bands.

For the 5- to 6-m/s wind speed band,  $C_{DN}$  is plotted against  $z/L$  in Figure 8. The 6- to 7-m/s band is similarly presented in Figure 9. The strong dependence of  $C_{DN}$  on  $z/L$  is consistent with the sonic-hot film intercomparison presented in section 4.1; i.e., stresses are underestimated by the dissipation technique during stable flow.

By successively sorting the full  $C_{DN}$  data set into narrower stability ranges about neutral, means and standard deviations of the neutral drag coefficient over the encountered wind

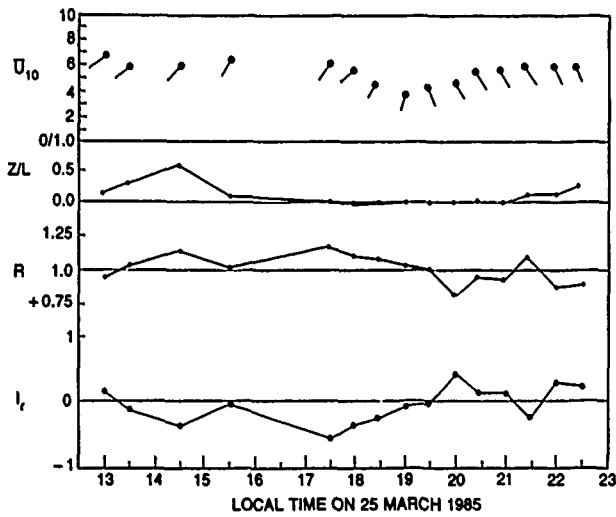


Fig. 4. Time series of meteorological conditions with the associated ratio of  $u^*$ (diss) to  $u^*$  and the residual imbalance term (denoted as  $I_r$ ) for March 25, 1985.

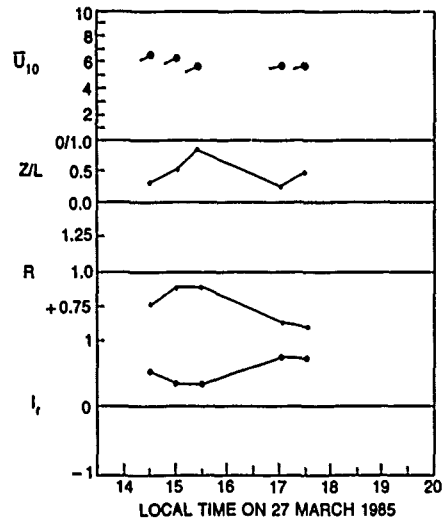


Fig. 6. Same as Figure 4 for March 27, 1985.

speed bands were calculated; these results are reported in Table 2. For the full TOWARD data set, the stratifications were on the average slightly stable, and as a consequence, estimates of the mean  $C_{DN}$  for each wind speed band increased as the range of stability was tightened about neutral.

Low wind speeds exhibited the largest scatter in the neutral drag coefficients, as depicted in Table 2, and this scatter is consistent with maximum uncertainties and errors at low wind speeds. A criterion for accurate surface stress calculations is that the sensor height must be within the surface layer. For neutral conditions, Tennekes [1973] determined that the surface layer height is approximated as  $0.03u_* / f$ , where  $f$  is the Coriolis parameter. Since our measurements were conducted at 22 m above the surface, neutral wind speeds must in general be greater than 2.5 m/s in order to satisfy this criterion. We arbitrarily chose our lower limiting wind speed to be 3.5 m/s in this study for better assurance. Further, the uncertainty in the  $u^*$  estimate by the dissipation method depends on both

the averaging time  $t$ , measurement height  $z$ , and wind speed  $U$ , according to [after Wyngaard, 1973]

$$p^* = 2(z/tU)^{1/2} \tag{41}$$

where the uncertainty is given by  $p^*$ . Given that  $z = 22$  m and  $t = 30$  min, a 3.5-m/s wind speed corresponds to a 12% uncertainty in the  $u^*$  estimate.

With the uncertainty criteria and a constraint on the stratification defined as  $|z/L| < 0.05$ , we have plotted the neutral drag coefficients as a function of wind speed in Figure 10. For the data associated with wind speeds above 4 m/s, a best fit regression line was found to be

$$10^3 C_{DN} = 5/U_{10} + 0.07U_{10} \tag{42}$$

with a standard deviation of 0.38, and the wind speed is in units of meters per second. These predicted  $C_{DN}$  magnitudes are in close agreement with the results of Large and Pond [1981] and Smith [1980]. While containing only low to moderate windspeeds, we have plotted in Figure 11 the distri-

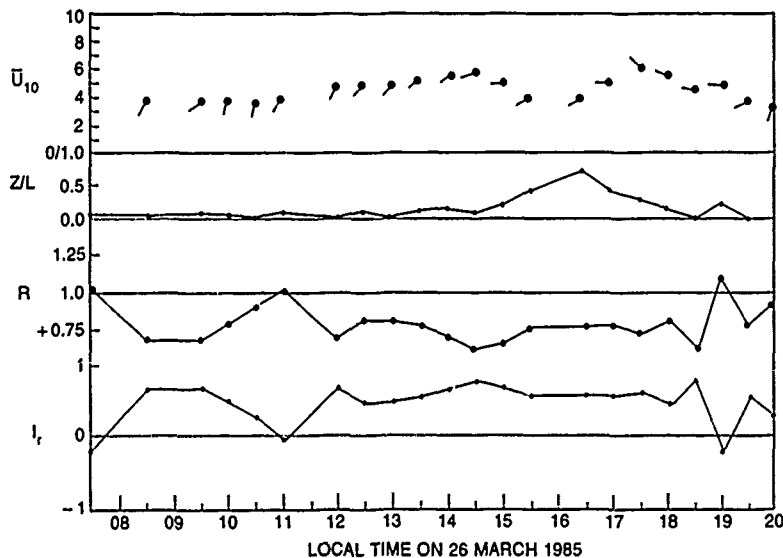


Fig. 5. Same as Figure 4 for March 26, 1985.

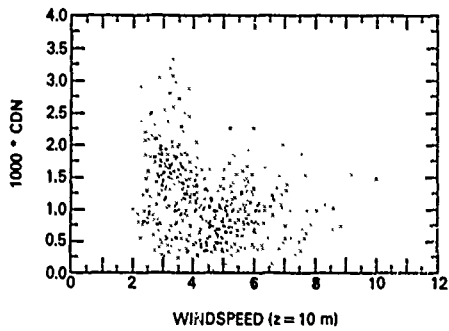


Fig. 7. Distribution of neutral drag coefficient measurements by the dissipation method as a function of the wind speed at 10-m height. The 486  $C_{DN}$  data records are based on 30-min averaging times and corresponding to wind directions from westerly through northeasterly.

bution of the sonic-derived eddy correlation neutral drag coefficients with the wind speed at 10-m height.

#### 4.3. Indications of a $C_{DN}$ Dependence on Wave State

Using only the subset of  $C_{DN}$  measurements reported in Figure 8, very little stratification dependence should be exhibited in the  $C_{DN}$  variability, and the remaining scatter is presumed here to depend in large part on the state of wave development. Although the Charnock relation is an implicit relation between  $C_{DN}$  and waves (since both the wave field grows and  $z_0$  increases as a result of the downward momentum (flux), several dynamic models have emerged which relate  $z_0$  and/or  $C_{DN}$  to specific energy densities of the wave spectrum. A bulk scaling parameter that is typically employed is the wave age  $C_0/u_*$ , where  $C_0$  is the phase speed of the dominant locally generated surface gravity wave. Steady state conditions have an associated value for  $C_0/u_*$  to be in the neighborhood of 25–30. Based on a statistical study of two North Sea experiments, Geernaert *et al.* [1987b] found that  $C_{DN}$  scales to first order according to  $(C_0/u_*)^{-2/3}$ .

For a typical coastal sea breeze circulation (observed in the San Diego region), the wind shifts from an easterly to a westerly direction within a very short period of time, and the wind speed rapidly increases. The seas additionally begin to grow with the onset of the westerly wind. When the sea breeze circulation is set in motion and the steady westerly winds are achieved, the surface wave spectrum continues to grow and asymptotically approaches equilibrium with the wind forcing.

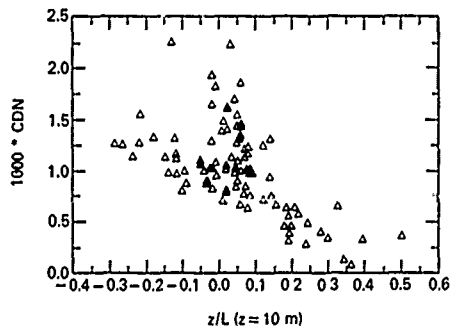


Fig. 8. Distribution of the calculated neutral drag coefficient by the dissipation method with atmospheric stratification, where  $z = 10$  m,  $L$  is the Monin-Obukhov length, and wind speeds are between 5 and 6 m/s.

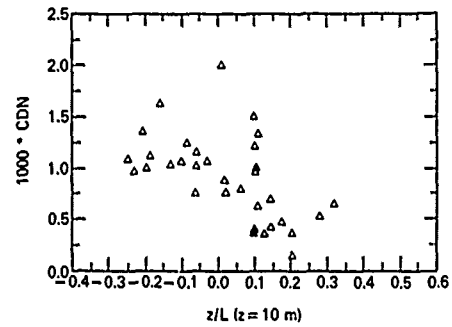


Fig. 9. Distribution of the calculated neutral drag coefficient by the dissipation method with atmospheric stratification, where  $z = 10$  m,  $L$  is the Monin-Obukhov length, and wind speeds are between 6 and 7 m/s.

As the spectrum gains energy, the peak frequency of the local equilibrium range decreases, and the corresponding phase speed of the dominant wave increases in magnitude. Since the overall evidence for  $C_{DN}$  variations corresponds to variations in the inverse of the ratio  $(C_0/u_*)$ , one would therefore also expect the neutral drag coefficient to decrease in magnitude during the course of a coastal sea breeze.

During TOWARD the trend in the neutral drag coefficient during the afternoon sea breeze at the NOSC tower was generally consistent with the above hypothesis, i.e., decreasing magnitudes of  $C_{DN}$  with time, particularly when the afternoon winds exceeded 6 m/s and the stability was near neutral. Illustrated in Figure 12 is a time series of neutral drag coefficients with the corresponding meteorology measurements for October 18, 1984.

Occasionally, high-quality measurements of the microscale wave structure were recorded during TOWARD. However, no adequate time series of wave statistics within the equilibrium range was available. Since the wave state can be modeled both as a function of time duration and wind forcing based on bulk parameters, the behavior of the drag coefficient during the course of the sea breeze may be predicted by applying the relation [after Titov, 1971]

$$\omega_0 = 1.5(tu_*^2/g^2)^{-1/3} \quad (43)$$

where  $t$  is the time duration since the onset of a steady wind after a rapid increase. Since  $C_0 = g/\omega_0$ , the neutral drag coefficient must scale with the quantity  $(gt, u_*)^{-1/3}$ . Geernaert [1988] has generalized the time duration problem by treating the wind drag through the roughness length such that

$$z_0 = 10 \text{ m} \exp(-1/15 u_*^{-4/9} g^{5/18} X^{1/6} t^{1/9}) \quad (44)$$

where  $X$  is the upwind fetch. Equation (44) is based on incorporating  $\omega_0$  as a function of the dimensionless fetch [Hasselmann *et al.*, 1973]. The roughness length is related to the drag coefficient through (18).

Equation (44) suggests that if the wind rapidly "turns on," as it often does during the daily San Diego sea breeze,  $C_{DN}$  should be initially large but should decrease with time, which is consistent with the  $C_{DN}$  time series in Figure 12. We have overlaid in Figure 12 the predicted distribution of  $C_{DN}$  with time duration for  $X = 25$  km and  $U = 7$  m/s.

Although  $C_0/u_*$  may provide a first-order description of a drag coefficient dependence on wave state, Barger *et al.* [1970] showed from field data that the attenuation of high frequency waves by an artificial surface slick dramatically reduced the

TABLE 2.  $C_{DN}$  Versus Wind Speed for Different Stability Constraints

Wind Speed, m/s	All $z/L$		$ z/L  < 0.1$		$ z/L  < 0.05$	
	$10^3 C_{DN}$	$N$	$10^3 C_{DN}$	$N$	$10^3 C_{DN}$	$N$
2-3	1.54 ± 0.73	85	2.02 ± 0.60	24	2.00 ± 0.48	16
3-4	1.43 ± 0.72	130	1.86 ± 0.72	50	1.97 ± 0.61	38
4-5	0.96 ± 0.42	109	1.10 ± 0.37	51	1.17 ± 0.40	27
5-6	1.02 ± 0.43	95	1.16 ± 0.34	59	1.23 ± 0.36	34
6-7	0.91 ± 0.40	34	1.00 ± 0.36	18	1.18 ± 0.48	4
7-8	0.85 ± 0.41	19	1.16 ± 0.40	8	1.22 ± 0.39	7
8-9	1.01 ± 0.26	9	1.24 ± 0.14	4	1.35 ± 0.04	2
9-10	1.45 ± 0.12	4	1.45 ± 0.12	4	...	...
10-11	1.48	1	1.48	1	...	...

$N$  is the number of data records per wind speed range.

value of  $C_{DN}$ . In that study, the higher-frequency roughness elements were shown to have as important an impact on the magnitude of the drag coefficient as did the form drag over longer waves. Surface tension variability in the natural environment is very prevalent during low to moderate wind speeds, particularly in regions of biological activity and/or internal waves. Such variability not only influences the growth rate of short waves but also affects the dispersion rate for capillary waves.

During TOWARD, surface tension measurements were collected at 3-min intervals during selected periods [Garrett, 1986]. In our wind stress study, the surface tension measurements were averaged to produce 30-min means; these values were subsequently matched with the simultaneous measurements of the 30-min averaged neutral drag coefficient. The set of data pairs ( $C_{DN}$ , surface tension) was then reduced by requiring that  $|z/L| < 0.05$  and by specifying wind speeds within the range of 4 to 6 m/s. The data pairs of this subset are plotted in Figure 13.

A linear best fit relation between  $C_{DN}$  and surface tension  $G$  was found to be

$$10^3 C_{DN} = 1.17 + C_{st}(G - 72) \tag{45}$$

where  $C_{st}$  was found to be  $0.0363 \text{ cm}^2/\text{dyn}$ . The scatter in (45) was determined to be  $\pm 0.242$ . By treating the 42  $C_{DN}$  data alone, the corresponding mean was 1.105 with a scatter of  $\pm 0.254$ . The 95% confidence interval for the slope  $C_{st}$  was found to be  $\pm 0.0242$ . We additionally found that the data supported a value of  $C_{st}$  to be positive at the 98% confidence level. The positive value of  $C_{st}$  is consistent with both the results of Barger *et al.* [1970] and the wind drag modeling of

Kitaigorodskii [1973] and additionally follows the principles of scatterometer detection of the surface wind stress according to variations in short wave slope.

The data subset comprising the analysis of  $C_{DN}$  as a function of surface tension was derived from measurements collected both in the autumn (1984) and spring (1985). Sea surface temperatures in the spring were in the neighborhood of  $13.0^\circ \pm 0.5^\circ\text{C}$ , while in the autumn the sea surface temperatures were  $18.0^\circ \pm 1.0^\circ\text{C}$ . Since 35 of the 42 data records were collected during the autumn, we analyzed these 35 records separately so as to avoid any possible temperature dependence on the drag coefficient and/or surface tension. For both  $C_{DN}$  and  $T$ , temperature effects on the magnitude of water viscosity have a significant impact on the growth rates and dynamics of capillary waves [Kinsman, 1965]. The results of this analysis at a nearly constant surface temperature of  $18^\circ\text{C}$  shows a similar trend, i.e.,

$$10^3 C_{DN} = 1.18 + C_{st}(G - 72)$$

where  $C_{st} = 0.0356 \text{ cm}^2/\text{dyn}$ . The 95% confidence interval about  $C_{st}$  was determined to be  $\pm 0.0263 \text{ cm}^2/\text{dyn}$ .

5. SUMMARY

The TOWARD wind stress results raised high uncertainty in employing the set of equations based on the dissipation method when stratifications were stable and/or when the lower atmosphere was unstationary. However, during homogeneous neutral flow, the comparison between the directly determined wind stress (by the sonic anemometer) and the dissipation-derived stress (from the hot film) yielded close agreement. Drag coefficients determined from the full TOWARD set of dissipation measurements yielded means

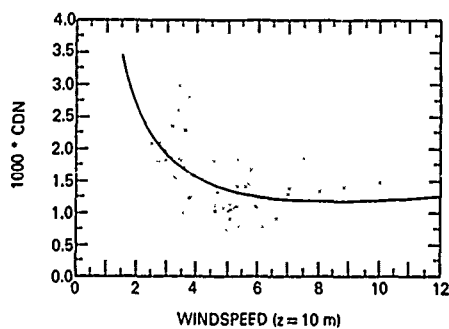


Fig. 10. Distribution of measured drag coefficients  $C_{DN}$  with wind speed for  $|z/L| < 0.05$  and  $z = 10 \text{ m}$ . The best fit line is  $10^3 C_{DN} = 5/U + 0.07U$ .

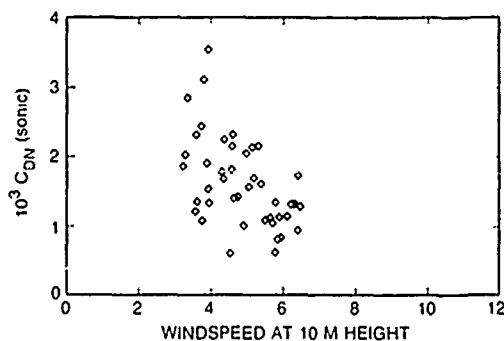


Fig. 11. Neutral drag coefficients determined by the eddy correlation method distributed according to wind speed.

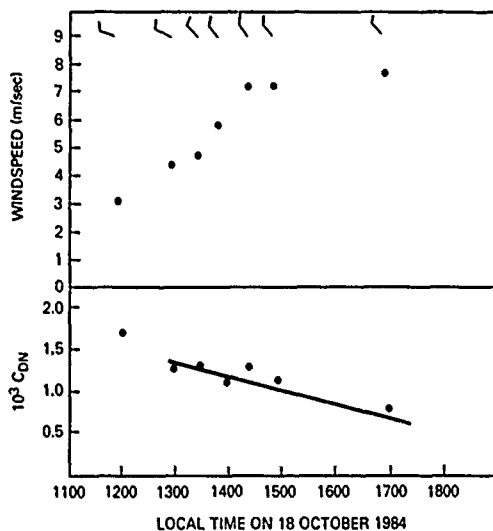


Fig. 12. Time series of neutral drag coefficients and weather data during a sea breeze circulation on October 18, 1984. The overlaid line represents predicted values of  $C_{DN}$  based on a 25-km fetch and time duration after a sea breeze beginning at 1300 LT.

that were in close agreement with past data sets only if the data were screened for stabilities close to neutral. These results suggest that the stratification corrections and the nature of the pressure transport and energy-divergence terms of the TKE equation need to be investigated in a comprehensive field experiment to be conducted over an ocean surface. The utility of such an investigation will provide higher-quality stress estimates using the dissipation technique for stable stratifications. Since remote sensing of the ocean surface using synthetic aperture radars, scatterometers, and passive systems requires information on the wind stress, it is likely that dissipation systems will be employed routinely on buoys and ships to meet the operational needs of the validation programs.

Using only near-neutral and moderate wind speeds (at least 4 m/s), the dissipation-derived drag coefficients exhibited an increasing dependence on surface tension. This dependence was found to be consistent with the results of Barger et al. [1970] and the modeling efforts of Kitaigorodskii [1973]. Since the scatterometer predicts smaller values of  $u^*$  for small short wave slopes, the  $C_{DN}$ -trend with surface tension is consistent with the scatterometer-model function which predicts  $u^*$ . The observed decrease of  $C_{DN}$  during the course of the sea breeze is consistent with the simultaneous increase in the parameter  $C_0/u^*$  which was modeled with time duration.

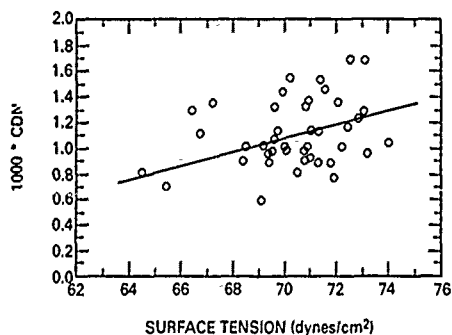


Fig. 13. Distribution of  $C_{DN}$  with surface tension where wind speeds are between 4 and 6 m/s and  $|10 m/L| < 0.05$ . The best fit line is  $10^3 C_{DN} = 1.17 + 0.038(G - 72 \text{ dyn/cm}) \pm 0.24$ .

**Acknowledgments.** We gratefully acknowledge Hans Dolezalek and Omar Shemdin for organizing the Tower Ocean Wave and Radar Dependence Experiment. Credit is additionally due to the staff of the Naval Ocean Systems Center, who not only provided the measurement platform but also provided transportation to and from the tower during the experiment. This research was sponsored by both the Office of Naval Research Coastal Oceanography Program and the Naval Research Laboratory Basic Research Program.

#### REFERENCES

- Anderson, G., and S. D. Smith, Evaporation coefficient for the sea surface from eddy flux measurements, *J. Geophys. Res.*, **85**, 443-452, 1981.
- Barger, W. R., W. D. Garrett, E. L. Mollo-Christensen, and K. Ruggles, Effects of an artificial slick upon the atmosphere and ocean, *J. Appl. Meteorol.*, **9**, 396-400, 1970.
- Boyle, P. J., K. L. Davidson, and D. E. Spiel, Characteristics of over-water surface stress during STREX, *Dyn. Atmos. Oceans*, **10**, 343-358, 1982.
- Businger, J. A., J. C. Wyngaard, and Y. Izumi, Flux profile relationships in the atmospheric surface layer, *J. Atmos. Sci.*, **28**, 181-189, 1971.
- Byrne, H. M., The variation of the drag coefficient in the marine surface layer due to temporal and spatial variations in the wind and sea state, Ph.D. dissertation, Univ. of Wash., Seattle, 1982.
- Charnock, H., Wind stress on a water surface, *Q. J. R. Meteorol. Soc.*, **81**, 639-640, 1955.
- Davidson, K. L., Observational results on the influence of stability and wind-wave coupling on the momentum transfer and turbulent fluctuations over the ocean, *Boundary Layer Meteorol.*, **6**, 305-331, 1974.
- De-Leonibus, P. S., and L. S. Simpson, Near neutral drag coefficients over open ocean waves, *J. Oceanic Eng.*, **11**, 480-484, 1986.
- Donelan, M. A., The dependence of the aerodynamic drag coefficient on wave parameters, in *First International Conference on Meteorology and Air-Sea Interaction of the Coastal Zone*, pp. 381-387, American Meteorological Society, Boston, Mass., 1982.
- Fairall, C. W., and S. E. Larsen, Inertial-dissipation methods and turbulent fluxes at the air-ocean interface, *Boundary Layer Meteorol.*, **34**, 287-301, 1986.
- Garrett, W., Surface tension measurements, in *2nd Interim Report on the TOWARD Experiment*, Office of Naval Research, Arlington, Va., 1986.
- Geernaert, G. L., On the importance of the drag coefficient in air-sea interactions, *Dyn. Atmos. Oceans*, **11**, 19-38, 1987.
- Geernaert, G. L., Influence of long and short waves on the drag coefficient in coastal regions, paper presented at the Conference on Meteorology of the Coastal Zone, Am. Meteorol. Soc., Boston, Jan. 31-Feb. 5, 1988.
- Geernaert, G. L., K. B. Katsaros, and K. Richter, Variation of the drag coefficient and its dependence on sea state, *J. Geophys. Res.*, **91**, 7667-7679, 1986.
- Geernaert, G. L., B. J. Byars, K. L. Davidson, S. E. Larsen, and T. Mikkelsen, Meteorology results from the Tower Ocean Wave and Radar Dependence Experiment, *Techn. Rep. NPS-63-87-001*, 117 pp., Naval Postgrad. School, Monterey, Calif., 1987a.
- Geernaert, G. L., S. E. Larsen, and F. Hansen, Measurements of the wind stress, heat flux, and turbulence statistics over the North Sea during storm conditions, *J. Geophys. Res.*, **92**, 13,127-13,139, 1987b.
- Graf, W. H., N. Merzi, and C. Perrinjaquet, Aerodynamic drag measured at a nearshore platform on Lake Geneva, *Arch. Meteorol. Geophys. Bioklimatol., Ser. A*, **33**, 151-173, 1984.
- Guest, P. S., and K. L. Davidson, The effect of observed ice conditions on the drag coefficient on the summer East Greenland Sea marginal ice zone, *J. Geophys. Res.*, **92**, 6943-6954, 1987.
- Hasselmann, K., et al., Measurements of wind wave growth and decay during the Joint North Sea Wave Project (JONSWAP), *Dtsch. Hydrogr. Zeitung*, **12**(8), suppl. A, 95 pp., 1973.
- Hsu, S. A., A dynamic roughness equation and its application to wind stress determination at the air-sea interface, *J. Phys. Oceanogr.*, **4**, 116-120, 1974.
- Hühnerfuss, H., On the variability of surface tension with wind speed, *J. Phys. Oceanogr.*, **5**, 567-571, 1975.
- Kaimal, J. C., J. C. Wyngaard, Y. Izumi, and O. R. Cote, Spectral characteristics of surface layer turbulence, *Q. J. R. Meteorol. Soc.*, **98**, 563-589, 1972.

- Keller, W. C., W. J. Plant, and D. E. Weissman, The dependence of X band microwave sea return on atmospheric stability and sea state, *J. Geophys. Res.*, **90**, 1019-1029, 1985.
- Kinsman, B., *Wind Waves*, 675 pp., Prentice-Hall, Englewood Cliffs, N. J., 1965.
- Kitaigorodski, S. A., *The Physics of Air-Sea Interaction*, translated from Russian by A. Baruch, Israel Program for Scientific Translation, Jerusalem, 1973.
- Kondo, J., Air-sea bulk transfer coefficients in diabatic conditions, *Boundary Layer Meteorol.*, **9**, 91-112, 1975.
- Large, W. G., The turbulent fluxes of momentum and sensible heat over the open ocean during moderate to strong winds, Ph.D. dissertation, 180 pp., Univ. of B.C., Vancouver, Canada, 1979.
- Large, W. G., and S. Pond, Open ocean momentum flux measurements in moderate to strong winds, *J. Phys. Oceanogr.*, **11**, 324-336, 1981.
- Lo, A. K., and G. A. McBean, On the relative errors in flux calculations, *J. Appl. Meteorol.*, **17**, 1704-1711, 1978.
- McBean, G. A., and J. A. Elliott, The vertical transports of kinetic energy by turbulence and pressure in the boundary layer, *J. Atmos. Sci.*, **32**, 753-766, 1975.
- Panofsky, H. A., and J. A. Dutton, *Atmospheric Turbulence*, 397 pp., Wiley-Interscience, New York, 1984.
- Paulson, C. A., The mathematical representation of wind speed and temperature profiles in the unstable atmospheric surface layer, *J. Appl. Meteorol.*, **9**, 857-861, 1970.
- Sheppard, P. A., D. T. Tribble, and J. R. Garratt, Studies of turbulence in the surface layer over water (Lough Neagh), 1, Instrumentation, programme, and profiles, *Q. J. R. Meteorol. Soc.*, **98**, 627-641, 1972.
- Smith, S. D., and E. G. Banke, Wind stress and heat flux over the ocean during gale force winds, *J. Phys. Oceanogr.*, **10**, 709-726, 1980.
- Smith, S. D., and E. G. Banke, Variation of the sea surface drag coefficient with wind speed, *Q. J. R. Meteorol. Soc.*, **101**, 665-673, 1975.
- Titov, L. F., *Wind-Driven Waves*, translated from Russian by D. Lederman, 244 pp., Israel Program for Scientific Translation, Jerusalem, 1971.
- Wyngaard, J. C., On surface-layer turbulence, in *Workshop on Micrometeorology*, pp. 101-149, American Meteorological Society, Boston, Mass., 1973.
- Wyngaard, J. C., and O. R. Cote, The budgets of turbulent kinetic energy and temperature variance in the atmospheric surface layer, *J. Atmos. Sci.*, **28**, 190-201, 1971.
- 
- K. L. Davidson, Department of Meteorology, Naval Postgraduate School, Monterey, CA 93943.
- G. L. Geernaert, Code 8314.3, Naval Research Laboratory, Washington, D. C., 20375
- S. E. Larsen and T. Mikkelsen, Riso National Laboratory, DK-4000 Roskilde, Denmark.

(Received December 2, 1987;  
accepted February 22, 1988.)